THERMODYNAMIC ANALYSIS OF INDIRECT INJECTION DIESEL ENGINE OPERATION

by

Mostafa M. Kamel

B.Sc., M.Sc., D.I.C.

Thesis submitted for the degree of

Doctor of Philosophy

in the Faculty of Engineering of the

University of London

1977

Department of Mechanical Engineering,
Imperial College of Science and Technology,
London SW7 2BX

To my

MOTHER

ABSTRACT

An investigation is presented which analyses, both theoretically and experimentally, the operation of the Indirect Injection Diesel Engine.

A computer program was developed to mathematically simulate the thermodynamic processes involved in the operation of the indirect injection diesel engine. The quasi-steady filling and emptying approach was employed to describe gas flow and changes in thermodynamic conditions. Numerical techniques were used to integrate the governing equations describing the engine thermodynamics along equal crank angle increments over the full engine cycle.

In the simulation program a correlation was developed for heat flux calculations. This was based on a Nu-Re relationship, in which velocity estimates representative of the chamber charge are obtained via the kinetic energy conservation concept. The correlation provided good predictions of heat fluxes in the cylinder and the prechamber when compared with measured behaviour.

The discharge coefficient of the connecting passage was found to be dependent on its shape. It was also found to be a function of the flow direction and pressure ratio. The effect of piston proximity was also investigated and accounted for.

Ignition delay periods were measured and correlated to chamber conditions. Both physical and chemical parts of the delay were considered.

An extensive experimental programme has been carried out to obtain steady state data for the engine under test. From the measured pressure diagrams of both chambers, rate of heat release curves were calculated. These were used in conjunction with the cycle analysis program to evaluate

engine performance.

The simulation program was finally used to isolate and quantify losses in the indirect injection diesel engine, and investigate the sources of its high specific fuel consumption in relation to the direct injection engine.

ACKNOWLEDGEMENTS

The author would like to express his sincere gratitude to Dr. N. Watson for his advice and guidance while supervising this work.

The help and advice of Drs. M. Marzouk and B. Holness, during the writing of the thesis, are also appreciated.

Thanks are also due to Mr. R.D. Bloxham and the technical staff of the Thermal Power Section, for their help throughout the experimental part of the work.

The author is also grateful to Miss S. Chambers for careful and rapid typing of the manuscript.

LIST OF CONTENTS

NOTATION

Unless otherwise stated in the text, symbols are defined as follows;

Symbols

a, a_1, a_2	Constants
A	Geometric or heat transfer area
A_L	Instantaneous liner area
A_P	Passage geometric area
A_{TDC}	Cylinder liner area at TDC
b, b_1, b_2	Constants
B_o	Boltzmann number
c, c_1, c_2	Constants
C_c	Contraction coefficient
C_d	Discharge coefficient
$C_{d_{inj}}$	Discharge coefficient of injector nozzle
C_f	Friction torque coefficient
C_i	Incompressible contraction coefficient
C_m	Current jet centre-line concentration
C_o	Initial jet centre-line concentration (1.0)
C_p	Specific heat at constant pressure
C_r	Concentration at any jet core radius
$C_{r)_{\frac{1}{2}}}$	Half radius concentration
d_j	Injector nozzle diameter
D_c	Characteristic dimension
D_e	Cylinder bore
D_v	Vena contracta diameter
e	Internal energy
E_a	Activation energy

E_r	Radiation energy
f	Force defect coefficient
f_f	Wave fundamental frequency
f_i	Incompressible force defect coefficient
f_s	Stoichiometric (Fuel/Air) ratio
F	Equivalence ratio
F_d	Force defect
G	Swirl speed ratio (ω_g/ω_d)
h	Instantaneous heat transfer coefficient
h_f	Heat of reaction of fuel
h_g	Gas enthalpy
H_L	Percentage heat loss to total fuel
H_r	Percentage heat loss relative to IDI engines
K	Gas thermal conductivity
K_a	Absorption coefficient
K_n	Orifice flow constant
K_s	Average absorption coefficient
K_{s_o}	Average absorption coefficient at atmospheric pressure
ℓ	Physical depth
ℓ_w	Wall thickness
L	Radiation length
L_e	Connecting rod length
L_{op}	Optical depth
m	Mass
$\dot{m}$	Mass flow rate
m_f	Cumulative products of fuel combustion in the control volume
m_g	Cumulative gas flow
$\dot{m}_g$	Gas mass flow rate

M	Charge mass
M_{a_o}	Initial trapped mass of air
M_b	Mass of fuel burnt
M_{f_o}	Initial trapped mass of fuel products
M_o	Initial trapped mass
N	Engine speed
Nu	Nusselt number
p	partial pressure
P	Pressure
$P^{\cdot}$	Rate of change of pressure
P_b	Back pressure
P_{exh}	Exhaust manifold pressure
P_{inj}	Injection pressure
P_{inl}	Inlet manifold pressure
P_o	Total pressure upstream
P_r	Pressure ratio (downstream/upstream)
P_w	Pressure at orifice wall
Q	Total heat flux
Q_r	Radiant heat flux
Q_w	Heat flux to the wall
r	Pressure ratio across the orifice (static-static)
r_c	Critical pressure ratio
r_d	Radius of rotating disc
r_e	Engine crank radius
r_j	Any radius inside jet core
R	Gas constant
Re	Reynolds number
Re_d	Reynolds number for rotating disc
R_j	Outer radius of jet cross section

R_1	Radius of approach pipe
R_2	Radius of the orifice
S_a	Arc distance travelled by the jet
S_d	Width of rotating disc enclosure
S_e	Engine stroke
S_j	Distance from injector to impingement point
t	Time
t_{ch}	Chemical delay
t_d	Ignition delay period
t_{ph}	Physical delay
T	Temperature
$T^{\bullet}$	Rate of change of temperature
T_c	Average wall temperature on the coolant side
T_f	Flame temperature
T_g	Gas Temperature
T_o	Average wall temperature on the gas side
T_w	Wall temperature
u	Flow velocity through orifice
u_w	Velocity at orifice wall
u_1	Approach velocity
v	Characteristic velocity
v_a	Air velocity
v_c	Jet centre line velocity
v_{J_m}	Mean jet velocity
v_{J_o}	Initial jet velocity
V	Volume
$V^{\bullet}$	Rate of change of volume
V_c	Instantaneous cylinder volume

V_{TDC}	Cylinder volume at TDC
$X(\theta)$	Heat release fraction
X_J	Distance measured in a perpendicular direction to the jet centre line, from the injector
X_w	Distance within the wall
y_i	Concentration of constituent (i) of chamber charge
y_J	Distance measured on jet centreline

Greek Symbols

α_f	Specific gravity of fuel
α_K	Amplitude of the Kth cosine harmonic of temperature signal
β	Diameter ratio (R_1/R_2)
β_K	Amplitude of the Kth sine harmonic of temperature signal
γ	Specific heat ratio
δ	Thermal diffusivity
ε	Emissivity
ε_f	Flame emissivity
ε_g	Non luminous gas emissivity
ε_s	Soot emissivity
η_i	Indicated thermal efficiency
η_{i_r}	Indicated thermal efficiency relative to IDI engine
θ	Current crank angle
$\Delta\theta$	Crank angle increment
λ	Wave length
μ	Viscosity
ν	Kinematic viscosity
ρ	Density
ρ_a	Air Density
ρ_f	Fuel density

ρ_o	Upstream fluid density
σ	Stefan-Boltzmann constant
τ_f	Frictional torque
ϕ	Excess air factor
ψ	Tolerance
ω	Angular frequency of temperature signal
ω_d	Rotation speed of rotating disc
ω_g	Rotation speed of chamber charge

Abbreviations

ADC	Analogue-to-digital converter
ATDC	After top dead centre
BTDC	Before top dead centre
DI	Direct ignition
$DI)_{eq}$	Equivalent direct ignition
DLCU	Data logging control unit
IDI	Indirect injection
IMEP	Indicated mean effective pressure
MEP	Mean effective pressure
PC	Prechamber
ROHR	Rate of heat release
SC	Swirl chamber

CHAPTER 1

INTRODUCTION

1.1 INDIRECT INJECTION DIESEL ENGINE CHARACTERISTICS

The internal combustion diesel engine has been in service as a reliable and efficient prime-mover for a long time. Recently there has been growing interest in the study of diesel engine operation due to increasing concern about energy resources and the environment. The diesel engine is now being considered as a potential replacement for the spark ignition engine for automotive propulsion.

This new market for diesel engine demands high speed, high torque and economy combined with an acceptable level of exhaust emissions. Compared to the petrol engine, the diesel engine is more efficient, uses fuel that is generally cheaper than petrol, and hence is more economical to run. Most diesel engines emit less carbon monoxide and unburned hydrocarbons than comparable petrol engines. Diesels are however noisier and suffer from smoky and odorous exhaust. Additionally, limiting values of maximum operating speed and torque for the diesel engine are lower than corresponding values for the petrol.

Two major types of diesel engines are suitable for high speed operation, the bowl-in-piston direct injection (DI) and the indirect injection (IDI) engine. The configuration of a DI combustion chamber (a) and two IDI chambers (b and c) are shown in Fig. (1.1). The IDI engines are sometimes referred to as divided chambers or prechamber engines, and classified according to the geometry of the combustion chamber e.g. swirl chamber engine Fig. (1.1c) or prechamber engine Fig. (1.1b).

In divided chamber engines, fuel is always injected in the pre-

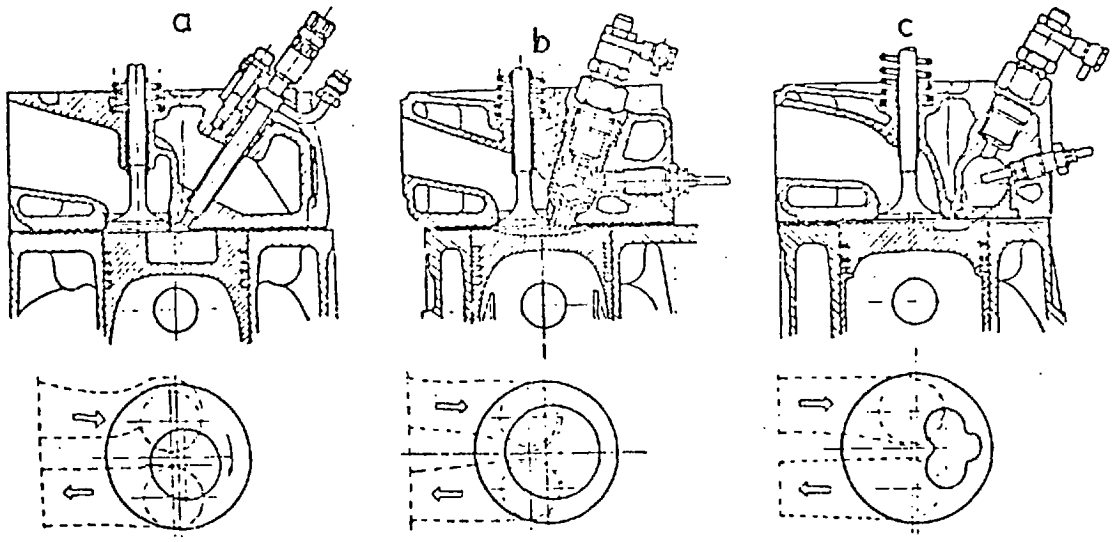

Fig. (1.1) High Speed Diesel Engines Geometry

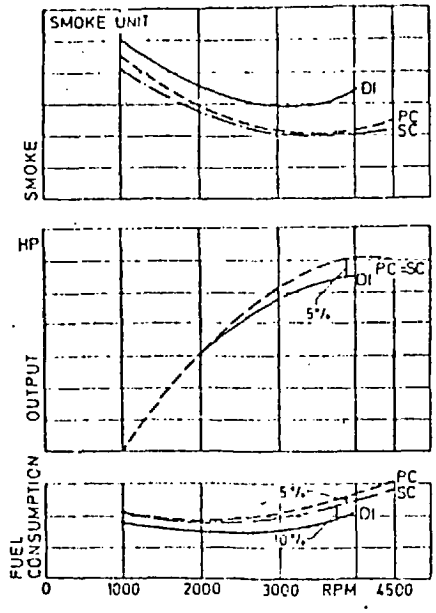

Fig. (1.2) Performance Comparison Between DI, PC and SC Engines (51)

chamber where combustion is initiated and then burning gases are transferred to the main cylinder. Fuel and air mixing is mainly attained by using the kinetic energies produced by the flow of air into the prechamber during the compression stroke, and the flow of combustion products from the prechamber to the main chamber during expansion. Depending on the geometry of the prechamber, the flow of air charge inside it could be either the swirling mode (e.g. Fig. 1.1c) or the turbulent mode (e.g. Fig. 1.1b). In either case the mixing energy is high, hence the demand for a high energy fuel jet is considerably less than in the case of DI engine. Accordingly, injection pressures in divided chamber engines are lower than those of DI engines. Another advantage of the IDI engine is the high air utilization due to higher mixing velocities, which aids combustion, and the availability of extra air in the cylinder for the burning gases leaving the prechamber. This results in higher specific output of the IDI engine compared to the equivalent DI. IDI engines also have shorter ignition delay periods than DI engines, which aids performance at high engine speeds.

1.2 PREVIOUS WORK ON INDIRECT INJECTION DIESEL ENGINES

The IDI engine is less widely used than the DI engine and consequently less published work is available on IDI engines than the DI version. Although the IDI engine has several advantages over the DI engine (Section 1.1), its higher specific fuel consumption is a major drawback, which has made it less attractive.

In the following subsections, previous work on IDI engines is reviewed. Different research areas are considered under the separate headings of engine performance and combustion, ignition delay, heat transfer, exhaust emission and noise and engine simulation.

1.2.1 Engine Performance and Combustion

The combustion mode of the swirl chamber type IDI engine has been investigated and explained by Lyn (71), Alcock (4), Dicksee (32) and Ricardo (89). Their work provided an improved understanding of the combustion phenomenon in such a chamber.

An organised swirl motion is produced in the prechamber during the compression stroke by the flow of air through a tangential throat. The fuel jet (from a pintle type injector usually) penetration is reduced by the strong air swirl and deflected by it. Fuel is generally injected downstream of the air swirl and the fuel particles are, therefore, transferred with the air stream towards the peripheral area. Ignition occurs as the jet comes in contact with very hot chamber wall, or near the front of the connecting passage where the fuel comes in contact with the incoming air of higher temperature. In this instance, the rich mixture at the periphery of the chamber is able to flow out into the cylinder. Soon after ignition, the flames moves towards the centre of the prechamber, due to the increase in the buoyant force acting on the hot products of combustion in the centrifugal field created by the swirl. Also, cooler air at the chamber core is pushed towards the chamber periphery due to centrifugal effects. This process is known as "Thermal Mixing" and has been detected by several research workers via combustion photography (4, 67, 76, 79 and 111).

In other types of IDI engines, (e.g. Fig. 1.1b) the volume of the prechamber and the area of the throat are smaller than in the swirl type. In these cases, the air motion is not tangential to the prechamber wall and the fuel is injected along the chamber axis towards the connecting passage (or passages). High turbulence is produced after the start of combustion by the flow of the products from the pre-

chamber into the main chamber where combustion is completed. The number and shape of the connecting passages affects the extent of mixing of the products from the prechamber and the air in the main chamber.

A comparison between the performance and smoke of three different combustion chambers for a light duty diesel engine has been given in Ref. (100). This has been discussed by Henein (51) and is shown in Fig. (1.2). The DI engine has the better fuel consumption but the highest smoke. The swirl chamber engine shows an improvement of fuel economy over the prechamber engine of about 5% which was explained by Henein to be due to the lower pumping loss between the swirl chamber and the main chamber.

Fig. (1.2) shows a difference of about 10% in fuel consumption of the IDI engine compared to the DI. The sources of the high specific fuel consumption of IDI engines are expected to be;

* Pumping of gases through the passage between the prechamber and the main chamber.
* Excessive heat transfer to the chamber walls due to high charge velocities.
* Combustion mode effects due to the differences in the fuel mixing and burning processes in the IDI engine as compared to the DI engine.

Combustion and performance studies of divided chamber engines also included considerations of prechamber geometry, passage position and area, and fuel spray direction. Nagao and Kakimoto (76) studied the effect of the direction of fuel injection on the engine performance and combustion. Fig. (1.3) clearly shows the advantages of fuel injection downstream of the air swirl on both specific fuel consumption and

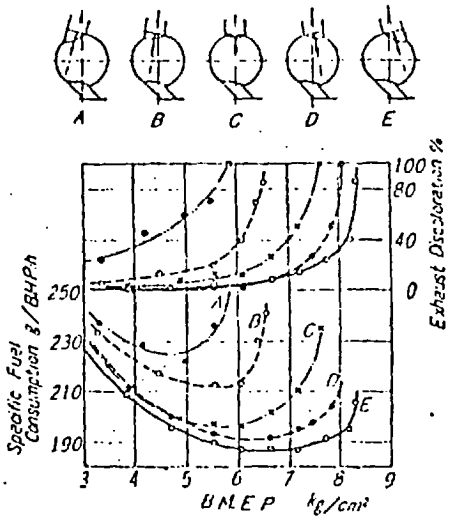

Fig. (1.3) Influence of the direction of fuel injection (76).
Engine speed: 1,500 r.p.m., Injector: DN8S1 (opening pressure: 120 at), Cross-sectional area of the passage: 1.0% of piston area

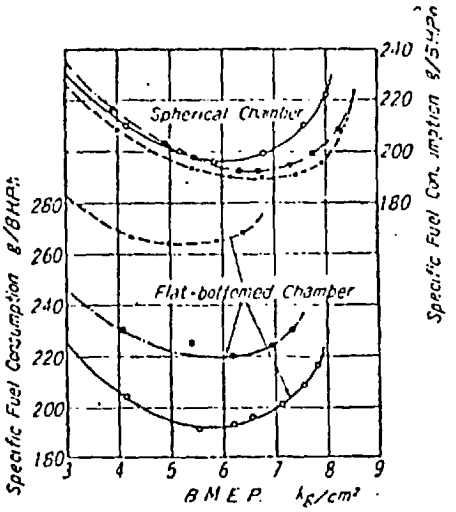

Fig. (1.4) Influence on the performance of the cross-sectional area of connecting passage in the spherical and the flat-bottomed chamber (76).
Engine speed: 1,500 r.p.m., Fuel injection: spherical chamber; DN8S1, E, flat-bottomed chamber; DN15S3, D
--- × --- area ratio 1.0%
—·— • —·— " 1.5%
—— o —— " 2.0%

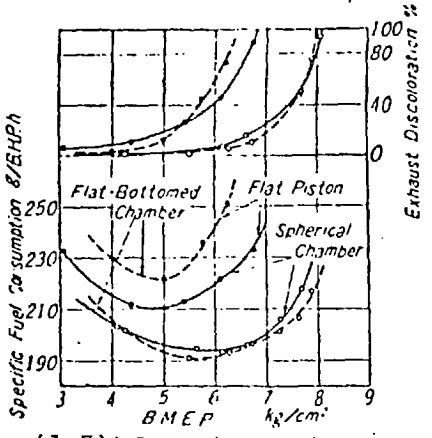

Fig. (1.5) Influence on the performance of the piston crown cavity (76).
Engine speed: 1,500 r.p.m., Connecting passage: 2.0% of piston area, Fuel injection: spherical chamber; DN8S1, E, flat-bottomed chamber; DN15S3, D

exhaust smoke. Effects of the swirl chamber shape, connecting passage area and piston crown cavity are given in Figs. (1.4) and (1.5). Fig. (1.4) shows for the spherical chamber, that decreasing the passage flow areas improved the fuel consumption, which is thought to be a result of improvement in combustion due to better mixing. For the flat bottomed chamber, however, the effect is reversed and the performance deteriorated. With such a geometry, the smaller area of the passage is no more effective in strengthening the air swirl, but results in increasing heat and passage throttling losses, and in retarding the outflow of rich mixture into the main chamber, with the resulting loss in engine performance. Fig. (1.5) demonstrates the importance of the piston crown cavity on the divided chamber engine performance. The figure also shows a slight improvement in performance when using a flat bottomed chamber. This could be due to reduced heat loss and improvement of combustion for a flat bottomed chamber.

In Ref. (78) Nagao et al studied the effect of projections introduced in the swirl chamber on engine performance and flow velocity distribution inside the swirl chamber. They concluded that a suitably dimensioned projection placed upstream of the injector, could improve the performance and smoke emission. An excessively large projection would result in poor combustion and performance deterioration.

Tanaka et al (103) studied the influence of different aspects of prechamber geometry on engine performance. Their results are shown in Figs. (1.6), (1.7) and (1.8). A flat bottomed swirl chamber (Fig. (1.6)) rendered best performance. For this geometry, the effect on engine performance of connecting passage area, its shape and inclination was studied, and the existance of optimum geometry conditions were reported. A jet hole area corresponding to 1-1.3% of the piston

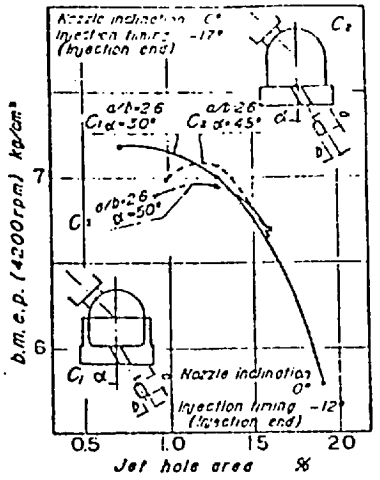

Fig. (1.6) - Jet hole area and its effect on engine performance (103).

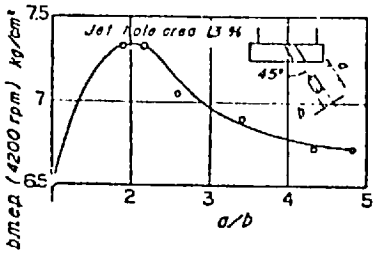

Fig. (1.7) - Jet hole shape and its effect on engine performance (103).

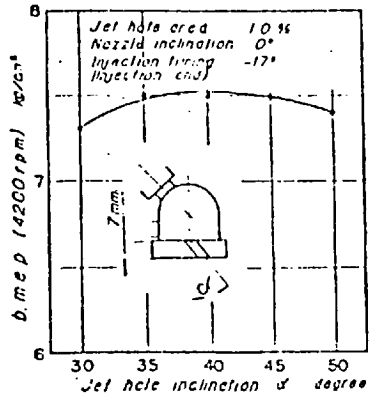

Fig. (1.8)- Jet hole inclination and its effect on engine performance (103).

area is most desirable, and an elliptic hole cross section of (a/b) ratio of 2 resulted in the best performance. An elliptical hole is thought to create additional turbulence which is favourable from the combustion view point; however, an excessive ellipse produced adverse effects (Fig. (1.7)). Fig. (1.8) shows the effect of the passage inclination. There is hardly any difference in the range of 30^{o}-50^{o} and the best result is realised in the vicinity of 40^{o}.

1.2.2 Ignition Delay

Owing to the high compression ratios generally used in IDI engines, high swirl velocities and high wall temperatures inside the prechamber, ignition delay periods are shorter than normal DI engine values. Limited evidence of research in IDI engines, compared with the DI version, also exists in the field of ignition delay. Lyn and Valdmanis (71) studied the effects of physical factors on ignition delay and included the decrease of ignition delay periods with increase of swirl speed. Ilmari (55) measured and correlated ignition delay periods for IDI engines. Anisitis (6) also measured delay periods in a divided chamber engine and proposed a correlation for his measured values based on charge temperature and pressure.

The very short delay periods encountered in IDI engines represent added difficulty in measurements. In order to measure the ignition delay periods and study the influence of engine speed, load and fuel injection timing on them, high accuracy and very rapid data acquisition are required.

1.2.3 Heat Transfer

Once again, instantaneous heat flux measurements inside the IDI engine combustion chambers are not as widely reported as those from DI engines. Knight (60) measured and correlated heat flux rates for

a swirl chamber engine. French and Hartles (43), also measured fluxes inside a swirl chamber engine and correlated flux values with gross fuel flow of the engine. Hassan (48) measured heat fluxes and flow velocities inside a cylindrical chamber of a divided chamber engine under motored conditions. Sitkei (97) presented a (universal) correlation to calculate instantaneous heat fluxes in DI and IDI diesel engines. Instantaneous heat flux measurements in both DI and IDI engines (8, 10, 35, 49, 60, 66, 97, and 117) have established that heat loss to the walls of an IDI engine is in excess of that for a DI engine, the reason being the higher charge velocities. Radiation losses are also recognized as being appreciable (97) and should be taken into consideration.

1.2.4 Exhaust Emissions and Noise

Fig. (1.9) shows a comparison of the emission behaviour of both DI and IDI engines given by Torpey et al (105). It is evident that, in general, the IDI engine produces less NO, hydrocarbon and CO emissions than the DI engine. It was concluded from the study that the low NO emission of the IDI engine could be attributed to the ability of the IDI to run more retarded than the DI engine. Low smoke and hydrocarbon emissions of the IDI engine are thought to be a result of further oxidation reactions taking place in the main chamber, for the over-rich smoky gases flowing from the prechamber.

Perez and Landen (87) studied the IDI engine emission characteristics for naturally aspirated (NA) and turbocharged (T) operation. Fig. (1.10) is a comparison of their results of DI and IDI emissions. An apparent reduction in the hydrocarbons emitted is achieved by turbocharging. Emissions and noise of DI and IDI engines were also studied by Frank and Hardenberg (42).

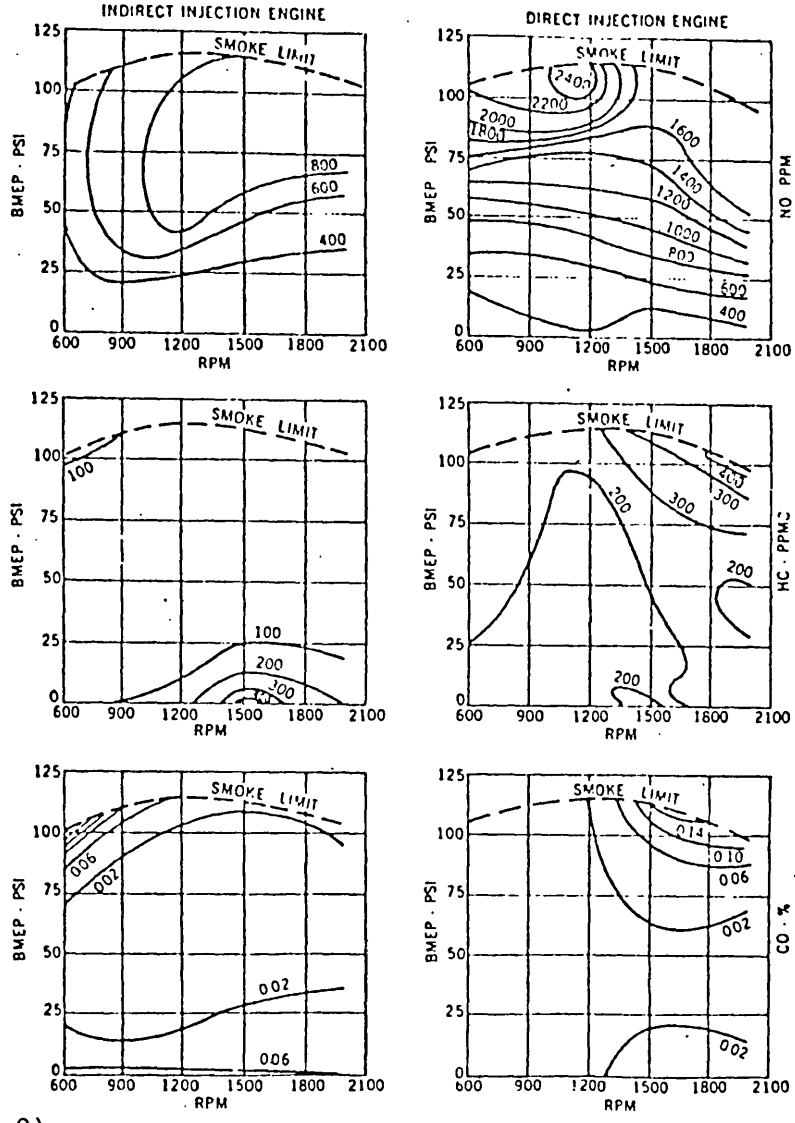

Fig. (1.9) Comparison between the emissions in D I and I D I diesel engines. (105).

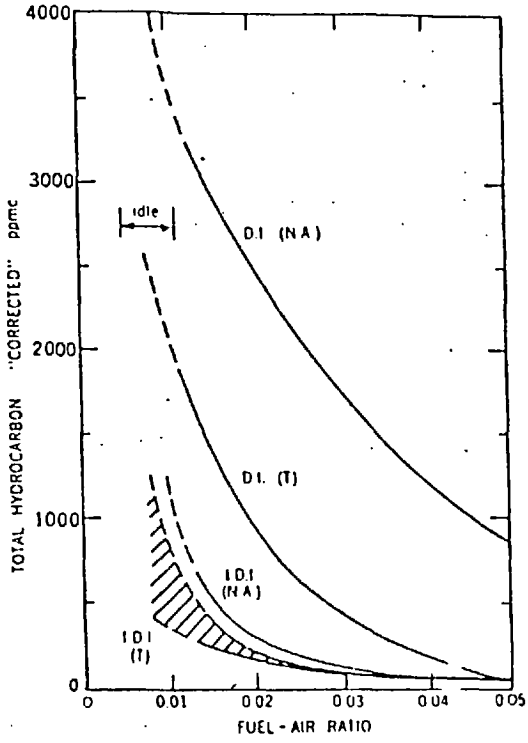

Fig. (1.10) Effect of fuel air ratio on the unburned hydrocarbon emissions in D.I. and I.D.I. engines. (N.A.): Naturally aspirated; (T): Turbocharged (87).

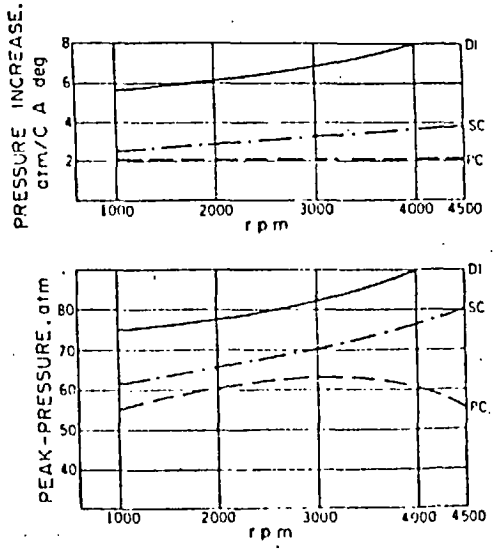

Fig. (1.11). Comparison between the peak pressure and the rate of increase in pressure due to combustion in the D.I., S.C., and P.C. automobile engines. (91).

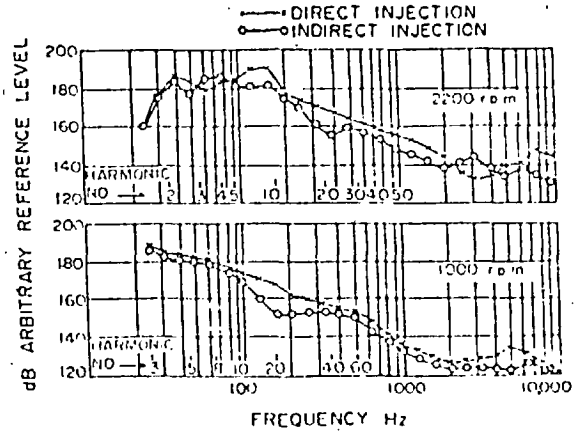

Fig. (1.12) Comparison of cylinder pressure spectra from I.D.I. and D.I. engines (91).

Due to the shorter delay period in an IDI engine, the amount of fuel-air mixture prepared during the delay period is less than that in a DI engine. As a result, the initial high rate of pressure rises and the corresponding peak pressure for IDI engines would be less than the DI engine. This has been reported in Refs. (51, 100) and is shown in Fig. (1.11). A direct result of this is a considerable reduction in engine noise at high loads. Fig. (1.12), from Ref. (91), shows a comparison between the frequency spectra of the pressure diagrams in DI and IDI engines. The IDI engine shows a low intensity. Scott (91) reported that the comet IDI engine gave a noise level of 79.5 dBA, while the corresponding level for a DI version under the same engine conditions was 84.5 dBA.

1.2.5 Engine Simulation

The obvious importance and usefulness of mathematical simulations of internal combustion engines has resulted in an increased amount of research in this area. Mathematical simulation of IDI engines has only recently been attempted. The work of Nakajima (80), probably the earliest, was only concerned with heat release calculations. Lyn et al (72) were also concerned with heat release calculations and, in addition, cycle predictions. A major disadvantage of their work was the treatment of the IDI engine cylinder as one control volume only. To the author's knowledge, the most complete investigation of IDI mathematical simulation so far, is that by Anisitis (6). This study was more concerned with heat release calculation than cycle prediction. However, the thermodynamic treatment of the problem is basically sound since it deals with each of the combustion chambers simultaneously.

1.3 OBJECTIVES AND OUTLINE OF THE PRESENT WORK

From the previous two sections it can be concluded that further research is required for a fuller understanding of IDI engine operation. Knowledge is lacking in the areas of measurements and calculations of heat transfer and ignition delay period. Mathematical engine simulation is a tool which has not yet been thoroughly employed in IDI engine research.

In the present work, the operation of the IDI diesel engine has been investigated. The engine cycle has been analysed thermodynamically and the engine modelled by a series of control volumes interconnected via orifices. The prechamber was considered as a separate control volume connected to the main cylinder via an orifice. All thermodynamic aspects of mass, heat and energy transfer were included.

The thermodynamic behaviour of IDI engines was then expressed mathematically in a full cycle analysis computer program. The ultimate objective of the present work was to develop a simulation computer program which satisfactorily describes the IDI engine operation and to use this to investigate the sources of the IDI engine high specific fuel consumption in relation to the DI engine.

An IDI engine was extensively instrumented and tested to provide detailed experimental behaviour data. The test rig developed, and data acquisitions systems are discussed in Chapter 2.

The thermodynamic and mathematical simulation techniques are presented in Chapter 3. A simulation method to calculate rate of heat release simultaneously in the prechamber and the main chamber is also discussed.

In the cycle analysis program, heat release to the combustion chamber walls is calculated using a Nu-Re relationship. The development of this correlation and of the methods of calculation are described in Chapter 4.

The predicted instantaneous heat fluxes to both main chamber and pre-chamber walls are compared with measured values. The experimental arrangement for heat flux measurements is also explained.

Chapter 5 describes theoretical and experimental considerations for the passage discharge coefficient calculations. The actual passage discharge coefficients were also measured and the effect of piston proximity was studied.

The rapid data logging system, used in the present work, was utilised in measuring the ignition delay period under varying engine running conditions. Chapter 6 presents the measurement method and the correlation procedure. Both physical and chemical delay periods were included in the correlation.

An evaluation of the simulation technique is presented in Chapter 7. It includes comparisons of predicted and measured performance and shows full cycle predictions for both the main and prechamber.

The simulation computer program is then used in Chapter 8 to isolate and quantify the sources of extra losses in the IDI engine compared to the equivalent DI.

The final conclusions of the present work and the recommendations for future work are presented in Chapter 9.

CHAPTER 2

TEST RIG AND DATA ACQUISITION SYSTEMS

2.1 INTRODUCTION

Unlike the DI engine, the combustion chamber of the IDI engine consists of two volumes connected via one or more passages. Conditions in either volume are different at any instant of time throughout the engine cycle. Detailed understanding of an IDI engine thermodynamics and fluid flow requires accurate measurements of conditions inside each control volume simultaneously.

Little work has been published showing instantaneous pressure measurements in an IDI engine. Both Nakajima (80) and Anisitis (6) measured pressures in each volume of an IDI engine cylinder, and obtained corresponding rates of heat release curves in each volume. In the present work, greater accuracy was achieved in pressure measurement by critical consideration of the pressure difference between the main and prechamber.

Conventional instrumentation was also used to measure injector fuel line pressure, needle lift and exhaust emissions.

In the first part of this work, pressures and pressure differences were logged via a link to an on-line computer. The results were used for heat release calculations. The second part of the investigation dealt with ignition delay periods. For this, a digital tape recorder data acquisition system was used. The final part of the work involved measurements of instantaneous heat fluxes in both chambers of the engine cylinder; the tape recorder system was also used for this work.

In this chapter a description of the test engine is given. Details of the instrumentation used and data logging systems adopted are also presented.

The experimental results for each part of the investigation are shown in the corresponding chapters.

2.2 THE ENGINE AND TEST BED

The test engine was of the swirl chamber indirect injection type, with the following data:-

Engine make and model:		Perkins, 6.372
Engine type	:	4-stroke, compression ignition, IDI, naturally aspirated engine
Prechamber type	:	swirl chamber, Ricardo Comet VB
Number of cylinders	:	6
Bore	:	0.101 m
Stroke	:	0.127 m
Connecting rod length:		0.219 m
$\frac{\text{Passage Area}}{\text{Piston Area}}$ %	:	1.24
$\frac{\text{Prechamber Volume}}{\text{Total clearance"}}$	:	0.476
Engine Compression Ratio	:	21:1
Valve Timing	:	Exhaust Valve open 52^{o} BBDC
		Exhaust Valve close 16^{o} ATDC
		Inlet Valve open 19^{o} BTDC
		Inlet valve close 49^{o} ABDC

The engine test bed arrangement is shown in Fig. (2.1). The engine was flexibly mounted to a large concrete base, and coupled to a hydraulic brake for load control. The brake (Heenan-Frouds G41 dynamometer) was rigidly fixed to the common base.

Engine speed and load were adjusted manually via the fuel rack and the hydraulic brake controls.

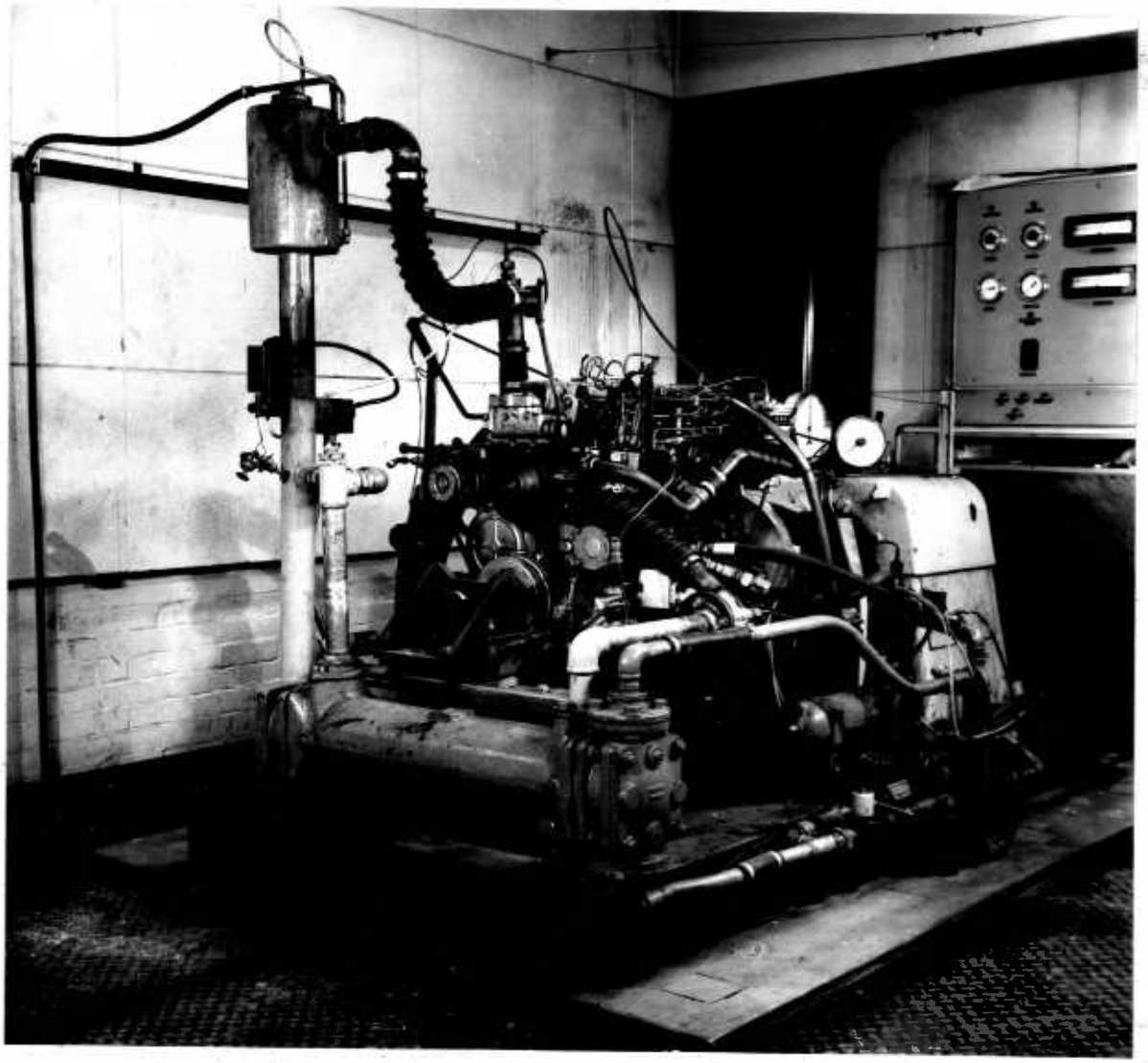

Fig. (2.1) The Engine

Both cooling water and oil were temperature controlled via external heat exchangers. These consisted of a by-pass system which was thermostatically controlled for the temperature not to exceed a pre-set value. Oil temperature and water temperatures in and out of the heat exchangers, and the lubricating oil pressure, were also displayed.

2.3 OVERALL PERFORMANCE VARIABLES

At any engine running condition, sufficient time was allowed for the engine to stabilize thermally. When this was achieved the following measurements were recorded. (Exhaust emissions measurements are presented separately in Appendix B).

2.3.1 Engine Power

The engine brake mean effective pressure (BMEP) was calculated from the hydraulic dynamometer load reading

Brake Mean Effective Pressure [Bar] = 0.7345 x Dynamometer load [Lb]

Engine speed was measured by means of a digital pulse counter which displayed the period in (ms) of one engine revolution. One pulse per engine revolution was obtained by means of an electromagnetic pickup monitoring the passing of a sharp-edged steel element fitted to the engine flywheel. An electronic counter was used to measure the period between successive pulses and this indicates the engine speed accurately.

2.3.2 Manifold Conditions

Sheathed thermocouples were used for manifold temperature measurements, copper/constantin for the inlet manifold and chromel/alumel for the exhaust. U-tube water manometers were used to measure pressures in the manifolds.

2.3.3 Fuel and Air Flows

Steady state measurements of the overall fuel consumption of the

engine were carried out using a conventional mass balance system. Several readings were averaged to ensure repeatability and to obtain representative values.

Engine air flow measurements were obtained by a standard orifice plate technique. The pulsating characteristics of engine breathing were damped by means of a large chamber between the engine and the orifice plate arrangement. Ambient pressure and temperature were also recorded.

2.4 DETAILED INSTRUMENTATION

2.4.1 Pressure Measurements

Cylinder Pressures

Initially, experiments were conducted using three different types of piezo-electric pressure transducers and with different mountings. The criteria for acceptability of the transducer was a realistic pressure difference signal between the two chambers, with one transducer fitted in the cylinder head and the other in the prechamber. The transducers used were AVL 8QP 500C, AVL 12QP 500C and a special heat shielded AVL 12QP 505CLK transducer. The instrumented cylinder was number 5. (see Fig. (5.2)).

The AVL 8QP 500C transducer in the prechamber suffered from thermal shock effects, detected by a high unrealistic, pressure in the prechamber far down the expansion stroke. A special flame trap in front of the transducer eliminated the thermal shock effect but caused a pressure drop.

Thermal shock also introduced a significant error on the AVL 12QP 500C transducer when fitted in the prechamber. Thermal shock effects were, however, undetectable for the same transducer fitted in the cylinder, except at high engine speed, when more fuel is burnt in the cylinder.

The transducer with a thermal shield (AVL 12QP 505CLK) gave acceptable signals, free from thermal shock effects. It was, therefore, used

for the prechamber in all tests. The conventional (12QP 500C) transducer was used in the main chamber in all tests except the two high speed runs, when a second heat shield transducer was used.

The thermal shock effect on pressure transducers has been investigated fully and is documented in Appendix A.

An AVL 359HICF charge amplifier was used to adapt the signal from each transducer. To prevent the occurence of any negative pressure signals, the amplifiers were set to allow a sufficient positive offset on the output signals. This was necessary since the analogue to digital converter used, digitized positive signals only. Extreme care was given to transducers calibration, with both amplifiers set such that the pressure difference signal was zero when both transducers were subjected to the same pressure.

The instantaneous pressure difference between the two chambers was of a particular interest. It served as a means of checking the transducer-amplifier system.

The difference between the outputs of the two amplifiers was amplified using a bridge amplifier unit (Bryans Southern Instruments, type no. MO 4/900) after modification to suit the application required. A sufficient offset on the output from this amplifier ensured the output voltage was always positive. Using this arrangement, errors in transducer behaviour, or amplifiers gain, were readily detectable.

Injector Fuel Line Pressure

An AVL 31DP 500E strain gauge transducer was used to measure the pressure in the fuel line. It was mounted in the fuel line immediately prior to the injector of cylinder number 5.

The transducer was used in conjunction with a Bryans Southern Instruments bridge amplifier (type no. MO 4/900) which supplied the

excitation voltage for the transducer and amplified the signal. The transducer was calibrated statically using a deadweight tester.

2.4.2 Position Measurements

Injector Needle Lift Transducer

The injector needle lift was measured using a Ricardo variable inductance transducer oscillator and modulator system. The output signal was very faint and had to be amplified before being digitized. Trouble was experienced with spurious signals in some of the tests.

Although the transducer was dynamically calibrated by limiting the injector lift with different thickness shims, it was not possible to make use of the calibration. The transducer/electronics system failed to maintain its tune for a sufficient period of time. Each set of tests (a group of three engine loads) were, therefore, performed at a different arbitrary system gain. The needle lift results are shown as a percentage of the maximum lift value at the full load condition. The injector manufacturer stated a maximum lift of 0.001 m.

Crank Angle Marker

The technique employed for measuring the instantaneous crank angle was first presented by Bloxham et al (22). A commercial, optical shaft encoder was used. It was driven from the free end of the crank shaft via a transversely flexible, but torsionally stiff, coupling and shaft arrangement. The encoder mounting was rigidly connected to the engine body to minimise relative vibration stresses and errors. For the early part of the work a Mesonix (model 157A) encoder was used. For the rest of the work, a superior, heavy duty Ferranti encoder (type 28 H2/M4) was used.

The principle of operation of such encoders is that a Moire-fringed glass disc rotates between a solid state light source and a light sensitive

pick-up. The alternate illumination and darkness produce a sinusoidal voltage from the light sensitive element which may be electronically processed and transformed into square wave pulses i.e. digitizer pulses. The encoder also had an additional track which produced one pulse per revolution (Gate Pulse). This was used for absolute position indication within the engine cycle.

The TDC position for the instrumented cylinder was determined both statically and dynamically. The dynamic TDC position was identified from the motoring cylinder pressure diagram at each engine speed as the position of the peak pressure. This was considered to be satisfactory and proved to be acceptable as its variation over the entire engine speed range was very small (0.5^{o}CA). This speed dependence was taken into consideration.

2.4.3 Combustion Chamber Wall Temperatures and Instantaneous Heat Flux Measurements

A commercial, fast response, surface thermocouple was used to measure instantaneous heat fluxes in both the prechamber and the cylinder head. It also provided wall temperatures for both chambers under different running conditions. A chromel-alumel sheathed thermocouple was also used for temperature traversing through the prechamber wall to obtain passage wall temperatures. These are fully described in Chapter 4.

2.5 DATA ACQUISITION SYSTEMS

2.5.1 Link to On-Line Computer

For the early part of this work, which involved measurements of cylinder pressure, pressure difference, injector fuel line pressure and needle lift, an on-line PDP15 computer received and processed digitized data from the engine via a permanent link. Fig. (2.2) shows

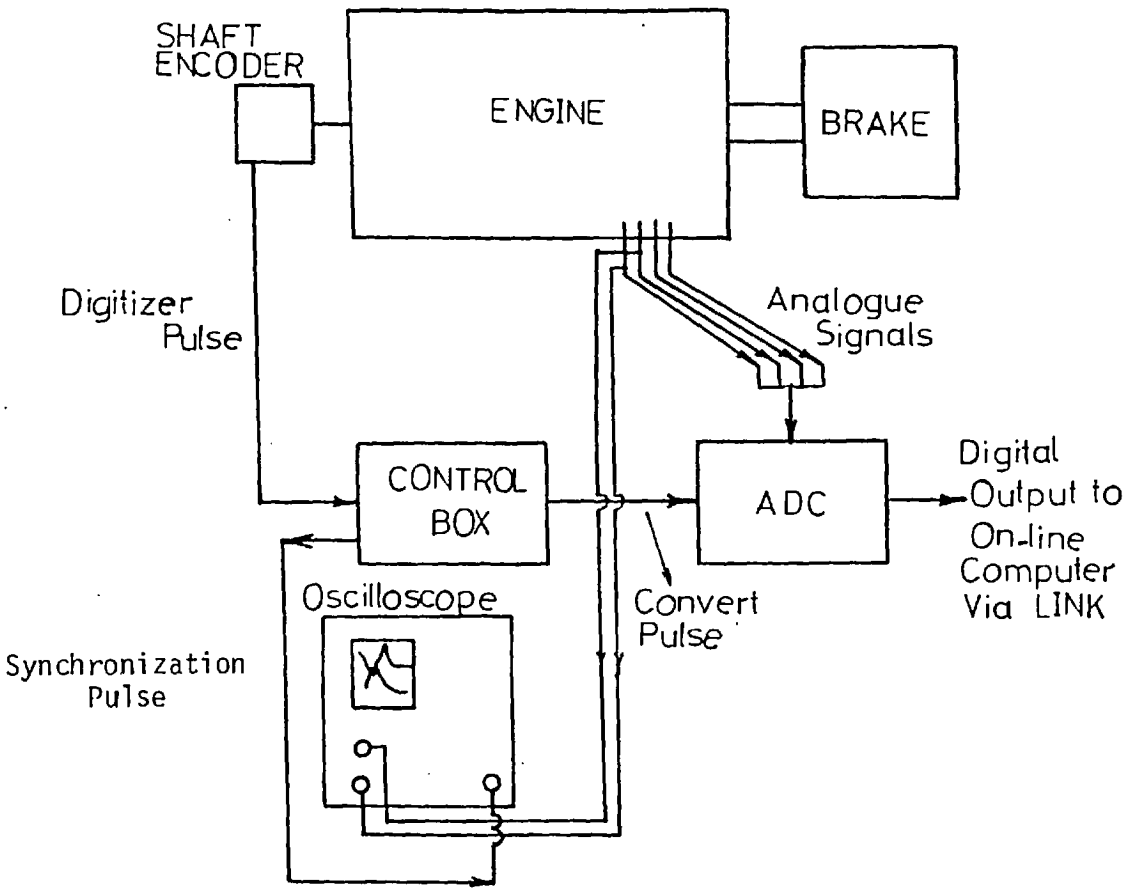

Fig. (2.2) Data Logging System Via Link to On-line Computer.

a schematic diagram of the data logging system. The two signals out from the engine driven shaft encoder are offered to a control box. These two signals (see Section 2.4.2) are the gate pulse and the digitizer pulse train. The CB (control box), controls the handling of these pulses before being offered to a 10 bit word analogue-to-digital converter (1/1023V resolution). With a push-button control, pulses could be started to flow or stopped at any time.

The CB only considers one gate pulse for every two pulses offered by the shaft encoder, i.e. one gate pulse is considered per engine cycle. This one pulse per engine cycle is also used for triggering the oscilloscope. For every pulse per engine cycle, only 768 of the digitizer pulses are allowed to be transferred to the ADC, the rest are blocked off. This allows 768 conversions to be performed for every engine cycle, which covers one full engine revolution.

The analogue signals from the transducers are successively connected to the ADC. For every convert pulse from the CB, one conversion is made and the digital signal is passed through the link to the computer. The sequence is repeated 768 times for every engine cycle. The overall sequence is also repeated for successive engine cycles, starting from the gate pulse position until the stop button is depressed.

The batches of 768 digitized signals are handled by the computer. A real time computer program was used to control the operation of the computer regarding reading and processing the digitized data. All 768 data values were read in, but only 512 were processed. Also, when sampling the needle lift and fuel line pressure data, only 200 values were considered; the early parts of either signals during compression and expansion were neglected. The above limitations were imposed primarily by the need to minimize the computer memory requirements.

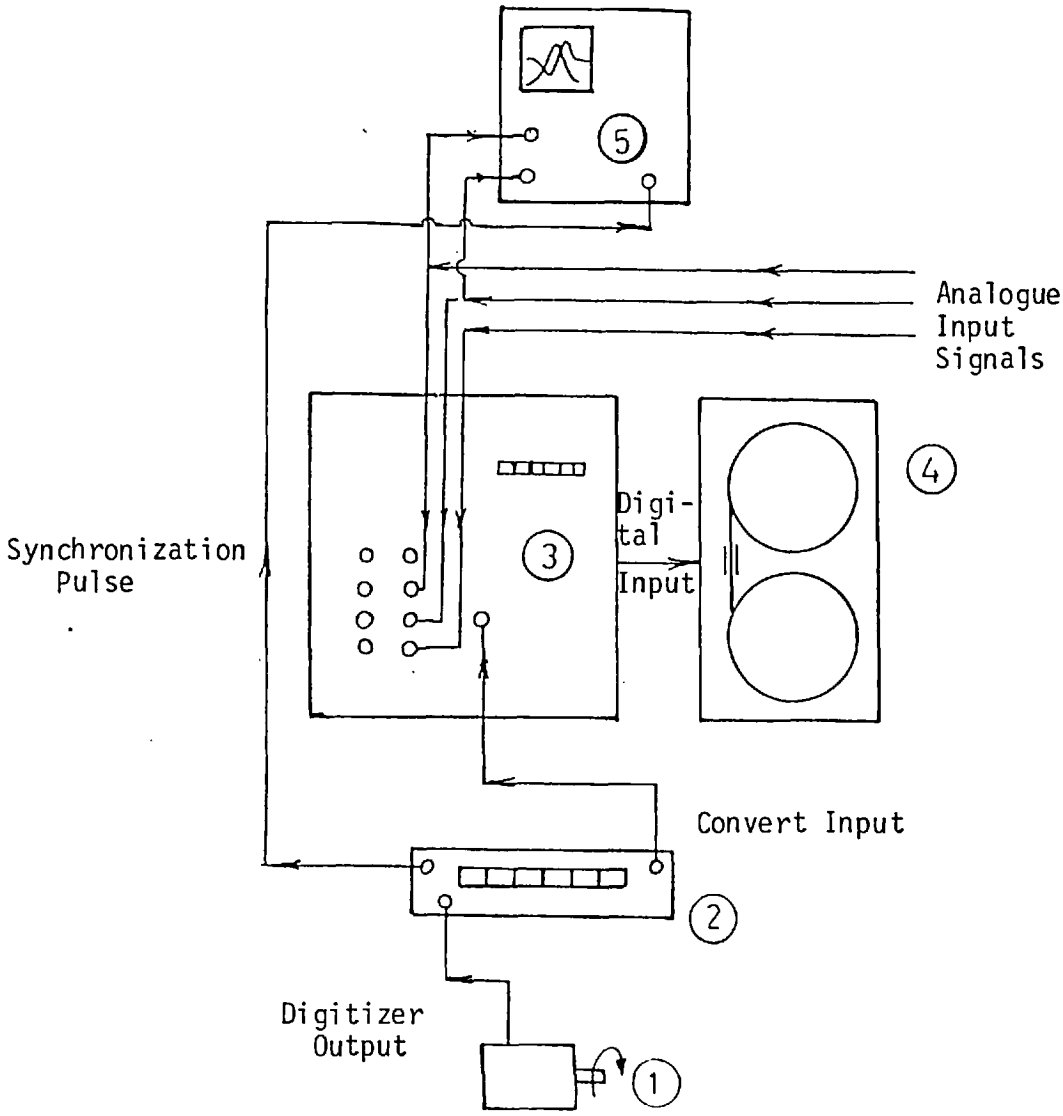

1) Shaft Encoder
2) Data Logging Control Unit
3) Signal Processing Box
4) Tape Recorder
5) Oscilloscope

Fig. (2.3) Tape Recorder System

Statistical considerations were included in the sampling procedure and fifty engine cycles were sampled. Averaging and standard deviation calculations were performed at each crank position. Only the standard deviation values for the cylinder pressures were punched out on paper tape as they were of particular importance for the heat release calculations.

The sampling resolution used was 0.46875 ^{o}CA. The sampling sequence was repeated for the four analogue signals successively and the paper tape output from the online computer was then converted into punched card form via a CDC computer.

2.5.2 Tape Recorder System

The tape recorder system was not available during the early part of this work. Once developed, it was used for the rest of the work. Fig. (2.3) shows a schematic diagram of the different elements of the data logging system.

The principle of the operation is to digitize the analogue signals from the transducers and record them on a magnetic tape. The details of each of the system elements are given below:

Shaft Encoder : This has been described in detail in Section (2.4.2). It provides an engine related train of square pulses at a specific resolution; typically 1/4 ^{o}CA. It also provides one pulse per engine revolution (gate pulse). The gate pulse and digitizer pulses provide the base for all the sampling sequences.

Tape Recorder : To allow very rapid digitized data recording, the recorder is designed to operate in a burst-mode. All data offered to the tape recorder are stored in two storage buffers capable of 1024 words each. Actual recordings on the magnetic tape only commence after the two buffers are full. Two limitations are imposed by the mode of operation of the recorder. Firstly a specific time (25 μs) must be allowed

without data sampling - for the recorder to switch from one storage buffer to the other. Secondly, a certain pause in the sampling requirement is needed to allow data transfer from the two buffers to the magnetic tape, as well as the physical movement of the tape.

These two limitations hinder the tape recorder system from being used for continuous data logging. The maximum continuous sampling rate varies with the quality of the tape; 5 to 12 kHz.

The intermittent operation of the tape was overcome by a special data logging control box which was specially built for engine data logging application.

Data Logging Control Unit (DLCU): The input to the control unit comprises two pulse trains from the shaft encoder, the digitizer pulses and the gate pulses. Inside the box these raw pulses are processed to suit both the sampling requirements and the tape recorder operation.

Referencing of the sampled zone within the engine cycle is made with respect to the gate pulse. The position of the gate pulse in the cycle is externally controlled according to need. Only one gate pulse is considered for every engine cycle and this is available on the output for signals synchronization purposes. The position of the sampled zone, relative to the gate pulse, could also be varied externally. The internal design of the DLCU allows 1024 digitizer pulses to pass to the output after which two digitizer pulses are skipped. After the two skipped pulses, another 1024 pulses are passed to the output. This skip period was particularly designed to allow sufficient time for the recorder to switch to the second storage buffer.

To allow a pause in the data offered to the tape recorder after every 2048 words, a certain number of engine cycles are skipped before

the sampling sequence is repeated. The number of cycles skipped is externally controlled and is a function of engine speed.

Another available facility in the DLCU is the ability to omit or multiply the raw digitizer pulses. For every pulse passed from input to output, any number of digitizer pulses (up to 99) could be skipped before the following pulse is passed to output. Similarly, for every pulse passed from input to output, as many as 99 pulses could be generated and passed to output before the following raw digitizer pulse arrives. Extreme case has to be taken when using this facility in the (multiply) mode regarding resolution of the generated pulses and their interference with the following raw digitizer pulse.

Signal Processing Box (SPB) : In this box signal multiplexing and analogue to digital conversion take place. It is controlled by the conversion pulses offered by the DLCB output. It is capable of sampling up to eight channels successively. The multiplexing time is approximately 1.2 μs. The converter has a full range of 10 volts and a resolution of 1 part in 1023. For every (convert) pulse, an ADC conversion is made and the multiplexer moves to the next channel. Converted values are offered to the recorder system where they are stored in its two buffers. Conversion errors, tape busy errors or any other error messages are displayed by red warning lights if encountered during sampling.

The number of channels sampled and the number of cycles required to be recorded for any test condition, are preset to control the operation of the SPB.

Oscilloscope : Visual monitoring of the sampled signals was obtained via a double beam oscilloscope. It was used in the external triggering made with the synchronization output from the DLCB as the triggering pulse.

Table (2.1) Measured Overall Performance

Speed	R.P.M.	1200									1600									2200									2800					
Dynamic Timing	^{o}CA	7^{o}			2^{o}			12^{o}			7^{o}			2^{o}			12^{o}			7^{o}			2^{o}			12^{o}			7^{o}			2^{o}			12^{o}		
Load	%	100	70	40	100	70	40	100	70	40	100	70	40	100	70	40	100	70	40	100	70	40	100	70	40	100	70	40	100	70	40	100	70	40	100	70	40
Dynamo. Load	Lb.	10.25	7.05	4.0	10.0	7.0	4.0	9.7	6.8	3.83	9.95	7.0	4.0	9.85	6.9	3.95	9.75	6.8	3.8	9.45	6.63	3.8	9.3	6.5	3.7	9.25	6.5	3.7	8.4	5.05	3.35	8.4	5.3	3.35	7.9	5.5	3.2
Exhaust Gas Temp.	^{o}C	532	328	210	535	340	220	520	315	205	565	365	235	552	332	245	565	355	230	600	358	265	612	410	275	583	376	253	525	432	316	552	470	335	560	425	322
Inlet Air Temp.	^{o}C	31.5	28.3	28.0	30.0	25.0	23.0	30.0	27.0	25.0	34.0	31.0	28.5	35.0	31.0	32.5	34.0	31.0	31.5	35.0	28.0	25.5	30.0	26.0	24.0	28.5	24.0	24.0	31.5	23.0	23.0	32.0	27.0	25.0	31.5	23.5	22.0
Pman.	Cm_{H_2O}	27.3	17.4	12.9	28.7	19.0	14.5	28.1	17.5	14.5	36.6	26.0	17.7	36.3	26.6	17.9	38.7	25.4	17.5	49.0	34.2	24.8	46.4	38.0	23.9	47.4	37.3	25.3	50.8	49.1	41.0	51.5	51.5	44.0	52.1	43.3	43.3
Pinlet	Cm_{H_2O}	18.1	18.9	19.7	19.0	19.4	19.2	18.5	19.0	19.7	28.3	29.0	31.0	28.7	29.7	31.0	28.7	29.7	30.6	45.6	52.6	54.0	46.3	51.0	52.8	49.0	51.2	51.6	75.5	73.3	79.3	74.3	75.3	78.5	74.5	77.0	78.4
Fuel Flow	kg/hr	12.34	9.04	6.25	12.69	9.15	6.03	13.08	8.95	6.31	16.20	11.4	7.52	16.16	11.39	7.74	16.16	11.34	7.75	20.48	14.04	10.32	20.61	14.82	10.56	20.61	14.82	10.29	25.27	18.47	13.47	25.59	19.03	13.61	26.08	19.44	13.49
Air Flow	Kg/hr	233.0	237.3	245.7	235.9	241.9	244.7	239.2	241.4	246.5	293.1	300.4	305.6	293.6	300.1	305.0	293.6	299.6	303.1	375.3	390.4	397.8	373.3	382.9	389.1	376.7	380.7	384.2	462.6	472.1	473.5	466.9	465.0	470.7	455.9	465.3	469.1
Smoke	Bar.	53.0	14.5	4.5	19.0	7.5	3.5	64.9	15.0	7.0	41.5	12.5	4.0	18.5	8.0	4.0	71.0	12.0	5.0	34.0	10.0	2.0	16.0	3.5	2.5	51.0	12.5	4.0	26.0	7.0	2.0	9.5	3.3	1.0	73.5	17.5	5.0
Ambient	Cm_{Hg}	76.34	76.37	76.5	76.66	76.9	76.9	76.9	76.9	76.9	76.43	76.43	76.43	76.43	76.43	76.43	76.33	76.33	76.33	76.93	76.93	76.93	74.99	74.99	74.99	74.99	74.99	76.50	76.73	75.73	75.73	76.34	76.34	76.34	76.41	76.41	76.41
Ambient	^{o}C	21.5	20.0	22.5	21.0	20.5	20.5	20.5	20.5	20.5	21.5	21.5	21.5	21.5	21.5	21.5	20.5	20.5	20.5	20.5	19.5	19.5	19.0	19.0	19.0	19.0	19.0	19.0	19.3	19.3	19.3	19.5	19.5	19.5	19.8	19.8	19.8

Visual monitoring was essential to make sure that all signals remained synchronized within the engine cycle during data recording. This was very important, particularly at the top engine speed runs, when some synchronization problems were experienced.

Analysis of recorded data was achieved using the Imperial College CDC computer. A special computer program was developed to convert the data recorded on magnetic tape into CDC computer code. Fifty cycles were sampled at every running condition. Averaging and statistical analysis were also performed with the same computer program.

2.6 TEST PROGRAM

Ignition delay measurements and the corresponding running conditions are explained in Chapter 6. Running conditions for heat flux measurements are covered in Chapter 4. The test runs mentioned here are those conducted for performance evaluation and study of main chamber pressure, pressure difference, fuel line pressure and needle lift behaviour.

The effects of engine speed, load and injection dynamic timing, were investigated. Four engine operating speeds (1320, 1680, 2200 and 2800 rpm) and three loads (100%, 70% and 40% loads) were considered. The above running conditions were repeated for three dynamic injection timing, 2^{o}, 7^{o} and 12^{o} CA, BTDC. At every engine speed, the position of the fuel injection pump was altered to obtain the required dynamic timing. The slight variation of injection point with engine load change was neglected. Injection point was obtained by displaying the needle lift diagram on an oscilloscope and using the time scale and known TDC position to calculate the injection point. Table (2.1) summarises the overall performance data obtained.

Ignition delay measurements and the corresponding running conditions will be described in Chapter 6. Running conditions for heat flux measurements are covered in Chapter 4.

CHAPTER 3

ENGINE SIMULATION

3.1 INTRODUCTION

Engine simulation by computer modelling has become increasingly important in recent years. A computer program which mathematically simulates the different thermodynamic and mechanical aspects of engine operation has proved a powerful tool, both in engine research and design.

In the area of DI diesel engine, numerous investigations have been reported concerning engine simulation to obtain rate of heat release diagrams, and full cycle analysis programs aimed at overall investigation of engine performance. However, there is little evidence of such work in the field of IDI diesel engines. Compared to the DI engine, the IDI engine is more difficult to simulate mathematically, and less widely used, which has affected the amount of research in the field. However, due to the worldwide fuel shortage, engine manufacturers have been looking for an automotive primemover which is more efficient than the petrol engine. High speed application is a field where the indirect injection version of the diesel engine is paramount.

As explained in the Introduction, a computer program simulation can be very useful in studying the operation of such engines and could detect areas of potential performance improvement. To the author's knowledge, the first published work attempting to simulate indirect diesel engine operation, was that by Nakajima (80). Although Nakajima did not indicate his method of calculation or simulation technique, he presented graphs of rate of heat release curves in both the prechamber and the main chamber.

The investigation was primarily concerned with the effect of swirl chamber geometry on the shape of the rate of heat release curve. Another attempt, although less refined, was reported by Lyn et al (72). Their investigation was aimed at calculating heat release rate and predicting cylinder pressure diagram. However, they only considered a short portion (about 60^{o}CA), during the closed part of the cycle and did not consider the pressure difference between the main and prechambers. They treated the engine cylinder as one whole control volume. Numerous assumptions were involved regarding trapped conditions and heat fluxes. However, the investigation revealed a good understanding of the combustion phenomena in a divided chamber engine, with an attempt to correlate the calculated rate of heat release curves.

A simplified simulation of the divided chamber engine compression stroke was reported by Jankov (56), whose investigation concerned mass flows and passage flow velocities. A proper thermodynamic mathematical simulation of the engine type investigated was not used, but the effects of the adiabatic compression exponent, the angle of start of compression and (stroke/connecting rod length) ratio on the passage flow velocities and induced swirl in the prechamber, were studied.

Anisitis (6,7) reported a study of heat release calculations for a divided chamber diesel engine, utilizing a sound simulation procedure, and taking into consideration all thermodynamic aspects involved. By treating the engine cylinder as two separate control volumes connected by a passage, a separate heat release rate diagram for each volume was obtained.

It is clear from the above introduction that published work on indirect injection engine simulation is very limited, and that the need for a better and more extensive investigation of the thermodynamic simulation

of divided chamber diesel engines is apparent. In view of this, the author has developed a full cycle analysis simulation program. In addition, an analysis technique to calculate instantaneous rate of heat release inside both chambers of the indirect injection engine from experimentally obtained pressure diagrams was developed.

The simulation techniques are discussed in the following sections.

3.2 BASIC THERMODYNAMIC RELATIONS INVOLVED

Figure (3.1) is a diagram of an engine considered as a series of control volumes connected together via orifices. For any of these control volumes, the First Law of thermodynamics can be expressed as follows

$$\frac{d(M.e)}{dt} = - P \frac{dv}{dt} + \dot{Q}_w + h_f \frac{dM_b}{dt} + h_{g_{in}} \frac{dm_{g_{in}}}{dt} - h_{g_{out}} \frac{dm_{g_{out}}}{dt} . \qquad (3.1)$$

which is essentially:

Rate of change of internal energy = Rate of work exchange with the boundaries + Rate of heat exchange with the boundaries + Rate of heat released within the control volume + Enthalpy added or subtracted due to gas flow to or from the control volume.

Rate of change of mass = $\frac{dM}{dt}$

$$\dot{M} = \frac{dM}{dt} = \frac{dm_g}{dt} + \frac{dM_b}{dt} \qquad (3.2)$$

and

$$\frac{dm_g}{dt} = \frac{dm_{g_{in}}}{dt} - \frac{dm_{g_{out}}}{dt} \qquad (3.3)$$

Hence, from (3.1) we have

$$\frac{dM}{dt} e + M \frac{de}{dt} = e \left(\frac{dM_b}{dt} + \frac{dM_g}{dt}\right) + M \frac{de}{dt} = - P \frac{dV}{dt} + \dot{Q}_w + h_f \frac{dM_b}{dt} + h_{g_{in}} \frac{dm_{g_{in}}}{dt} - h_{g_{out}} \frac{dm_{g_{out}}}{dt}$$

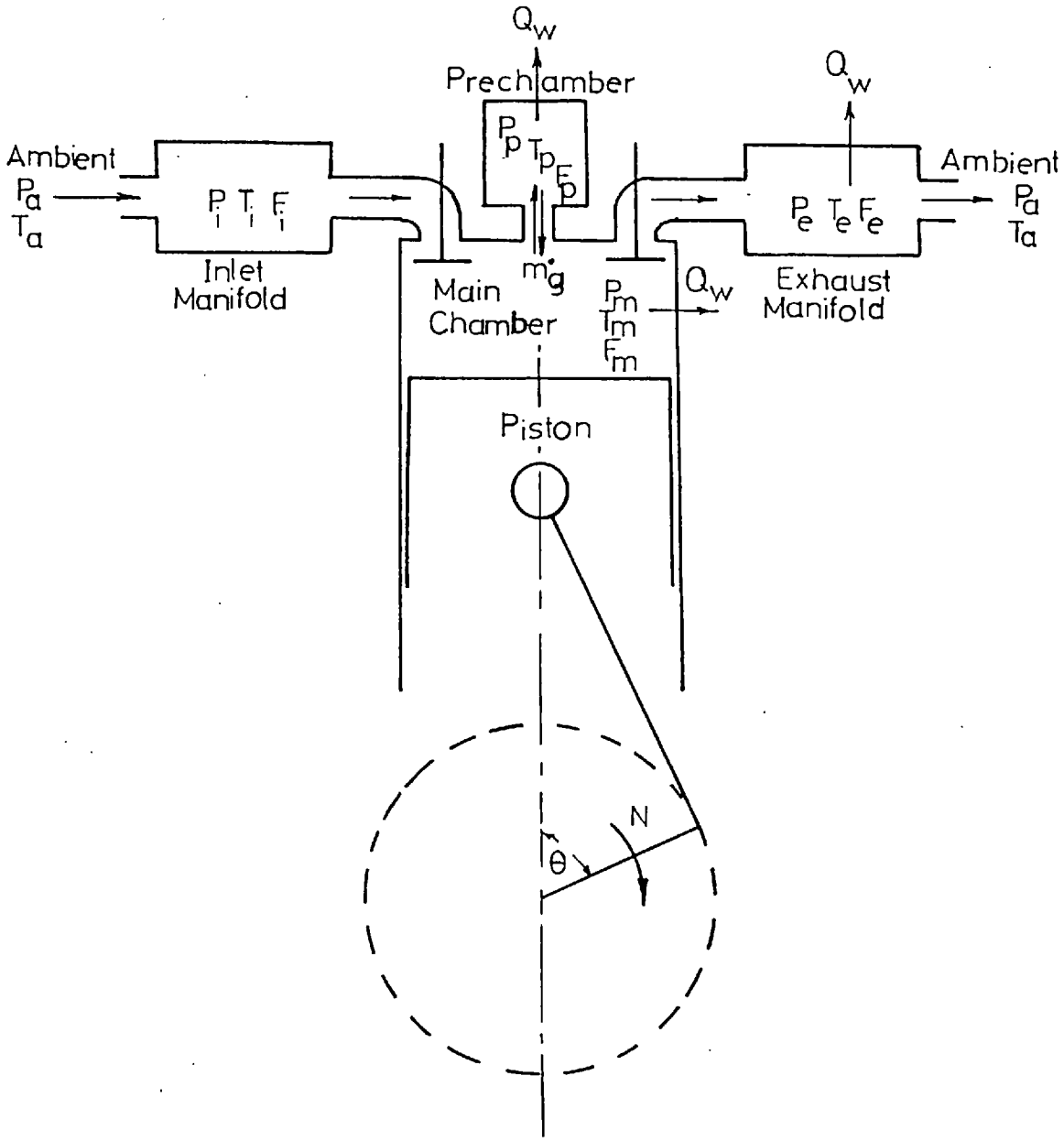

Fig. (3.1) Engine Thermodynamic Simulation System.

$$\frac{dM_b}{dt}(e-h_f) = -P\frac{dV}{dt} + \dot{Q}_e - M\frac{de}{dt}$$

$$- e\frac{dm_g}{dt} + h_{g_{in}}\frac{dm_{g_{in}}}{dt} - h_{g_{out}}\frac{dm_{g_{out}}}{dt} \qquad (3.4)$$

Both the internal energy of the charge (e) and the gas constant (R) can be expressed as functions of pressure (P), temperature (T) and equivalence ratio (F)

$$e = e\ (T,P,F)$$

$$R = R\ (T,P,F)$$

hence;

$$\frac{de}{dt} = \frac{\partial e}{\partial T}\cdot\frac{dT}{dt} + \frac{\partial e}{\partial P}\cdot\frac{dP}{dt} + \frac{\partial e}{\partial F}\cdot\frac{dF}{dt} \qquad (3.5)$$

$$\frac{dR}{dt} = \frac{\partial R}{\partial T}\cdot\frac{dR}{dt} + \frac{\partial R}{\partial P}\cdot\frac{dP}{dt} + \frac{\partial R}{\partial F}\cdot\frac{dF}{dt} \qquad (3.6)$$

The equation of state may also be applied to the control volume contents

$$PV = MRT \qquad (3.7)$$

or in its differential form

$$P^{\cdot} = \frac{dP}{dt} = \frac{MRT}{V}\left[\frac{M^{\cdot}}{M} + \frac{R^{\cdot}}{R} + \frac{T^{\cdot}}{T} - \frac{V^{\cdot}}{V}\right]$$

$$\frac{T^{\cdot}}{T} = \frac{V}{MRT}\cdot\frac{dP}{dt} + \frac{V^{\cdot}}{V} - \frac{M^{\cdot}}{M} - \frac{R^{\cdot}}{R}$$

and from (3.6)

$$\frac{T^{\cdot}}{T} = \frac{V}{MRT}\frac{dP}{dt} + \frac{V^{\cdot}}{V} - \frac{M^{\cdot}}{M} - \frac{1}{R}\left[\left(\frac{\partial R}{\partial T}\cdot\frac{dT}{dt} + \frac{\partial R}{\partial P}\frac{dP}{dt} + \frac{\partial R}{\partial F}\frac{dF}{dt}\right)\right]$$

$$\frac{T^{\cdot}}{T}\left(1 + \frac{T}{R}\frac{\partial R}{\partial T}\right) = \frac{dP}{dt}\left(\frac{V}{MRT} - \frac{1}{R}\frac{\partial R}{\partial P}\right) + \frac{V^{\cdot}}{V} - \frac{M^{\cdot}}{M} - \frac{1}{R}\frac{\partial R}{\partial F}\frac{dF}{dt} \qquad (3.8)$$

The total trapped mass at any instant of time may be expressed as;

$$M = M_o + (M_{g_{in}} - M_{g_{out}}) + M_b$$

and the trapped mass of fuel or its combustion products as

$$m_f = M_b + M_{f_o} + M_{g_{f,in}} - M_{g_{f,out}}$$

hence;

$$M - m_f = (M_o - M_{fo}) + (M_{g_{a,in}} - M_{g_{a,out}})$$

From the above, the equivalence ratio at any time is;

$$F = \text{Current Equivalence Ratio}$$

$$= \frac{m_f}{M_{a_o} + M_{g_{a,in}} - M_{g_{a,out}}} \quad \frac{1}{f_s}$$

Differentiating;

$$F' = \frac{dF}{dt} = \frac{1}{f_s} \left(\frac{1}{M_{a_o} + M_{g_{a,in}} - M_{g_{a,out}}} \right)^2$$

$$\left[(M_{a_o} + M_{g_{in}} - M_{g_{out}}) \frac{dm_f}{dt} - m_f \left(\frac{dm_{g_{a,in}}}{dt} - \frac{dM_{g_{a,out}}}{dt} \right) \right]$$

and since $$\frac{dm_f}{dt} = \frac{dM_b}{dt} + \frac{dm_{g_{f,in}}}{dt} - \frac{dm_{g_{f,out}}}{dt}$$

and $$M_{g_{in}} = M_{g_{a,in}} (1 + F_{in} \cdot f_s)$$

and $$M_{g_{out}} = M_{g_{a,out}} (1 + F_{out} \cdot f_s)$$

Hence the rate of change of trapped mass of fuel products is;

$$\frac{dm_f}{dt} = \frac{dM_b}{dt} + \frac{dm_{g_{in}}}{dt} \cdot \frac{F_{in} \cdot f_s}{1 + F_{in} \cdot f_s} - \frac{dm_{g_{out}}}{dt} \cdot \frac{F_{out} \cdot f_s}{1 + F_{out} \cdot f_s}$$

hence, the rate of change of equivalence ratio is expressed by;

$$F^{\cdot} = \frac{1}{(M_{a_o} + M_{g_{a,in}} - M_{g_{a,out}})} \left[\frac{1}{f_s} \left(\frac{dM_b}{dt} + \frac{dm_{g_{in}}}{dt} \cdot \frac{F_{in} \cdot f_s}{1 + F_{in} \cdot f_s} - \frac{dm_{g_{out}}}{dt} \frac{F_{out} \cdot f_s}{1 + F_{out} \cdot f_s} \right) - F \left(\frac{dm_{g_{in}}}{dt} \cdot \frac{f_s}{1 + F_{in} \cdot f_s} - \frac{dm_{g_{out}}}{dt} \cdot \frac{f_s}{1 + F_{out} \cdot f_s} \right) \right] \quad (3.9)$$

From equation (3.4) and (3.5)

$$\frac{dM_b}{dt} (e - h_f) = - P \frac{dV}{dt} + Q_w^{\cdot} + \left(h_{g_{in}} \frac{dm_{g_{in}}}{dt} - h_{g_{out}} \frac{dm_{g_{out}}}{dt} - e \frac{dm_g}{dt} \right) - M \left(\frac{\partial e}{\partial T} \cdot \frac{dT}{dt} + \frac{\partial e}{\partial P} \cdot \frac{dP}{dt} + \frac{\partial e}{\partial F} \cdot \frac{dF}{dt} \right)$$

$$= - P \frac{dV}{dt} + Q_w^{\cdot} + \left(h_{g_{in}} \frac{dm_{g_{in}}}{dt} - h_{g_{out}} \frac{dm_{g_{out}}}{dt} - e \frac{dm_g}{dt} \right) - M \frac{\partial e}{\partial P} \cdot \frac{dP}{dt} - C_1 M \frac{\partial e}{\partial T} \left(\frac{V}{MRT} - \frac{1}{R} \frac{\partial R}{\partial P} \right) \frac{dP}{dt} + \frac{V^{\cdot}}{V} - \frac{M^{\cdot}}{M} - \frac{1}{R} \cdot \frac{R}{F} \frac{dF}{dt} - M \frac{e}{F} \cdot \frac{dF}{dt}$$

Rearranging, the rate of fuel burning is expressed as,

$$\frac{dM_b}{dt} (e - h_f) = - P V^{\cdot} + Q_w^{\cdot} + \left(h_{g_{in}} \frac{dm_{g_{in}}}{dt} - h_{g_{out}} \frac{dm_{g_{out}}}{dt} - e \frac{dm_g}{dt} \right) - M \frac{\partial e}{\partial P} P^{\cdot} - C_1 M \frac{\partial e}{\partial T} \cdot P^{\cdot} \left(\frac{V}{MRT} - \frac{1}{R} \frac{\partial R}{\partial P} \right) - \left(\frac{V^{\cdot}}{V} - \frac{M^{\cdot}}{M} \right) C_1 M \frac{\partial e}{\partial T} + F^{\cdot} \left(\frac{MC_1}{R} \frac{\partial R}{\partial F} \frac{\partial e}{\partial T} - M \frac{\partial e}{\partial F} \right)$$

Rearranging, the rate of change of charge pressure is expressed as,

$$P^{\cdot}\left(M\frac{\partial e}{\partial P}+C_1 M\frac{\partial e}{\partial T}\left(\frac{V}{MRT}-\frac{1}{R}\frac{\partial R}{\partial P}\right)\right)=-P\,V^{\cdot}+Q_w^{\cdot}-\frac{dM_b}{dt}\left(e-h_f-C_1\frac{\partial e}{\partial T}\right)$$

$$-\frac{V^{\cdot}}{V}C_1 M\frac{\partial e}{\partial T}+\frac{dm_g}{dt}\left(C_1\frac{\partial e}{\partial T}-e\right)+\left(h_{g_{in}}\frac{dm_{g_{in}}}{dt}-h_{g_{out}}\frac{dm_{g_{out}}}{dt}\right)$$

$$+F^{\cdot}\left(\frac{M C_1}{R}\frac{\partial R}{\partial F}\frac{\partial e}{\partial T}-M\frac{\partial e}{\partial F}\right) \qquad (3.10)$$

where

$$C_1=1/\left(1+\frac{T}{R}\frac{\partial R}{\partial T}\right)$$

$$F^{\cdot}=\left(1/\left(Ma_o-M_{g_{a,in}}-M_{g_{a,out}}\right)\right)$$

$$\frac{1}{f_s}\frac{dM_b}{dt}+\frac{dm_{g_{in}}/dt}{1+F_{in}\cdot f_s}\left(F_{in}-F\right)-\frac{dm_{g_{out}}/dt}{1+F_{out}\cdot f_s}\left(F_{out}-F\right) \qquad (3.11)$$

Equation (3.11) describes the rate of change of trapped equivalence ratio inside the control volume due to mass exchange or fuel burning. Equation (3.10) fully describes the control volume thermodynamically at any instant of time. All expected operations within the control volume or at its boundaries are taken into consideration within the control volume or at its boundaries (e.g. heat and mass transfer). Equations (3.2), (3.10) and (3.11) represent the basic equations which describe any of the engine control volumes at any instant of time. They represent the basis for the rate of heat release calculation method as well as the full cycle analysis program. These together with the mathematical simulation technique are discussed in the following sections.

3.3 THE MATHEMATICAL SIMULATION TECHNIQUE

In the previous section the governing differential equations describing the thermodynamic state of charge in any engine control volume were derived.

In this section the mathematical simulation and manipulation of those thermodynamic equations, together with all other relations involved, are considered.

Thermodynamic Properties

In equation (3.10) and (3.11) all thermodynamic properties of the charge in any control volume and the appropriate partial differentials are expressed in analytical form. Thermodynamic equilibrium and ideal gas behaviour are assumed at all times. At any instant, it is also assumed that any individual control volume contains a homogeneous mixture of air and combustion products. The effects of spacial variation within any control volume, non-equilibrium composition, fuel vapour phase before combustion, pressure waves, etc. are not included.

Perfect mixing is also assumed between any two flow streams at different thermodyanmic states and/or different species.

Diesel fuel is assumed to have the chemical structure ($C_n H_{2n}$). The thermodynamic properties for combustion products of such a hydrocarbon, were introduced by Powell (88), who used an absolute enthalpy system which transforms air and products of combustion into one continuous medium where thermodynamic state is determined by temperature, pressure and equivalence ratio. These properties were presented as analytical expressions:-

$$e = e(T,P,F)$$

$$R = R(T,P,F)$$

The required formulae for lean mixtures ($F \leq 1.0$), including dissociation effects at high temperatures, were taken from Krieger (61). Other expressions were used for rich mixtures ($1.0 < F \leq 1.6$) properties (45, 73). In the neighourhood of ($F = 1.0$) interpolation between the two sets of expressions was used to avoid the consequences of discontinuities in the properties and their derivatives.

Mass Flows

Extensive work has been reported on the flow through engine valves and ports. It has been shown by several workers (21,23) that the flow through valves and ports can be reasonably represented by one-dimensional quasi-steady flow, based on standard compressible flow principles. This model was used in the present work.

Direct effects on the flow of gas inertia and pressure waves together with deviations from one dimensional flows are neglected. The rate of mass flow ($\dot{m}$) of an ideal gas through an orifice is given by

$$\dot{m} = A.\ C_d\ .\ P \sqrt{\frac{2\gamma}{(\gamma-1)RT} \left((P_r)^{2/\gamma} - (P_r)^{\frac{\gamma+1}{\gamma}} \right)} \qquad (3.12a)$$

When the pressure ratio (P_r) reaches the critical value (P_{r_c})

$$P_{r_c} = \left(\frac{2}{\gamma+1}\right)^{\gamma/\gamma-1}$$

sonic flow rates would be reached in the orifice. The mass flow may then be obtained from

$$\dot{m} = A\ C_d\ P \sqrt{\frac{\gamma}{RT} \left(\frac{2}{\gamma+1}\right)^{\left(\frac{\gamma+1}{\gamma-1}\right)}} \qquad (3.12b)$$

For flow through the connecting passage between main cylinder and prechamber, a special experimental investigation was conducted to decide upon the flow discharge coefficient. This will be discussed under a separate heading (Chapter 5).

Engine Geometry and Time Domain

Physically, the angular position (θ) of the crank shaft governs the instantaneous geometry of each of the engines cylinders. It was, therefore, convenient to choose the crank angle as a time domain for the analytical simulation of the engine kinematics. The cylinder volume (V_c)

and liner area (A_L) exposed were calculated according to the kinematics of a slider crank mechanism

$$V_c(\theta) = \frac{\pi}{4} D_e^2 \left(\frac{L_e}{r_e} + 1 - \cos\theta - \sqrt{\left(\frac{L_e}{r_e}\right) - \sin^2\theta}\right) + V_{TDC}$$

$$A_L(\theta) = D_e r_e \left(\frac{L_e}{r_e} + 1 - \cos\theta - \sqrt{\left(\frac{L_e}{r_e}\right) - \sin^2\theta}\right) + A_{L,TDC}$$

The valve areas were calculated as a function of crank position ($A_V(\theta)$). The method used in Ref. (58) was adopted to arrive at valve flow areas using cam lift diagrams together with valve geometry, valve seat angle and rocker arm and push rod arrangements.

Heat Transfer

Heat transfer to the walls of all control volumes was accounted for except in the inlet manifold.

Both radiative and convective heat loss were considered.

$$\dot{Q}_w(\theta) = h(\theta).\ A(\theta)\ (T_g(\theta) - T_w) + \dot{Q}_r$$

Radiative heat flux was neglected in the exhaust manifold. Details of the heat transfer calculation for the main chamber and prechamber are described in Chapter 4.

3.4 THE NUMERICAL SOLUTION

The solution procedure adopted for the equations described above, was based upon the step-by-step quasi-steady calculation technique (23, 58, 73). A computational scheme based on the numerical integration of formulae (3.2), (3.3), (3.10) and (3.11) was employed to compute thermo-

dynamic properties and contents of all engine control volumes at any crank angle position (θ) using information from the previous crank angle position. The problem is an initial value one, which requires initial conditions inside each control volume to be known. An iterative approach based on initial estimates was used. The solution methods are then self-correcting.

Details of the numerical solution methods are given below.

3.4.1 The Numerical Method

Numerical integration of differential equations is a wide subject and the literature describes several techniques that can be used. In the field of engine simulation the two most commonly used methods are the Runge-Kutta and the Predictor-Corrector techniques (27). Neither of the two methods are superior in all problems. Annand (9) studied the different methods of numerical analysis used in the field of engine cycle simulation and indicated that the iterative techniques (e.g. predictor-corrector) were more suited for such application. He also showed that the iterative methods, compared to a Runge-Kutta fourth order method, were more efficient and less prone to numerical instability during the gas exchange processes. Moreover, iterative methods provide estimates for the final truncation error which allows further correction for a specified accuracy.

Considering the simulation of a prechambered engine, two main control volumes, namely the main chamber and the prechamber, are always connected via a passage. This was expected to render numerical instability problems. It was therefore decided to use a second order predictor corrector method for integration due to its advantage in that area. The method was an Euler type formula for prediction

$$Y_p(\theta) = Y(\theta-\Delta\theta) + \Delta\theta . \dot{Y} (\theta-\Delta\theta) \qquad (3.13)$$

and the modified Euler type integration formula for correction:

$$Y_c(\theta) = Y(\theta-\Delta\theta) + \frac{\Delta\theta}{2}\left(Y^{\cdot}(\theta-\Delta\theta) + Y_p^{\cdot}(\theta)\right) \qquad (3.14)$$

where

$Y^{\cdot}$ = $dY/d\theta$

$Y(\theta)$ = Value of the function (Y) at (θ)

$Y(\theta-\Delta\theta)$ = Value of the function (Y) at ($\theta-\Delta\theta$)

Y_p = Predicted value

Y_c = Corrected value

The predictor formula (3.13) provides a first approximation of the value of the function (Y_p) at time (θ). The corrector formula (3.14) evaluates a better estimate of the function (Y_c). An iterative sequence is then used to check the convergence of equation (3.14). The difference between two successive iterations must be within a specified tolerance (ψ).

$$|Y_{c_2} - Y_{c_1}| / Y_{c_1} \leqslant \psi$$

The step size for integration was chosen to be 1^{o}CA for the full cycle analysis program. Streit (102) reported that smaller step sizes did not yield significant improvement in accuracy.

3.4.2 Rate of Heat Release Program

Rate of heat release (ROHR) calculations are based on experimentally obtained cylinder pressure diagrams. At any step throughout the calculation, an energy balance of the control volume under consideration would indicate any increase of the energy level due to an external source other than piston work. In a DI engine this would be directly due to fuel burning. For IDI engines however, the increase in energy level could be due to charge enthalpy increase with inflow from the other chamber, or fuel burning. Heat release calculations are conducted during the closed cycle part of the experimental pressure diagram. For DI engines, the

calculation procedure can be started very close to injection point as the trapped mass is constant. For IDI engines, however, trapped mass in either chamber is a function of the crank angle position. The prechamber equivalence ratio is also a function of the crank angle position. A special calculation procedure has been developed to overcome these added difficulties.

The dominant factor affecting (ROHR) calculations is the rate of change of chamber pressure. Quantization of the actual continuous pressure signal, if in error, result in spurious derivatives and oscillations of the ROHR values. The spline function method recommended by Streit (102) was, therefore, used to fit a smooth curve in the experimental pressure diagrams before differentiation.

Experimental cylinder pressure diagrams from a fired engine were carefully analysed to estimate (ROHR) values. A computer program was developed for this purpose. Fig. (3.2) shows a flow chart of this program. The calculation procedure is summarised as follows:-

1. Read the experimental pressure and pressure difference values and standard deviations.
2. Smooth pressure diagrams for both main chamber and prechamber and obtain values of rate of pressure rise at every point sampled in the engine cycle.
3. Equations (3.2, 10, 11), are solved starting from the position of inlet valve closure, assuming approximate trapped conditions of P, T and F inside both the main and prechambers. The integration procedure continues until a position in the cycle (before injection point) is reached where the (ROHR) calculations are to be started. Predicted pressure values are then compared with experimental values. If the difference is more than a specified value

Figure (3.2)

Heat Release Programme Flow Chart

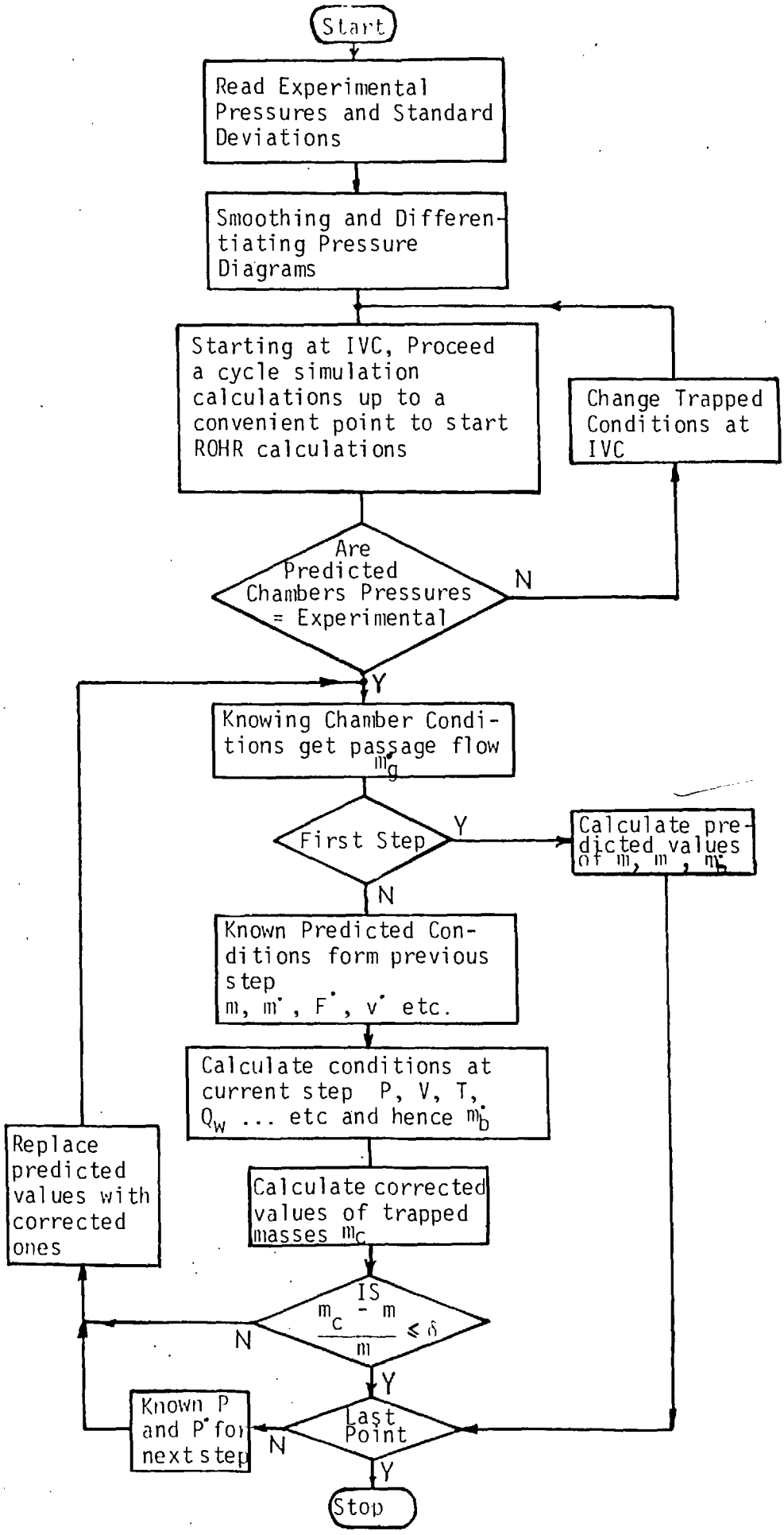

(1%), the initial trapped conditions are modified and the procedure repeated. When the specified accuracy is reached the (ROHR) calculation is started. This procedure ensured that the trapped conditions (in both chambers) of pressure, temperature, equivalence ratio and mass are not in error at the beginning of ROHR calculations.

4. Equation (3.10) is then solved for both chambers. The rate of pressure (P') is known from the analysis of the experimental pressures in both chambers and equation (3.10) can be solved to get (ROHR) values $(\frac{dM_b}{dt})$.
5. The pressure ratio across the passage and flow conditions provide passage flow (dm_g/dt).
6. Iterations are made for both chambers for convergence of mass in each chamber. The tolerance limit used is 0.01%.
7. The calculations usually continue for $(70^{o}CA)$ after TDC, or longer if the ROHR has not decreased to zero.

3.4.3 Full Cycle Analysis Program

A full cycle analysis program has been developed to study the operation of indirect injection diesel engines. The program solves the governing equation described earlier in this chapter for all control volumes of a multi-cylinder engine. Wave action in the inlet and exhaust systems is not included. Only steady state, natural aspiration conditions were considered. The program is also capable of simulating DI engine operation.

Input data for the computer program is as follows:-

1. Engine geometric data, e.g. bore, stroke, connecting rod length, prechamber and clearance volumes and areas etc.

2. Flow areas of the connecting passage, inlet pipe to inlet manifold and exit pipe from exhaust manifold, and instantaneous flow areas of inlet and exhaust valves.
3. Heat transfer areas of prechamber, clearance volume and exhaust manifold.
4. Wall temperatures of the prechamber and the main chamber.
5. Valve timing, number of cylinders and firing order.
6. Instantaneous fuel burning rate for prechamber and main chamber (for fired runs).
7. Engine speed.
8. Ambient conditions and initial conditions (estimates) in all control volumes.

Fig. (3.3) is a schematic flow chart describing the main features of the computer program. It comprises the following basic steps:

1. All input data are read in.
2. Geometric parameters for all cylinders are determined.
3. The predictor formula is used to estimate new conditions in every control volume.
4. The new thermodynamic properties of the contents of all control volumes are obtained.
5. Rates of mass transfer, fuel burning, and energy transfer for all control volumes are calculated.
6. Heat transfer for all control volumes is evaluated.
7. Rates of change of mass and pressure in all control volumes are evaluated using equations (3.3) and (3.10).
8. Using the corrector formula, new estimates of the charge mass and pressure in each control volume are obtained.
9. The predicted and corrected values are then compared for each control

Figure (3.3)

Block Diagram for Full Cycle Analysis Programme

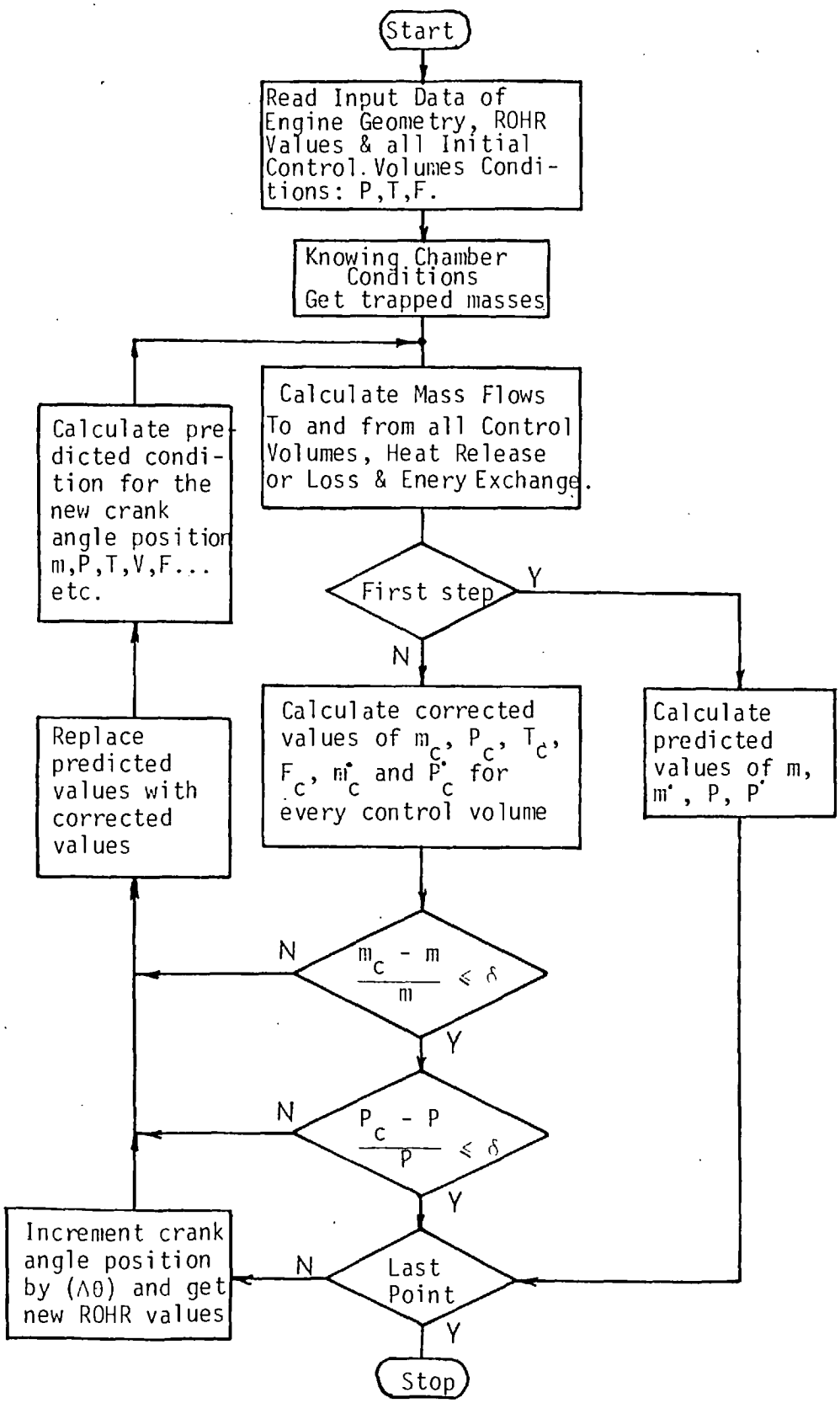

volume. If the percentage difference between the predicted and corrected values in any control volume exceeds a specified volume (0.1%) the calculations are restarted from step number 4. The corrected values would in this case be considered as a second prediction.

10. When the necessary accuracy has been achieved, average charge velocity estimates are calculated for all cylinder chambers by applying conservation of kinetic energy concept (see Chapter 4).
11. All rates of change of mass and pressure in all control volumes are stored to be used in the subsequent calculation step.
12. The crank angle position is incremented (by 1^{o}CA) for all cylinders and the sequence repeated from step 2.

The output from the program comprises:-

1. Instantaneous values, in every control volume, of charge mass, pressure, temperature and equivalence ratio.
2. Instantaneous velocity estimate in main and prechamber of every cylinder.
3. When the engine cycle is concluded, the program prints out; total fuel and heat loss in every control volume, total air and exhaust gas flows through the manifolds and indicated mean effective pressure from all cylinders.

For the specific purpose of studying IDI engine performance in relation to DI engine, the program was developed to be used in different modes of operation:-

a) Motored operation

b) Fired operation

Both the above modes could be used for;

a) Direct injection engine simulation

b) Indirect injection engine simulation

Heat flux rates could either be calculated in the prgram or read in as instantaneous input data. The details of the losses isolation technique are given in Chapter 8.

CHAPTER 4

HEAT TRANSFER

4.1 INTRODUCTION

Heat transfer to the walls of Internal Combustion Engines is a complex process. The properties and state of the charge inside an engine cylinder are both time and position dependent. Although extensive research has provided an overall description of events inside the cylinder, there is little detailed information of various thermodynamic, heat transfer and gas dynamics factors involved.

An ability to predict the magnitude of heat exchange between the working fluid in a reciprocating engine, and the walls of the combustion chamber, is of paramount importance. Although performance or efficiency calculations might only require approximate knowledge of the heat losses, more precise information would be required to predict thermal loading or for optimisation studies.

Work in the field of engine heat transfer through the past fifty years has outlined the general mode of heat flux between the cylinder charge and the walls. It is now evident, and clearly understood, that although the major proportion of the heat is transferred by forced convection, heat radiation cannot be ignored. Radiation has been shown to be the source of about 25-30% of the total heat loss in some cases.

Due to the extreme complexity and immense importance of the phenomenon of heat transfer, impirical correlations between engine variables and the instantaneous heat transfer coefficient are currently used for engine heat transfer calculations. Since these correlations are based on experimental investigations, on different types of engines, the different magnitudes of

predicted heat fluxes are not surprising. Large variations must arise from engine to engine, or even from point to point in the same engine, because of variations in the flow pattern which can only be vaguely characterised. Engine geometry, apart from cylinder bore and stroke, has not been included in the correlations.

Although correlations as early as Eichelberg's (35) are still being used, the general trend recently has been towards a more sound approach to correlating the instantaneous heat transfer coefficients. Accurate heat flux measurements inside the engine cylinders have resulted in a better understanding of the problem. It has become clear that both convective and radiant components of heat transfer are present. The relative importance of radiative heat flux differs from one engine type to another.

In this chapter, the problem of heat transfer inside the prechamber and main chamber of an IDI engine is considered. Available work on engine heat transfer is reviewed. A method for calculating estimates of instantaneous "characteristic" gas velocities in either chambers, is explained. These velocity estimates are then used in a (Nu-Re) relationship which correlates convective heat flux to the chamber walls. The method of calculation for velocity and heat flux is first checked against Hassan's (49) results. It is then compared with the experimental results of the present work. Radiative heat flux calculations are also presented. Techniques employed in the measurement and analysis of heat flux are also described.

4.2 CONVECTIVE HEAT TRANSFER

Forced convective heat transfer for theory implies that Re and Nu may be related as follows

$$Nu = a\ Re^{b}$$

where a, b and c are constants.

This relationship is based largely on flat plate and pipe flow heat

transfer, but appears also to be representative of other convective heat transfer situations. Convective heat transfer inside the internal combustion engine has been modelled by a relationship of the above form,

where,

$$Nu = \frac{hD}{K} \quad \text{and} \quad Re = \frac{\rho v D_c}{\mu}$$

where the Prandtl number is approximately constant and its effect neglected.

Several investigations on engine heat transfer calculations used a Nu-Re relationship (8,10,49,60,97,117). Although the same form of relationship was used, large variations in the values of a and b are evident in the data. These variations are expected, since in the various correlations, different definitions have been used for the characteristic dimension (D_c) and velocity (v). Different engine types and geometries were used to obtain the background data, a factor which contributed to the differences in constants a and b.

The characteristic velocity should represent the flow field near the surface. The increase of heat flux with engine speed encouraged the use of mean piston speed as the characteristic velocity (8,97,117). Alternatively, instantaneous gas velocities (49), average swirl speeds calculated from induction generated swirl (66), or instantaneous estimates of gas velocities (10,60), have been utilised.

Undoubtedly, if local instantaneous values of gas velocity at the walls of the combustion chamber, together with spacial distribution of the chamber charge pressure and temperature, were available, they could be used to provide better predictions of the actual heat flux. Unfortunately, such information is not available. A very detailed and thorough investigation is needed to provide this data, but it remains questionable whether an experimental or theoretical study of this kind would provide sufficiently accurate information to justify its cost.

The Nu-Re relationship has proved to be useful. When used by different researchers for different engines with wide variations and under different operating conditions, reasonable agreement with the actual heat flux measurements and trends has been achieved. Three major parameters are needed when using the Nu-Re heat flux relation; a characteristic dimension D_c, a characteristic velocity v and a representative temperature at which gas properties should be calculated. These will be discussed in the following sections.

4.2.1 Gas Velocity Measurements

Experimental results of actual velocity distributions inside diesel engines throughout the cycle are needed. These would set the guide lines for, and allow verification of, theoretical calculations aimed at finding instantaneous characteristic velocities to be used for heat flux calculations.

Little accurate data on instantaneous gas velocities in engine cylinders is available due to the extreme complexity of the flow field, accessability problems and rapid variation of properties of the cylinder charge. Hot wire anemometry has been applied in engine research for velocity measurements. For the DI engine the work of Dent (30), Hussmann (54), Semenov (92) and Williams (114) is available. For the IDI engine, work by Hassan (49), Nagao (78) and Nakajima (80) has been published. The accuracy of gas velocity measurements in engines is generally poor. However, the outlines of the general flow phenomenon has been established.

Examination of available experimental results of velocity measurements in cylinders of different geometry, permits identification of three different modes of gas flow fields under motoring conditions.

- Direct Injection, Flat Piston — Fig.(4.1)
- Direct Injection, Bowl in Piston — Fig.(4.2)
- Indirect Injection, Swirl Chamber — Fig.(4.3)

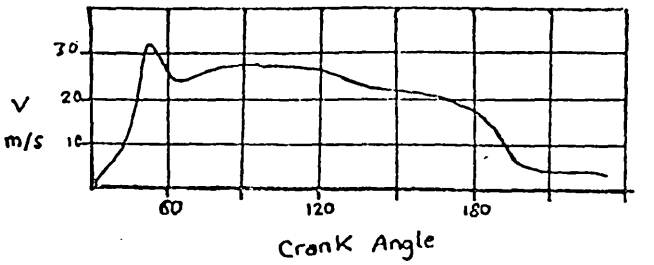

Fig. (4.1) Swirl velocities near the wall of a flat piston engine cylinder (900 rpm) (92)

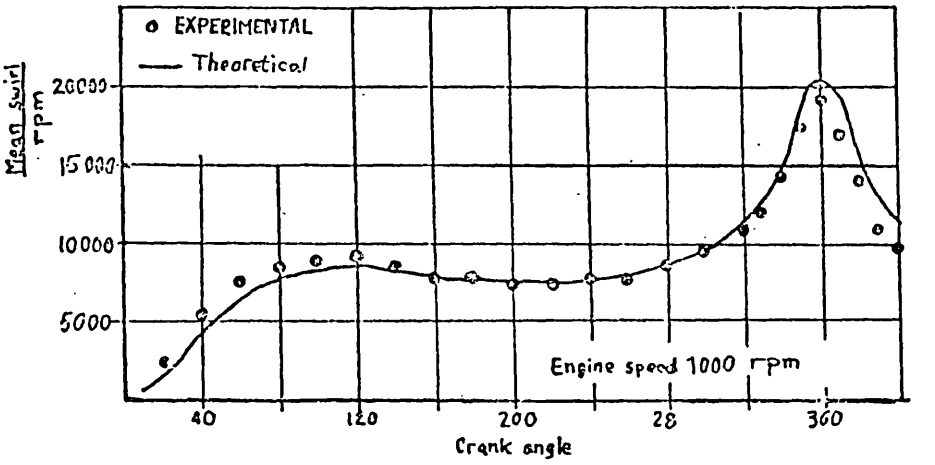

Fig. (4.2) Mean swirl variation in the bowl of a DI engine piston (30)

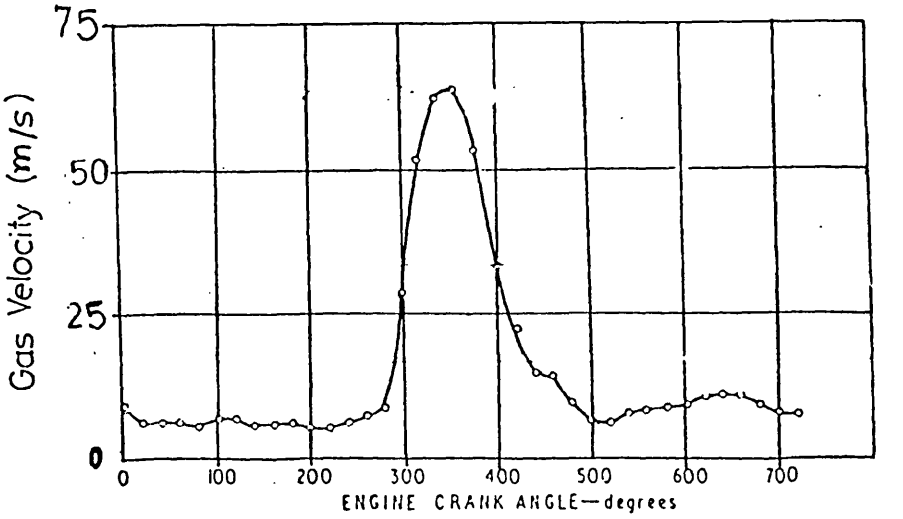

Fig. (4.3) Swirl velocity at the wall of a swirl chamber (49)

Combustion chamber charge motion is governed by the induction generated motion in DI engines or passage flow in IDI engines. Viscous and wall friction effects always act to reduce the charge velocity and dissipate some of its kinetic energy (as heat).

With a flat piston, Fig. (4.1), the swirling gas velocity, measured near the cylinder wall, attains a maximum and then starts to drop due to frictional effects. In the case of the bowl in piston geometry, Fig. (4.2), (where measurements shown are in the bowl) the swirl velocity of the charge continues to increase as the piston approaches the TDC position. This is due to the shift of gases from the main chamber to the bowl, with the corresponding increase of rotation velocity from momentum, or kinetic energy consideration. In the case of an IDI swirl chamber engine, Fig. (4.3), swirl velocity in the prechamber continues to increase as more gas is delivered through the passage, due to the upward movement of the piston. When the piston starts to return down the bore, gases flow from the prechamber back to the main cylinder. This, together with viscous and friction effects, results in a reduction of velocity in the swirl chamber.

4.2.2 Gas Velocity Calculations

Very few investigations report attempts to calculate instantaneous gas velocities in the cylinder of an internal combustion engine. Probably the work of Fitzgeorge and Allison (39) was the first realistic attempt to estimate instantaneous values of swirl and squish velocities for a bowl in piston DI engine. The basis of their calculation was conservation of kinetic energy of incoming air during the induction period. The works of Shimamoto (93) and Henein (50) were more concerned with squish.

Knight (60) introduced a method of calculating instantaneous gas velocities, which he applied for a swirl chamber engine. He assumed that the kinetic energy of the gas coming into the cylinder is conserved as it

mixes with the charge already in the cylinder. When the valves are closed, the kinetic energy of the charge reduces through wall friction.

The same concept is applied to the swirl chamber charge. Knight assumed uniform density throughout the cylinder and the swirl chamber. This assumptions could introduce significant error when used for divided chamber engines. It implies that gas flows between the two chambers are due to change in volume only. Thus calculated velocities would be the same regardless of whether the engine were motored or fired. This is apparent from Fig. (4.4a,b). The figure also shows a significant difference between velocities at the beginning and the end of the engine cycle. This again identifies another drawback in the calculation, namely, inadequate energy dissipation by friction.

It may be expected that combustion could have a greater influence on the level of turbulence of the charge than the mean gas velocity. This could have an effect on the heat transfer coefficient at the chamber wall. Dent (31) studied the results of high speed combustion photography in a high swirl diesel engine (by Stock (101)), and concluded that there was an increase in swirl level due to combustion.

A recent attempt to calculate instantaneous gas velocities was presented by Derham and Dent (30), for a bowl in piston DI engine. A similar calculation technique to that of Fitzgeorge and Allison (39) was followed, but assuming conservation of momentum of the charge, and allowing for friction effects. Their main assumption of forced vortex velocity distribution across the cylinder bore, appeared to be reasonably valid during the induction stroke. Near TDC, however, experimental results by Hussmann (54) show a deviation from solid body rotation. Fig. (4.2) shows Dent's comparison between experimental and calculated velocities. Good agreement is apparent.

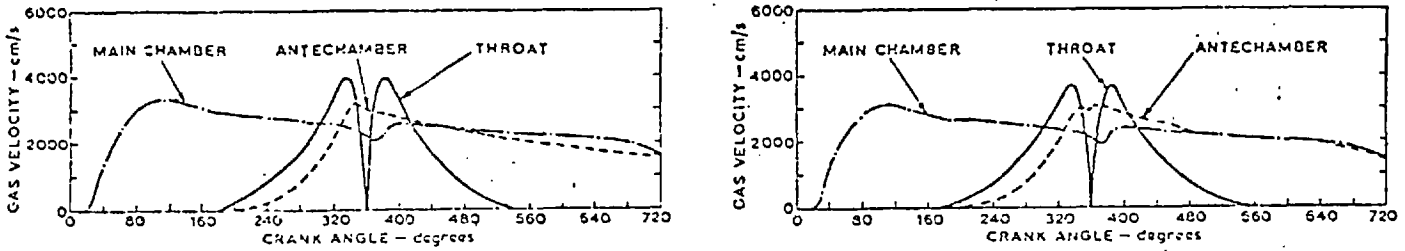

a. *Calculated gas velocities, 500 rev/min motored*

b. *Calculated gas velocities, 500 rev/min fired*

Fig. (4.4) Kinetic energy mean velocities by Knight (60)

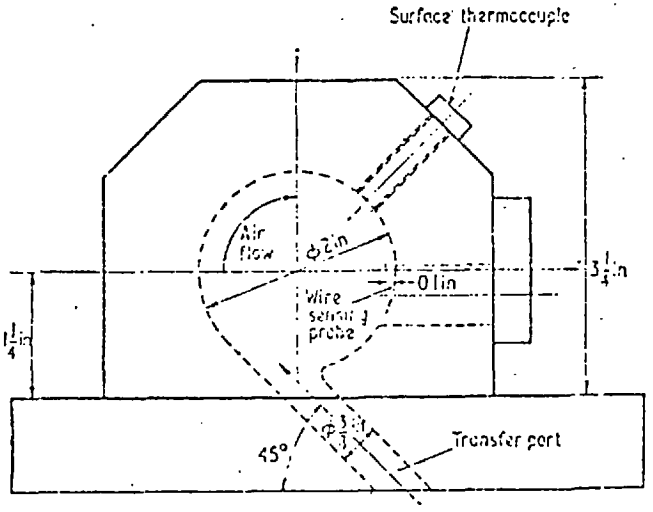

Fig. (4.5) Cylinder head arrangement by Hassan (49)

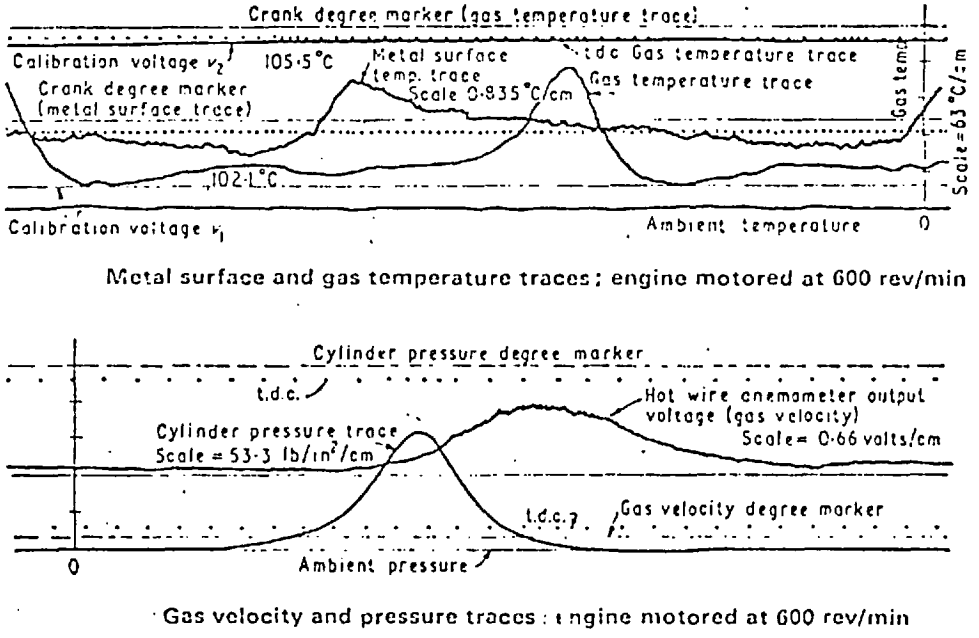

Fig. (4.6) Sample of signal traces of Hassan's tests (49)

4.2.3 The Experimental Investigation by Hassan

Test Arrangement

Hassan (43) used a hot wire anemometer for instantaneous velocity measurements inside the swirl chamber of an indirect injection engine, a RUSTON-WB air cooled engine, with a modified cylinder head. The cylinder head carried a cylindrical swirl chamber connected via a long passage to the main cylinder. The swirl chamber was equipped with three probes (Fig. 4.5), a hot wire probe to measure instantaneous gas velocity, a film type thermocouple to measure instantaneous wall temperature and a resistance type thermocouple for gas temperature measurements. Measurements were made for a motored engine only. Gas velocity and temperature traces were recorded using a high speed camera. All the measured and recorded traces were then tabulated, at 10 or 20^{o}CA steps, for analysis. The wall temperature traces were analysed using a conventional Fourier analysis technique to derive corresponding heat flux values. Engine compression ratio was varied by altering the distance between the cylindrical swirl chamber side walls, thus changing the clearance volume. Tests were conducted at three engine speeds and three compression ratios. An example of the output traces recorded, appears in Fig. (4.6). This figure also includes a pressure trace from the main cylinder.

Results and Accuracy of Measurements

The three compression ratios used were 8.5, 9.8 and 11.5:1 and at each compression ratio three speed tests at 600, 900 and 1100 rpm were conducted. At every running condition the recorded traces were analysed to calculate instantaneous Reynold's and Nusselt's numbers. All gas properties were calculated at the mean film temperature (the mean of instantaneous wall and gas temperatures). The estimated Reynold's numbers, heat fluxes and temperature differences between the gas and wall were

plotted against the corresponding crank angle (Figs. 4.7 and 4.8).

As the aim of the work was to study the phenomenon of heat transfer in a swirl chamber engine, a correlation was sought between the measured instantaneous values of Re and Nu numbers. These were plotted, as shown in Fig. (4.9), and were found to be reasonably correlated by a relationship of the form,

$$Nu = a \ Re^{b}$$

where $a = 0.023$

$b = 0.8$

The correlation agreed with the measured behaviour to an accuracy of ±20%. In other words, better agreement between the proposed correlation and experimental results could be obtained if the parameter (a) was allowed to vary within ±20%.

Although this could imply that parameter (a) is not a constant, a better judgement could be obtained when taking the accuracy of measurements into consideration. Hassan, stated that instantaneous velocities in the high temperature, high density flow conditions inside the swirl chamber could be measured to an accuracy of ±12%. The accuracy for temperature measurements was quoted as ±6%. These inherent errors in measurements would be expected to affect the value of the constant (a), and thus could explain some of the variation of (a) within the cycle, and at different conditions, as shown in Fig. (4.9).

Figs. (4.7), (4.8) and (4.9) summarise the experimental results obtained by Hassan. With his measurement accuracy in mind, and remembering the complex phenomena of heat transfer and velocity measurements, they provide a useful picture of the trends and magnitudes expected for instantaneous gas velocities and heat flux in the swirl chamber of IDI engines under motored conditions.

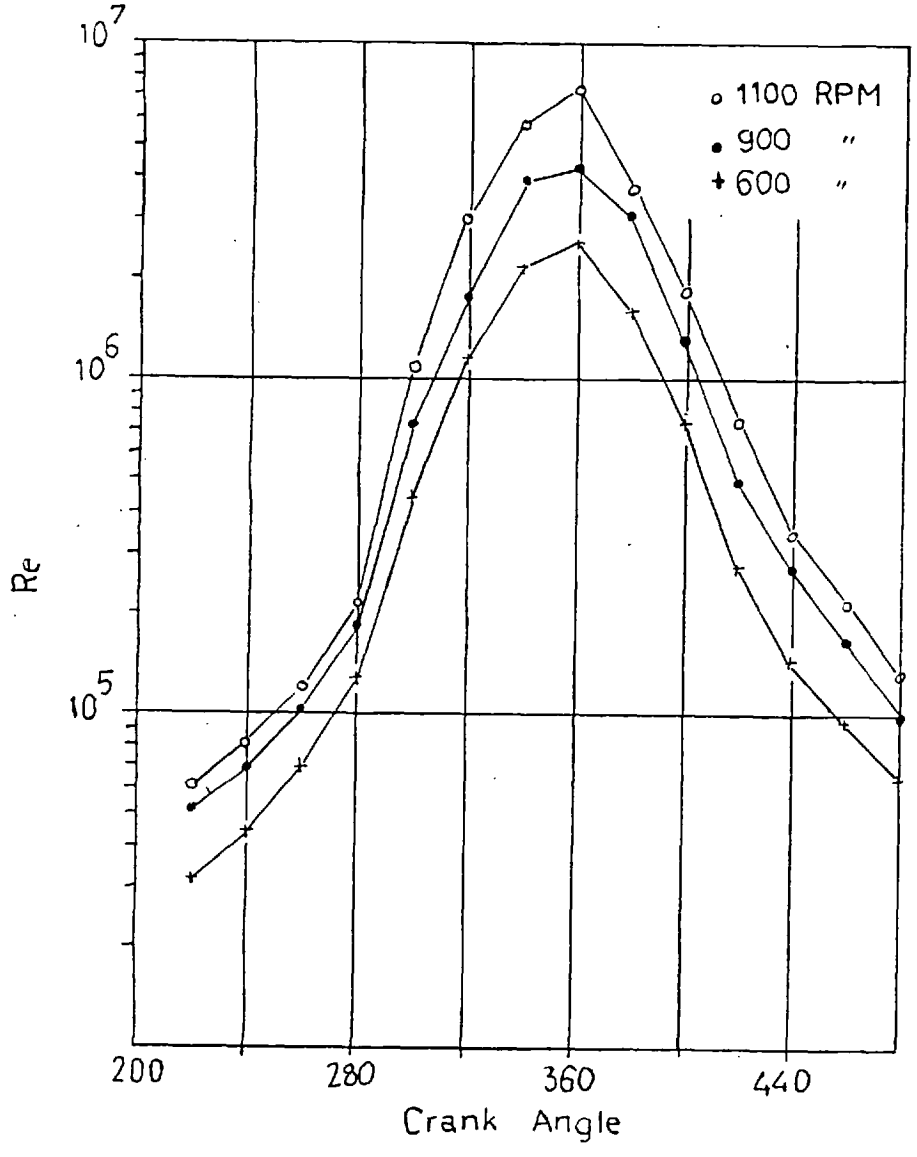

Fig. (4.7) Measured Reynolds numbers at the chamber wall (49)

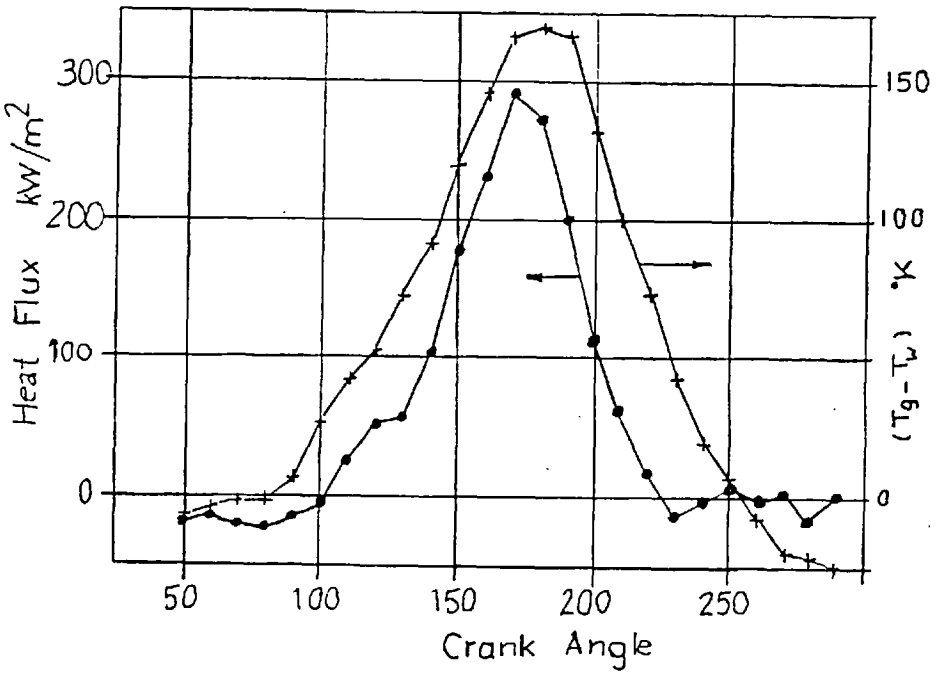

Fig. (4.8) Instantaneous gas temperature and heat flux (49)

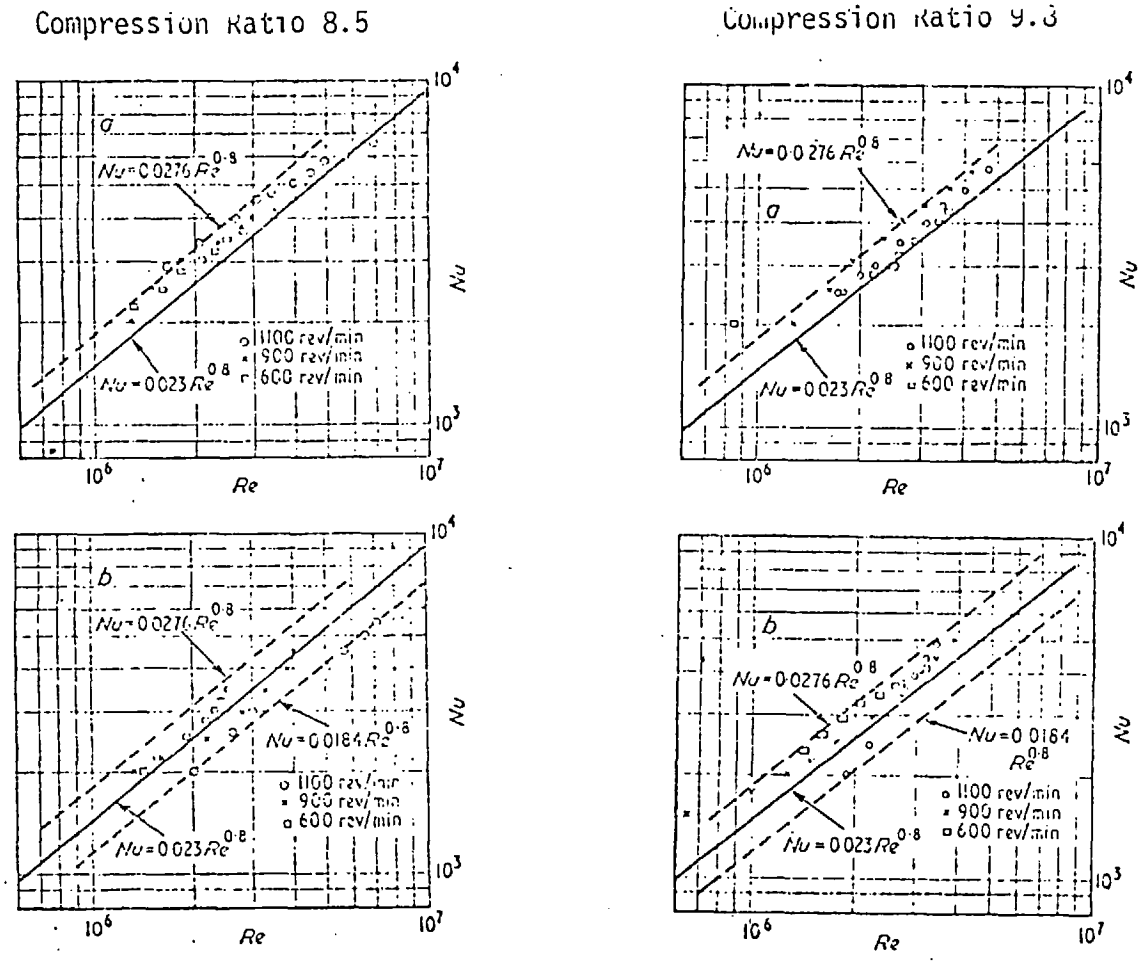

Fig. (4.9) Local Nusselt and Reynolds number (49)

4.2.4 Present Calculation Method of Gas Velocity

Recently, there has been a growing interest in the understanding of flow phenomena within the cylinders of internal combustion engines, as reports of both experimental and theoretical studies, indicate. Flow fields inside the combustion chamber affect the spacial distribution of properties, the fuel and air mixing process and combustion.

Another important objectiveof gas velocity calculations has been to establish a characteristic velocity enabling realistic heat flux correlations to be obtained using the normal Nu-Re relationship.

The investigation by Knight (60), Lefeuvre (66), Shroff (94) and Annand (10) had the same objective; velocity calculation for heat transfer calculations. The work of Dent (30), although at first directed towards actual velocity calculation and comparisons with experimental behaviour, was later used (31) for heat transfer calculations.

Instantaneous velocity estimates of the charge were obtained in the present investigation to be used as a characteristic velocity representing the flow field in a Nu-Re heat transfer relationship. The calculation method and assumptions involved are described in the following subsections.

4.2.4.a. Kinetic Energy and Momentum Conservation Concepts

Knight (60), Annand (10) and Shroff (94) used the kinetic energy conservation concept for their calculations. Dent (31) used the conservation of angular momentum concept for instantaneous velocity calculation. Lefeuvre (66) calculated induction induced swirl velocities which he assumed constant throughout the cycle.

The concept of kinetic energy conservation assumes that the chamber charge retains its kinetic energy, unless kinetic energy is added to it or dissipated from it through viscous friction effects.

The concept of momentum conservation assumes that the angular momentum of the charge will be retained unless further angular momentum is added or

dissipated through viscous friction effects.

To examine the two concepts, an ideal case is first considered. Consider a mass of charge (m), rotating in a cylindrical chamber of a diameter (D) and thickness (L). The mode of rotation is assumed to be a forced vortex. Clearly, in the absence of frictional effects, both concepts apply. A clear difference would emerge when trying to calculate a representative average velocity of the charge. If the speed of rotation is assumed to be (ω_g), then the average velocity based on the average kinetic energy concept would be

$$V_{KE} = (\omega_g \frac{D}{2}) \; / \; \sqrt{2}$$

while that based on the average momentum would be

$$V_m = (\omega_g \frac{D}{2}) \; / \; (3/2)$$

Undoubtedly, both the V_{KE} and V_m are representative of the flow, but in two different ways. In any momentum calculation (V_m) must be used, while in any energy calculations (V_{KE}) should be used. Problems arise, however, when looking for a velocity representative of the flow to be used for heat flux calculations.

In an actual engine the flow is three dimensional, transient and turbulent, therefore, neither of the two concepts truly represents the flow field, i.e. both concepts are approximations. Momentum is a directional quantity and ignores all other components of the velocities except that of swirl. This may cause a significant error. Furthermore, the level of flow turbulence inside the engine cylinders has been reported to be quite high (92,115), yet turbulent components of velocity are entirely ignored in the momentum conservation concept. Kinetic energy is a scalar quantity and takes all velocity components into consideration. This leads to an over-estimate of the characteristic velocity, since not all components contribute

to the representative Reynolds number value.

When the inlet valve opens, air is introduced to the cylinder. In the momentum conservation principle only the swirling component at gas velocity is considered. The kinetic energy concept considers all velocity components. Neither concept takes into consideration turbulent mixing losses and velocity transformation into eddies and hence heat. It could however be argued that if the total gas velocity were considered, as in the case of kinetic energy conservation, the turbulence energy which intensifies heat transfer rates, would also be taken into account. This is considered to be an advantage of the kinetic energy concept. Another advantage is that it permits addition of energy from different sources which would intensify the kinetic energy of the flow, and therefore heat transfer rates. An important energy source is the extra kinetic energy due to fuel jet, which would increase heat transfer. This has been included in the present calculations, and is explained later.

The kinetic energy conservation concept, with special considerations of energy dissipation and combustion induced turbulence, has been used in the present work.

4.2.4.b Energy Dissipation

Fluids in motion relative to stagnant boundaries are subject to flow losses due to viscous friction. Viscous shear forces between adjacent layers of the fluid, and at the boundaries, are always acting to decelerate the flow and dissipate some of the flow energy into heat.

Previous attempts at calculating gas velocities inside engine combustion chambers either neglect energy dissipation, or use pipe flow friction data to estimate it. Fig. (4.4) shows the results of Knight (60) in which pipe-flow friction data was used. The figure shows that although initial velocities were zero, charge velocities at the end of the engine cycle had positive values, and therefore the inadequacy of the pipe flow friction data

to express such energy dissipation application is apparent. Although pipe flow friction adequately estimates the energy dissipation due to the walls, it does not take into consideration the dissipation due to sharp velocity gradients within the combustion chamber charge. Lefeuvre (66, Appendix B) used the relations presented by Okaya(83), for rotating disc friction, and calculated an average value of swirl deceleration over one engine cycle of 10-20% of the value at inlet valve closure.

The phenomenon of gas motion inside the engine cylinder or prechamber has been investigated by means of combustion photography and water models (78), electric charge visualization (80) and hot wire anemometry (30, 49, 54,92,114). Some examples of velocity distribution inside swirl chambers are shown in Fig. (4.10). The velocities shown were obtained from two dimensional cylindrical chambers. The actual three dimensional situation is different, but two dimensional results are accepted as reasonable approximation of the flow field. Mathematical representation of the velocity distribution for the chamber charge is needed. An assumption had to be made in this respect to simplify the calculations; a forced vortex distribution was assumed. Although Fig. (4.10) shows that the actual distribution is different from that of a forced vortex; it is an acceptable approximation.

For a thin disc rotating inside an enclosure and surrounded by a fluid (Fig. (4.11a)), the fluid would be set into swirling motion of a forced vortex nature. The resemblance between such a flow situation and that of the assumed flow field inside the engine combustion chamber is detected. It was concluded that the data available on frictional resistance of enclosed rotating discs would be more appropriate for modelling frictional resistance for swirling charges in engines, than pipe friction data.

Okaya (83) in 1939, presented a study on the friction of a disc rotating in a cylinder. Numerous studies have been carried out since then.

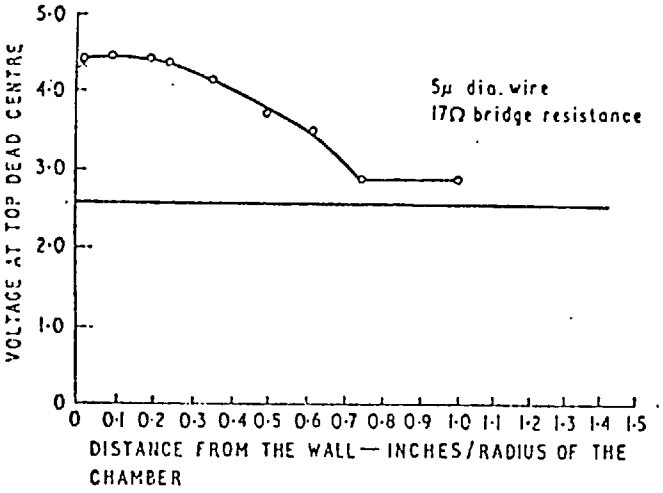

a. Variation of anemometer output voltage with position in pre-chamber (49)

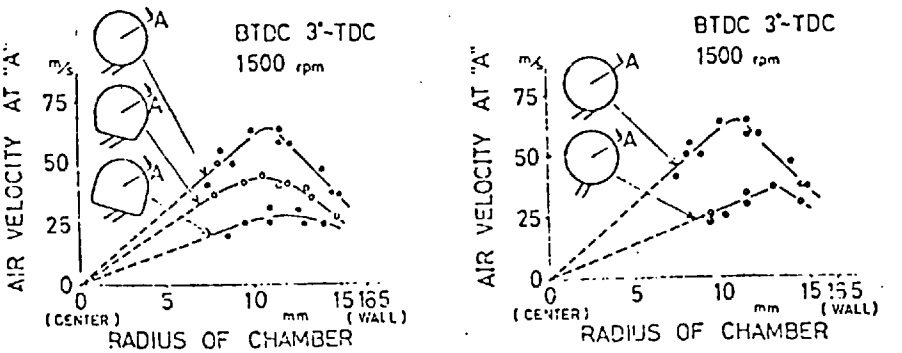

b. VELOCITY DISTRIBUTION (80)

Fig. (4.10) Velocity distributions inside swirl chambers

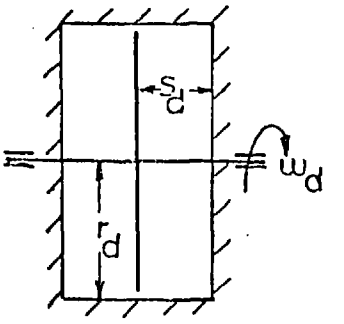

a. Geometry of Rotating Disc

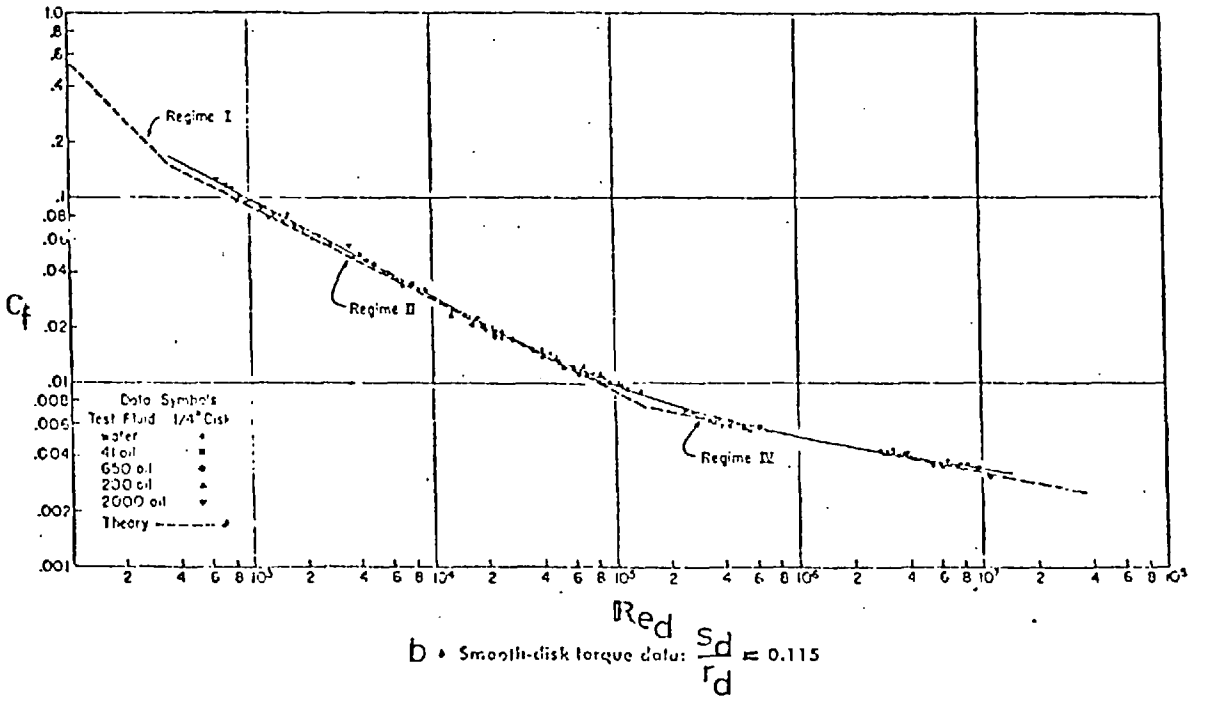

b. Smooth-disk torque data: $\frac{s_d}{r_d} = 0.115$

Fig. (4.11) Geometry and friction coefficient for a rotating disc (28)

Of these, the work by Daily (28) was considered most suitable for the present case. He was the first to include the effect of cylindrical walls in the calculation. He developed four empirical equations for the friction torque coefficient c_f, dependent of the flow regime (Fig.(4.11b)).

I Laminar flow, close clearance.

II Laminar flow, separate boundary layers.

III Turbulent flow, close clearance.

IV Turbulent flow, separate boundary layers.

Regime	Correlation
I	$C_f = 2\pi/(s_d/r_d)\ Re$
II	$C_f = 3.7\ (s_d/r_d)^{0.1}\ Re^{\frac{1}{2}}$
III	$C_f = 0.08/(s_d/r_d)^{1/6}\ Re^{1/4}$
IV	$C_f = 0.0102\ (s_d/r_d)^{0.1}/\ Re^{1/5}$

$$Re_d = \omega_d\ r_d^2/\nu$$

Daily suggested that

- Regime I exists for all spacings if Re is made sufficiently small.
- For a small (s_d/r_d), Regime II may never exist.
- For a large (s_d/r_d), Regime III may never exist.
- Regime IV exists for all (s_d/r_d) only if Re is sufficiently high; as (s_d/r_d) increases the transition to regime IV occurs at a lower Re.

It is noted that for $(s_d/r_d) \geqslant 0.05$, regimes II and IV cover all but the lowest Re_d range. These two regimes are the ones expected inside the engine cylinder and prechamber, and therefore were adopted in the calculations.

4.2.4.c Method of Calculation

The mathematical simulation technique developed in the present work is explained in Chapter 3. The calculation method allows conditions inside

all control volumes of the engine and mass flows through the valves and passages to be established throughout the engine cycle at 1^{o} increments.

The kinetic energy conservation concept was applied in the simulation program to obtain average estimates of characteristic charge velocities, instantaneously, in both the main and prechamber. The principle of the calculation is, kinetic energy of the flow to either chamber is conserved and augments the kinetic energy of the charge already in that chamber. Viscous friction acts to dissipate some of the charge kinetic energy. Flows from either chamber reduce the overall kinetic energy of the charge in that chamber accordingly.

Inlet valve flow is the major source of charge kinetic energy in the main chamber, while the passage is responsible for the prechamber flow. Step-by-step calculations in the simulation program, provide knowledge of valve and passage flows and hence the flow kinetic energies. Rotating disc data was used for kinetic energy dissipation calculations. The method of calculation requires initial values of average charge velocities in both chambers at the beginning of the cycle calculation. Only reasonable estimates are needed due to the iterative nature of the simulation program which is self-correcting.

The velocity estimates obtained using the kinetic energy concept are average values for the total charge in each control volume. The velocity at each chamber wall is arrived at by assuming the velocity distribution to be that of solid body rotation (forced vortex). This gives the ratio between the average velocity (based on the average kinetic energy) and the maximum velocity at the wall to be $1.0/\sqrt{2}$.

Care has to be taken with regard to using the rotating disc friction data. For the disc friction calculation the Reynold's number is defined as

$$Re_d = \omega_d \, r_d^2/\nu$$

which means that the characteristic velocity and dimension are $(\omega_d \, r_d)$ and

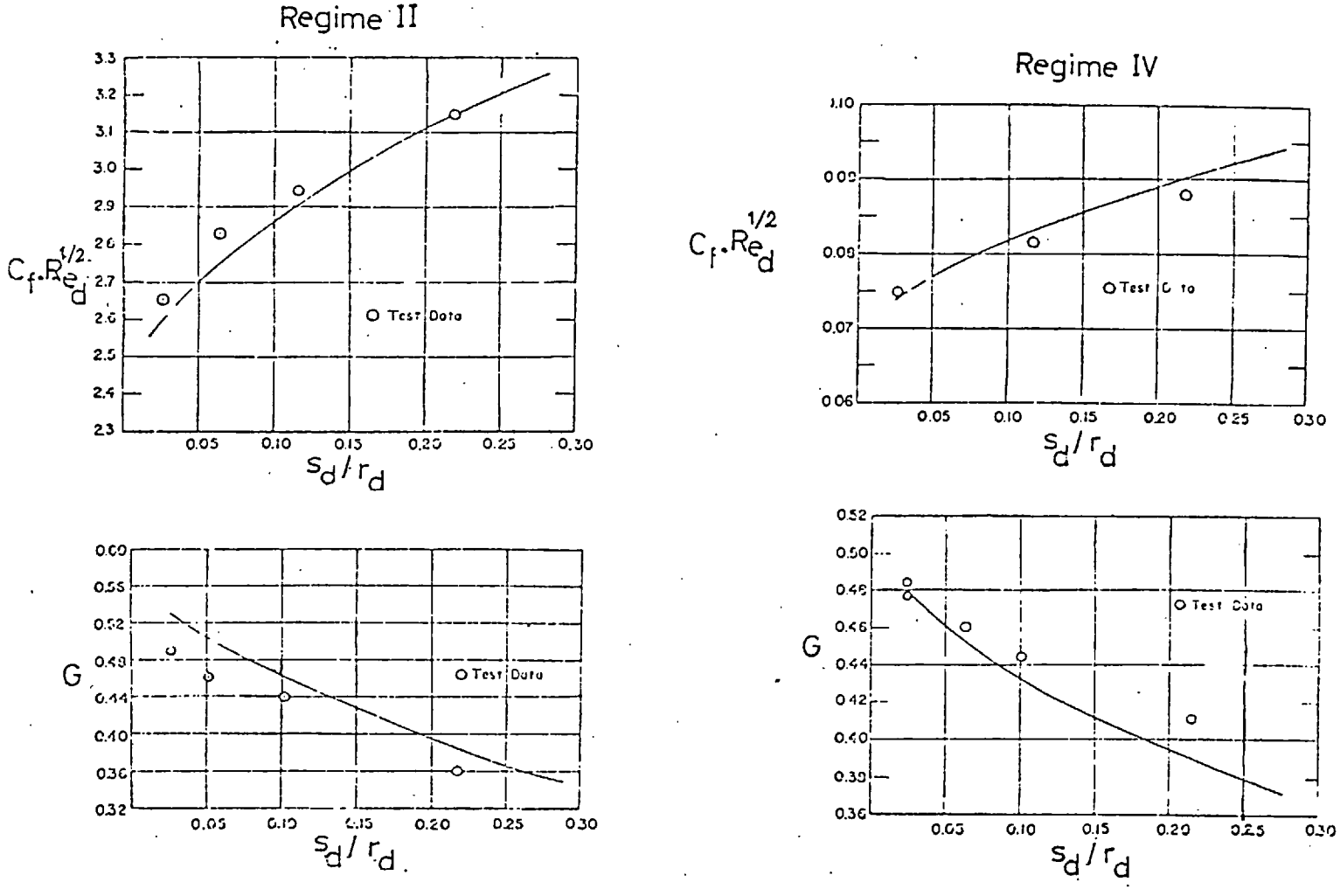

Fig. (4.12) Friction coefficient and swirl ratio as a function of $(\frac{s_d}{r_d})$ ratio (28)

where $$F_g = \sqrt{\frac{K\omega}{2\delta}}$$

Similarly for a cosine signal

$$T_{(0,\theta)} = \alpha_K \cos K\omega\theta$$

the solution is $$T_{(0,\theta)} = \alpha_K \; e^{-F_g x} \; \cos(K\omega\theta - F_g x)$$

The idea of Fourier Analysis of the measured surface temperature is based on this principle. Fourier Analysis of a periodic signal reduces it to its sine and cosine harmonics. The summation of these harmonics leads back to the original temperature signal. Each one of these harmonics can be used - in the general solution mentioned above - to obtain the corresponding temperature distribution in the wall. The summation of these distributions provides the total temperature distribution in the wall, and since

$$Q/A = - K_\omega \frac{\partial T}{\partial x}$$

then differentiation of the temperature distribution arrived at, gives the required transient heat flux at the chamber wall. The mean heat flux is calculated knowing the mean wall temperature and another temperature inside the wall at a known depth.

Fourier analysis of the wall temperature $T_{(0,\theta)}$ gives

$$T_{(0,\theta)} = T_o + \sum_{K=1}^{n/2} (\alpha_K \cos K\omega\theta) + \sum_{K=1}^{n/2-1} (\beta_K \sin K\omega\theta)$$

where $\omega = 2\pi f_f$

and T_o = mean of (n) temperature values

(r_d) respectively. The frictional torque is then given by

$$\tau_f = C_f \cdot \frac{1}{2} \rho \omega_d^2 r_d^5$$

and hence

$$\text{Frictional energy} = \tau_f \cdot \omega_d \cdot \Delta\theta$$

When applying the rotating disc frictional data to the swirling charge inside each chamber, an equivalent speed of disc rotation is needed. This is the speed of rotation of an imaginary disc which would generate a swirling gas rotation at angular velocity ω_g, for a gas surrounding it, equal to that of the actual charge in the chamber. Cylindrical geometry is assumed for both chambers as the rotating disc enclosure. Fig. (4.12) shows the ratio $G(= \omega_g/\omega_d)$ for different flow regimes and different (s_d/r_d) ratios. Knowing the angular velocity of the gas (ω_g) at any step during the cycle, the corresponding value of ω_d, and hence the frictional energy, could be calculated.

This provided a calculation procedure for each chamber which included the effects of viscous friction, Reynolds number, geometry (s_d/r_d) and flow regime (whether laminar or turbulent).

The flows through valves and passage are functions of pressure ratios and flow areas, thus giving realistic dependence of the corresponding kinetic energy calculations on flow conditions.

Although kinetic energy is a scalar quantity, the obtained velocity estimates are considered to be of a swirling nature due to the experimental evidence explained earlier. This is due to (in the case of the swirl chamber) the tangential configuration of the connecting passage. This supports the assumption of swirling motion. For the main chamber, however, the flow field is less well defined, and the assumption of kinetic energy retaining a swirling motion is a major simplification. For this reason, it was expected that velocity estimates in the main chamber would always result in over-estimates of the swirl velocities.

4.2.4.d Induced Velocity Due to Fuel Jet

It was reported by Annand (11), that measurements of instantaneous Nu numbers for motored and fired engines, showed an increase in Nu under fired operation, greater than that which could be accounted for by the change of the charge properties alone. Dent (31) also reported that the swirl velocity inside a DI engine cylinder increases due to combustion effects. As a result of charge velocity enhancement, the heat transfer rate from the charge to the walls should increase.

Woschni (117) accounted for combustion effects through a "pressure increase due to combustion" term in his correlation. This term, however, does not differentiate between velocity enhancement and radiation effects of combustion. Dent (31) accounted for radiation separately. Velocity enhancement was obtained by multiplying the velocity calculated for motored conditions, by the square root of the ratio of apparent mean charge density under motored and fired conditions.

Shroff (94,95) adopted Knight's technique for gas velocity calculations, i.e. the kinetic energy concept. He added a new term to account for combustion induced velocity. This term calculated the increase of kinetic energy of the charge, resulting from the work done by the expansion of the burning mass.

In the present work, Woschni's (117) method could not be included since radiative heat flux is accounted for separately. Dent's method (31) was also excluded since it has no physical support. Shroff's method (94) was tried but produced very high overestimates of the heat flux in both the prechamber and main chamber.

The kinetic energy of the fuel jet is significantly higher than the kinetic energy of the prechamber charge during injection. This was thought to introduce an enhancement of the charge velocity after fuel injection and was therefore introduced in the calculation.

The velocity of the fuel jet v_J is obtained from,

$$v_J = \sqrt{29 \frac{\Delta P}{\rho_f}}$$

where

ΔP = Instantaneous pressure difference between injection pressure and cylinder pressure

The injection rate diagram was assumed to be of a trapzoidal shape, of duration ($\Delta\theta$), which is equal to the injection duration obtained from the needle lift diagram. The total fuel injected (m_f) is known at every running condition hence,

$$\Delta m = m_f/\Delta\theta$$

Consequently, the incremental kinetic energy added due to the fuel jet during one calculation step is,

$$\Delta \text{ K.E.} = \frac{1}{2g} \Delta m \; v_J^2$$

$$= \Delta m \cdot \frac{\Delta P}{\rho}$$

The above method was included in the calculation procedure of the representative velocity for both ROHR calculation and the cycle anaylis program. Fig. (4.13) shows the considerable effect of velocity enhancement due to the fuel jet on the predicted heat flux for the prechamber. The fuel jet effect is generally more pronounced for low engine speeds, since charge velocities are considerably lower than those at high speeds. Variation of injection pressure and injection duration with both engine speed and load was included in the calculations.

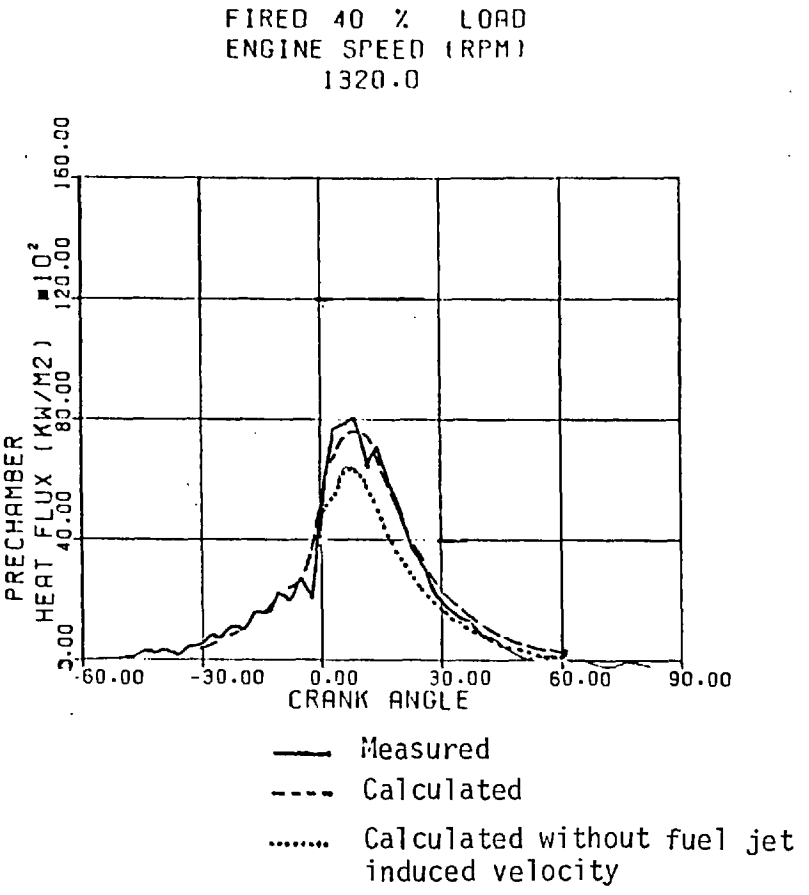

Fig. (4.13) Effect of Fuel Jet induced velocity on heat flux calculation

4.2.5 Comparisons With Hassan's Results

In section (4.2.3), Hassan's experimental investigation was reviewed. The final conclusion of his work was that measured instantaneous values of Nu and Re numbers inside the prechamber of a motored engine can be correlated using,

$$Nu = 0.023 \quad Re^{0.8}$$

In section (4.2.4), a method was introduced for the calculation of representative velocities in the combustion chambers of the engine. These velocities were needed to be used as characteristic velocities in a similar Nu-Re relationship, to obtain instantaneous heat flux rates to the chamber walls.

In this section the data obtained by Hassan was used as experimental basis for comparison with the calculated values of Re numbers and predicted heat flux rates. The simulation program described in Chapter 3 was used to model Hassan's engine under motoring conditions. Calculated instantaneous charge velocities were used, in the above Nu-Re relationship, to obtain instantaneous heat transfer coefficients. The aim was to use Hassan's data to establish the validity of the calculation method of velocity and test the potential of the Nu-Re relationship before further investigation.

Since not all of the engine data required to mathematically simulate Hassan's engine was available, some assumptions had to be made. These are mentioned below;

- Inlet and exhaust valves flow areas were not available. The cam lift diagram together with valves geometric dimensions were used to calculate valve areas. A constant coefficient of discharge was then used to obtain the actual flow area.

• The coefficient of discharge of the connecting passage was unknown. Values had to be assumed. High values were assumed (0.8 inflow - 0.85 outflow), considering the geometry of the passage which resembled a thick orifice (see Chapter 5).

• Detailed experimental data concerning the main cylinder was not available. There is no doubt that conditions inside the main cylinder affect those in the swirl chamber strongly.

• The wall temperature was given only at one test condition. Assumptions had to be made regarding wall temperatures at other test conditions.

It is important to stress that in a simulation program, the Nu-Re relationship is used to calculate the heat transfer coefficient. Values of heat flux are then obtained by multiplying this coefficient by the temperature difference between gas and wall. Hence any error in these temperatures is directly transformed into an error in the estimated heat flux.

Test results at two engine speeds and two compression ratios were evaluated using the simulation program. In the Re number, the choice of v and D_c used by Hassan was different from that used for rotating disc data.

$$Re_H = \frac{v\, D_c}{\nu}$$

where v = Measured gas velocity near the wall (2.54mm from the wall)

The characteristic dimension was taken by Hassan to be the circumferential distance from the passage entrance to his hot wire probe. This was three times the chamber diameter. For proper comparison, the same values were used in the prediction program.

Instantaneous values of Reynold's number and heat flux obtained by means of the simulation program are plotted together with Hassan's experimental values in Fig. (4.14-21).

In Figs. (4.14-17) measured and calculated Re numbers are compared for

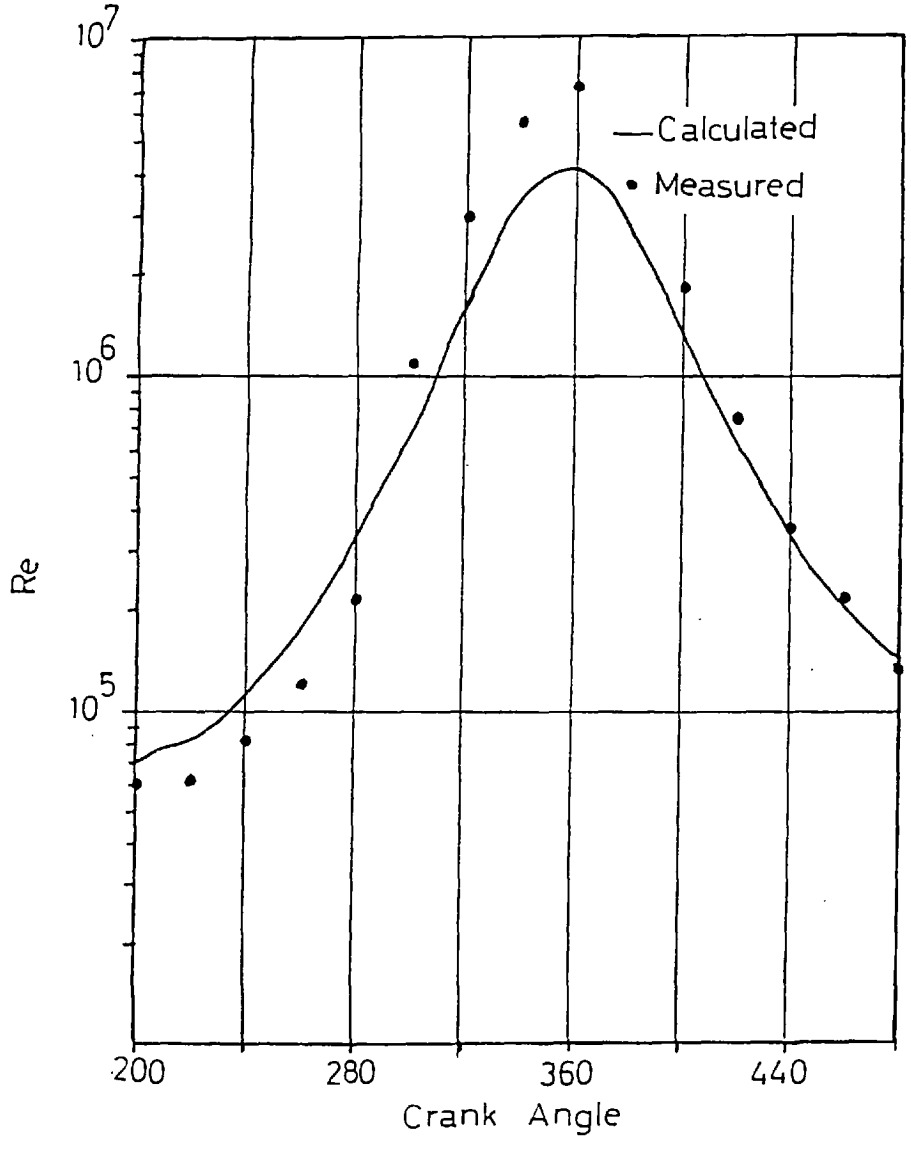

Fig. (4.14) Reynolds numbers for 1100 rpm and 8.5 compression ratio

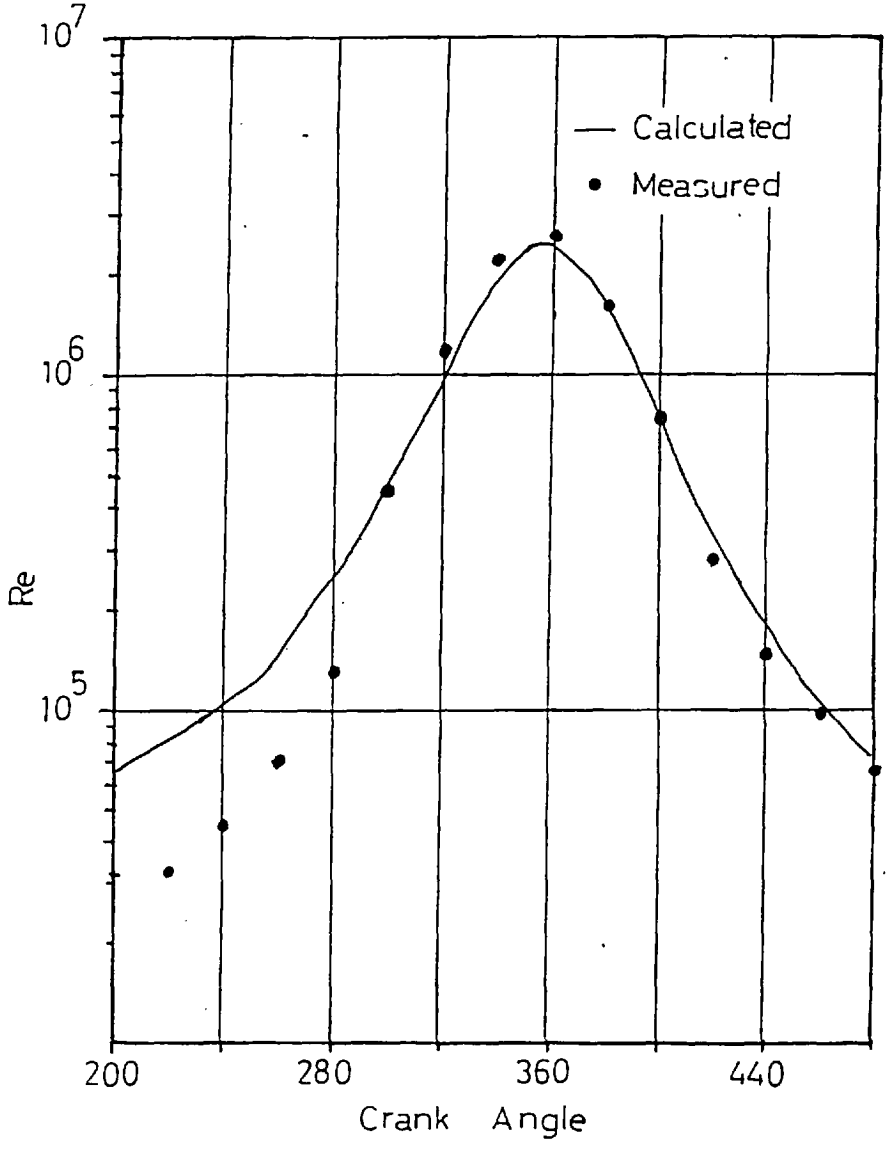

Fig. (4.15) Reynolds numbers for 600 rpm and 8.5 compression ratio

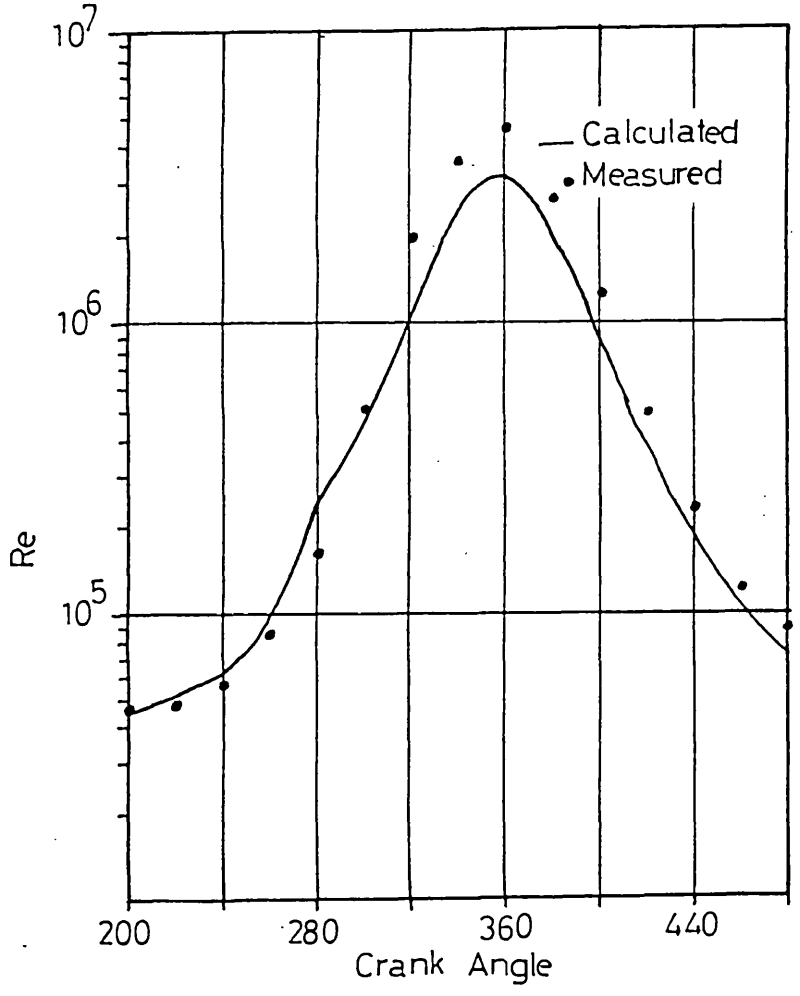

Fig. (4.16) Reynolds numbers for 1100 rpm and 9.8 compression ratio

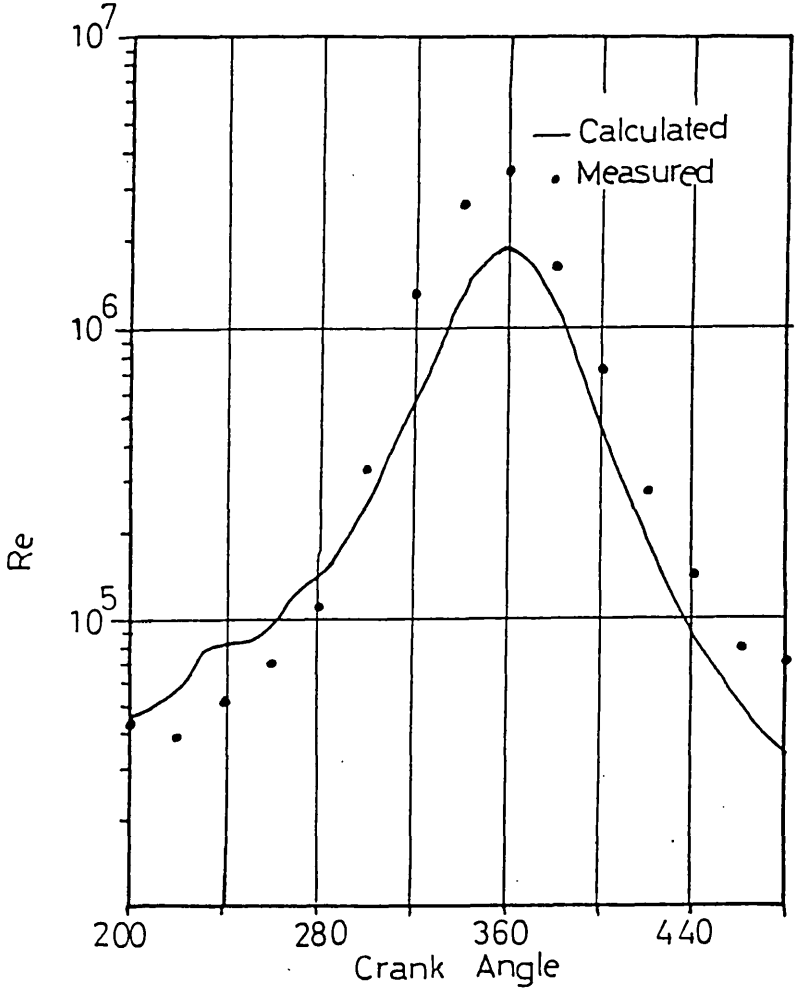

Fig. (4.17) Reynolds numbers for 600 rpm and 9.8 compression ratio

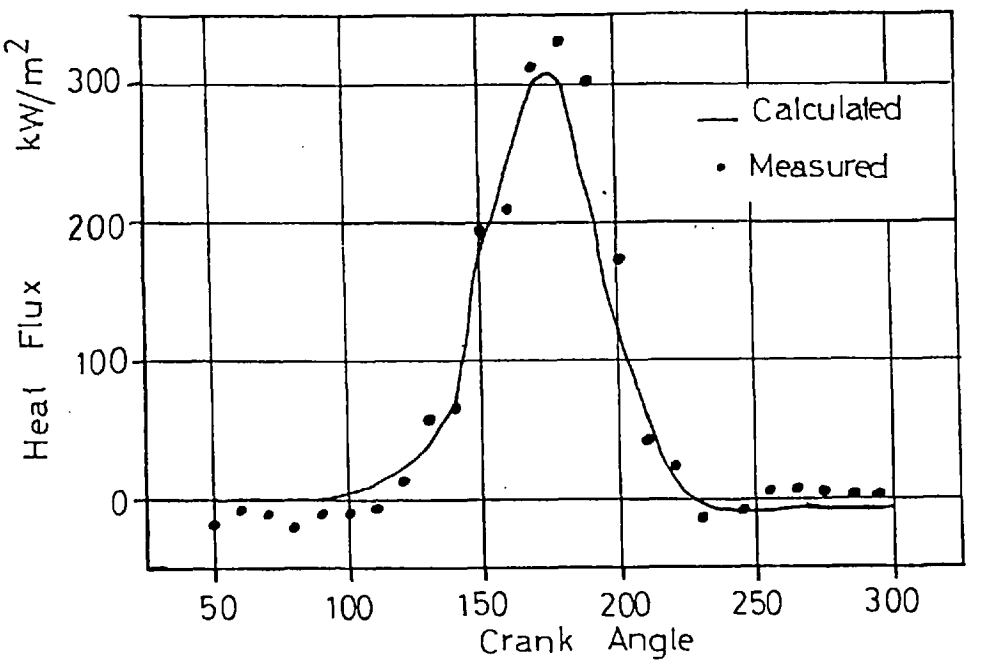

Fig. (4.18) Instantaneous heat flux,compression ratio 9.8 and 1100 rpm

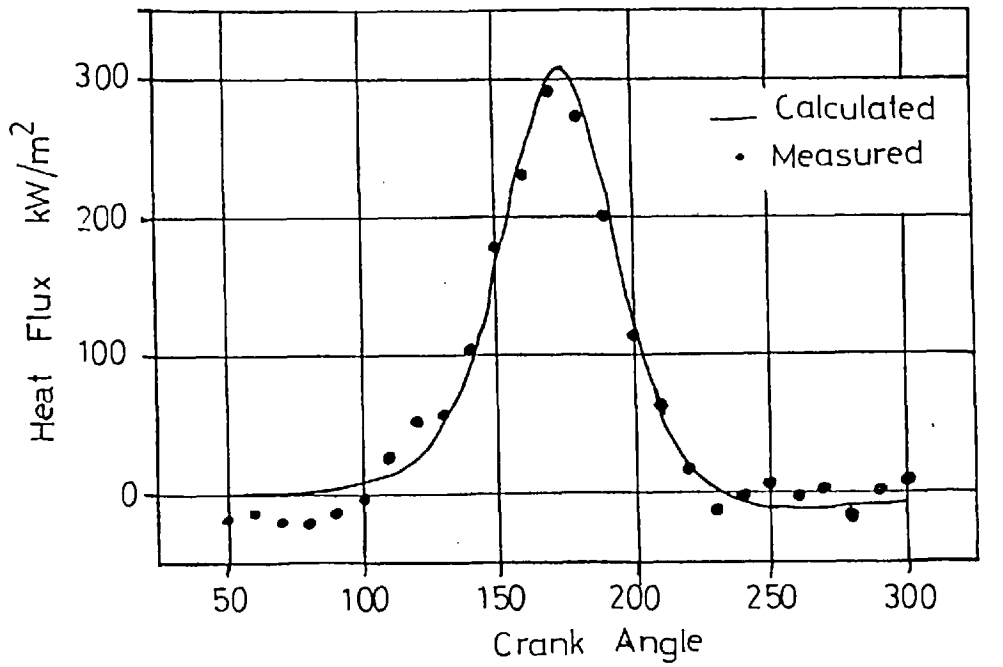

Fig. (4.19) Instantaneous heat flux,compression ratio 8.5 and 1100 rpm

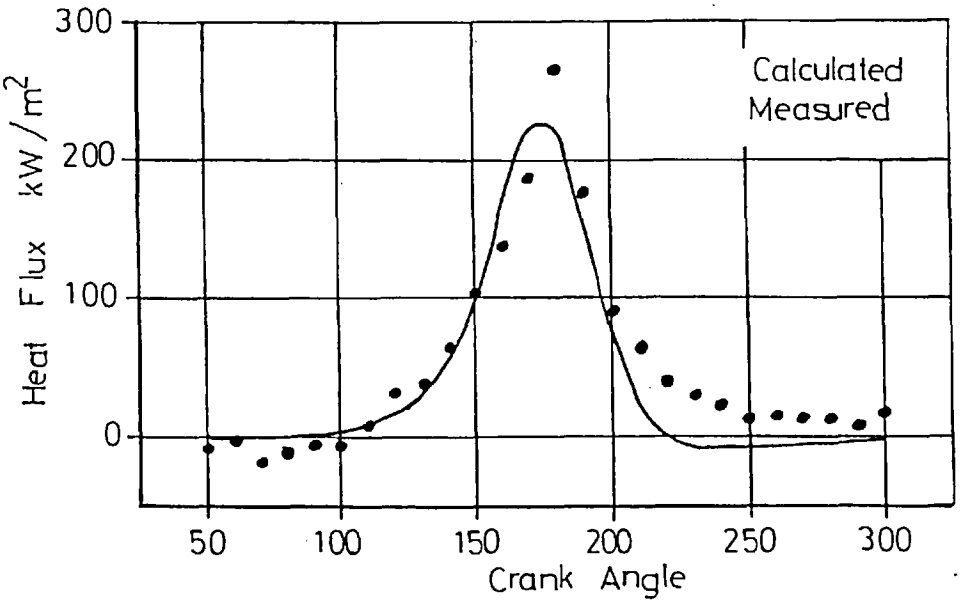

Fig. (4.20) Instantaneous heat flux,compression ratio 9.8 and 600 rpm

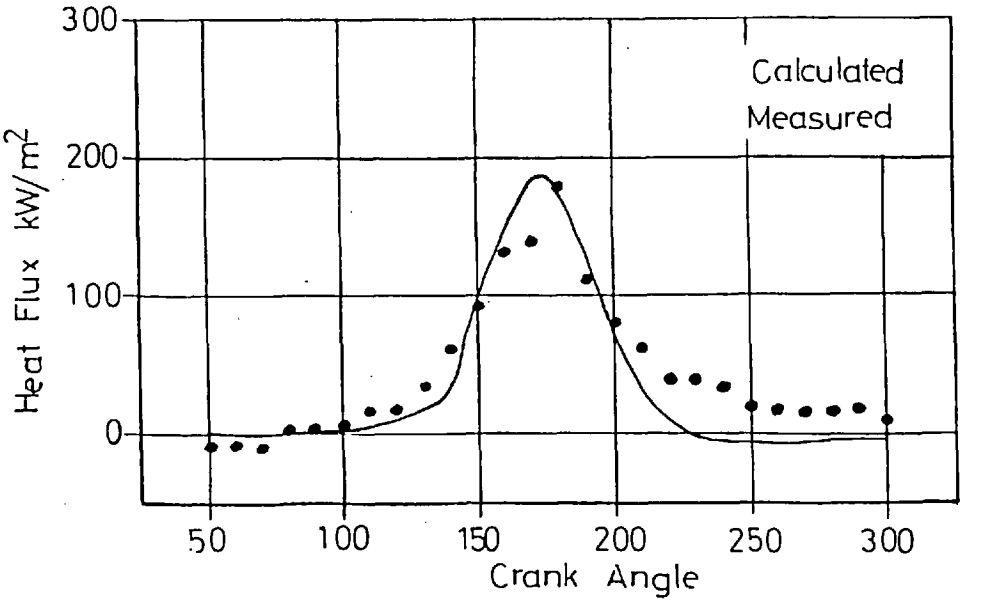

Fig. (4.21) Instantaneous heat flux,compression ratio 8.5 and 600 rpm

two compression ratios and two engine speeds. Although some difference exists, especially near TDC, the predictions follow the measured trend of variation of Re within the engine cycle satisfactorily. The calculation method also predicts reasonably, the measured behaviour of Re when changing the engine compression ratio and speed. The magnitudes of predicted Re values are of a reasonable order.

Comparisons between measured and calculated heat fluxes are shown in Figs. (4.18-21). Reasonable agreement is noticed for all the running conditions attempted. Although, some small deviations existed, between measured and predicted values, they are expected as a result of the assumptions that were necessary considering the engine data. Heat flux behaviour with engine speed and compression ratio was also satisfactorily predicted as shown in the figures.

4.2.6 Conclusions

From the previous discussion and keeping in mind the accuracy of measurements together with limitations mentioned concerning the engine data assumed, it is apparent that the simplified technique proposed for calculating velocities of the contents of the main chamber and swirl chamber is promising. The velocity values arrived at are only estimates, to be used for heat transfer calculations. Although predicted velocities follow the expected trend throughout the cycle and their magnitudes are not far from those measured by Hassan, they are not claimed to be a prediction of the actual charge velocities. The velocity field inside the engine cylinder is very complex. A full study of the velocity distribution inside the cylinder is beyond the scope of this work and could not be justified.

Although deviations between the experimental and calculated values are present, they are small and expected. It is believed that without the assumptions made concerning engine data and with detailed information

on the conditions in the cylinder, better agreement could be achieved.

It is concluded that a method of calculation has been established, and that the assumptions made concerning the velocity distribution across the chamber and energy dissipation within it, are reasonable.

To test the applicability of the technique to another engine, a test program was conducted to measure heat fluxes for both prechamber and cylinder head under motored and fired conditions. The same technique for velocity calculation was then used to predict the heat flux. The results of this investigation are reported later in this chapter.

4.3 RADIATIVE HEAT TRANSFER

4.3.1 Review of Available Work

The rate of heat transfer from one black body at a temperature T_1 (^oK) to another at temperature T_2(^oK), parallel to it across a space containing no absorptive material, is given by

$$Q_r/A = \sigma (T_1^4 - T_2^4)$$

Real bodies are not 'black' and it is customary to deal with the deviations from black body behaviour by a multiplying factor in the black body equation. This factor is known as the body's emissivity (ε). Thus,

$$Q_r/A = \varepsilon \sigma (T_1^4 - T_2^4)$$

Radiation from gases is observed to occur only in certain wave-length bands. A study of temperature levels reached in industrial furnaces (98), and in combustion chambers of internal combustion engines (14,41,69,109) show that the radiation capacity of monoatomic and diatomic gases is rather limited. Significant radiation capacity is exhibited only by multiatomic gases such as carbon dioxide (CO_2) and water vapour (H_2O). Gas radiation in engines was evaluated by Sitkei (97,98) using emissivity charts given by

Hottel (53). He suggested that gas radiation was a negligible part of the total heat transfer. Detailed studies of gas radiation have been published by Edwards (34) and Abu-Romia (2), who presented average values of gas emissivities over a range of wavelengths.

Flame radiation is a complex process, depending on the physical and chemical character of combustion. Generally, flames can be divided into two groups. The first contains the luminous or optically non-transparent flames which have a continuous radiation spectram due to the particles of soot and carbon burning within them. The major part of the flame in a diesel engine is in this group. The second group contains the optically transparent or non-luminous flames which radiate in certain frequency bands. Generally, the flame in a petrol engine belongs to this group. The total energy emitted by non-luminous flames is generally small compared to those of luminous flames. Thus radiative heat loss can usually be neglected in a petrol engine but not in most diesels. According to Hottel (53) the emissivity (ε) at any wave length (λ) could be expressed by the formula

$$\varepsilon_{\lambda} = 1 - e^{-\frac{K_a L_{op}}{\lambda^{\alpha}}}$$

Thus, emissivity will vary with wave length. This is particularly true in the case of gas radiation and the above equation would have to be integrated with wave length, to obtain a representative emissivity. Belinski (14) investigated flames in diesel engines and concluded that they were of the grey radiation type, that is, their emissivity would remain constant with wave length, thus (λ^{α}) is a constant.

Hence $$\varepsilon = (1 - e^{-K_a L_{op}})\, \varepsilon_o$$

$L_{op} = p\,\ell$

ε_o = Emissivity of an infinitely large radiation optical depth

Flame radiation in industrial furnaces and boilers has been closely

studied and correlated. However, conditions inside a small high speed diesel engine are very different, comprising high pressures and very rapid energy release. Thus, direct application of most published flame data to engines is not possible. Kunitomo (62,63) has conducted extensive work on flame radiation, particularly at high pressures, and correlated gas and flame emissivities. The results proved satisfactory and useful for engine radiative flux calculation when used by Oguri (82).

Because of the complexity of the radiation process, research workers have resorted to correlations supported by experimental data. The experimental procedure for measuring the radiant component of the engines instantaneous heat flux is not easy to perform with accuracy and therefore data is scarce. Annand (8) analysed the data of Elser (37) and obtained a correlation for radiative flux calculations,

$$Q_r/A = C_1 (T_g^4 - T_w^4)$$

$$C_1 = \text{Constant} = 0.7256 \times 10^{-12}$$

In a later paper, Annand (6) suggested another value for the constant "C_1", namely,

$$C_1 = 1.5\,\sigma$$

Whitehouse (113) also derived a value of C_1 such that the emissivity was apparently greater than one. Since black body radiation represents the peak of the radiant heat, a constant in the radiation equation greater than (1.0) is considered unrealistic.

Ebersole's investigation (33) provided evidence regarding the importance of radiant heat loss relative to the convective heat loss. He showed that in some cases radiation contributed more than 40% of the total heat loss in an engine.

More recently Oguri (82) measured total and radiant heat fluxes, and reported that radiation contributes up to 30% of the total heat loss to the walls of his engine.

Sitkei (97) and Flynn(41) studied the radiation problem with broader objectives. They included examination of the fundamental radiation data such as radiant temperature, flame emissivity and optical thickness. Sitkei tested a modified prechambered engine while Flynn used a direct injection diesel. Both studied effects of engine variables on radiation and flame emissivity. Emissivities of up to (0.43) were reported by Sitkei while Flynn showed values of up to (1.0). Flynn attempted to correlate radiant heat flux with engine variables but the correlation obtained was complex with numerable parameters and many constants.

Recently, Annand (11) acknowledging the need for a proper treatment of radiant heat calculations, reviewed the work of Flynn and Sitkei and suggested that radiation calculations should be based on emissivity and temperature values of the combustion chamber charge.

Kunitomo and Oguri (82) detected similarity between the radiation behaviour throughout the engine cycle and the shape of the ROHR diagram. Using the ROHR values they introduced a method for predicting radiative heat flux in diesel engines. They compared measured and predicted values and good agreement was obtained. Emissivities obtained were less than 0.5.

4.3.2 Calculation Procedure

Reviewing the work published on radiation in diesel engines, it was concluded that both gas and soot radiation ought to be included in any calculation. The radiation temperature is different from the mean gas temperature. It was decided to follow the method of calculation proposed by Kunitamo abd Oguri (82),with some modifications where needed. The general approach is to obtain the radiative heat flux (Q_r) by the relation,

$$Q_r = \varepsilon_f \cdot \sigma \cdot (T_f^4 - T_w^4) \qquad (4.1)$$

$$\varepsilon_f = 1 - (1 - \varepsilon_s)(1 - \varepsilon_g) \qquad (4.2)$$

where $$\varepsilon_g = 1 - (1 - \varepsilon_{g_1})(1 - \varepsilon_{g_2})(1 - \varepsilon_{g_3})$$

where

ε_{g_1}, ε_{g_2}, ε_{g_3} ... are emissivities of infra-red active gases.

In the present work, those of carbon dioxide and water vapour (CO_2 and H_2O) are included.

hence $$\varepsilon_g = 1 - (1 - \varepsilon_{CO_2})(1 - \varepsilon_{H_2O}) \qquad (4.3)$$

Sitkei (98) quoted the following expressions for CO_2 and H_2O radiation energies, based on experimental data,

$$E_{CO_2} = 0.0405\ (pL)^{0.333}\ \left(\frac{T}{100}\right)^{3.5}$$

$$E_{H_2O} = 0.0402\ p^{0.8}\ L^{0.6}\ \left(\frac{T}{100}\right)^{3}$$

E_r = Radiation Energy kw/m^2

p = Partial Pressure (Bar)

L = Radiation Path Length (m)

T = Gas Temperature (^oK)

Due to the simplicity of the above equations it was decided to use them to obtain the gas emissivities in preference to the integration method proposed by Edwards et al (34) and used by Kunitomo and Oguri. By definition the gas emissivity is expressed by;

$$\varepsilon_g = \frac{E_r}{\sigma(T/100)^4}$$

$$\varepsilon_{CO_2} = \frac{E_{CO_2}}{\sigma\left(\frac{T}{100}\right)^4} \quad \text{and} \quad \varepsilon_{H_2O} = \frac{E_{H_2O}}{\sigma\left(\frac{T}{100}\right)^4}$$

$$\varepsilon_{CO_2} = 0.711\ (p.L)^{0.333}/\left(\frac{T}{100}\right)^{\frac{1}{2}} \qquad (4.4)$$

$$\varepsilon_{H_2O} = 0.707\ (p.L)^{0.6}\ (p)^{0.2}/\left(\frac{T}{100}\right)$$

The radiation length (L) for the prechamber was considered to be equal to the chamber diameter. This assumes that each gas fills the total volume at its corresponding partial pressure (p). For the main chamber-cylinder - the radiation length at any crank angle position $L(\theta)$ is given by Sitkei (98) as;

$$L(\theta) = 3.6\ V(\theta) / A(\theta)$$

To calculate the partial pressures of (CO_2) and (H_2O) the relations published by Kunitomo (63) were used. The concentration of (CO_2) and (H_2O) as a ratio of the volume of the total products of combustion were expressed as functions of excess air factor and fuel composition.

$$\begin{aligned}
y_{CO} &= 2.2\ (1.0 - \alpha_f)\ (\phi - 1.2)^2 && \text{for } \phi \leq 1.2 \\
&&& \text{and } \alpha_f \leq 1.0 \\
y_{CO} &= 0 && \text{for } \phi > 1.2 \text{ or } \gamma > 1.0 \\
y_{CO_2} &= 0.038\ \alpha_f - 2.619\ (1.01 - \alpha f)\ (\phi - 1.05)^2 + 0.092 \\
&&& \text{for } \phi \leq 1.1 \\
&= - 0.075\ \phi + 0.033\ \alpha_f + 0.175 && \text{for } \phi > 1.1 \\
y_{H_2O} &= 0.126 - 0.72\ |\ \phi + 0.887\ \alpha_f - 1.724 \\
&\quad - 1.42\ (\alpha_f - 0.805)^2\ |^2 && \text{for } \phi < 1.05 \\
&= - 0.0783\ \alpha_f - 0.068\phi + 0.259 && \text{for } \phi \geq 1.05
\end{aligned} \tag{4.5}$$

where ϕ = Excess Air Ratio

α_f = Specific Gravity of Fuel

y_{CO_2} and y_{H_2O} give the volume fraction of these gases at the end of combustion. Hence, throughout the cycle the partial pressure $P_i(\theta)$ for each radiative gas can be expressed as follows

$$P_i(\theta) = x\ (\theta)\ .\ y_i\ .\ P(\theta) \tag{4.6}$$

The fraction $x(\theta)$ is obtained from the rate of heat release calculation with knowledge of the total fuel to be burnt.

Kunitomo (62) proposed a correlation giving soot cloud emissivities at atmospheric conditions (ε_{s_o}) as a function of gas emissivities, ϕ and ρ_f.

$$\varepsilon_{s_o}/\varepsilon_{g_o} = 0.09/\ (\phi - \alpha_f^2 + 0.35\ \alpha_f - 0.35) + 6.3\ \alpha_f - 5.95 \qquad (4.7)$$

Oguri and Kunitomo (82) reviewed the published work on soot formation and flame radiation and concluded that the pressure dependence of soot formation may be expressed as,

$$K_s = K_{s_o} \cdot p^{C_2}$$

p^{C_2} is known as the soot concentration ratio. The constant (C_2) is given by

$$C_2 = \frac{4.95}{\phi + 1.5} - 0.25 \qquad (4.8)$$

The soot emissivity $\varepsilon_s(\theta)$ may finally be expressed as

$$\varepsilon_s(\theta) = 1 - \mathrm{EXP}\ \left[P(\theta)^{C_2} \mathrm{lin}\ (1 - \varepsilon_{g_o}(\theta) \cdot \left(\frac{0.09}{\phi^2 - \alpha_f^2 + 0.35\ \alpha_f - 0.38} + 6.8\ \alpha_f - 5.95\right)) \right] \qquad (4.9)$$

Gas emissivities at high pressures are, in this work, calculated using the mean absorption coefficients obtained by Abu-Romia (2). Those of (CO_2) and (H_2O) were curve fitted as follows;

$$\begin{aligned} K_{CO_2} &= 102.280 - 0.11108\ T_g + \\ &\quad 0.42221 \times 10^{-5}\ T_g^2 - 5.36838 \times 10^{-9}\ T_g^3 \\ K_{H_2O} &= 52.054 - 0.08882\ T_g + 5.26603 \times 10^{-5}\ T_g^2 \\ &\quad - 10.4314 \times 10^{-9}\ T_g^3 \end{aligned} \qquad (4.10)$$

K = mean absorption coefficient $(Bar.m)^{-1}$

The calculation procedure can be summarised as follows;

a) Knowing the total excess air ratio ϕ , y_{CO_2} and y_{H_2O} can be obtained from equation (4.5).

b) $x(\theta)$ is known from the heat release calculations.

Assuming atomospheric pressure and using equations (4.4) and (4.6) enables ε_{CO_2} and ε_{H_2O} and hence (from (4.3)) ε_{g_o} to be obtained.

c) Knowing the total pressure $P(\theta)$, the soot emissivity $\varepsilon_s(\theta)$ can be calculated using equation (4.9)

d) Equations (4.10) can now be used to obtain (K_{CO_2}) and (K_{H_2O}) and since;

$$\varepsilon_g = (1 - e^{K p L})$$

equation (4.6) can be used, together with the above relation and equations (4.10) and (4.3) to obtain gas emissivity (ε_g) at the cylinder pressure $P(\theta)$.

e) Using equation (4.2) the total flame emissivity (ε_f) is obtained.

f) Knowing ε_f, T_f and T_w the radiative heat flux (Q_r) is obtained.

An attempt was made to calculate flame temperatures throughout the engine cycle using Belinski's (14) results as quoted by Sitkei (98), relating flame temperature to gas temperature, together with knowledge of the Boltzmann-Number. (B_o) (see Fig. (4.22)).

$$B_o = \frac{B_e \quad \Sigma V_{c_p}}{\sigma \varepsilon_p \; A \; T_f^{\,3}}$$

where B_e = Fuel consumption per hour

V_{c_p} = Mean total specific heat of combustion products of 1 Kg fuel.

A = Heat absorbing area

However, calculated flame temperatures were unrealistic, hence the method

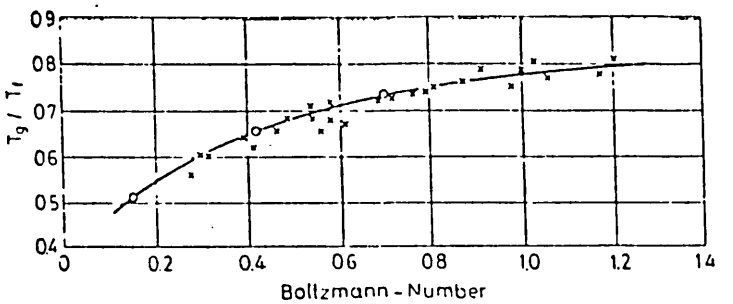

Fig. (4.22) Variation of the ratio of gas and flame temperature, in the function of the *Bo* number (98)

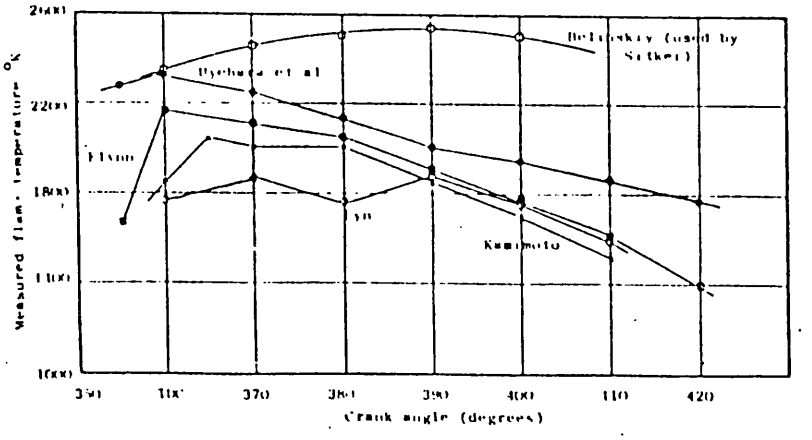

Fig. (4.23) - Measured flame temperatures in diesel engines (31)

was abandoned.

Dent (31) quoted flame temperatures as measured by others, Fig. (4.23). Flame temperatures by Kamimoto et al (59) and Belinski (14) are for the DI engine, while those by Lyn (69) and Uyehara et al (109) are for the IDI engine. It is apparent from the figure that with the exception of Belinski's results, the variation of flame temperature with engine crank angle position follows a similar trend in all the results. In the present work, the flame was assumed to start at the beginning of ROHR, with a temperature of 2200^{o}K which linearly decreases during the expansion stroke and approaches the chamber gas temperature at the end of the ROHR diagram.

4.4 HEAT FLUX MEASUREMENTS

Review of published work concerning heat transfer in IDI diesel engines, revealed that information was lacking in the particular area of heat flux measurement in the prechamber and main chamber of high compression engines (typically 21:1 in the present investigation). As discussed in section (4.2.5), conditions inside the cylinder of an IDI engine affect those in the prechamber. It was, therefore, decided to investigate experimentally the phenomena of heat transfer in both the prechamber and main cylinder of an IDI engine. The main aim was to obtain experimental instantaneous heat flux values for both chambers, under motored and fired operation. The results would then be used for comparisons with values predicted by the method explained in the previous sections. Thus the validity of the simplifying assumptions made and the applicability of the calculation method were to be examined.

4.4.1 Test Arrangement

Fig. (4.24) shows the surface thermocouple used in the heat flux measurement investigation. The thermocouple is manufactured by A.S.E.A. of Sweden. The main specifications of the thermocouple are:

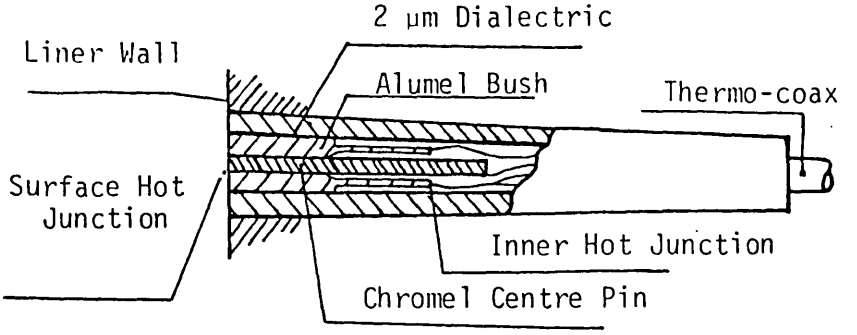

Fig. (4.24) Surface Thermocouple Sensor

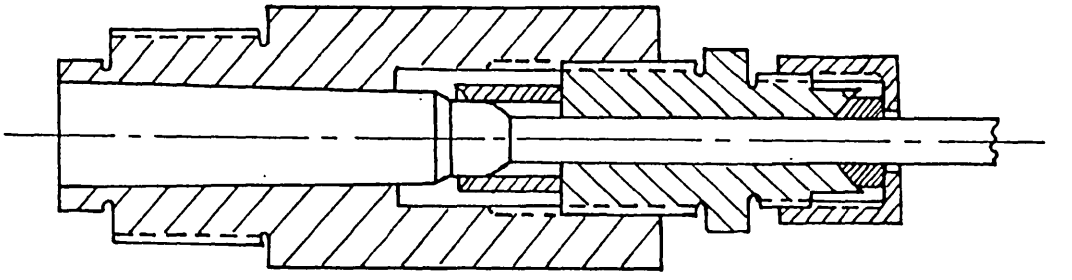

Fig. (4.25) Mounting Adaptor for Thermocouple Sensor

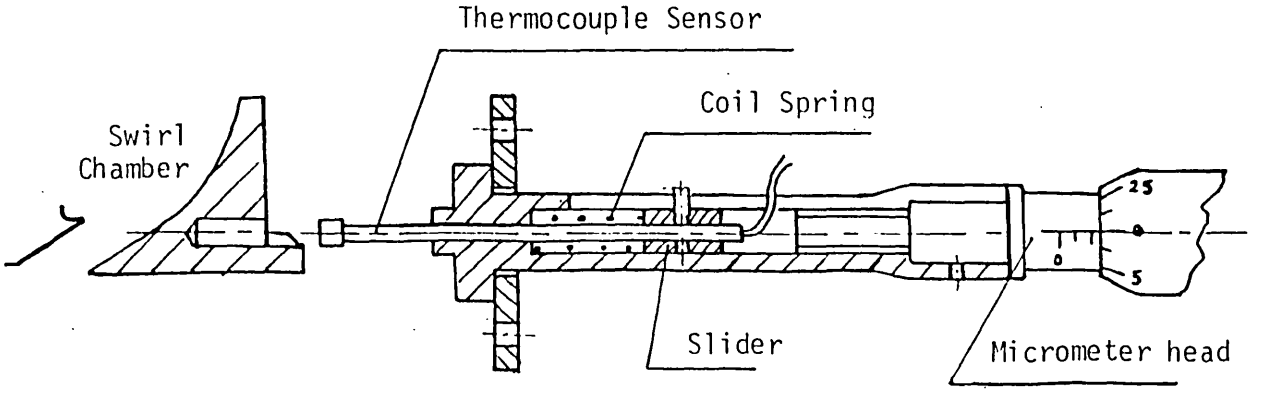

Fig. (4.26) Arrangement for Traversing Thermocouple

Thermocouple Type:	Nickel/nickel-chromium (DIN437109 model QHFF268)
Temperature Limit:	$700^{o}C$ + superimposed flashes up to $1500^{o}C$
Temperature Response:	Pulse rise time 100 μs
Pressure limit:	Tested at 10^{5} bar

The sensor is capable of measuring extremely fast variations of surface temperatures. The thermocouple junction was reported by the manufacturer to be located less than one μm from the surface. The electrical connection between the nickel-chromium centre pin and the surrounding nickel bush is made across a 2 μm thickness of insulating material. This insures very small heat capacity of the thermocouple, hence rapid response and a temperature measurement which is very close to the true surface temperature.

The surface thermocouple was calibrated in a thermostatically controlled oil bath and was found to have linear sensitivity of ($4.1x10^{-5}$ Volts/^{o}C), which closely follows the published standards for such a thermocouple. The response of the thermocouple was tested using an electronic flash light. The output from the thermocouple was amplified 200 times before being displayed on a storage oscilloscope. The flash light created a sudden temperature rise of ($11.0^{o}C$). The surface thermocouple was found to reach 90% of the measured temperature in about (180 μs). This was found to be adequate for the range of harmonic analysis intended in the following study.

The surface thermocouple assembly incorporated a second thermocouple mounted at a distance (6.0mm) from the surface.

Fig. (4.25) is a sketch of the adapter designed to carry the surface thermocouple. The special protruding head of the adapter was designed to allow the sensor to be carried through a hole in the swirl chamber wall, allowing it to sit flush with the inside surface. This protruding head was later machined off and the sensor remounted flush with its holder. The sensor was then used to measure instantaneous cylinder head surface wall

temperature. The sensor was mounted in pressure transducer positions, Fig. (5.2).

The output from the surface thermocouple was amplified (1000:1) times using a high response voltage amplifier (Bryans Southern Instruments, No. MO 41900). The output from the inner thermocouple was connected to a direct reading instrument which gave the sensor body temperature. The mean surface temperature was also displayed.

Information regarding temperature of the connecting passage is limited. Sitkei (98) reported measurements at several points in a swirl chamber, but not the passage. French and Hartles (43) measured wall temperatures at several points in their single cylinder swirl chamber engine, under high loads. Mean temperatures were arrived at by extrapolating the temperature curve obtained from three thermocouples buried in the chamber wall at different depths.

In the present work, a temperature traversing thermocouple holder was designed (Fig. 4.26) to fit a hole bored in the prechamber wall near the throat as shown in Fig. (4.26). A shielded chromel-alumel thermocouple was used. The clearance between the sensing part of the thermocouple was made as small as possible, whilst permitting free movement of the thermocouple, in order to measure wall, not gas, temperatures.

The instantaneous wall temperature signal obtained by the surface thermocouple was - after amplification - sampled using the Tape Recorder System (Chapter 2). For every engine cycle (2048) values of wall temperatures were sampled. Fifty cycles were sampled for every running condition. Wall temperatures were sampled at four engine speeds (1320,1680,2200,2800 rpm), motored and fired operation, full load, 70% and 40% load all at 7^{o} BTDC dynamic timing. A further set of tests were also conducted at 2200 rpm and 2^{o} BTDC dyanmic timing, varying load. All test runs were repeated for measurements of cylinder head heat flux. Full cycle pressure diagrams for both prechamber and main cylinder were also sampled at every running condition.

4.4.2 Analysis of Experimental Results

In any of the engine chambers, heat is transferred from the gaseous charge by convection and radiation to the chamber walls. During the engine cycle this heat transfer operation is in an unsteady mode. This heat is itself transferred to the engine coolant via unsteady conduction through the chamber walls. All transient components of the heat flux are damped out in the walls, which leads to a constant wall temperature at the coolant side. The wall temperatures on the gas side however, are continuously in a transient mode.

The following equation describes the transient heat conduction in three dimensions for a solid, with constant thermal properties;

$$\frac{\partial T}{\partial \theta} = \delta \left[\frac{\partial^2 T}{\partial x^2} + \frac{\partial^2 T}{\partial y^2} + \frac{\partial^2 T}{\partial z^2} \right]$$

where x,y,z = Distances along mutually perpendicular axes.

Previous work by different investigators (6,8,31,49,66) showed that the assumption of one dimensional conduction in the particular case of a surface thermocouple element fitted perpendicular to the cylinder wall, is well justified. Thus, the above equation reduces to,

$$\frac{\partial T}{\partial \theta} = \delta \frac{\partial^2 T}{\partial x^2}$$

which is the Fourier heat conduction equation in one dimension. This equation has an exact solution for the particular case of sinusoidal variation of temperature (T) with time (θ),

$$T_{(0,\theta)} = \beta_K \sin K\omega\theta$$

and the solution is

$$T_{(x,\theta)} = \beta_K \, e^{-F_g x} \sin (K\omega\theta - F_g x)$$

Thus

$$T_o = \frac{1}{n} \sum_{J=0}^{n-1} T_j$$

$$\alpha_K = \frac{2}{n} \sum_{J=0}^{n-1} T_j \cos\left(J K \frac{2\pi}{n}\right)$$

$$\beta_K = \frac{2}{n} \sum_{J=0}^{n-1} T_j \sin\left(J K \frac{2\pi}{n}\right)$$

where $K = 1, 2, \ldots\ldots\ldots \left(\frac{n}{2} - 1\right)$

if $K = \frac{n}{2}$ then, $\beta_K = \beta_{\frac{n}{2}} = \sum_{J=0}^{n-1} T_j \sin J\pi = 0$

$$T_{(0,\theta)} = T_o + \sum_{K=1}^{n/2} (\alpha_K \cos K\omega\theta + \beta_K \sin K\omega\theta)$$

Hence, fourier analysis of the measured wall temperature reduces the problem into a form where the solution is known.

Hence,

$$T_{(x,\theta)} = \sum_{K=1}^{n/2} e^{-F_g x} \left[\alpha_K \cos(K\omega\theta - F_g x) + \beta_K \sin(K\omega\theta - F_g x)\right]$$

which is the transient component of the temperature distribution at a time (θ) and at a distance (x_ω) from the wall surface.

The steady state component of the wall temperature is

$$T_{(x,\theta)} = T_o - (T_o - T_c) \frac{x_\omega}{\ell_\omega}$$

The total temperature distribution in the wall is;

$$T_{(x,\theta)} = T_o - (T_o - T_c) \frac{x_\omega}{\ell_\omega} + \sum_{K=1}^{n/2} e^{-F_g x} \left[\alpha_K \cos(K\omega\theta - F_g x) + \beta_K \sin(K\omega\theta - F_g x)\right]$$

The rate of change of wall temperature with distance (x) is expressed as,

$$\frac{\partial T}{\partial x}_{(x,\theta)} = - \frac{T_o - T_c}{\ell_\omega} + \sum_{K=1}^{n/2} - F_g \, e^{-F_g x}$$

$$\left[(\beta_K - \alpha_K) \sin K\omega\theta + (\beta_K + \alpha_K) \cos K\omega\theta \right]$$

The instantaneous heat flux (H) at the wall surface is then obtained by putting ($x = 0$) and multiplying by the thermal conductivity (K_ω) of the wall,

$$H = Q/A = K_\omega \frac{(T_o - T_c)}{\ell_\omega} + K_\omega \sum_{K=1}^{n/2} \left[(\beta_K - \alpha_K) \right.$$

$$\left. \sin K\omega\theta + (\beta_K + \alpha_K) \cos K\omega\theta \right]$$

4.4.3 Measured Heat Fluxes and Temperatures

The experimentally obtained surface thermocouple outputs were recorded on a fast tape recorder. They were then analysed on a (CDC) computer. A computer program was developed to convert the voltage signals into temperatures, to average results of 50 cycles, and to use the average cycle in the fourier analysis subroutine, which calculated the corresponding heat flux values. As mentioned earlier, (2048) values of temperature at the wall were sampled for every engine cycle. This enabled the temperature signal to be reduced up to its 1000th harmonic. The computer time required for such an analysis is huge. This, together with the fact that the surface thermocouple response restricted high frequency resolution (20 khz), limited the number of harmonics analysed. At the top speed of the engine, this is equivalent to the 200th harmonic. The analysus of the experimental results was tested for 256 and 128 harmonics, but no difference was detected in the resulting heat fluxes. It was therefore decided to use the (128) harmonics analysis for all the results.

Fig. (4.27-31) shows typical instantaneous temperatures and heat fluxes at the wall of the prechamber. Figs. (4.32-36) show measured values for the cylinder head. The figures are for motored, full and part load operation of

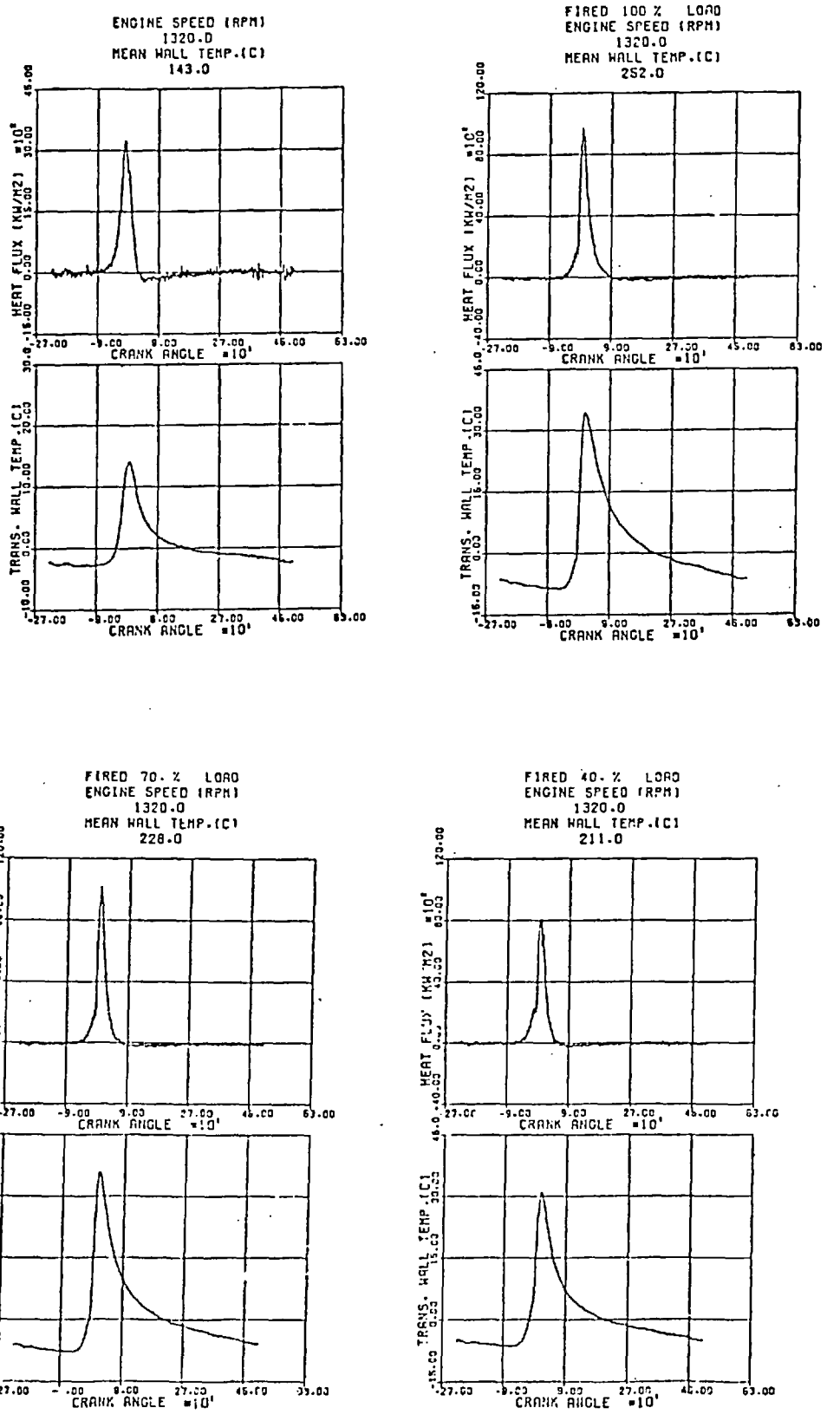

Fig. (4.27) Measured Instantaneous Prechamber Wall Temperature and Heat Flux at 1320 rpm

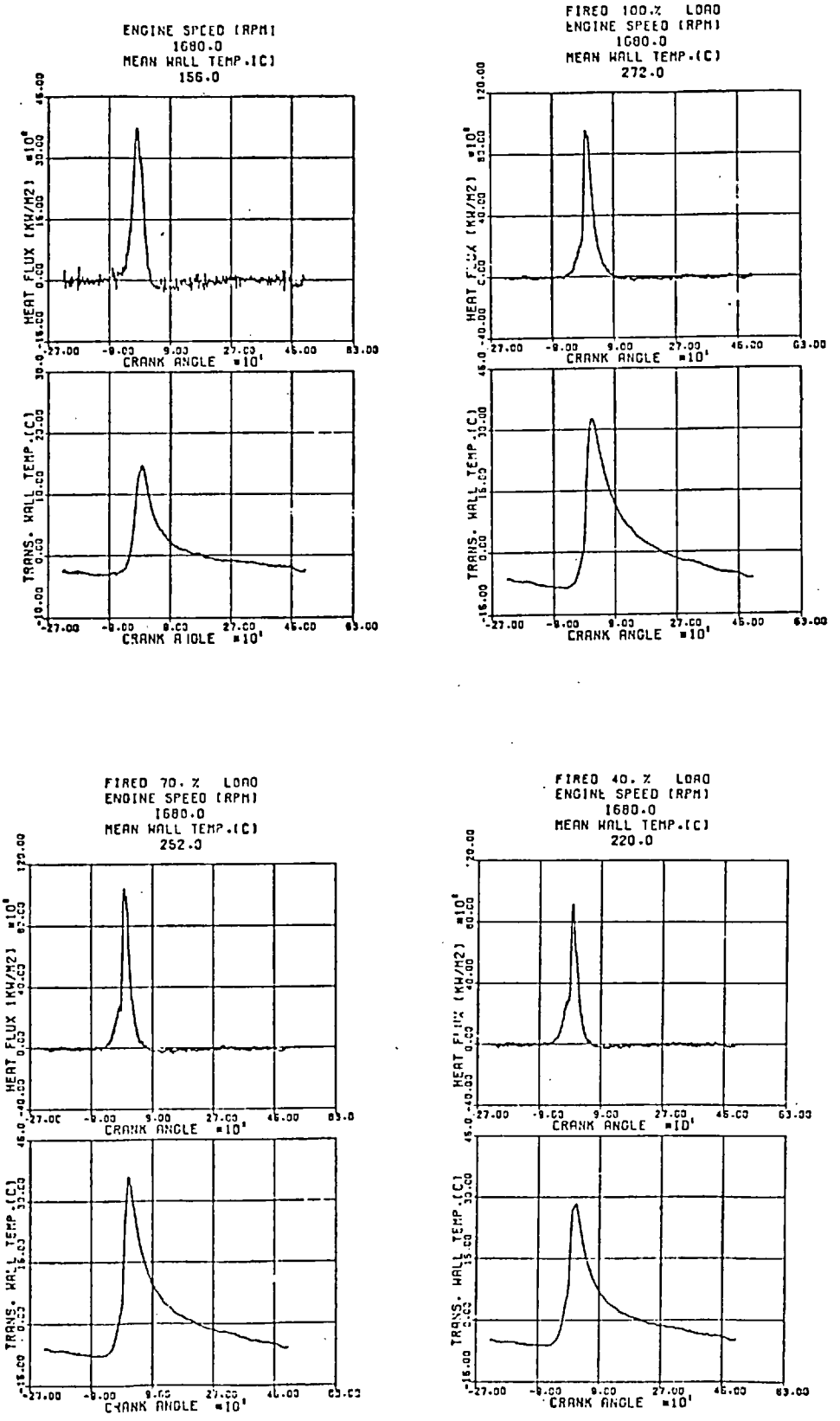

Fig. (4.28) Measured Instantaneous Prechamber Wall Temperature and Heat Flux at 1680 rpm

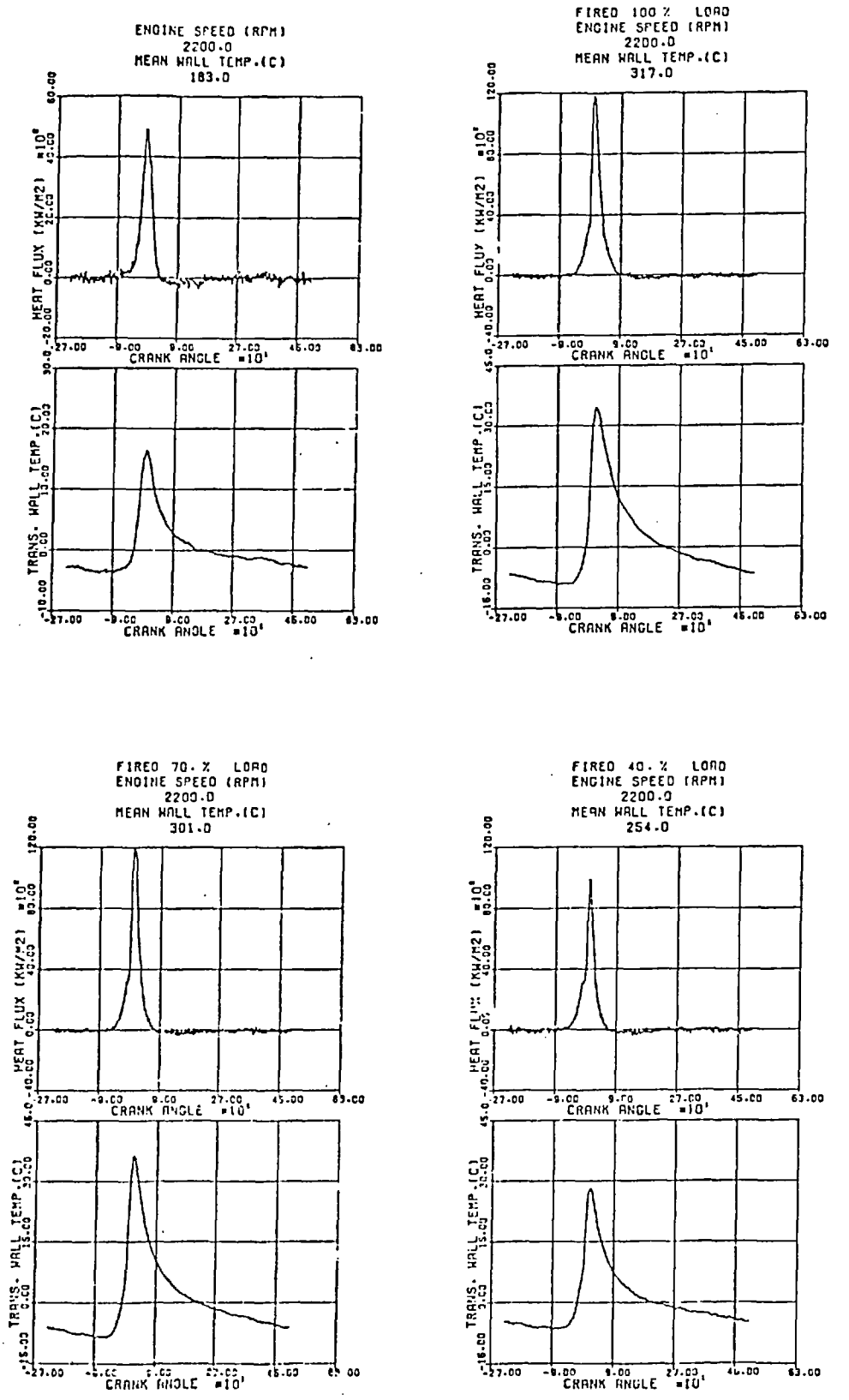

Fig. (4.29) Measured Instantaneous Prechamber Wall Temperature and Heat Flux at 2200 rpm

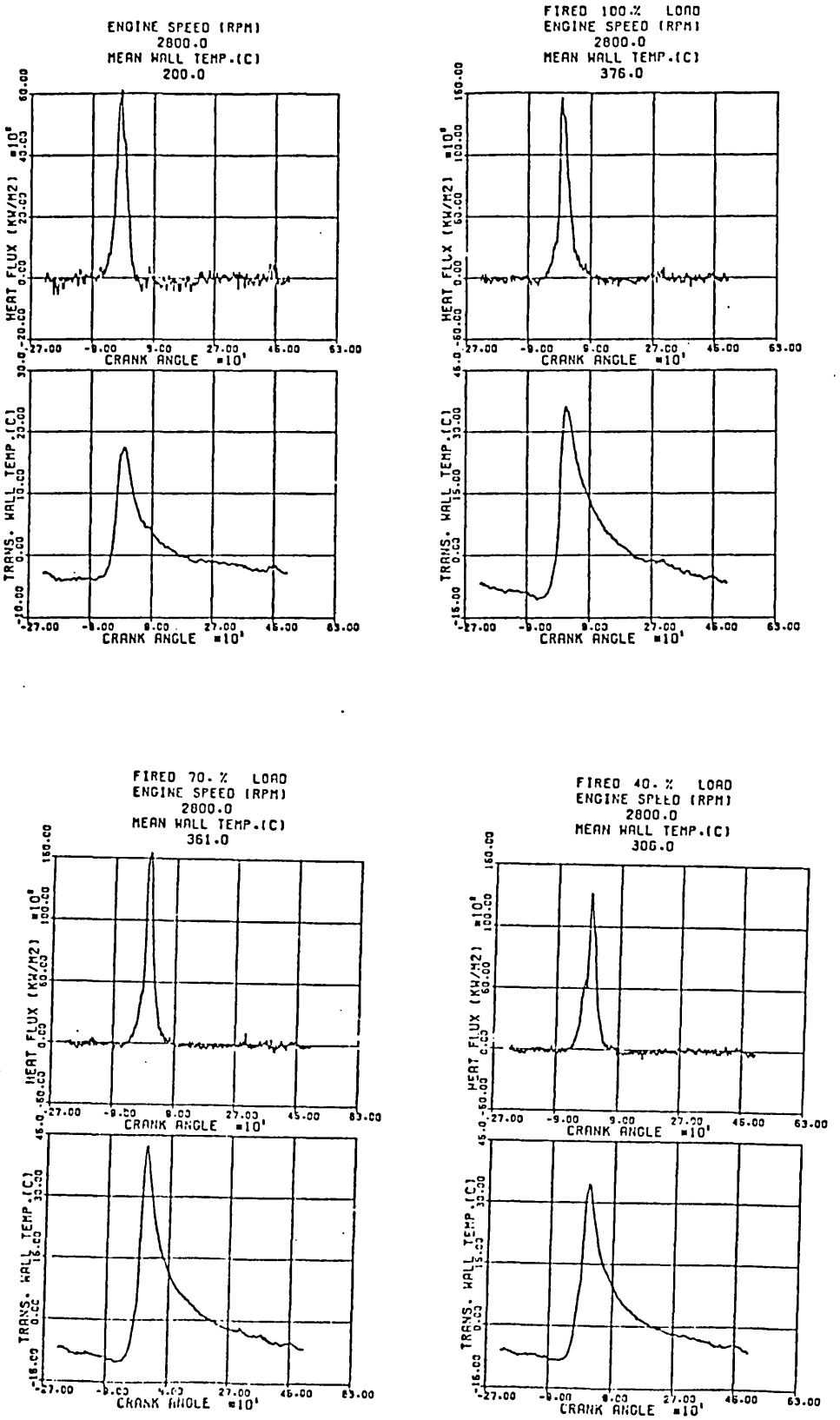

Fig. (4.30) Measured Instantaneous Prechamber Wall Temperature and Heat Flux at 2800 rpm

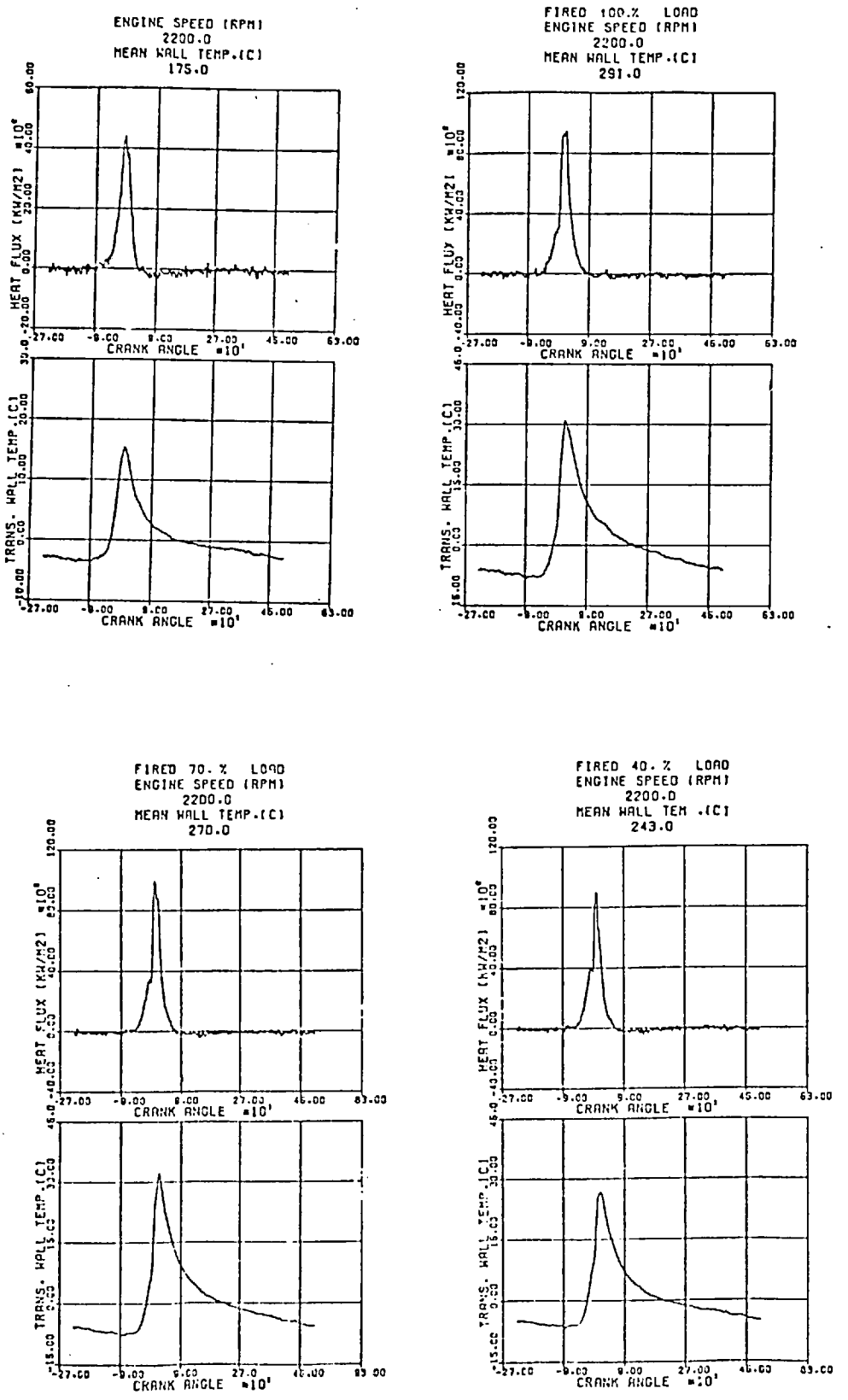

Fig. (4.31) Measured Instantaneous Prechamber Wall Temperature and Heat Flux at 2200 rpm and D.T. = 2^{0} BTDC

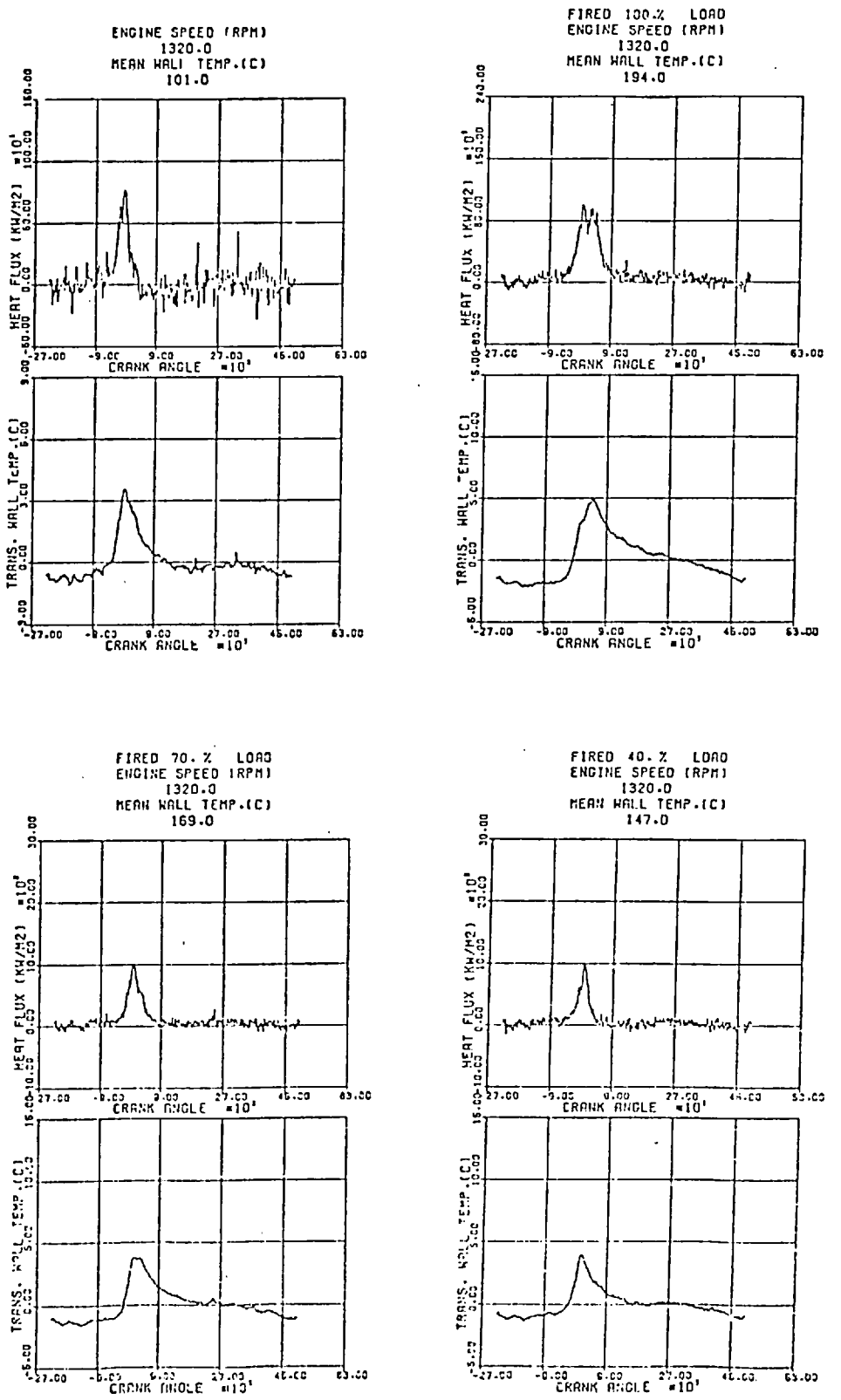

Fig. (4.32) Measured Instantaneous Cylinder Head Temperature and Heat Flux at 1320 rpm

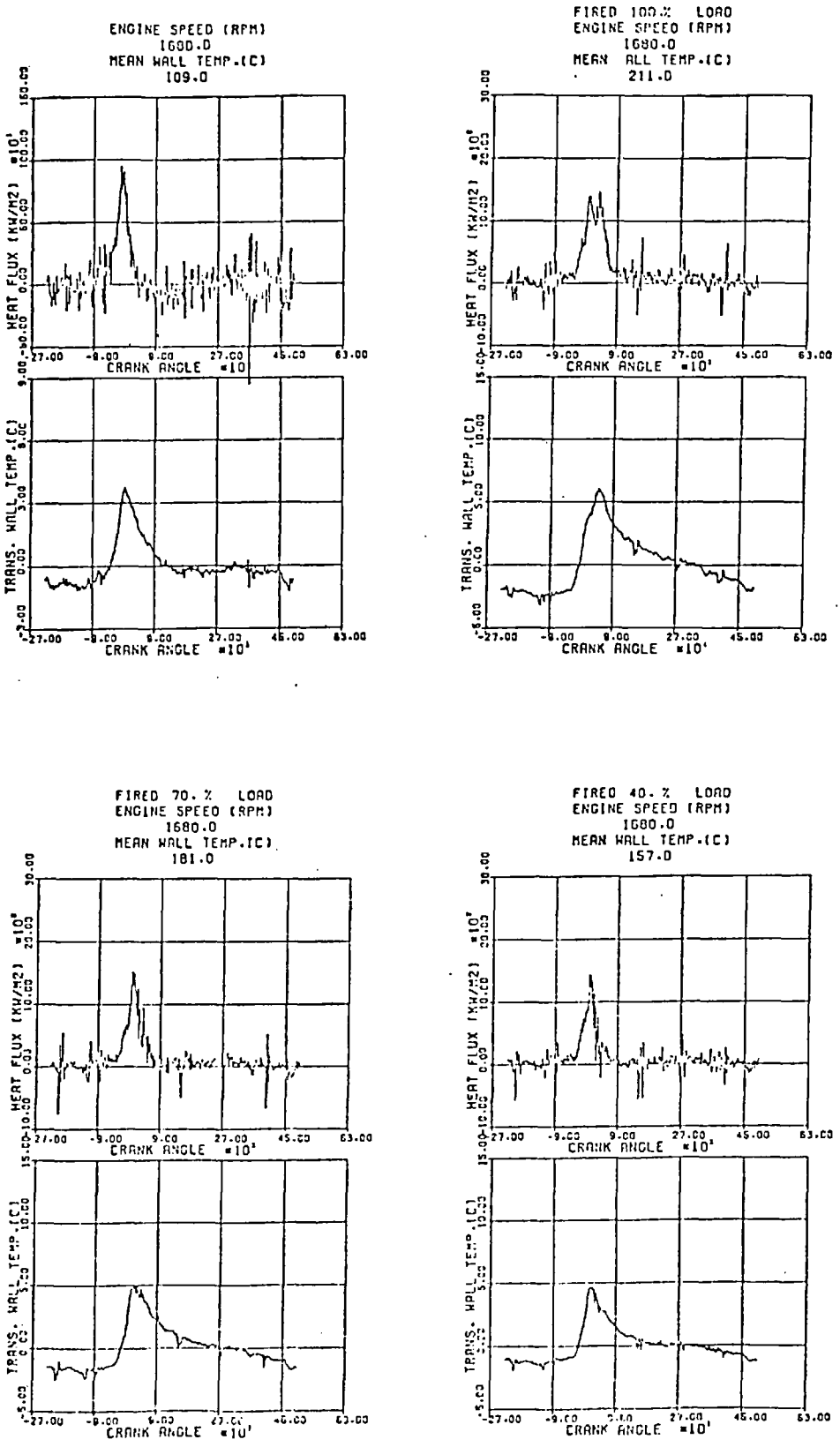

Fig. (4.33) Measured Instantaneous Cylinder Head Temperature and Heat Flux at 1680 rpm

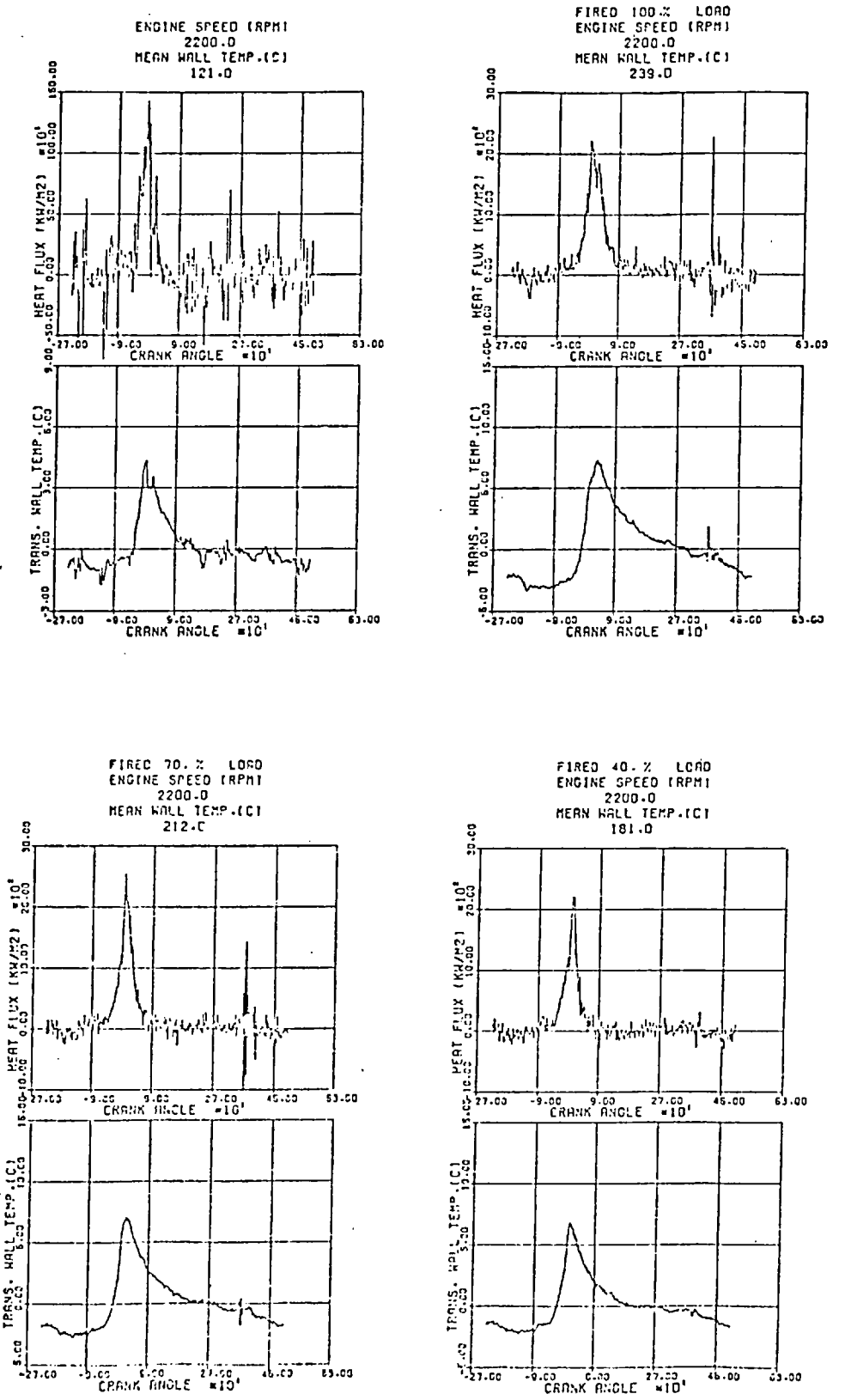

Fig. (4.34) Measured Instantaneous Cylinder Head Temperature and Heat Flux at 2200 rpm

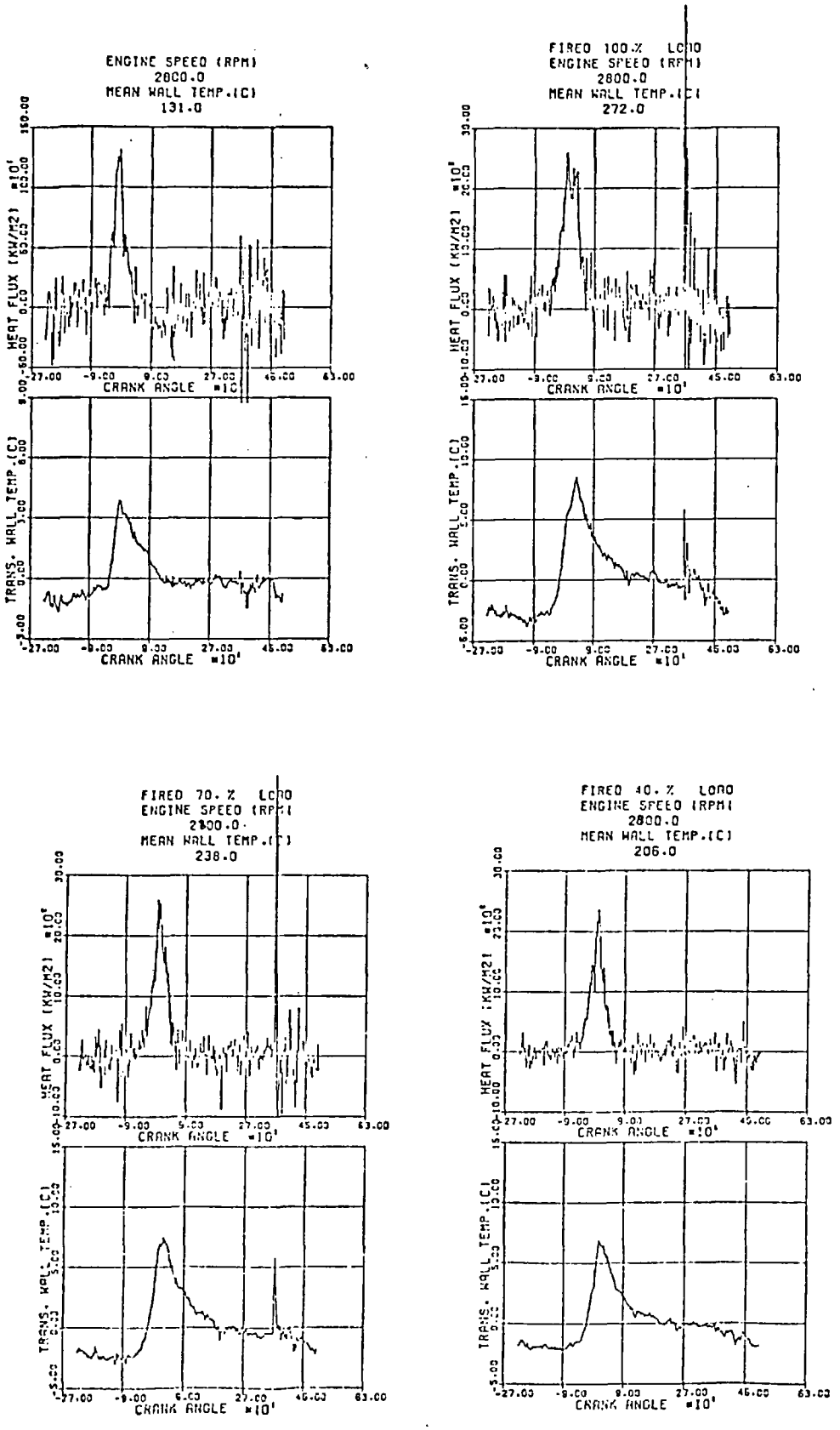

Fig. (4.35) Measured Instantaneous Cylinder Head Temperature and Heat Flux at 2800 rpm

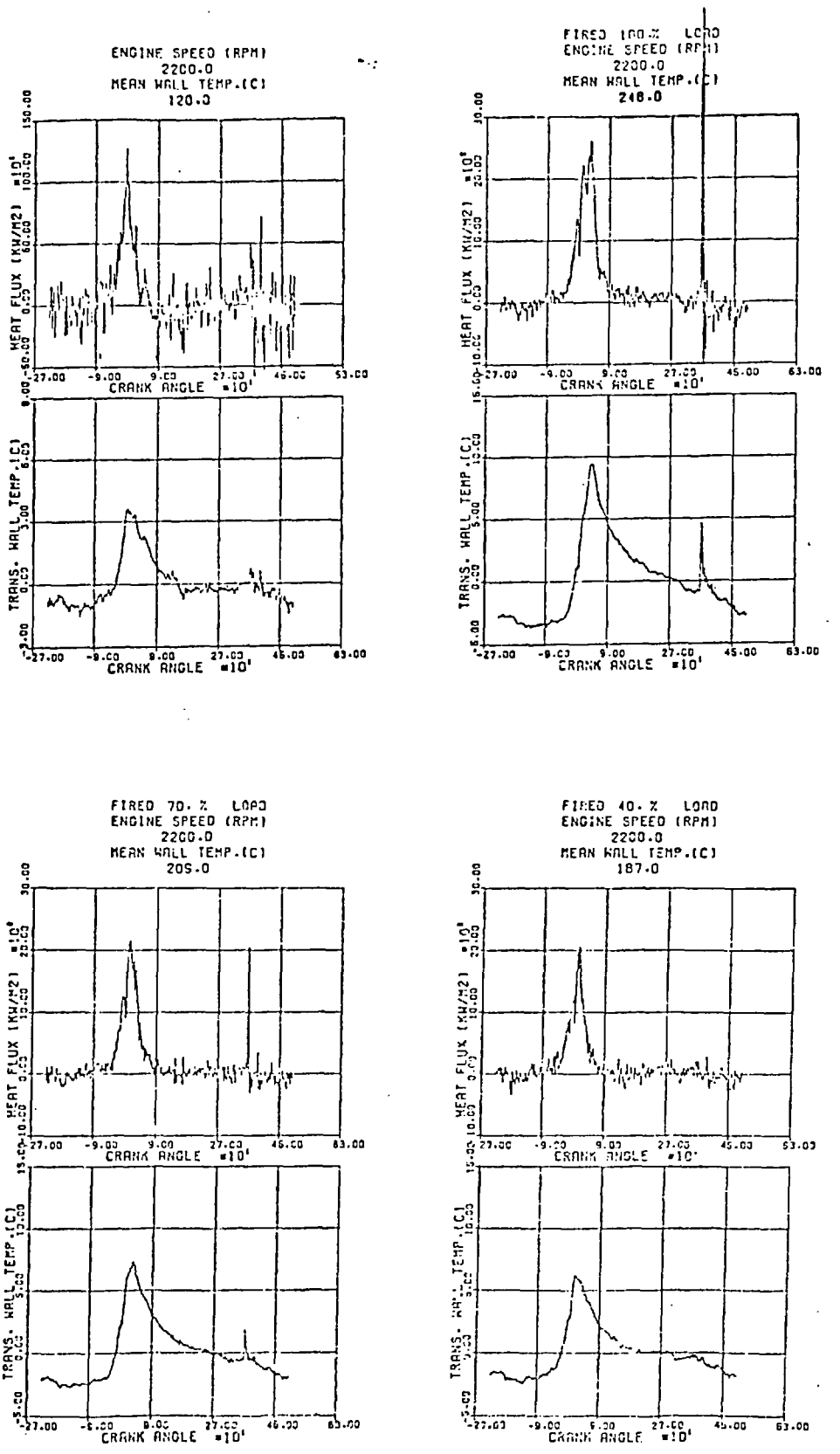

Fig. (4.36) Measured Instantaneous Cylinder Head Temperature and Heat Flux at 2200 rpm and D.T. = 2^{0} BTDC

the engine at four speeds. All runs are for injection dynamic timing of 7^{o} BTDC, except Figs. (4.31) and (4.36) which are for 2^{o} BTDC injection dynamic timing. The latter were recorded to study the effect of injection timing on the heat flux behaviour. Fig. (4.34) and Fig. (4.44) also show a motored run at (2200 rpm) sampled after a few hours of fired operation. Comparison between motored runs in Figs. (4.27) and (4.31) shows little difference, suggesting that soot deposits on the thermocouple surface have negligible influence. Examination of the surface thermocouple after fired operation supported the above conclusion, as it was fairly clean.

Although prechamber wall temperature fluctuations measured were greater than reported in other published work, the compression ratio of the engine tested was higher than the corresponding values in other investigations, and this was expected to be the reason. Wall temperature fluctuations for the cylinder head were significantly lower than those for the prechamber, under the same running condition. This gave confidence in the measured values.

The effect of engine speed on measured instantaneous heat fluxes followed the expected trend, i.e. increasing with engine speed increase, for both the prechamber and cylinder head. Effect of engine load was less pronounced in the case of the cylinder head fluxes. For the prechamber, it is noticed that peak heat fluxes always correspond to 70% load conditions. Although differences between peak fluxes for 100% and 70% loads are small, they are consistant at all running conditions. This excludes the possibility of experimental error. The reason for such behaviour is expected to be combustion mode related, possibly a result of increased charge velocity at 70% load, due to higher ROHR values as a result of longer ignition delay period and hence more rapid initial ROHR.

The level of noise in the calculated heat fluxes for the cylinder head is much higher than that for the prechamber. This is a direct result of a higher noise/signal ratio for the cylinder head wall temperature measure-

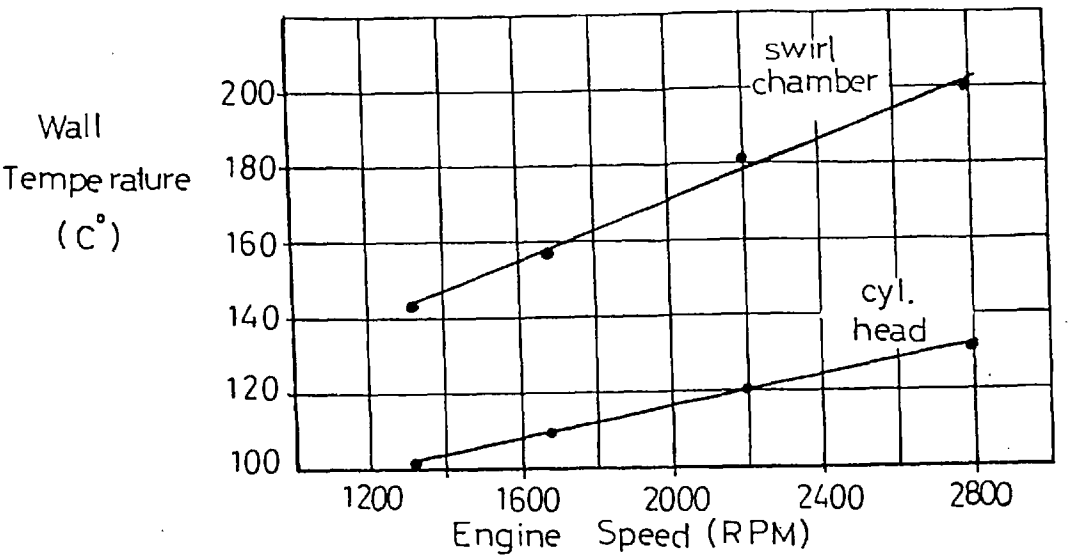

Fig. (4.37) Wall Temperature Under Motored Conditions

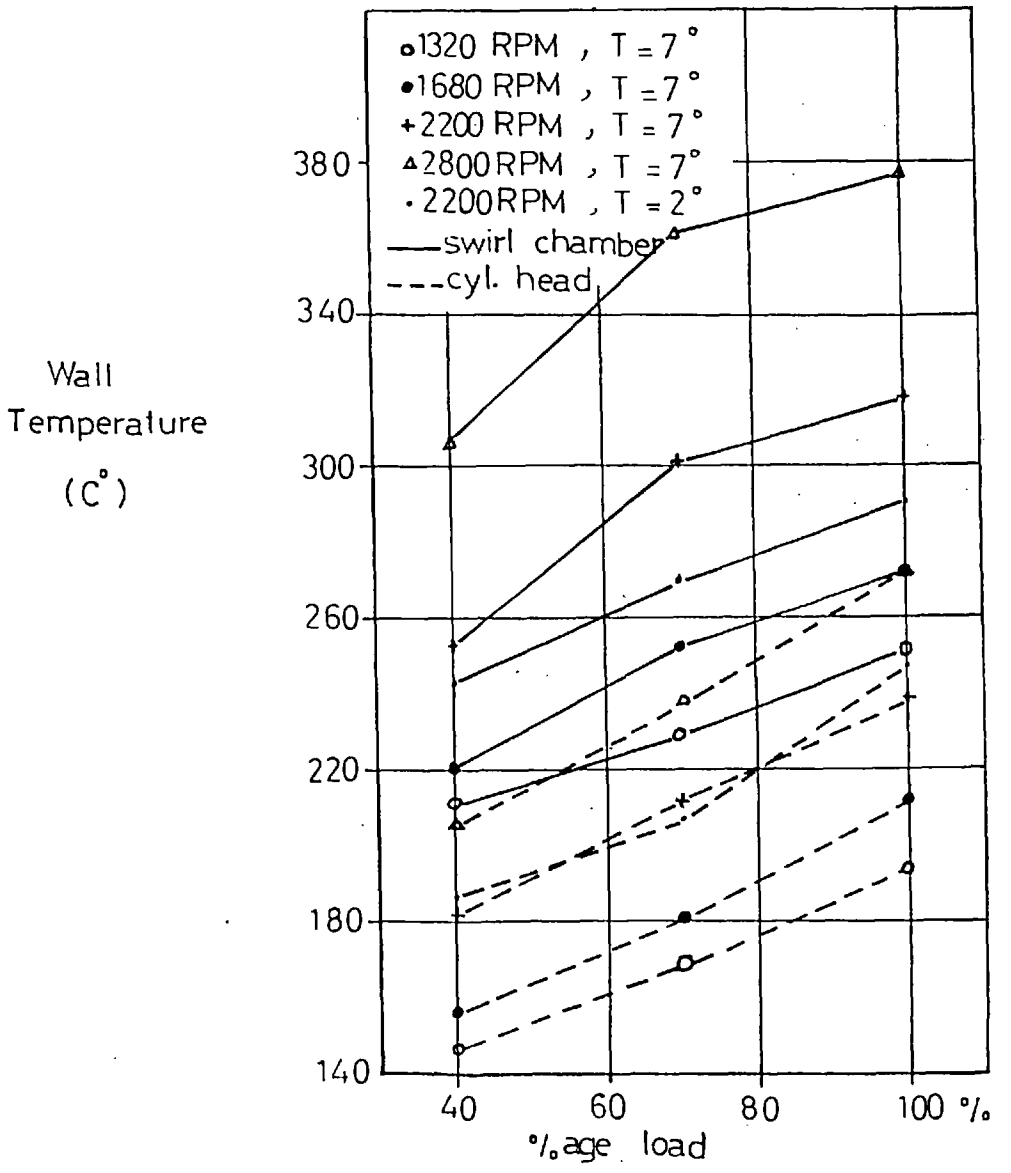

Fig. (4.38) Wall Temperature under Fired Conditions

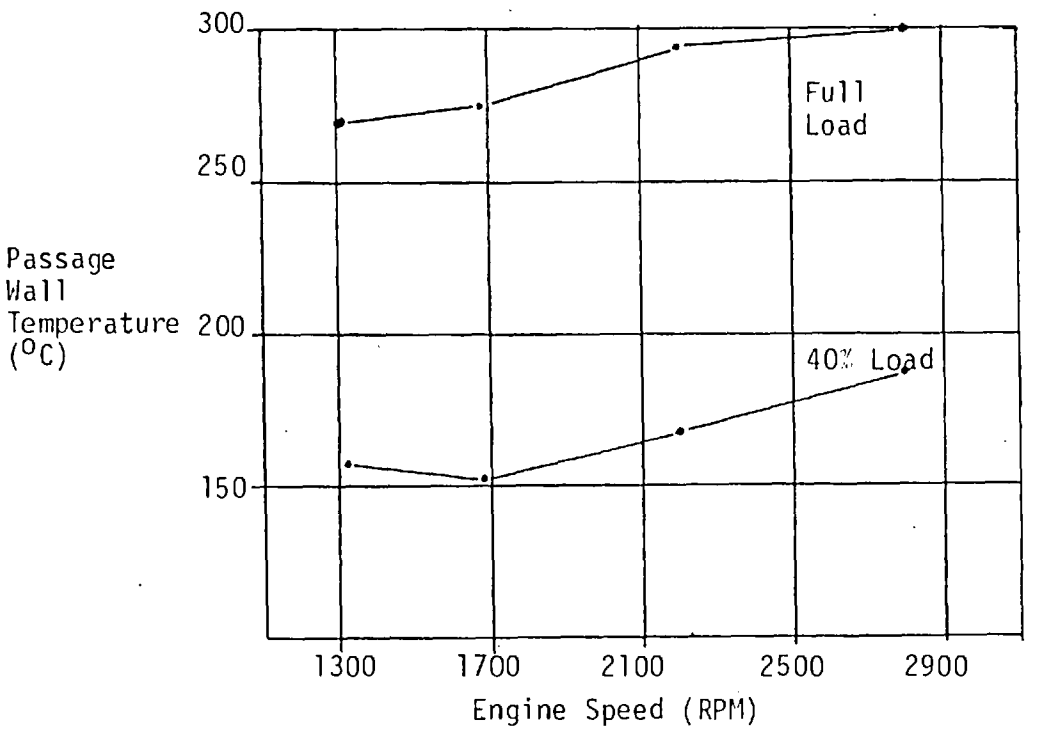

Fig. (4.39) Passage Wall Temperature Variation with Engine Speed and Load

ments, due to smaller surface temperature variation within the engine cycle.

Figs. (4.37-39) show the measured mean prechamber, cylinder head and connecting passage temperatures. The effects of speed, load and injection timing are indicated. The trends of wall temperatures for prechamber and cylinder head are reasonable. The values for the passage wall temperature show some discrepancy in the trend at part load conditions. It is believed that this might have been due to bad contact between the thermocouple and the walls of the traversing hole.

4.5 COMPARISONS OF MEASURED AND PREDICTED HEAT FLUXES AND CONCLUSIONS

4.5.1 Motored Operation

As established previously (section 4.2), the following relation reasonably predicts heat fluxes to the chamber walls of a motored engine.

$$Nu = a\ Re^{b}$$

By comparisons with Hassan's results, the constants a and b were determined to be

$$a = 0.023 \text{ and } b = 0.8$$

It was decided to test the above relationship and the velocity calculation model further, by comparisons with the experimental heat fluxes obtained in the present work. For this, the simulation program was used to model the engine under investigation, and predict instantaneous heat flux values for both prechamber and cylinder head, under motoring conditions.

Velocity estimates using the principle of kinetic energy conservation were used as flow characteristic velocities. The characteristic dimension was chosen to be the prechamber diameter, and cylinder bore (for the main chamber). All gas properties were calculated at the "mean film temperature" which is the average of gas bulk mean and wall temperatures. For the main chamber (cylinder), it was acknowledged that heat transfer rates are different at the liner than at the piston crown and cylinder head. Due to

the large distance from the cylinder bore centre, the cylinder liner is subjected to higher gas velocities, depending on the distance from the centre. This is assuming a forced vortex gas velocity distribution across the cylinder bore. The total heat flux in the main chamber was, therefore, considered to be the area average of each consistuent, namely, liner, piston crown and cylinder head.

In the Nu-Re relationship, the parameter (b) was fixed at (0.8) while (a) was varied independently, for both the main and prechamber, to obtain best predictions under motoring conditions. This value was decided upon not only by comparison of predicted and measured heat flux values for both chambers, but also by comparing predicted and measured cylinder pressure and pressure difference diagrams. The technique used was to obtain values of (a) for both chambers that would give the best prediction at one engine speed, and then examine the predictions with the same values of (a) at other engine speeds. The final values of (a) chosen were,

(a) for prechamber = 0.023

(a) for main chamber = 0.012

which is in good agreement with the fact that heat fluxes from the cylinder are less than those for prechamber.

Pressure diagram comparisons are shown in Chapter 7. Fig. (4.40) shows the comparisons between measured and predicted heat fluxes under motored conditions, for both the prechamber and cylinder head, at four engine speeds. The agreement is satisfactory for the entire speed range.

Predicted heat fluxes, for both prechamber and cylinder head, using published heat transfer correlations, were also considered. Fig. (4.41) shows a comparison of present work experimental results and predicted heat flux values obtained by using correlations by Eichelberg (35), Annand (8), Woschni (117), Sitkei (97) and the present model. For Woschni's correlation, the representative velocity was considered to be 6.18 times the mean piston

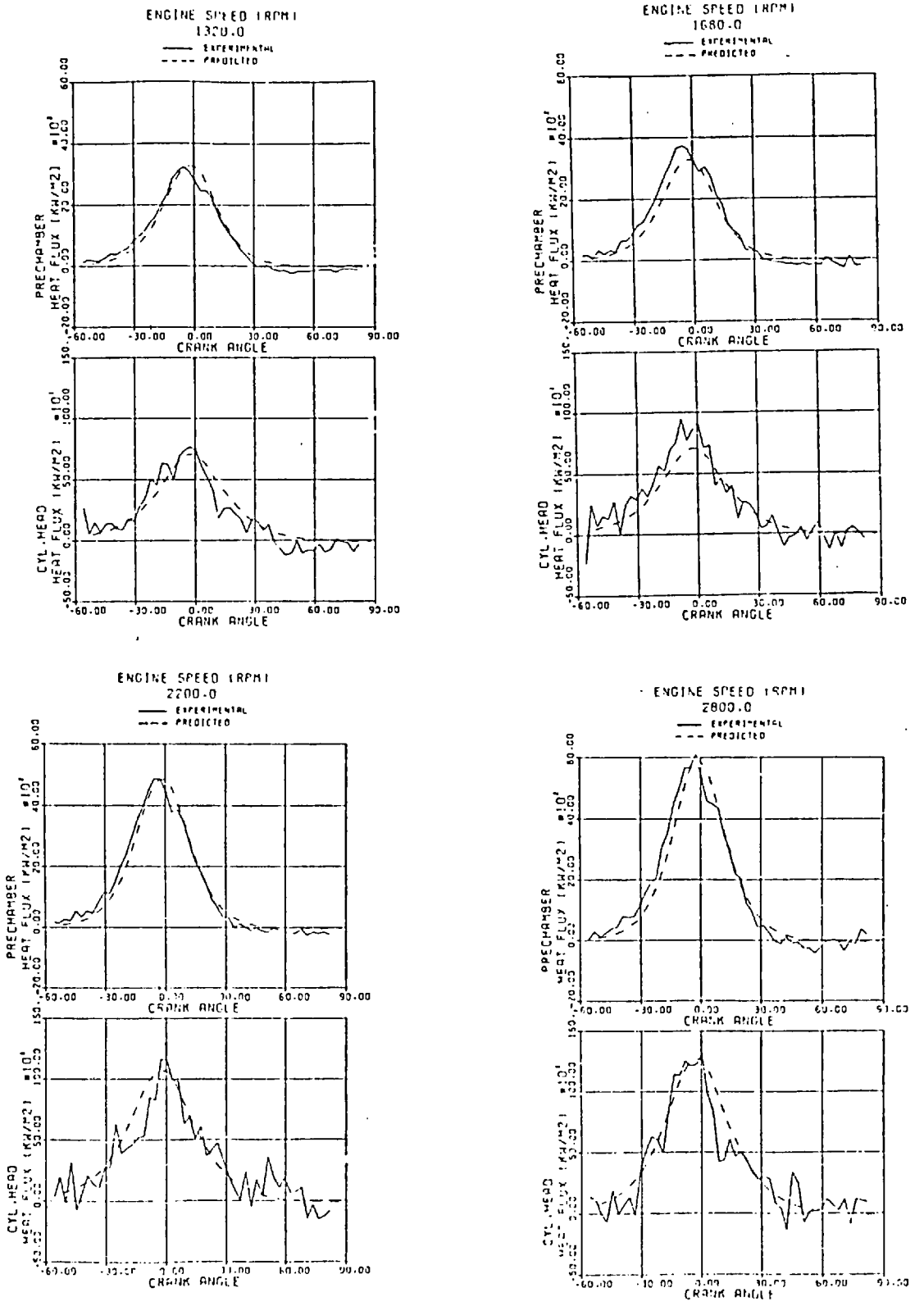

Fig. (4.40) Predicted and Measured Heat Fluxes under Motoring Conditions

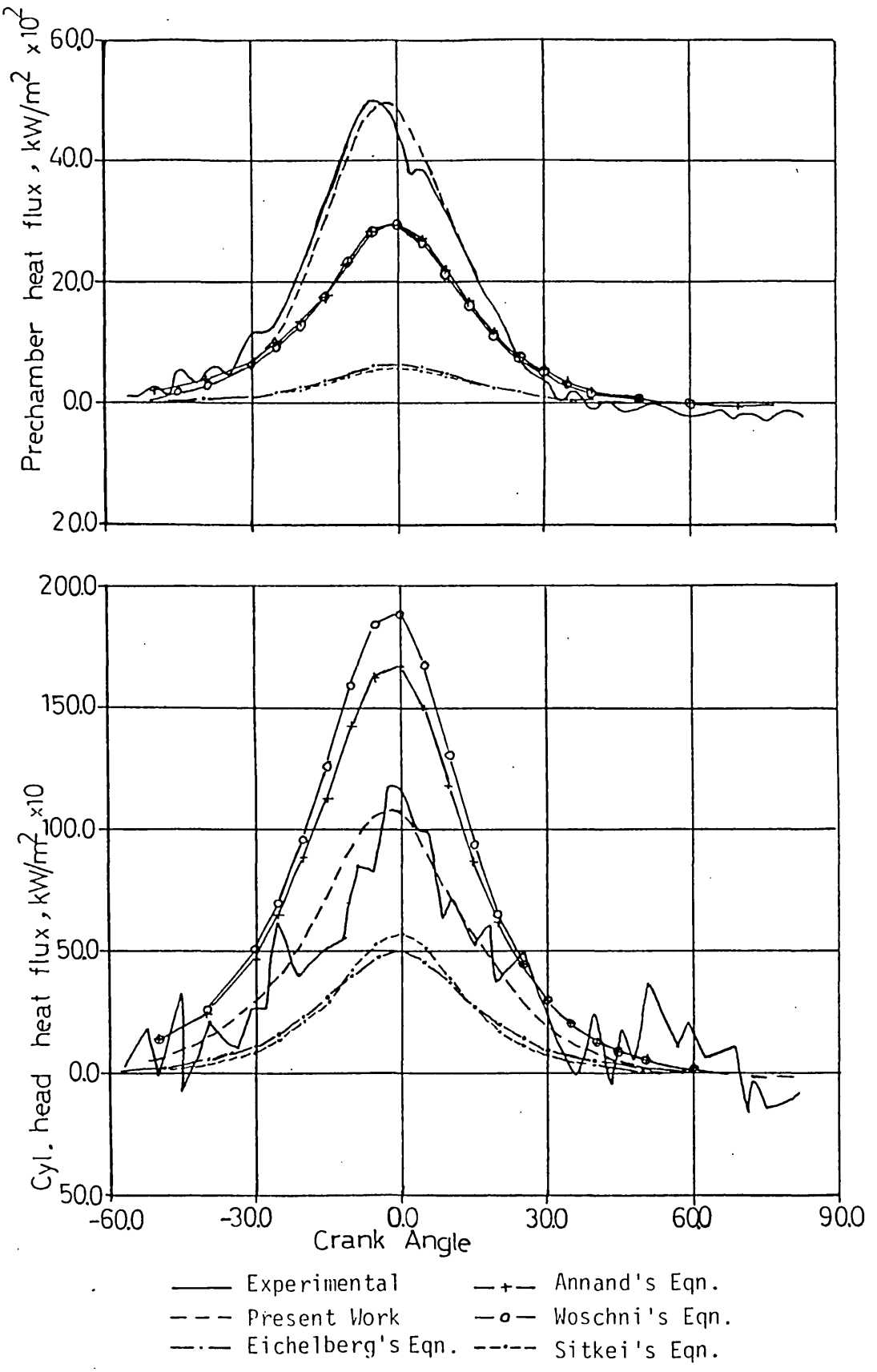

Fig. (4.41) Measured and Calculated Heat Fluxes using Different Correlations under Motored Conditions

speed as recommended by Woschni for the open part of the cycle, to account for extra charge motion. The superiority of the present model is apparent for both the prechamber and cylinder head.

The difference of the value of parameter (a) for the prechamber and the main chamber can be explained as being expected due to the assumption concerning the velocity discussed in section (4.2.4.c).

4.5.2 Fired Operation

Comparisons between predicted and measured heat fluxes for motored conditions showed good agreement. In the Nu-Re correlation the same values of (a) and (b) constants were used for all engine speeds. This provided good evidence for the validity of the correlation to predict heat flux rates.

Under fired operation two important additional factors are introduced in the heat transfer phenomena; radiative heat transfer and convective heat transfer enhancement due to fuel jet effect. The calculation procedure, and assumptions involved, for both were explained earlier in this chapter. To examine the Nu-Re correlation behaviour under fired operation and the added effects of velocity enhancement and radiation, comparisons were conducted between measured and calculated heat fluxes, to prechamber wall and cylinder head, under firing conditions. The results are shown in Figs. (4.42-45). Results were compared for different engine speeds, loads and injection timing.

The same Nu-Re relationship was used, and with the same constants as in motored conditions. Charge velocity enhancement due to the fuel jet was included for prechamber heat flux calculations. The improvement of prediction, obtained via including the fuel jet effect, has already been demonstrated in Fig. (4.13). Combustion effect on the main chamber heat flux, was considered to be due to increase of charge velocity as a result of high velocity gases for the prechamber.

Radiative flux calculations, were found to be dependent on the value chosen for (ϕ) in equation (4.9), as indeed was reported by Kunitomo and

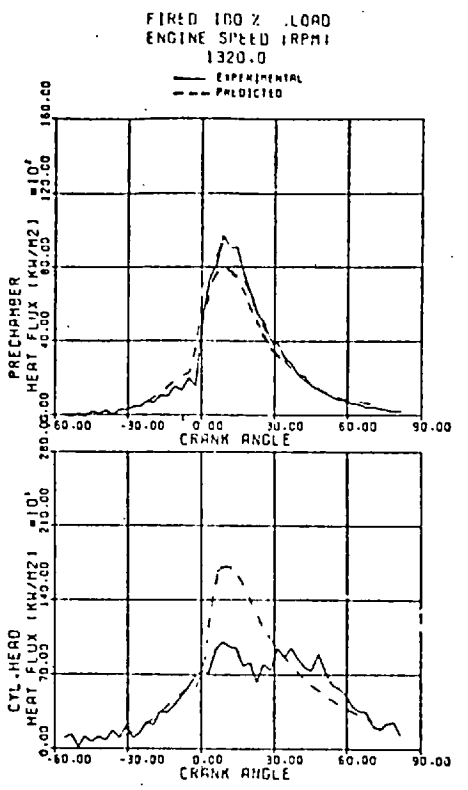

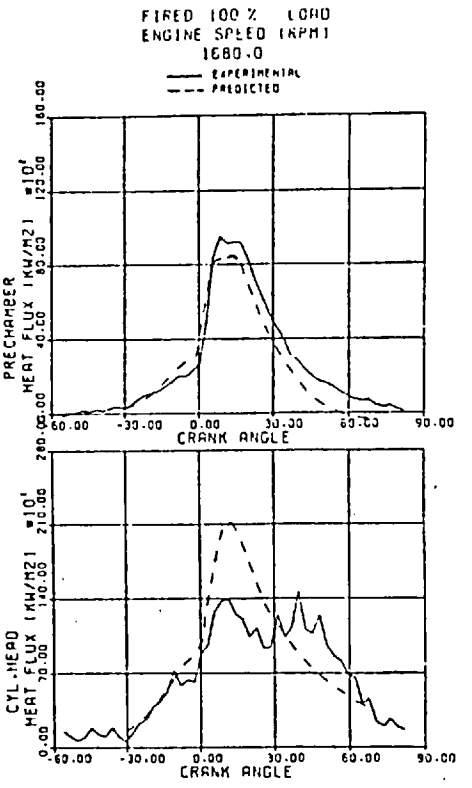

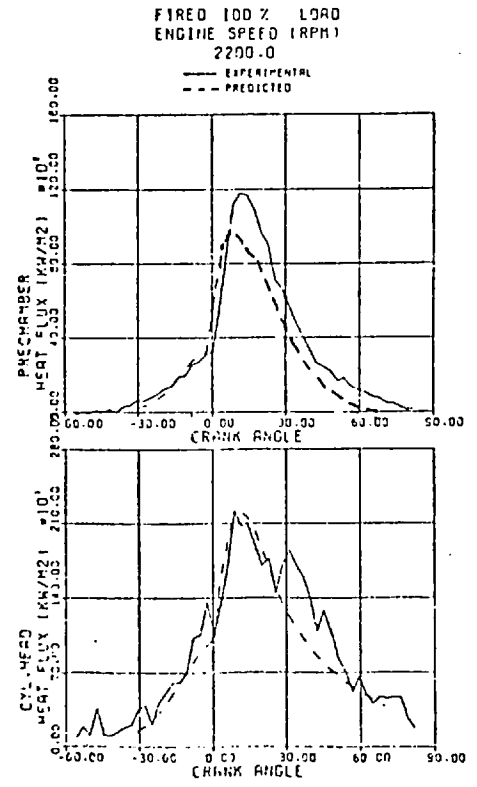

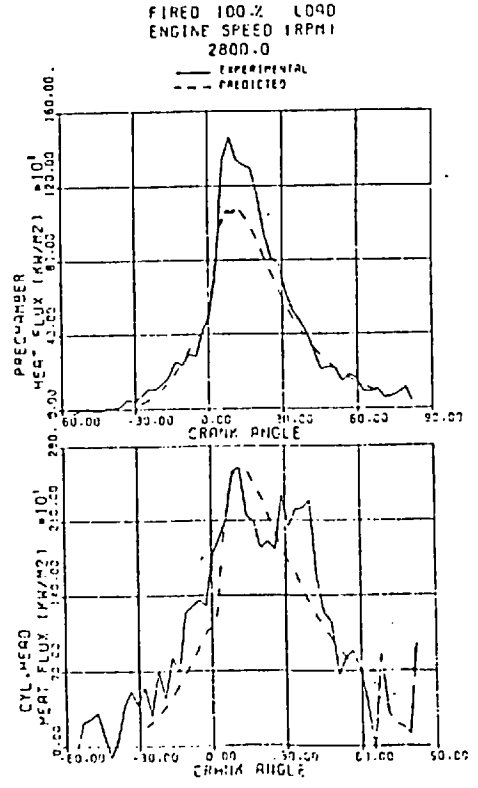

Fig. (4.42) Predicted and Measured Heat Fluxes under Full Load Conditions

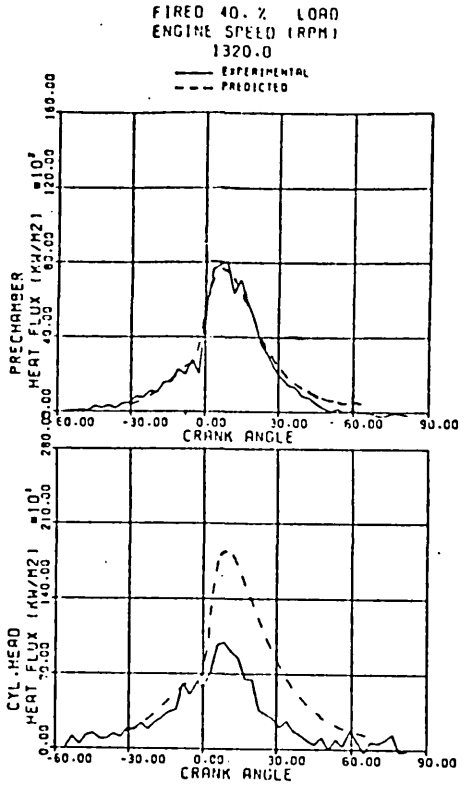

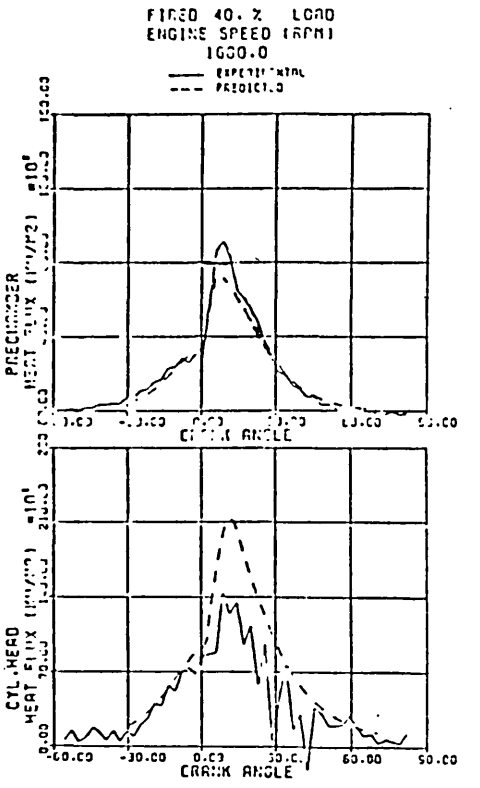

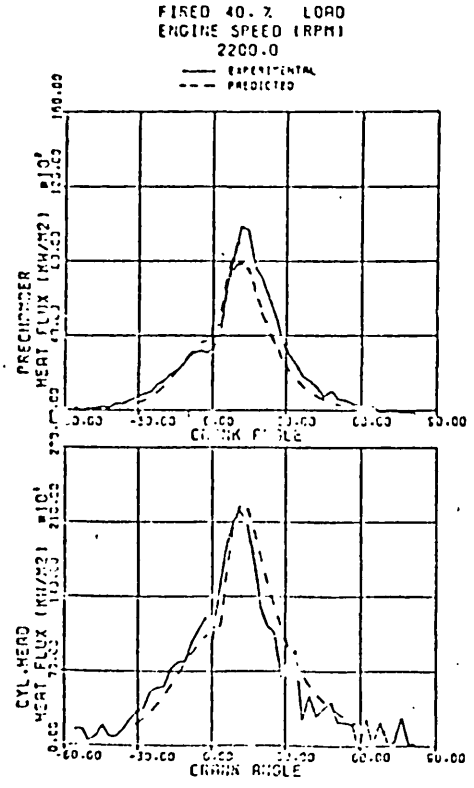

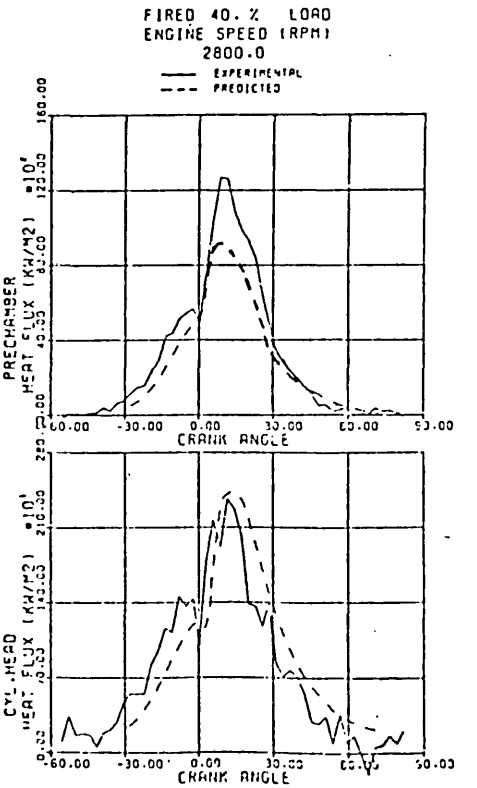

Fig. (4.43) Predicted and Measured Heat Fluxes Under 40% Load Conditions

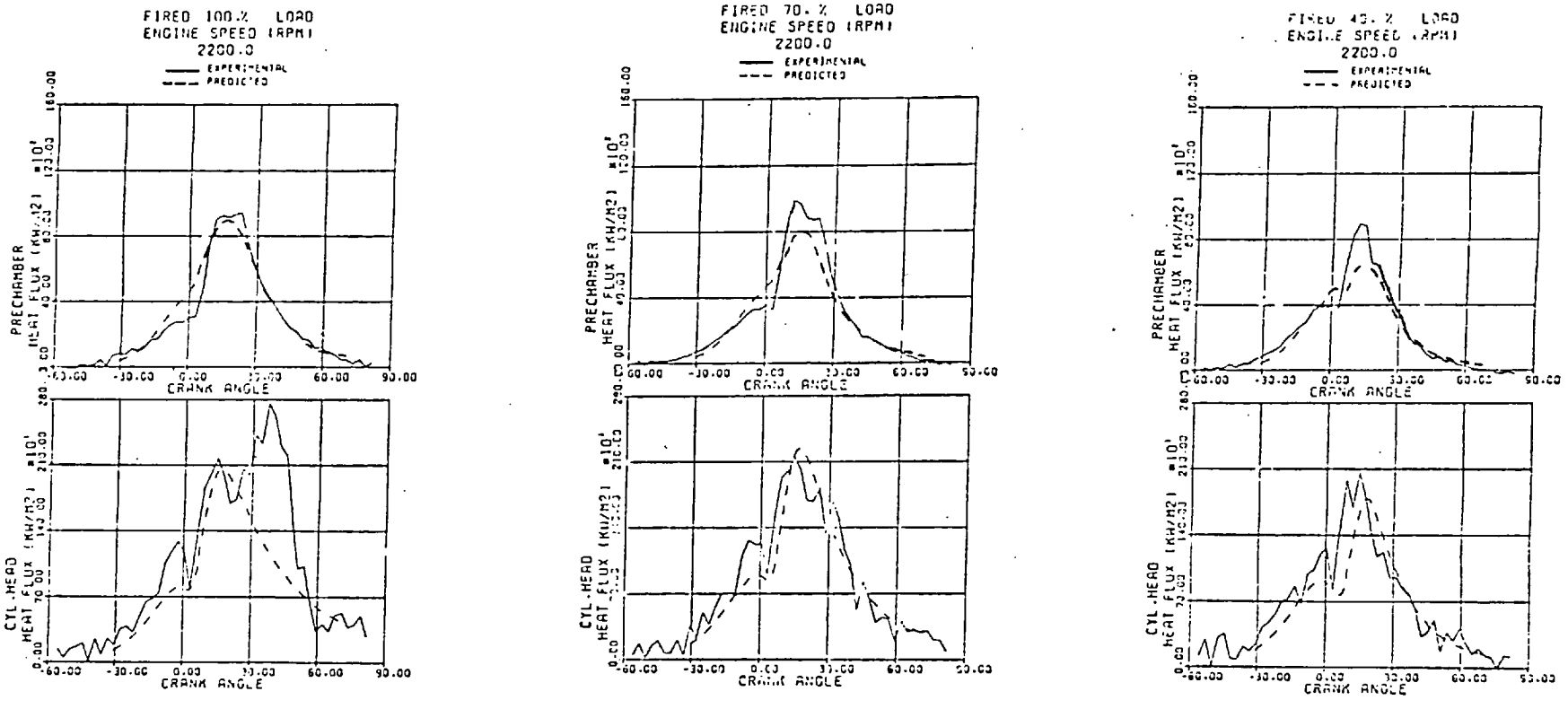

Fig. (4.44) Measured and Calculated Heat Fluxes for Retarded Injection Timing (2^{o}CA BTDC)

Oguri (82). Values for (ϕ) suggested by Kunitomo and Oguri (82), were obtained from comparisons between measured and predicted radiative fluxes in their DI engine. When their value of (ϕ) was used in the present calculations, it rendered excessive radiative, and hence total, heat fluxes in the main chamber. This is thought to be partially due to the higher smoke, and hence radiative heat fluxes, in DI engines compared to the IDI engine. A value of (ϕ=1.1) was, therefore, chosen for the present calculations which gave acceptable predictions of heat fluxes at one running condition, This was fixed for all other conditions and acceptable results were obtained.

Fig. (4.42) shows predicted and measured instantaneous heat fluxes for prechamber and cylinder head, under full load and four engine speeds conditions. Fig. (4.43) shows the corresponding results at 40% load conditions. Dynamic injection timing for all condition is 7^{o} BTDC, Fig. (4.44) shows the results of three load runs for 2200 rpm at 2^{o} BTDC dynamic injection timing.

Examining the figures, good general agreement is detectable between measured and predicted trends of the results. Some deviations exist in the magnitudes of heat fluxes, which are expected. Experimental heat fluxes were obtained from temperature measurements at one point on the wall of the prechamber and another point on the cylinder head wall. Temperature variations are expected along the walls of either chamber, specially under fired operation. This results in the measuring point being only an average of the actual case. Also, one dimensional conduction through the wall is an assumption which could introduce some small errors in the measurement.

From the above discussion, it is concluded that small deviations between experimental and predicted heat fluxes can be acceptable, since measured values are themselves average of the actual heat flux phenomena.

Agreement between experimental and predicted heat fluxes is generally better for the prechamber. The reason is probably due to the assumptions

made, concerning velocity distribution and kinetic energy conservations. These appear to be more suitable for the prechamber where swirl motion is more pronounced. The flatness of the measured heat flux diagram for the main chamber at low engine speeds, is probably due to the high velocity gases, issuing from the prechamber, being retained in the piston crown cavities and thus not introducing extra charge movement near the cylinder head. The diagram becomes more 'peaky' with increase in engine speed, which gives an indication of speed dependence. This may, although not conclusively, give some support to the above argument. The waviness of the cylinder head heat flux has been explained before as being due to high (noise/signal) ratio.

In Fig. (4.44), at full load, 2200 rpm and 2^{o} BTDC dynamic injection timing, a second peak exists in the experimental heat flux at the cylinder head. Similar, though less pronounced, peaks can be detected at the full load high speed runs in Fig. (4.42). This is expected to be combustion related behaviour which becomes apparent at high engine load, and even more apparent at retarded timing due to delayed combustion in the main chamber.

Calculated total heat fluxes, radiative flux components and emissivity values for both prechamber and main cylinder under different running conditions are shown in Figs. (4.45)-(4.48). The figures show predicted values for full and part load conditions at four engine speeds. Calculated emissivities are always less than 0.5, which supports the findings of Oguri (82) and Sitkei (97). Higher emissivity values are obtained for the prechamber than the main cylinder. In the vicinity of TDC, where high pressure exists in both chambers, the optical radiation length is longer for the prechamber, with the resultant high emissivities. During expansion, although the optical length in the main cylinder increases, the cylinder pressure is very much reduced which results in a reduction in emissivity.

Emissivity values are shown in the figures to increase, for both prechamber and main chamber, at 40% load. This is expected to be due to increased

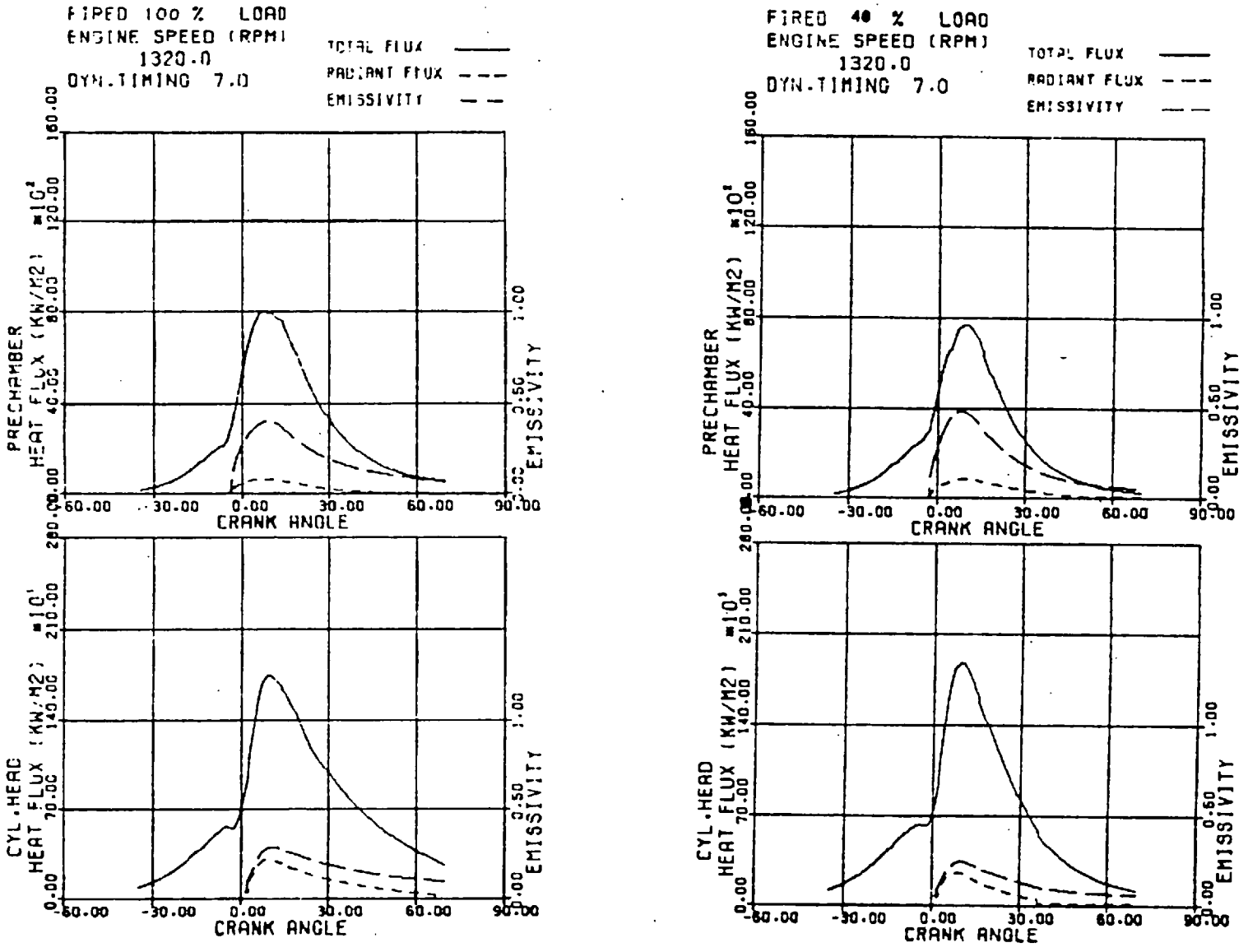

Fig. (4.45) Predicted Total and Radiant Heat Fluxes and Emissivities at 1320 rpm

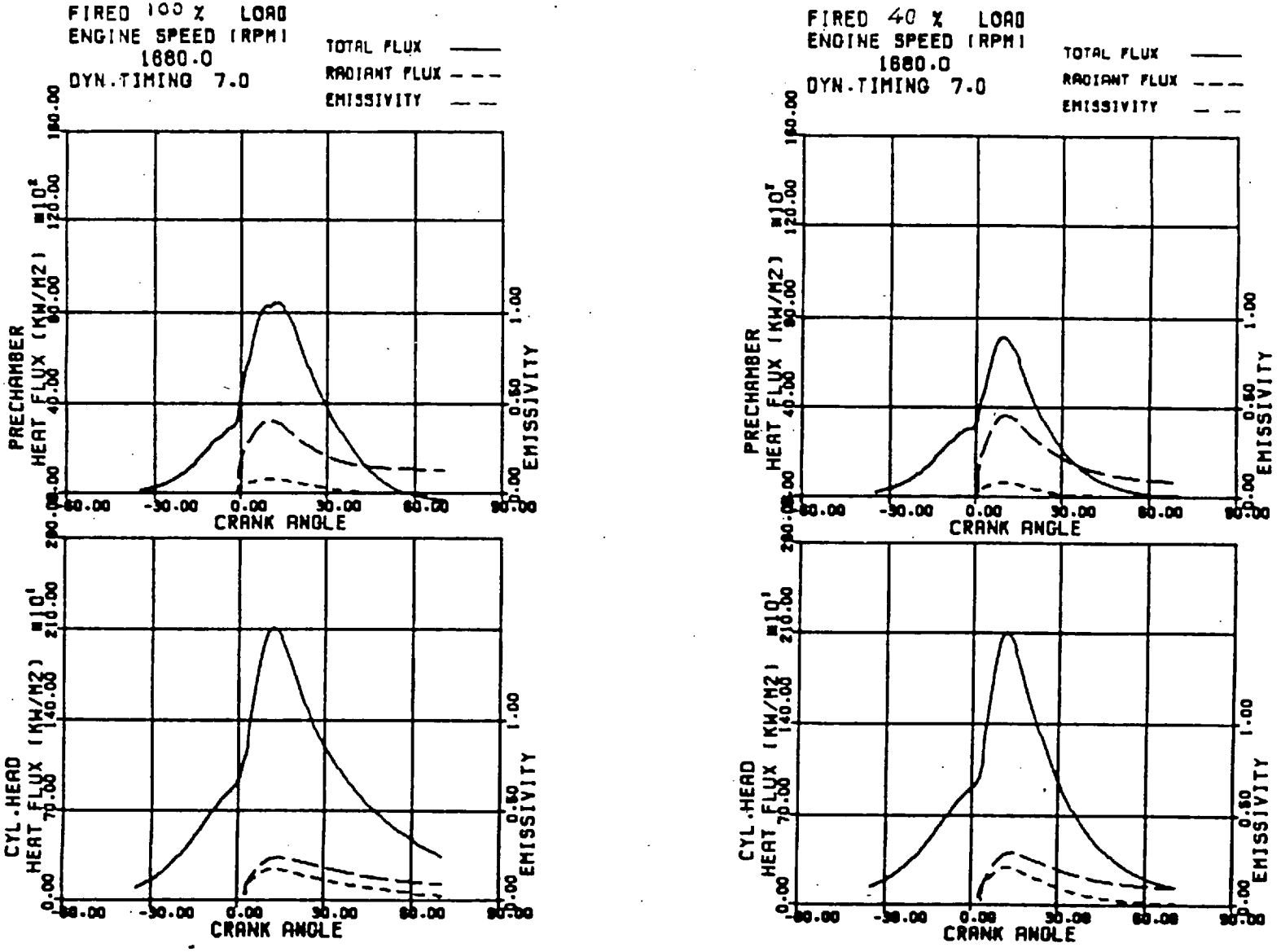

Fig. (4.46) Predicted Total and Radiant Heat Fluxes and Emissivities at 1680 rpm

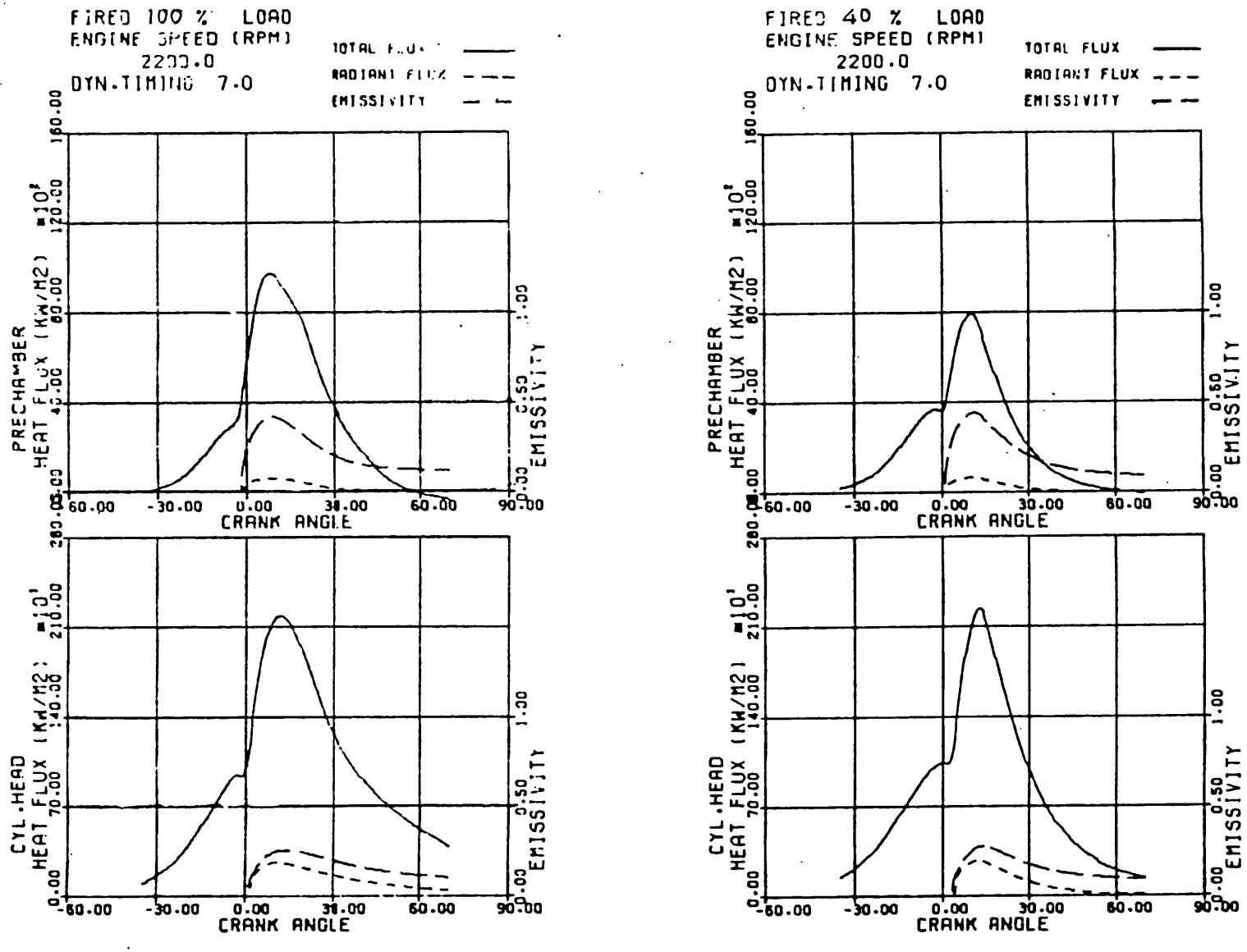

Fig. (4.47) Predicted Total and Radiant Heat Fluxes and Emissivities at 2200 rpm

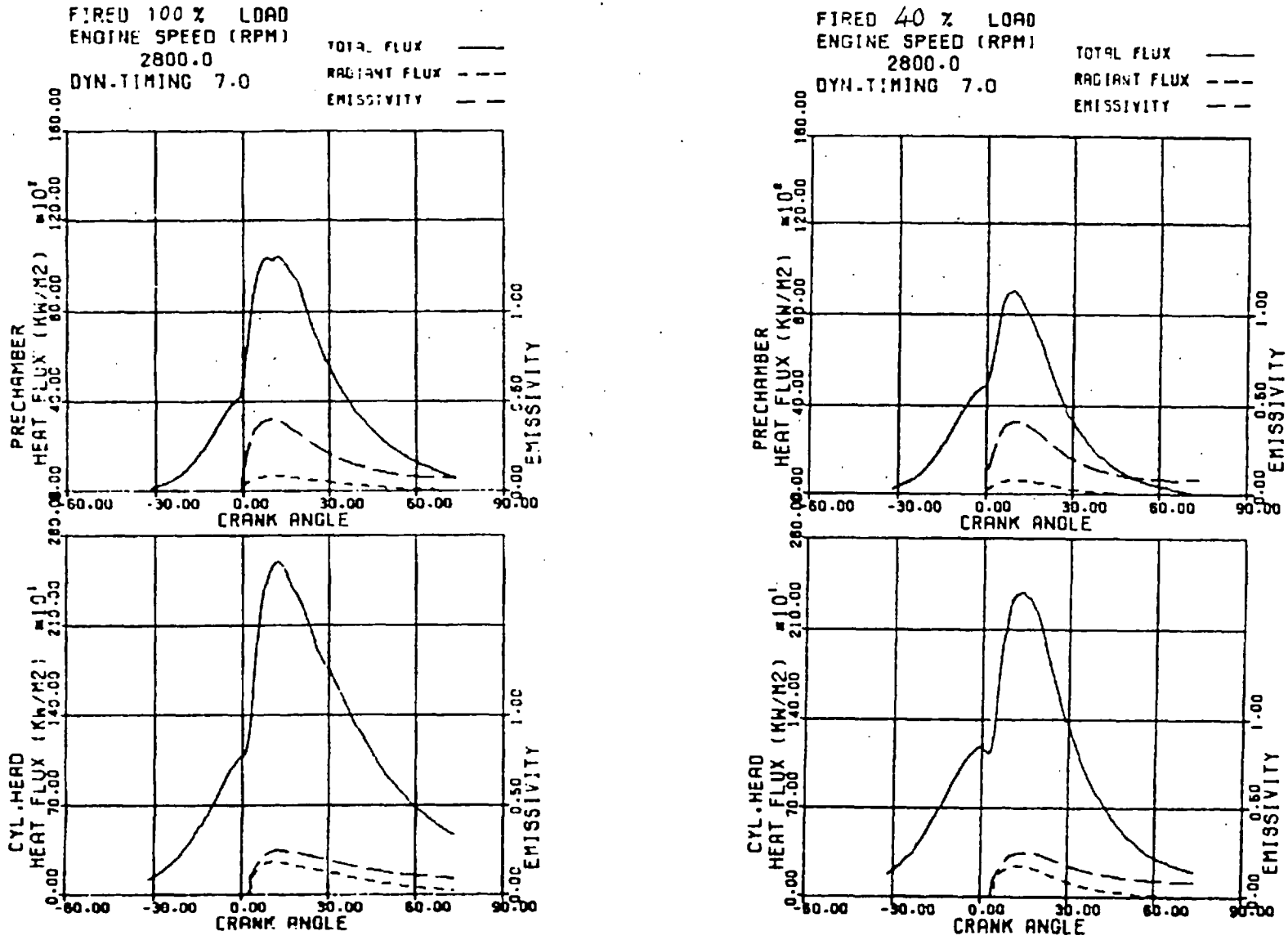

Fig. (4.48) Predicted Total and Radiant Heat Fluxes and Emissivities at 2800 rpm

amount of radiating gases, CO_2 and H_2O, due to higher Air/Fuel ratio.

As a percentage of the total flux, radiative heat flux is very small in the prechamber. For the main chamber, however, it forms a considerable proportion of the total flux, which decreases with engine speed increase (approximated from 20% to 10%).

Although the value of gas emissivity down the expansion stroke reduces to approximately 0.1, the radiative flux drops to zero. This is due to the assumption made concerning the reduction of the flame temperature down the expansion stroke which was explained earlier.

In conclusion, the prediction model for heat flux calculations under fired operation has been shown to give satisfactory results. The kinetic energy of the fuel jet has been shown to have a considerable effect on the heat flux calculations for the prechamber. The radiative heat flux calculation method rendered reasonable and acceptable emissivity and flux values. The combined model of calculation has been shown to predict heat fluxes, inside the engine combustion chambers, satisfactorily, under motored and fired operations.

CHAPTER 5

PASSAGE COEFFICIENT OF DISCHARGE

5.1 INTRODUCTION

In any IDI diesel engine the cylinder is generally divided into two chambers, connected via one or more passages. As the piston moves up the compression stroke, air is pushed through the connecting passage to the prechamber. Combustion is usually initiated in the prechamber. After ignition, burnt and burning charge is forced through the passage to the main chamber where useful engine work is obtained from the piston. The connecting passage is of vital importance in divided chambered engine performance. Prechambered engines vary in the geometry of the prechamber, and the passage geometry changes accordingly. The passage provides ordered tangential flow for a swirl chamber engine, while for a Steyr type prechamber, it provides a turbulent mode of flow.

The geometry of the passage and its effect on the engine performance has been studied by Nagao and Kakimoto (76), Nagao (77) and Tanak et al (103), whose results clearly indicate the importance of the connecting passage on the overall performance of the engine. Different passage designs were, however, outside the scope of the present work. The engine tested had a fixed geometry and no attempt has been made to investigate the effects of passage geometry change on engine performance. To correctly simulate the engine, the effective flow area of the passage was required.

By using the engine simulation program in the motored mode, it was found that the predicted engine behaviour was very dependent on the flow area used to represent the connecting passage. Flow areas were considered to be equal to the geometric areas multiplied by a flow coefficient of discharge (C_d). Although Nakajima (80) obtained heat release rate values

for a divided chamber engine, he did not report any values of flow discharge coefficient through the passage. Anisitis (6) quoted a value between 0.85 and 0.8 for his passage.

Using the motored version of the computer simulation program, and comparing predicted cylinder pressures and pressure difference values between the two chambers, it was deduced that the effective flow discharge coefficient for the engine under investigation was lower than that found by Anisitis (6).

Due to the importance of the passage flow area in engine simulation, a detailed investigation, both theoretical and experimental, was undertaken to examine passage flows. The theoretical part was aimed, at a thorough understanding of the parameters controlling flow through orifices, published work in the field of orifice flow was reviewed, and an attempt made to predict orifice flow coefficients. The experimental part of the work included testing of the actual passage under steady flow conditions, to determine the flow coefficient of discharge. Flow to and from the prechamber was investigated, the effect of piston position being simulated.

5.2 REVIEW OF PUBLISHED WORK ON DISCHARGE COEFFICIENT CALCULATIONS

A distinctive feature of flow through a sharp edged orifice, beyond choking conditions (i.e. when the flow Mach number reaches unity), is that it can be made to increase by further reduction of the back pressure. It is apparent that the orifice discharge coefficient rises when the back pressure of the orifice decreases (99). This results in an increase of the flow area and hence increase of the flow. A simplified, one dimensional approach of Plenum (zero approach velocity) orifice flow is reported by Jobson (57). He introduced the method of "force defect" based on the assumption that the velocity pattern at the walls, upstream of the orifice, was independent of flow rate.

Consulting Fig. (5.1), the flow "near the orifice wall" accelerates as it approaches the orifice edges. This flow acceleration results in a reduction of the flow pressure at the wall as it approaches the orifice edge. Equating the resultant force acting on the fluid contained within the boundaries (AA) and (BB) to the corresponding momentum flux, the following equation of motion is obtained

$$(P_o - P)\ A + F_d = \dot{m} u$$

where

F_d = Force defect = $\int_A^\infty (P_o - P_w)\ d\ A_w$

$\dot{m}$ = Mass flow rate

u = Flow velocity through orifice

P_w = Pressure at the wall

Jobson neglected flow compressibility upstream of the orifice. By dimensional considerations, he suggested that the force defect (F) may be expressed as,

$$F = f\ \frac{\dot{m}^2}{\rho_o A}$$

The force defect coefficient was assumed to be a function of orifice geometry only. Jobson obtained the following relation to give the contraction coefficient "C_c" as a function of the flow pressure ratio (r),

$$C_c = \frac{1}{2fr^{1/\gamma}} \left[1 - \sqrt{1 - \frac{(2\ r^{1/\gamma})^2 (1-r) f}{(K_n)^2}} \right]$$

where

$$K_n = \sqrt{\frac{2\gamma}{\gamma-1}\ r^{2/n} \left(1 - r\ \frac{\gamma-1}{\gamma}\right)}$$

The force defect coefficient (f) was assumed to be equal to that of the incompressible case (f_i) which was obtained from,

$$f_i = \frac{1}{C_i} - \frac{1}{2C_i^2}$$

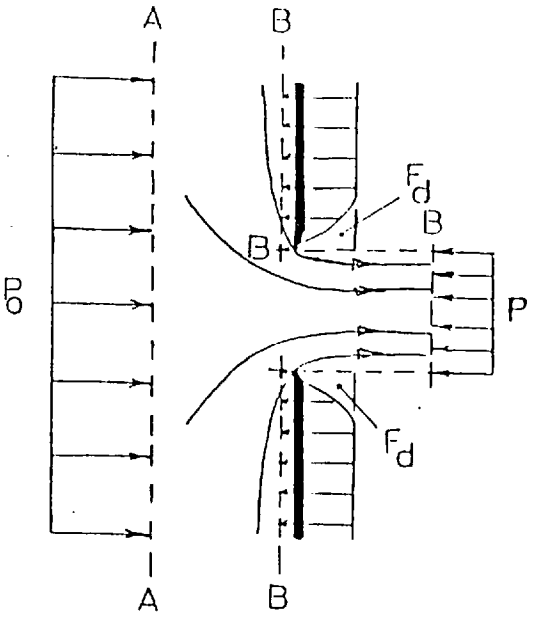

Fig. (5.1) Sharp Edge Orifice Flow

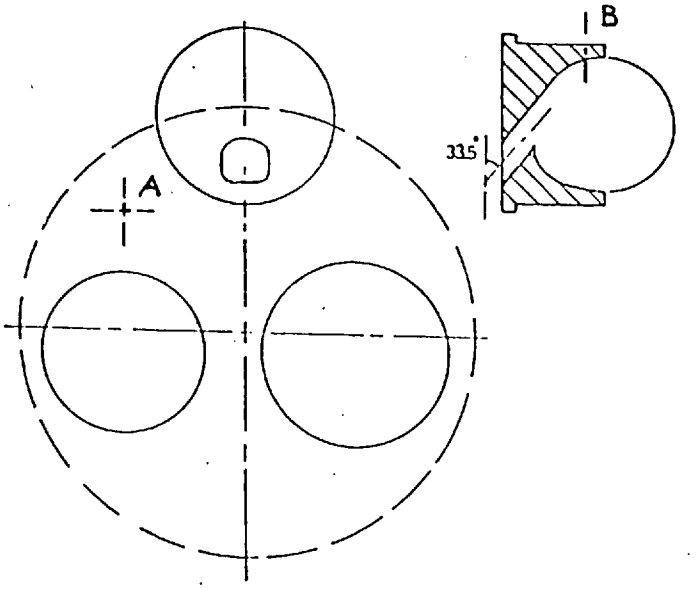

Fig. (5.2) Connecting Passage Geometry
(Shown are transducers positions A and B)

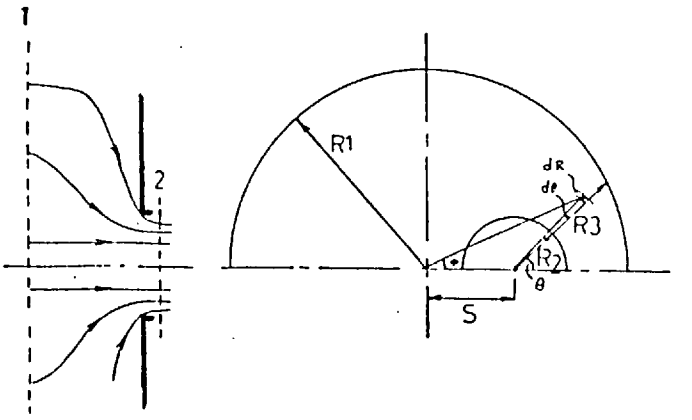

Fig. (5.3) Generalized Asymmetric Orifice Geometry

where (C_i) is the incompressible flow contraction coefficient.

The above expression yielded results that were in good agreement with experimental data from sharp-edge orifices. The method, however, breaks down and leads to demonstratably false results when the discharge coefficient is greater than about (0.65), with a pressure ratio far from unity. In such conditions the upstream velocity pattern is affected by compressibility. The limitations of the method were acknowledged by Jobson.

Bragg (24) suggested a further refinement of Jobson's method. He introduced an assumption about the flow pattern near the walls, which allowed for upstream compressibility effect. He assumed that the mass flux at the wall was proportional to the average mass flux through an area (A_w), where A_w is the area (measured perpendicular to the orifice axis) bounded by points on the wall, having the same conditions;

$$\rho_w u_w = K \dot{m} / A_w$$

K = Constant, a function of geometry only

Bragg obtained the following relations, which express the force defect coefficient for the compressible case (f) as a function of (K) and (f_i).

$$K^2 = 2 f_i$$

$$r_n^{2/\gamma} \left(1 - r_n \frac{\gamma-1}{\gamma}\right) = K^2 C_c^2 r^{2/\gamma} \left(1 - r \frac{\gamma-1}{\gamma}\right)$$

$$\frac{f}{f_i} = \frac{2}{r_n^{1/\gamma}} - \frac{(\gamma-1)(1-r_n)}{\gamma r_n^{2/\gamma}(1-r_n \frac{\gamma-1}{\gamma})}$$

where

r_n = Pressure ratio at the orifice edge

$= P_n/P_o$

Bragg compared his theoretical prediction with experimental results from a variety of sources and obtained good overall agreement. The introduction

of upstream compressibility effects reduced the limitation of the original force defect method.

Both Jobson and Bragg treated "Plenum" flow conditions, i.e. the flow upstream of the orifice was stagnant with negligible approach velocity. A generalised approach to the problem was attempted by Benedict (17), who included flows with approach velocity (Beta flows) in his calculations to obtain a general expression for orifice contraction coefficient for any geometry. He treated the incompressible case, following the assumptions of Bragg (24), and obtained the following expression which relates the general incompressible force defect coefficient (f_i) to that for plenum flow (f_{i_p}), as a function of the diameter ratio (β),

$$f_i = f_{i_p} - \beta_b^2 \left(1 - \frac{\beta_b^2}{2}\right)$$

where

$\beta_b = D_2/D_1$

D_1 = Approach tube diameter

D_2 = Orifice diameter

For the compressible case he assumed that the force coefficient for beta flow (f) could be explained as the compressible plenum flow value (f_p) modified by a beta correction term. By analogy he assumed that this correction would be the same as that of the incompressible case i.e.

$$f = f_p - \beta_b^2 \left(1 - \frac{\beta_b^2}{2}\right)$$

Benedict compared his prediction with various experimental results obtained by different researchers, as well as his own results. Good agreement was shown.

All the above mentioned investigations were applied to axisymmetric orifice flows. Begg (13) applied the force defect method to an asymmetric two-dimensional orifice, and obtained good agreement when comparing calculated and

measured contraction coefficient and jet angles. This again provided more evidence of the suitability of the force defect method of calculation. Benson (20) obtained good results when he compared his experimental and predicted flow discharge coefficients for compressible flow through a two dimensional slit (18,19) with Jobson's and Bragg's methods of calculations. His prediction method included a detailed two dimensional solution employing hodograph plane analogy.

Values of flow discharge coefficients through an orifice, considering the plenum flow case, were in the range of 0.62. This is very different from values reported by Anisitis (6). Examining the passage Anisitis tested, it was found to have a (length/diameter) L/D ratio of 0.76, which suggested that it could not be considered a sharp edged orifice. Deckker and Chang (29) studied steady compressible flow through thick orifices. They showed that the flow discharge coefficient depended greatly on the L/D ratio. When the L/D ratio was much greater than a critical value of 0.5 , the orifice was called a thick orifice and had a high discharge coefficient (typically greater than 0.8). This confirms the measurements of Anisitis. It did not, however, explain why a thick orifice would have such a high discharge coefficient relative to a sharp edged orifice of the same diameter, at the same pressure ratio.

In the following section a generalised approach to the calculation of contraction coefficient for sharp edged orifice of any geometry is explained. Consideration is given to thick orifice discharge coefficients and their flow patterns.

5.3 DISCHARGE COEFFICIENT CALCULATIONS

Fig. (5.2) is a sketch of the connecting passage for the engine under investigation. Depending on the pressure ratio across the passage, there could be flow in either direction. It was expected that due to the different upstream geometry of the passage, depending on which direction flow

occurred, the flow restriction would behave accordingly. The passage is positioned close to the edge of the cylinder bore, hence it is not concentric with the flow upstream. Also, piston position was expected to have an effect on the flow pattern approaching the passage, hence affecting the passage discharge coefficient. Detailed knowledge of orifice flows was required to understand the behaviour of the connecting passage discharge coefficient. The work documented below covers flows through different geometry orifices, which was essential for a detailed understanding of the flow phenomena.

5.3.1 Sharp Edged Orifice

Fig. (5.3) outlines the generalized approach adopted to investigate sharp edged orifice flow. A general geometry was considered, including the approach velocity upstream, and orifice eccentricity. In the previous section it was mentioned that Benedict (17) had studied beta flows through orifices. When dealing with the compressible flow case, however, he assumed that the correction for the force defect coefficient due to approach velocity, was similar to that of the incompressible case. In the present work both incompressible and compressible flows are studied.

For plenum flow, Bragg assumed that the flow velocity near the orifice wall (u_w) may be expressed by

$$u_w = \frac{K\, \dot{m}}{A_w\, \rho_w} \tag{5.1}$$

This implies a parabolic velocity distribution, in which the velocity (u_w) approaches zero value as the area (A_w) tends to infinity. For beta flows, however, the approach velocity (u_1) has a definite value. The velocity near the orifice wall should approach this value at the approach pipe radius (R1). The velocity distribution in this case can be considered as eliptical. Mathematically this is expressed in a non-dimensional form as follows;

$$1 - \left(\frac{R_1 - R}{R_1 - R_2}\right)^2 = v^2 \qquad (5.2)$$

$$u_w = a\,(1 - V) + u_1 \qquad (5.3)$$

where R = current radius

v = A function of position

The term (a) in the above expression is expected to be a function of the geometry, mass flow (m^*) and inlet density (ρ_1)

$$a = K \frac{m^*}{\rho_1 A_2} \qquad (5.4)$$

A_2 = Orifice geometric area

ρ_1 = Inlet flow density

K = Constant

where

$$u_w = \frac{K\, m^*}{\rho_1 A_2}(1 - v) + u_1 \qquad (5.5)$$

Comparing equations (5.1) and (5.5) it is clear that the velocity distribution is different. Equation (5.5), however, is more flexible, as it expresses beta flow conditions more closely and realisticly. The constant K, as indeed has been assumed by all other research workers, is a function of geometry only. K is taken to be a constant for incompressible and compressible flows, and links them together in the calculation procedure.

Incompressible Flows

Benedict (17) investigated incompressible flow through orifices, taking account of the approach velocity of the flow and concluded that;

$$f_i = f_{i_p} - \beta_b^2 \left(1 - \frac{\beta_b^2}{2}\right) \quad \text{(see Section 5.2)} \qquad (5.6)$$

The incompressible flow coefficient for plenum flow (f_{i_p}) was expressed by Jobson (see Section 5.2) as

$$f_{i_p} = \frac{1}{C_i} - \frac{1}{2C_i^2} \qquad (5.7)$$

By definition, the force defect (F_i) is expressed as,

$$F_i = \int_{A_2}^{A_1} (P_1 - P_w)\, d\, A_w$$

where

P_1 = Static upstream pressure

P_w = Static pressure at the wall

$d\, A_w$ = Element area of the wall

Neglecting frictional effects upstream of the orifice, the total inlet pressure (P_o) is retained;

$$P_o = P_1 + \frac{\rho u_1^2}{2g} = P_w + \frac{\rho u_w^2}{2g}$$

where

ρ = flow density

$$F_i = \oint \frac{\rho}{2g} (u_w^2 - v_1^2)\, d\, A_w$$

In the particular case of circular boundaries

$$F_i = 2 \int_o^{\pi} \int_{R_2}^{R_3} \frac{\rho}{2g} (u_w^2 - u_1^2)\, R\ dR\, d\theta \qquad (5.8)$$

$\oint$ = Integral over the wall surface

In equation (5.8) R_3 defines the external boundary of the orifice wall with respect to the orifice centre. From the geometry in Fig. (5.3);

$$R_3 = \sqrt{\left(\frac{R_1}{2}\right)^2 - (S.\sin\theta)^2} - S.\cos\theta \qquad (5.9)$$

by definition

$$F_i = f_i \left(\frac{m^{\cdot 2}}{\rho g\, A_2}\right) \qquad (5.10)$$

Combining equations (5.5), (5.8) and (5.10)

$$f_i = K^2/A_2 \int_o^{\pi} \int_{R_2}^{R_3} f^2 (R,\theta)\ R\ dR\ d\theta$$

$$+ \frac{2K}{A_2} \cdot \frac{A_2}{A_1} \int_0^{\pi} \int_{R_2}^{R_3} f\,(R,\theta)\; R\; dR \quad d\theta$$

and since

$$\frac{A_1}{A_2} = \beta^2$$

and $$A_2 = \pi\, R_2\, R_2$$

hence putting

$$\eta = d\theta/\pi$$

$$\bar{R} = R/R_2$$

$$d\bar{R} = dR/R_2$$

$$\bar{R_3} = R_3/R_2$$

The above equation reduces to

$$K^2 \int_0^1 \int_1^{\bar{R}_3} f^2\,(\bar{R},\eta)\; \bar{R}\; d\bar{R}\; d\eta + \frac{2K}{\beta^2} \int_0^1 \int_1^{\bar{R}_3} f\,(\bar{R},\eta)\; \bar{R}\; d\bar{R}\; d\eta - f_i = 0 \quad (5.11)$$

where

$$f(\bar{R},\eta) = 1.0 - \left(1.0 - \left(\frac{\bar{R}_1 - \bar{R}}{\bar{R}_1 - 1.0}\right)^2\right)^{\frac{1}{2}}$$

and

$$\bar{R_3} = \sqrt{\beta^2 - \left(\frac{S}{R_2}\sin\theta\right)^2} - \frac{S}{R_2}\cos\theta$$

Equation (5.11) is a second order algebraic equation in (K) having two solutions, of which only the positive solution is considered. The solution would provide a value for (K) for any value of (f_i).

Compressible Flows

For compressible flow, the force defect (F_d) can be expressed as,

$$F_d = \oint (P_1 - P_w)\; d\,A_w$$

$$= P_o \oint (r_1 - r_w)\; d\,A_w$$

where r_1 = static-to-total pressure ratio at inlet (P_1/P_o)

r_w = Static-to-total current pressure ratio at the wall $(P_w - P_o)$

Following the same dimensionless integration as before;

$$F = 2\, P_o \,.\, A_2 \int_0^1 \int_1^{\bar{R}_3} (r_1 - r_w)\, \bar{R}\, d\bar{R}\, d\eta \tag{5.12}$$

$$= 2\, P_o \,.\, A_2 \,.\, I \tag{5.13}$$

The velocity at the wall (u_w) can be related to the pressure ratio (r_w) as follows

$$u_w^2 = 2g\, \frac{P_o}{\rho_o}\, \frac{\gamma}{\gamma-1}\, (1 - r_w^{\frac{\gamma}{\gamma-1}})$$

$$r_w = \left[1 - \frac{(\gamma-1)}{2\gamma g}\, \frac{\rho_o}{P_o}\, u_w^2 \right]^{\frac{\gamma}{\gamma-1}}$$

from (5.5),

$$r_w = \left[1 - \frac{\gamma-1}{2\gamma g}\, \frac{\rho_o}{P_o}\, (a\,(1-v) + u_1)^2 \right]^{\frac{\gamma}{\gamma-1}}$$

$$= \left[1 - \frac{\gamma-1}{2\gamma g}\, \frac{\rho_o}{P_o} \,.\, \frac{K^2 \dot{m}^2}{\rho_1^2 A_2^2} \left((1-v) + \frac{u_1}{a} \right)^2 \right]^{\gamma-1}$$

and since

$$\frac{u_1}{a} = \frac{u_1\, \rho_1\, A_2}{K\dot{m}} = \frac{u_1\, \rho_1\, A_1}{\dot{m}\, K\, \beta^2} = \frac{1}{K\, \beta^2}$$

and

$$\frac{\gamma-1}{2\gamma g}\, \frac{\rho_o}{P_o}\, \frac{K^2\, \dot{m}^2}{\rho_1^2\, A_2^2} = \frac{\gamma-1}{2\gamma g}\, \frac{\rho_o}{P_o}\, \frac{K^2}{\rho_1^2\, A_2}\, (\rho_1\, u_1\, A_1)^2$$

$$= K^2\, \beta^4\, (1 - r_1^{\frac{\gamma-1}{\gamma}})$$

hence

$$r_w = \left[1 - K^2\, \beta^4 \left((1-v)^2 + \frac{2}{K\beta^2} (1-v) + \left(\frac{1}{K\beta^2}\right)^2 \right] \right]^{\gamma-1} \tag{5.14}$$

Combining equation (5.10), (5.13) and (5.14)

$$f = 2 P_o \frac{\rho_1 g A_2}{\dot{m}^2} A_2 \; I$$

$$= \frac{2 P_o \rho_1 g A_2^2}{2g \frac{P_o}{\rho_o} \frac{\gamma}{\gamma-1} (1-r_1 \frac{\gamma-1}{\gamma}) A_1^2 \rho_1^2} \; I$$

$$f = \frac{\gamma-1}{\gamma} \frac{1}{\beta^4} \frac{1}{(1-r_1 \frac{\gamma-1}{\gamma})} \frac{1}{\frac{1}{r_1 \gamma}} \; I \qquad (5.15)$$

Equation (5.15) gives the compressible force defect coefficient (f) as a function of the inlet pressure ratio (r_1) which is obtained from (applying continuity),

$$r_1 \frac{2}{\gamma} (1-r_1 \frac{\gamma-1}{\gamma}) = \frac{C_c^2}{\beta^4} r \frac{2}{\gamma} (1-r \frac{\gamma-1}{\gamma}) \qquad (5.16)$$

where r = Pressure ration (static to total)

Once the value of (f) is obtained the contraction coefficient can be calculated from the equations obtained by Benedict (15,17).

$$C_c = \frac{1-(1-2 Z X)^{\frac{1}{2}}}{2 r_s \frac{1}{\gamma} \cdot X} \qquad (5.17)$$

where

$$X = f + \frac{1}{\beta^2} - \frac{Z}{2\beta^4}$$

$$Z = \frac{(1-r_b)(\gamma-1)}{\gamma(1-r_s \frac{\gamma-1}{\gamma})}$$

where

r_s = static-static, orifice pressure ratio

$r_b = P_b/P_1$

When the flow through the orifice is subsonic, (r_b) equals (r_s). For the supersonic flow however ($r_b \neq r_s$).

r_c = Critical pressure ratio

$$= (\frac{2}{\gamma+1})^{\frac{\gamma}{\gamma-1}}$$

$$r^* = r_c/r_1$$

and

$$C_c = \frac{\left[Y - \left(Y - \frac{4\left(f+\frac{1}{\beta^2}\right)\left(1-r_b\right)^{\frac{1}{2}}}{Y\, r^{*\frac{Y-1}{Y}}}\right)\right]}{2\, r^{*\frac{1}{Y}}\left(f+\frac{1}{\beta^2}\right)} \qquad (5.18)$$

where

$$Y = 1 + \frac{(r^* - r_b)}{r^*}$$

For any geometry the calculation procedure is as follows:

1. Knowing (C_i), f_{i_p} is calculated from (5.7).
2. f_i is then obtained from (5.6).
3. Equation (5.11) is then solved to obtain (K).
4. Guess a value of C_c.
5. From equation (5.16) deduce a value of (r_1).
6. Integrating over the wall using (5.14) and (5.15) a value of (f) is obtained.
7. Calculate a value for (C_c) using (5.17) or (5.18).
8. Iterate between steps 4 and 7 until (C_c) is obtained within the required accuracy (0.05%).

All surface integrals were evaluated numerically.

The wall surface is divided into small incremental values of radius and angle. The angular increment being 1.0 degree, the radial increment being a function of the β ratio. A computer program was developed to calculate the values of the integrals and iterate for the contraction coefficient values.

The input to the program consisted of r, γ, C_i, β and (S/R_2) and the output of C_c, f, K and r_1.

The present calculation procedure was checked against the experimental results of Benedict (17). Different cases were considered, different (β) ratios and different C_i values for similar (β) ratios. Fig. (5.4) shows

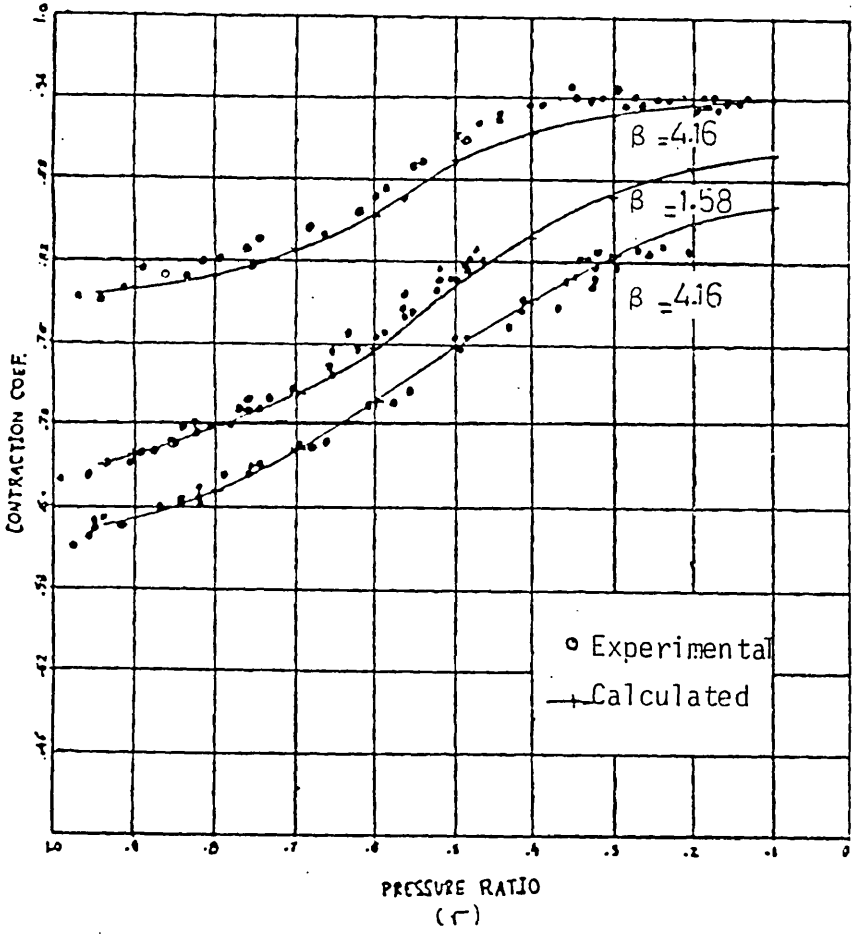

Fig. (5.4) Contraction Coefficient for Beta Flows

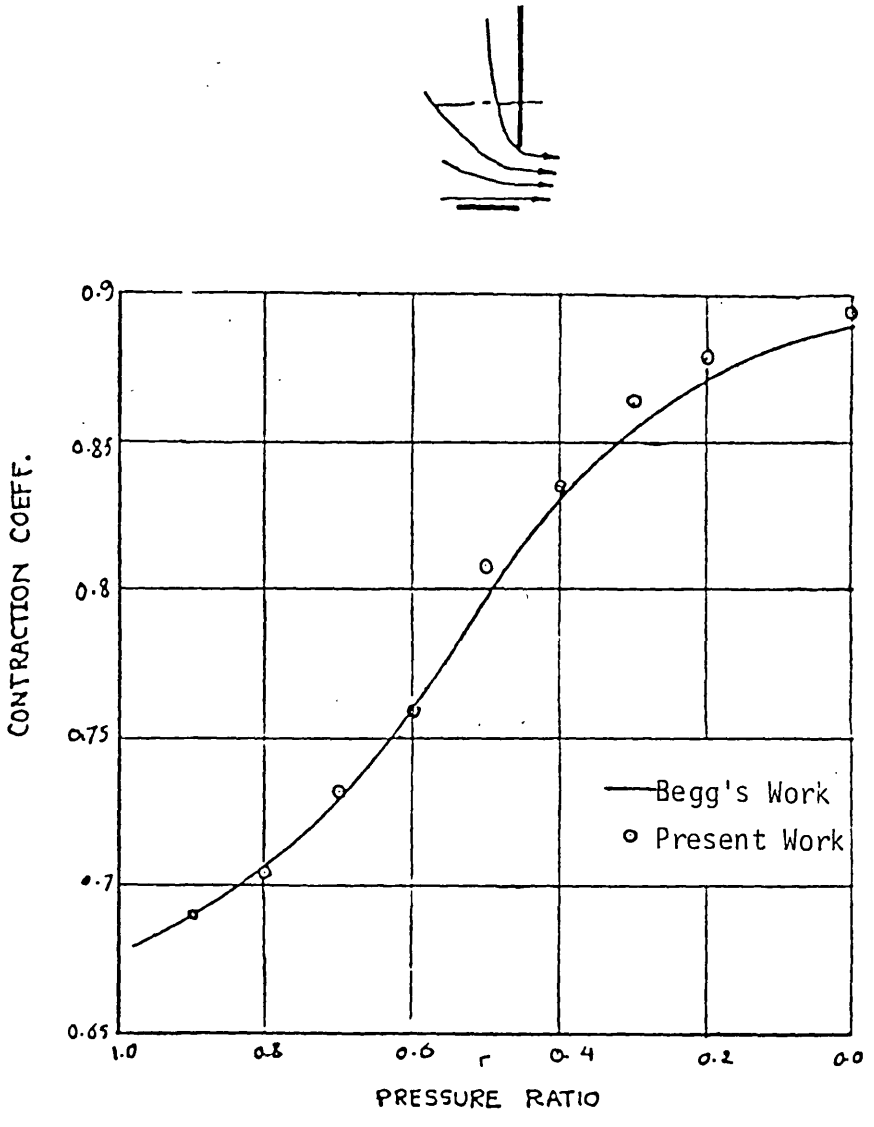

Fig. (5.5) Contraction Coefficient for an Asymmetric Orifice

the comparison between the calculated and experimental values of orifice contraction coefficient for a range of pressure ratios, indicating good agreement.

The calculation procedure was also applied for asymmetric orifice flow. Fig. (5.5) shows a comparison between calculated contraction coefficient values and those obtained by Begg (13). Good agreement is also seen in this case.

All methods discussed here for calculating the contraction coefficient of an orifice are not self starting. They all require a starting value for the incompressible flow contraction coefficient (C_i), from which the compressible behaviour of the orifice can then be predicted. Alternatively, if a value of C_c for a compressible flow is known at a certain pressure ratio, values at other pressure ratios can be readily calculated.

5.3.2 Thick Orifice

In the previous section sharp edge orifice flow was considered. This does not, however, explain the behaviour of an orifice which has a significant thickness compared to its diameter. This type of orifice is generally known as a tube or thick orifice.

Deckker and Chang (29) investigated the steady compressible flow through thick orifices. They considered orifices at different (Length/Diameter) L/D ratios, and the limiting case of a sharp edge orifice. They concluded that, for a given L/D ratio, the flow discharge coefficient (C_d) was only a function of the overall pressure ratio. They also reported that the L/D ratio was an important parameter in thick orifices because of the possibility of jet reattachment to the orifice wall, along its length.

Fig. (5.6) is an example of Deckker's results. Existence of hysteresis in the flow was detected when (L/D = 0.5), near the region of critical pressure ratio. Lightarowicz and his co-workers (18) suspected the occurence

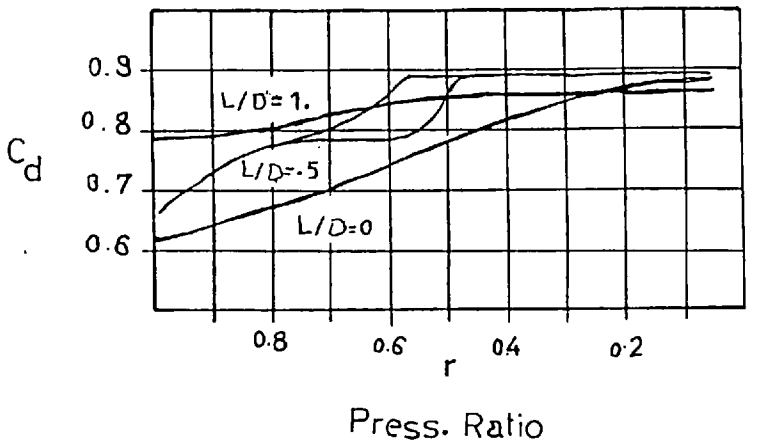

Fig. (5.6) Effect of Orifice (L/D) Ratio on Discharge Coefficient

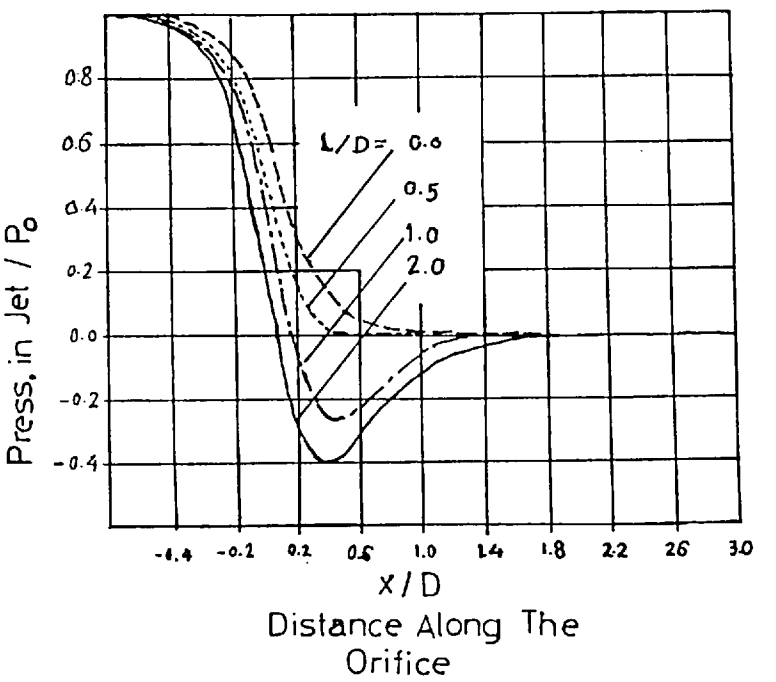

Fig. (5.7) Pressure Distribution Along Orifice Axis

of hysteresis effects in incompressible flow through orifices of L/D ratios between 0.5 and 1.5, although there does not appear to be strong evidence of such a disturbance in their experimental results.

Deckker, suggested that hysteresis effects would not occur in compressible flows through orifices other than those when L/D = 0.5. He explained this behaviour as arising from attachment or detachment of the flow jet, to or from the orifice wall. At L/D ratios higher than (0.5) a significant difference is observed between the discharge coefficient for a thick orifice and that of a sharp edged orifice at the same diameter and at the same pressure ratio.

Fig. (5.7) shows the pressure distribution along the axis of the orifice, as obtained by Deckker and Chang, for different L/D ratios. In the case of L/D> 0.5, the pressure within the orifice length is lower than the back pressure. This shows that there is some pressure recovery from the position of minimum pressure within the orifice length to its exit.

Based on the above mentioned behaviour of thick orifices, the flow field through such an orifice was expected to have the form sketched in Fig. (5.8). The sketch shows that the flow field could be divided into the following sections, and investigated accordingly.

a) From station 1 to 2 the flow could be examined and treated as flow through a sharp edge orifice of the same geometry. Indeed the static pressure at position 2 (which is the vena contracta position) is not equal to the back pressure of the orifice, and the pressure ratio between 1 and 2 is not the same as the pressure ratio across the thick orifice.

b) From 2 to 3, the flow diffuses from the vena contracta position until it attaches at the wall of the orifice at 3. Due to this diffusion effect, the flow velocity drops and static pressure increases. If the length of the orifice is too short for the flow to reattach to the wall, then no pressure recovery will be achieved.

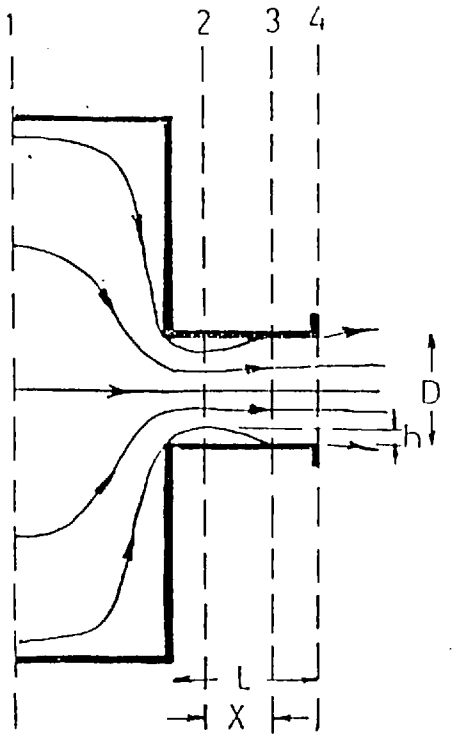

Fig. (5.8) Thick Orifice Flow

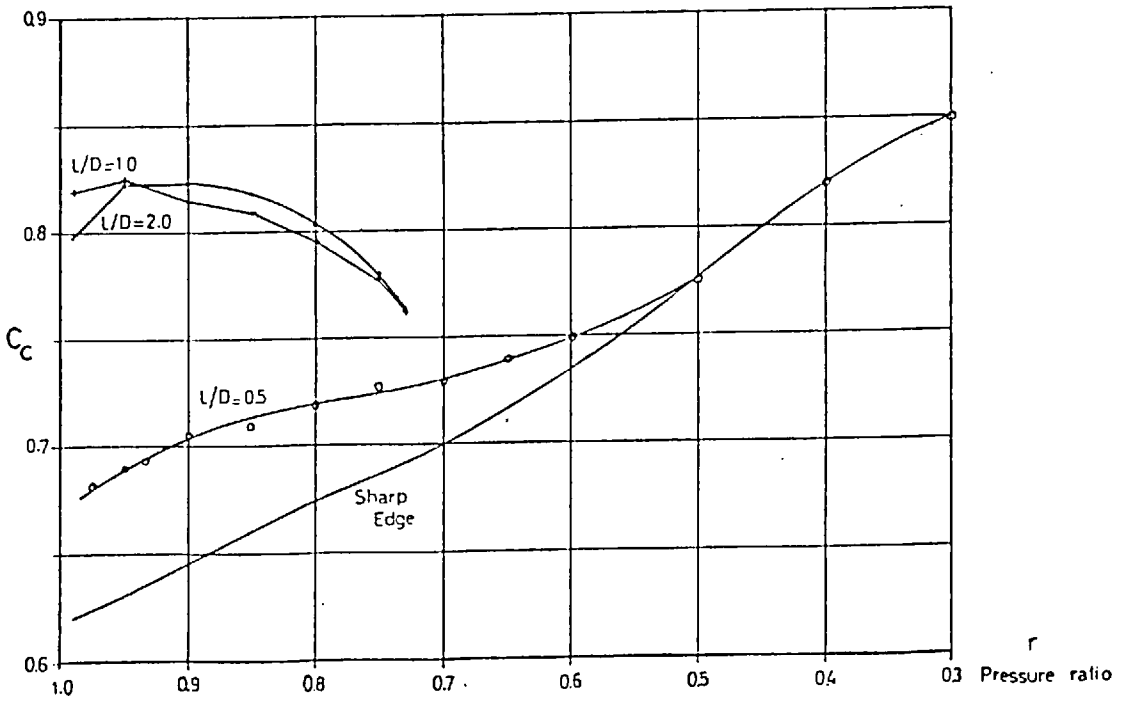

Fig. (5.9) Calculated Contraction Coefficient for Different Orifice Types

c) From 3 to 4 the orifice flow is full, and a pipe flow relationship for pressure drop due to friction can be applied, if friction is significant.

At any pressure ratio across a thick orifice, the flow through it is governed by the area of the vena contracta, as it represents the minimum flow area. Following the above approach, the high discharge coefficient of such orifices can be readily explained. Due to pressure recovery from 2 to 3, the flow pressure ratio at the vena contracta is less than the overall pressure ratio. Considering the flow through a sharp edge orifice at this new pressure ratio, its contraction coefficient (and hence discharge coefficient) will be higher than that expected under the overall pressure ratio. Following the same principle, the critical pressure ratio will be reached at the vena contracta well before the overall pressure ratio indicates choked condition, and as the pressure of the vena contracta cannot exceed the critical value, no change in the flow coefficient of discharge would be expected by further reducing the back pressure.

To investigate the validity of this theory, a mathematical formulation of the problem was attempted. The flow between 1 and 2 was treated as that of a sharp edged orifice, as explained earlier. Zone 2 to 3 was considered as a sudden enlargement of the flow. The position of the vena contracta was required for the flow reattachment calculation. Examination of the literature (40,99) relating to flow through orifices, revealed that the position of the vena contracta regresses towards the orifice as the orifice back pressure drops. It was not possible, however, to quantify this behaviour. The position of the vena contracta was therefore taken to be constant at 0.3 of the orifice diameter.

The flow in abrupt englargement and contractions was studied by Benedict (16). His relationship, which expresses the ratio between static pressures across an abrupt flow enlargement for incompressible flow, as a function of geometry and pressure ratio, was adopted here;

$$P_3/P_2 = 1 + \left(\frac{1-r_2}{r_2}\right)(1-2\phi^2 + \phi^4) \qquad (5.19)$$

where

P_2 and P_3 = static pressures at 2 and 3

r_2 = P_2/P_1

P_1 = Total inlet pressure

ϕ = D_v/D

D_v = Vena contracta diameter

$$\frac{P_3}{P_2} = \frac{P_3}{P_1} \cdot \frac{P_1}{P_2} = \frac{P_3}{P_1} \quad \frac{1}{r_2}$$

from (5.19), hence

$$P_3/P_1 = r_2\,(1-2\,(\phi^2 - \phi^4)) + 2(\phi^2 - \phi^4) \qquad (5.20)$$

The friction effect on the fluid between section 3 and 4 was neglected; hence

$$P_3 = P_4 \text{ and } \frac{P_3}{P_1} = \frac{P_4}{P_1}$$

As a result, equation (5.20) gives the overall pressure ratio of the orifice. Examining equation (5.20), it is clear that (P_3/P_1) is always greater than (r_2), which is essentially the reason for high discharge coefficients for thick orifices.

Examining the work of Abbot (1) and Moon (74) concerning the jet reattachment for a step enlargement, it was concluded that the reattachment length (X) could be taken as a ratio of the step height (h);

$$X/h = 6.0 \qquad (5.21)$$

Knowing the position of the vena contracta (estimated at 0.3D), and the total orifice thickness (L), it is possible to establish whether the flow reattaches at the wall within the orifice. If (L) is short, little

or no pressure recovery will be obtained. The above equations, (5.20) and (5.21) were included in a computer program which iterated to calculate flow discharge coefficients of thick orifices of different L/D ratios. The results are shown in Fig. (5.9).

It is quite apparent that the predicted change of C_d with changing L/D ratio, follows the expected trend. The behaviour of a thick orifice of (L/D >1.0) with changing pressure ratio is different from that measured by Deckker (19), It is believed that the assumptions made regarding the position of the vena contracta together with use of an incompressible flow equation (5.20), in a compressible flow situation, are the main sources for these differences. Further refinement for the analysis of the flow is believed to be possible, but not essential for this work. The main objective behind the investigation was to achieve a basic understanding of the flow within thick orifices, in order to explain their behaviour and to enable a realistic discharge coefficient to be obtained in the absence of test data. It is believed that these objectives have been achieved.

5.3.3 Conclusions

In the above two sections the flow discharge coefficients of sharp edged and thick orifices were considered. Due to flow acceleration near the wall of the orifice plate, a force is introduced which aids the flow pressure ratio to give the flow extra momentum. This force, the force defect, is the main reason why the contraction coefficient of a sharp edged orifice increases with decreasing orifice back pressure. The approach velocity of the flow is a very important factor in determining the orifice flow coefficient. A thick orifice has a high discharge coefficient compared to a similar sharp edged orifice under the same pressure ratio, due to the existance of a low pressure region within the orifice at the vena contracta.

In the present work, the passage considered is inclined as shown in Fig. (5.2). Although it seems to belong to the long orifice group, proper

consideration of the effective passage length, measured perpendicular to the flow direction, and effective passage diameter, provided a better judgement. The passage has an effective L/D ratio of approximately 0.0, which implies that it could be considered as a sharp edged orifice. The inclination of the passage was expected to affect the flow pattern through the passage and thus the passage discharge coefficient. Mathematical modelling of such a flow field is complex and attempts to simplify it failed. It was, therefore, opted to experimentally investigate the passage flow and determine its discharge coefficient behaviour. This is explained in the following sections.

5.4 EXPERIMENTAL INVESTIGATION

In the following section an experimental investigation is described, involving the passage from the engine under test. The aim of the study was to find the discharge coefficient of the passage, at different pressure ratios, for flow to and from the prechamber. The effect of piston position upstream of the passage on the discharge coefficient was also examined. The passage was tested under steady flow conditions. An examination of the work published by Trengrouse (106), concerned with the effect of flow transients on the C_d values for sharp edged orifices, led to the conclusion that, for the pressure ratios encountered in the passage flows, the effect of flow transients could be neglected.

5.4.1 Test Rig

Fig. (5.10) shows an outline of the test rig developed for flow testing of the passage. Static pressure upstream of the passage was measured by a pitot tube which had two radial holes. In some test conditions, this tube was also used to measure downstream static pressure. A standard sharp edged orifice with (D) and (D/2) tapings was used to measure actual flow through the passage. The orifice plate was mounted three meters downstream of the passage holder to avoid interaction (according to the British Standards

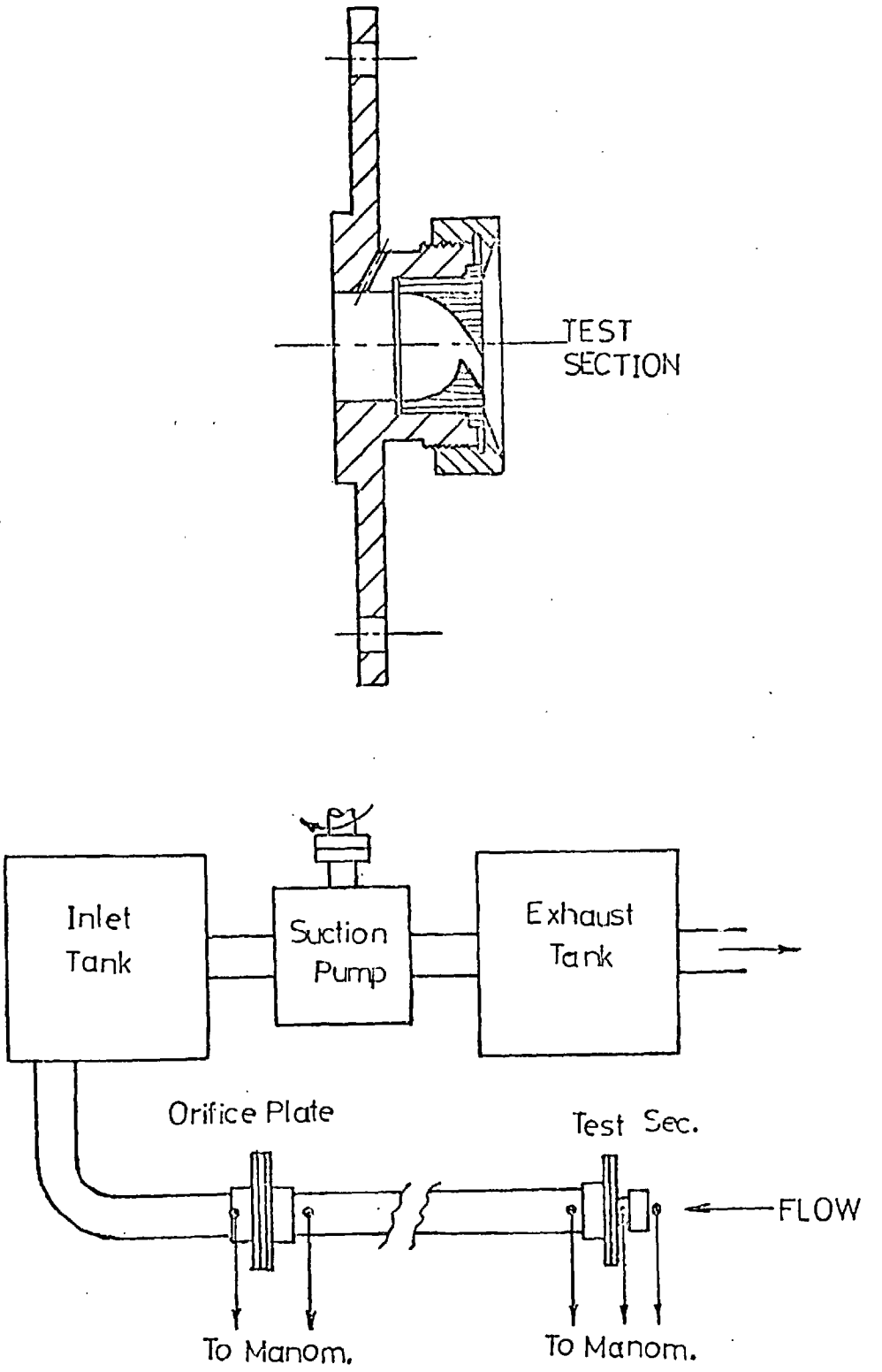

Fig. (5.10) Test Arrangement for Flow Measurements

B.S. 1042. ref.26). A suction pump, driven by a variable speed electric motor, was used to create the required flow through the test section. Water or mercury manometers were used for pressure measurement depending on the range of pressure. Ambient conditions were measured for every test condition.

The theoretical flow rate through the passage was calculated from the static pressure ratio (r) across it, and its geometric area (A_p).

$$\dot{m}_{th} = A_p \cdot \sqrt{\frac{2\gamma g}{\gamma-1} P \rho \, r^{2/\gamma} (1 - r^{\frac{\gamma-1}{\gamma}})}$$

where P & ρ = Upstream pressure and density

The actual flow ($\dot{m}$) was calculated using the British Standard (B.S. 1042), knowing the orifice plate geometric area, inlet pressure and pressure ratio. The passage coefficient of discharge was then calculated from,

$$C_d = \dot{m}/\dot{m}_{th}$$

All geometric flow areas were accurately obtained by optical methods.

5.4.2 Test Conditions and Results

The passage was tested in both flow directions; to and from the pre-chamber. Pressure upstream of the passage was measured at a position very close to its inlet. A decision had to be made regarding the point of pressure measurement downstream of the passage. Different positions were tried, and the results are shown in Fig. (5.11), for flow to the prechamber. For position 1, the total downstream pressure is measured, for position 3 the static pressure at exit is considered, while for position 2 static pressure away from the issuing jet is measured. A recirculation zone is expected to be present near position 2 and, due to an evacuation effect, it is expected that the pressure drop will overestimate the actual value, this position was

discarded as unsuitable. Position 3 is probably the ideal measuring point for static downstream pressure, provided that it coincides with the vena-contracta position. However, due to difficulties in defining the vena-contracta position, position 3 was also considered unsuitable. Although the pressure values measured at 1 are expected to be close to the total downstream pressures, because of dynamic pressure effects, differences between C_d values in Fig. (5.11) for cases 1 and 3 are small ($\approx$1.0%). Position 1 has an added advantage in that, it is very close to the position of the prechamber pressure transducer.

As a result of the above discussion, position 1 was chosen to be the representative downstream measuring point, for all test conditions. The discussion also provided an explanation for the differences in C_d values obtained for every measuring point condition. Fig. (5.11) shows that the variation of C_d with pressure ratio follows a specific trend irrespective of the downstream measuring position. The figure also shows C_d values for passage flow from the prechamber (case 4). These, again, follow the same trend with pressure values but show higher values than flow to the prechamber (case 1). This is expected to be due to approach velocity effects in case 4, as was found for sharp edged orifice flow, earlier in this chapter.

The effect of upstream approach velocity on the C_d values of the passage was acknowledged. The position of the piston was, therefore, expected to influnece the flow upstream of the passage in the case of flow to the pre-chamber. When the piston becomes close to the cylinder head, the effective flow area upstream of the passage is very much reduced, with the result that the approach velocity effect becomes more pronounced. Also close piston proximity to the cylinder head, provides better flow guidance towards the "inclined" passage.

To investigate the above experimentally, the piston position was simulated by a plate fixed upstream of the passage, as shown in Fig. (5.12). The

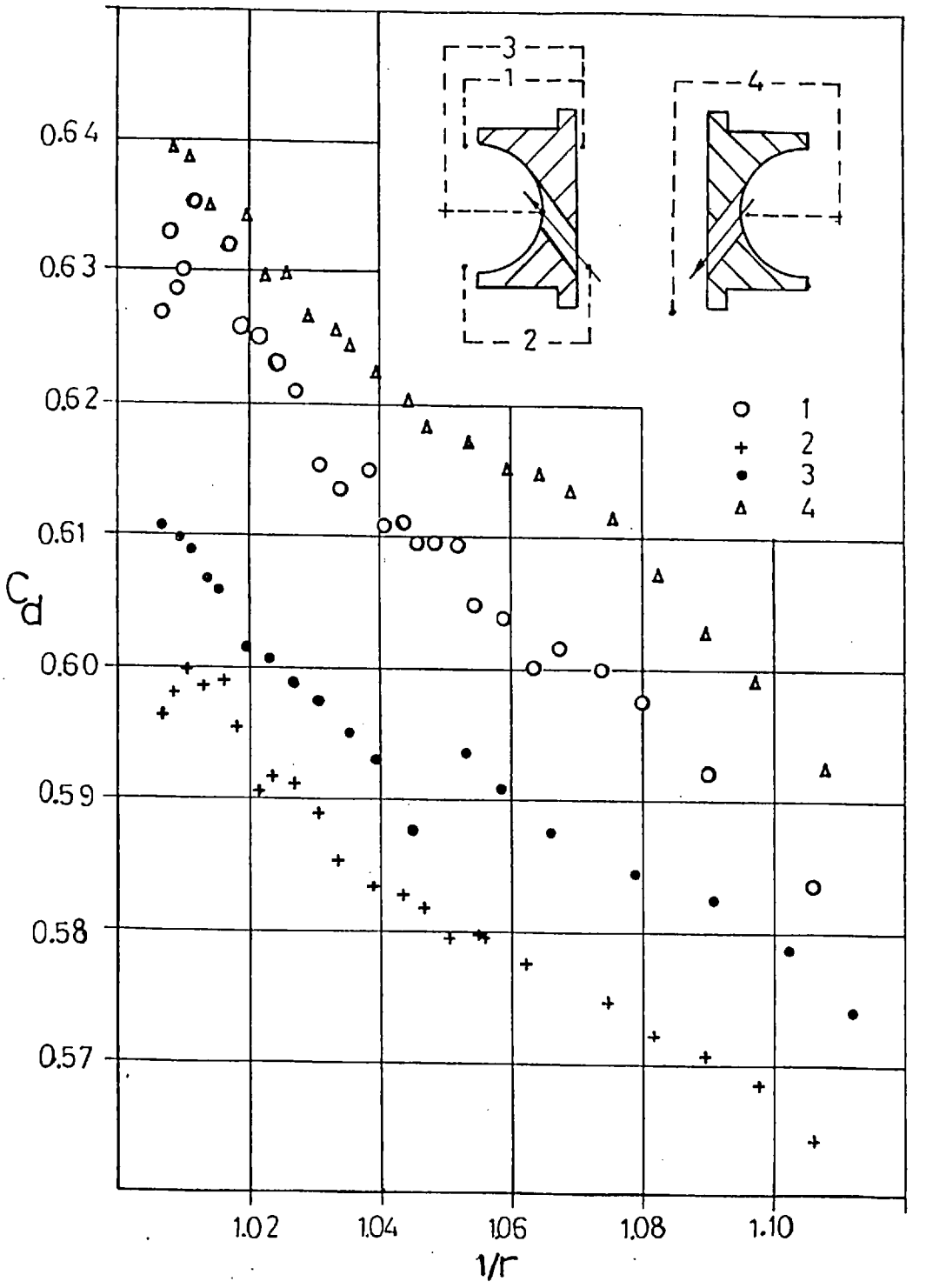

Fig. (5.11) Discharge Coefficients for Different Flow Directions and Sampling Points

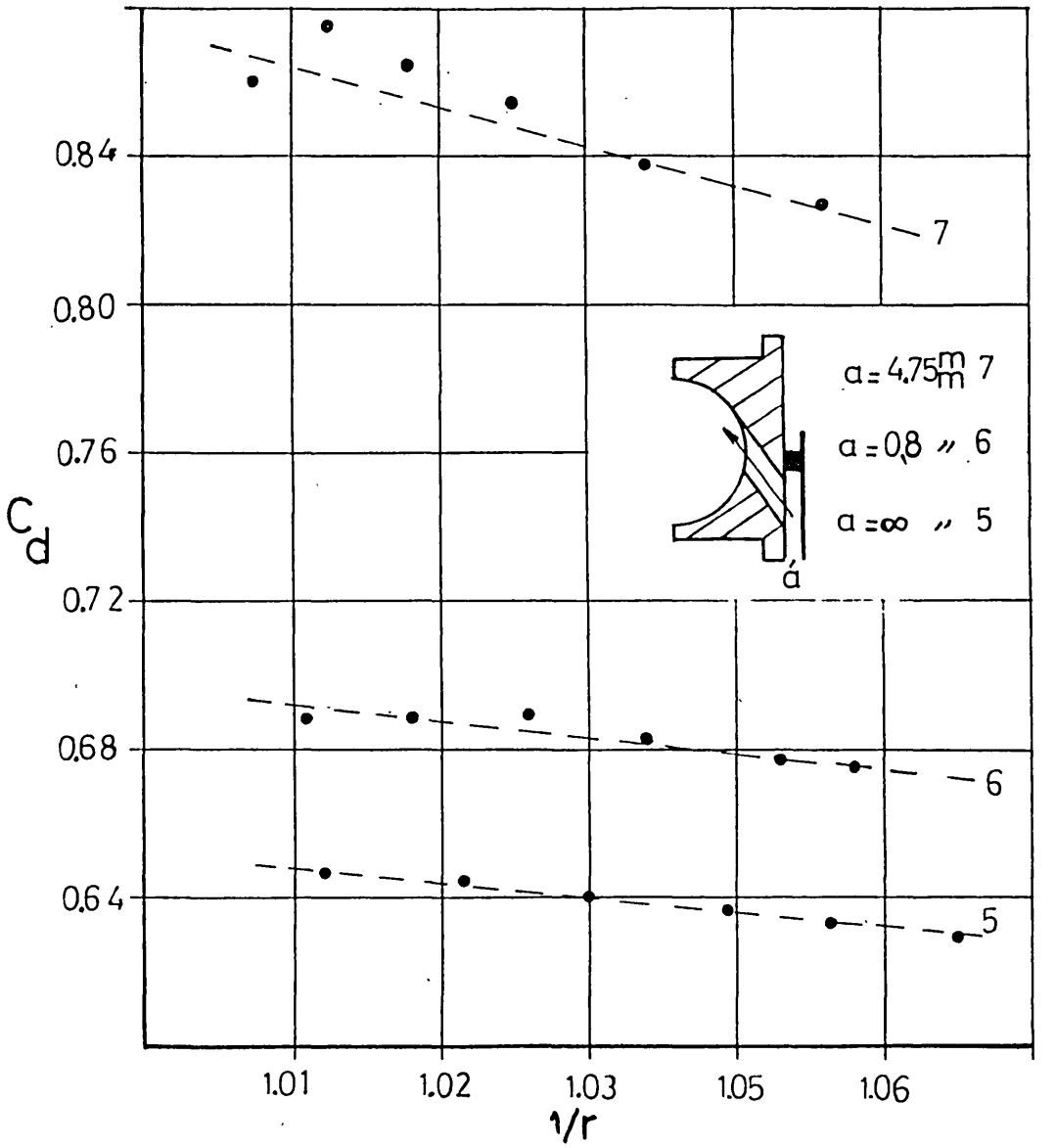

Fig. (5.12) Effect of Simulated Piston Position on Discharge Coefficient

distance between the plate and the passage inlet was varied, and the C_d variation with pressure ratio for every configuration obtained. The obtained results are shown in Fig. (5.12). C_d variation with pressure ratio followed the same trend, but the C_d values increased readily with decreasing the distance (a). This supports the argument mentioned above.

The decrease of C_d values with decreasing the flow back pressure, is expected to be due to the inclination of the passage. Theoretical attempts to study the effect of inclination angle of the passage on C_d value failed. The jet issuing angle from an asymmetric orifice was found by Begg (13) to vary with the flow pressure ratio. Further work is needed in this particular area.

Straight line relationships were fitted to the measured C_d values for flow cases 1 and 4. These were used in the mathematical simulation program, with allowance for C_d variation with piston proximity.

5.5 CONCLUSIONS

In this chapter the flow through orifices of different geometry has been considered. Sharp edged and thick orifice investigations provided a detailed understanding of the flow in either type. They also provided explanations for different C_d values reported by different researchers, involved in IDI engines research, for the connecting passage.

The importance of L/D ratio, passage inclination, approach velocity and piston proximity have been outlined.

CHAPTER 6

IGNITION DELAY

6.1 INTRODUCTION

When fuel is injected at high pressures through a small nozzle into the hot air of the combustion chamber, a spray of fine droplets is formed. It is now established that these droplets do not ignite immediately, even though the air temperature is above the ignition temperature of the fuel. The time that elapses between the moment of fuel injection and that of ignition, is defined as the ignition delay period.

Ignition delay varies with engine speed, load and timing, from which it is apparent that the position of the ignition point in the cycle cannot be kept constant under the whole range of engine operating conditions. Consequently, optimum burning conditions can only be achieved for part of the operating range of the engine. Variation in the length of the ignition delay period may lead to deviation from optimal conditions, and hence a loss in thermal efficiency.

Ignition delay is established to be an essential parameter governing the combustion mode and,performance of diesel engines, particularly at high speed. A thorough understanding of the processes that cause ignition delay, and how it varies with engine running conditions, is very important for close control of the combustion process, and therefore, of the overall performance and pollutants emission of an engine.

Recently, more widespread use of engine cycle simulation computer programs to assist engine design and development has emphasised the need for mathematical representation of the physical and chemical phenomena encountered within the engine cycle. Engine combustion studies, together with engine rate of heat release investigations, require accurate and reliable data concerning ignition

delay period. Although the effect of the length of the ignition delay period on the whole mode of combustion has been stressed it is a difficult characteristic to measure accurately. In the special case of high compression ratio, high speed diesel engines, the ignition delay period is very short. This requires very accurate measurement of the delay period, particularly when attempting to detect variation with engine running conditions.

In the present investigation the ignition delay period was measured for a high compression, swirl prechamber diesel engine, to an accuracy of within $\pm \frac{1}{8}$th of a crank angle degree at all speeds. The experimental results were correlated considering both the physical and chemical parts of the delay period.

6.2 DEFINITIONS OF IGNITION DELAY

Definition of the beginning of injection point and the moment of ignition, is required for the measurement, or theoretical treatment, of ignition delay. Such definitions usually relate to the type of measurements involved and the theoretical basis for the investigation .

The injection point has been defined as

1. The moment when the fuel enters the combustion space.
2. The moment at which the first pressure wave from the fuel pump arrives at a pressure transducer placed in the fuel line near the injector.
3. The moment when the injector needle starts to rise.
4. The intersection of the tangent to the rising portion of an injector needle diagram with the zero lift line.

The first definition has been used with particular reference to optical observations. The second definition would always result in high ignition delay values, which are functions of the position of the transducer. The third definition has the drawback of difficulty of identification of the rise point. The fourth definition is the one most commonly used, and the one used in this investigation as it allows accurate determination of the beginning of

injection.

Some different definitions that have been used for the ignition point are:

1. The moment when the reacting system attains a certain temperature.
2. The moment when the first visible flame is observed.
3. The moment when the pressure decrease caused by the cooling effect of injected fuel has just been recovered.
4. The moment when the first deviation (+ve) from the pressure rise due to compression is detected.

The first definition has been used in theoretical studies in particular. From the practical point of view the whole concept of temperature is not meaningful in fast combustion reactions, since this temperature depends on the order of reaction encountered.

Furthermore, combustion temperature changes are very rapid and difficult to measure accurately. The second definition has the disadvantage that the reaction could begin considerably before the first visible flame bursts out. The third definition, involves considerable measuring difficulties, as it requires pressure recordings, under the same condition, of both air and inert gas. This requires special test arrangements, which is difficult to achieve due to changes in chamber charge and wall temperatures. The fourth definition is the one commonly used. It is quite practical since it is the pressure rise which is significant from the point of view of the purpose of combustion. This definition has been used in the present investigation.

In a diesel engine the point in space in the combustion chamber where ignition occurs is unknown. Ignition could be initiated anywhere, provided the conditions are favourable. This means that if one pressure transducer is used to monitor the cylinder pressure, and hence the ignition point in time, the ignition moment would be in error depending on how far the pressure transducer was from the position where ignition occurred. The error would be

due to the time taken for the first ignition pressure wave to reach the transducer, which means that the maximum unavoidable error due to using one transducer increases with increasing the chamber dimensions. In the present work the usage of a single pressure transducer was justified since the engine under investigation had a spherical swirl chamber of 0.03m diameter, and the error introduced by pressure wave effect was expected to be very small.

Different combinations of the definitions of the injection and ignition points result in different definitions of ignition delay. In the present study, the following definition of ignition delay is used as a basis for the measurement:-

> "The ignition delay is the time which elapses from the moment when the injector needle starts to rise to the moment when the first deviation from the pressure rise due to compression is detected".

6.3 REVIEW OF IGNITION DELAY CORRELATIONS

6.3.1 Ignition Theories and Foundations of Reaction Kinetics

As the fuel jet enters the combustion chamber of an engine it disintegrates into a spray of droplets. Due to the drag between the droplets and the air, the droplets undergo further disruption. Air drag also slows down the spray droplets at the jet tip. Hence it follows that there is less drag on the droplets which are moving in the spray core following the spray tip and, as a result, they remain large in size and penetrate further. Consequently a large number of droplets accumulate in the spray tip, these droplets being larger than average in size. This picture has been verified by both experimental and theoretical investigations of spray penetration and vapourization (46,65,110). The mixture strength is over-rich in the spray core and the droplets are very near each other. Hence, the fuel vapour content

of the air there attains saturation point, which means that vapourization is much slower than the spray edges where the droplets are exposed to the surrounding mass of hot air. As a result, the droplets at the spray edge are vapourized more rapidly and the concentration boundary layers of the neighbouring droplets do not influence its vapourization. For these reasons, the conditions for ignition are more favourable near the spray edge than in the core. This conclusion is supported by experimental observations (4,36, 38,65), which also show that ignition can occur near the chamber wall.

It is well established that the ignition process of a fuel spray takes place in the following order:

1. Injection
2. Disintegration
3. Vapourization
4. Mixing
5. Pre-flame reaction
6. Ignition

In an actual engine, it is obvious that all these processes are mutually linked and partly overlap. It is evident that during the heating-up period and vapourization, mixing of air and fuel vapour occurs. Processes 1-4 take place even when the mixture formation does not lead to ignition. Generally, ignition is usually preceeded by a series of chemical reactions known as the pre-flame reactions (which start after process 4). These are non-luminous reactions which essentially heat up the mixture to the ignition temperature of the hot flame. This process is followed by the appearance of a luminous flame which signifies an exothermic reaction at an increasing rate, leading to ignition.

The ignition delay is generally considered to be divided into two parts; Physical Delay, which is the time from injection until the pre-flame reactions start, and Chemical Delay, which is the time from then until ignition occurs.

Two major theories have been employed to describe the process of ignition, the Thermal Theory and the Chain Reaction Theory. According to the Thermal theory of ignition, the heat of the molecular reaction is transferred immediately into the surroundings and induces a rise in temperature. The mixture is ignited if the heat liberated in the reaction is sufficiently in excess of the heat conduction from the reactor vessel.

According to the Chain Reaction theory, however, the energy liberated in a unit reaction is transferred out of the system, to increase the energy of chain carrier or cause chain branching. The system in this case is therefore considered isothermal. The rate of reaction hence depends upon the rate of chain carriers formation, the rate of chain branching and the rate of chain destruction (e.g. at the wall). Explosion occurs when the rate of chain-branching is greater than the rate of chain destruction. Ignition is said to occur when a certain amount of the reaction is completed.

In an engine, the reactions which lead to ignition fall between the two extremes of the thermal and chain reaction theories. During the pre-flame reaction period, the temperature rise is very small and chain carriers continue the reaction. Once the reaction starts to accelerate, the temperature begins to rise, which enables the high energy molecules (chain carriers) to react with each other, thus reducing their number. This means that only the thermal theory can explain how the reaction proceeds at this stage.

Both theories, however, agree in the definition of ignition delay as the chemical delay needed for sufficient acceleration of the chemical reaction.

According to the above discussion, the length of ignition delay period may be arrived at by means of general Reaction Kinetics theories. For a bimolecular, second order reaction between reactants A, B

$$A + B \longrightarrow \text{Products}$$

the reaction rate (w) is expressed as follows

$$w = -\frac{d\,C_A}{dt} = -\frac{d\,C_B}{dt} = K.\,C_A\,.\,C_B \qquad (6.1)$$

where C_A and C_B are the concentrations of (A) and (B) respectively, and (K) is a constant.

After introducing the law of Arrhenius, and a collision frequency expression, the reaction rate equation is transformed into,

$$w = \beta \,.\, p. \,\sqrt{RT} \;.\; e^{-\frac{E_a}{RT}} \tag{6.2}$$

where p, T and R are pressure, temperature and the gas constant respectively (E_a) is the activation energy and (β) is a constant.

Following the assumption that ignition occurs when a certain part of the total reaction is complete;

$$t_d = \frac{a}{w} \tag{6.3}$$

where

a = constant

If the term $\sqrt{RT}$ in equation (6.2) can be neglected, and the term (p) in a general form is raised to a power (n) to account for reactions other than bimolecular reactions (for which n=1.0), the general expression for ignition delay for homogeneous reactants becomes

$$t_d = \frac{A}{p^n} \quad e^{\frac{E_a}{RT}} \tag{6.4}$$

This expression has been derived for homogeneous gas reactnats, which restricts it to include only the chemical part of ignition delay, but it has been used by research workers to correlate the total ignition delay period. Although this is basically incorrect, it could be acceptable if the physical delay was very short relative to the chemical delay.

Equation (6.4) has proved successful in correlating the results of ignition tests made with homogeneous gas mixtures in engines (90,104).

6.3.2 Wolfer's Correlation

The application of ignition delay theories to the diesel engine involves

some simplifications. In a diesel engine, the gas mixture is far from uniform, and the chemical reactions involved are complicated. Consequently, when using equation (6.4) to express the ignition delay period, some modification is required to achieve a useful correlation. The term (E_a) no longer denotes the activation energy of the chemical reaction alone, and the power (n) no longer defines the order of the reaction.

Ilmari (55) showed differences in the "constants" (in equation (6.4)) obtained by different authors.

	Wolfer (116)	Schmidt (90)	Zimmermann (118)
$B = \frac{E_a}{R}\ ^oK$	6330	4650	4650
n	1.08	1.19	1.05
A	6.6×10^{-5}	4.4×10^{-4}	4.0×10^{-4}

Wolfer's formula is expressed as

$$t_d = \frac{A}{p^n} \quad e^{\frac{B}{T}} \qquad (6.5)$$

where

t_d = ignition delay (sec.)

Although there are differences between the values of the constants A, B and n obtained by different investigators, they are of the same order of magnitude. Naturally, variations in the constants are expected for different engines due to the simplified approach of equation (6.4). However, the formula has been proved useful, and is reported to have given good agreement with measured values of ignition delay.

One drawback is the absence of a physical delay term in the formula. It has been established that although temperature, and to a lesser extent pressure, have a large effect on the chemical delay, the effect of both on physical delay is very small (32).

Anisitis (6) tested an indirect injection diesel engine with a compression ratio of 15.42:1, and used a formula of the Wolfer form to correlate ignition

delay values, but did not take a physical delay period into consideration. His final formula was

$$t_d = \frac{1.294}{p^{.35}} e^{\frac{990}{T}}$$

where t_d = Ignition Delay (ms)

P = Chamber Pressure (Bar)

T = Chamber Temperature (K)

6.3.3 Sitkei's Correlation

Sitkei (96) outlined the drawbacks of not accounting for physical ignition delay. He divided the chemical ignition delay into two parts t_1, t_2, and considered (t_1) as the time lag due to the pre-flame period and (t_2) to be the time from the appearance of luminous flame to the ignition point.

$$t_d = t_{ph} + t_{ch}$$

$$= t_{ph} + (t_1 + t_2)$$

The physical delay was taken to be 0.5 ms. The two chemical delays (t_1 and t_2) were assumed to follow the same form as equation (6.5), the constants being derived by fitting experimental results.

$$t_d = 0.5 + \frac{0.1363}{p_1^{0.7}} e^{\frac{7800}{R T_1}} + \frac{4.92}{p_2^{1.8}} e^{\frac{7800}{R T_2}} \qquad (6.6)$$

where

T_1, T_2, p_1 and p_2 denote the properly selected mean values of temperatures (K) and pressures (Bar) during t_1 and t_2 respectively.

Although the formula accounts for the physical delay, no explanation is given regarding the inclusion of the 0.5 ms used. To divide the chemical delay period into two parts in this way is not particularly practical, since the dividing point can only be detected optically and even then, it is far from being accurately defined or detectable.

6.3.4 Tsao's Correlation

Tsao (107) studied the effect of temperature, pressure, injection point and engine speed on ignition delay, deriving the empirical relationship;

$$t_d = \left(\frac{8.483}{P} + 0.415\right) \left\{ \left(\frac{-20.17}{T} + 0.0222\right) N + \left(\frac{26.36 \times 10^3}{T} - 26.66\right) + \left(\frac{T}{555.56} - 1.45\right) \left(\frac{1000-N}{60}\right) \right\} \quad (6.7)$$

where

t_d = Ignition delay, (ms)

T = Temperature at the point of injection K

P = Pressure at the point of injection (Bar)

N = Engine speed (r p m)

Good agreement was claimed with measured ignition delay values, though with seven constants in the equation this is not surprising. The formula has no theoretical background to support its form. It could be concluded that it is an ignition delay correlation for a particular engine.

6.3.5 Ilmari's Correlation

Ilmari (55) discussed in detail the different theories of ignition, and revised the available theoretical treatment for ignition delay calculations. He referred to the results of Gray and Harper (47), which showed that the thermal ignition theory would lead to the following expression for ignition delay if the critical temperature rise for ignition to start is assumed to be

$$\Delta T = \frac{R\,T^2}{E_a}$$

$$t = \bar{A}.\ \left(\frac{R\,T^2}{E_a}\right) e^{\frac{E_a}{RT}} \quad (6.8)$$

where

$\bar{A}$ = constant

Ilmari (9) then introduced a more detailed picture for the reaction rate which takes into account the probability that the total energy of the colliding molecules is equal to the activation energy (E_a). According to Hinhselwood (52) this is expressed by

$$\frac{e^{-\frac{E_a}{RT}} \left(\frac{E_a}{RT}\right)^{\frac{\bar{n}}{2}-1}}{\left(\frac{\bar{n}}{2}-1\right)}$$

where ($\bar{n}$) is the sum of the degrees of freedom, of the colliding molecules. The reaction rate formula, in this case, for a bimolecular second-order reaction, could be written analogous to equation (6.2) in the form,

$$w = P\sqrt{RT}\ \frac{e^{-\frac{E_a}{RT}} \left(\frac{E_a}{RT}\right)^{\frac{\bar{n}}{2}-1}}{\left(\frac{\bar{n}}{2}-1\right)!} \qquad (6.9)$$

In equation (6.8) the reaction rate was assumed to follow the simple Arrhenous expression (constant. $e^{-\frac{E_a}{RT}}$). Replacing this by expression (6.9), the following expression for a general reaction (which need not be of the second order).

$$t_d = \frac{A}{p^n} \left(\frac{RT}{E_a}\right)^m e^{\frac{E_a}{RT}} \qquad (6.10)$$

where $m = \frac{\bar{n}+1}{2}$

A = constant

He outlined an important observation with respect to equation (6.10), that it exhibits a minimum at ($T = \frac{E_a}{m\,R}$). Beyond this temperature, the delay (t) begins to rise again. This is not in accordance with experimental evidence but was brought about by using the expression ($\frac{RT^2}{E_a}$) as the critical temperature rise. This is regarded as a weakness of equation (6.10) which would limit its general validity.

In order to obtain the constants of equation (6.10), it was fitted to experimentally obtained ignition delay values, for a swirl prechamber diesel engine. Evaluation of the constants yielded:

$$t_d = \frac{1.57 \times 10^4}{\sqrt[3]{P}} \left(\frac{T}{10000}\right)^{11} e^{\frac{10000}{T}} \qquad (6.11)$$

where t_d = Ignition delay (sec)

P = Average chamber pressure during delay period (Bar)

T = Average chamber temperature during delay period (K)

The exponent 11 of the temperature term implies that the average number of degrees of freedom of the colliding molecules is (21). According to Ubbelohde (108) this is the correct order of magnitude.

Ilmari introduced what he called the "Spray Impingement Thoery of Ignition Delay" which essentially assumes that for engines where the spray is likely to hit the wall before ignition, the spray disintegrates into a cloud of fine mist on impingement. This fine mist behaves in a similar way to a gas mixture. This means that the total ignition delay may be divided into two parts:

1. Physical ignition delay, t_{ph}, which is the time needed by the spray to travel from the injector to the wall.
2. Chemical Ignition delay, t_{ch}, which is the time from the moment of impingement to ignition.

A more realistic correlation was achieved by introducing the physical delay term. This led to his final correlation:

$$t_d \text{ (sec.)} = t_{ph} + t_{ch}$$

$$= 0.4 \times 10^{-3} + \frac{0.43 \times 10^{10}}{\sqrt[3]{P}} \left(\frac{T}{15000}\right)^{16} \cdot e^{\frac{15000}{T}} \qquad (6.12)$$

Ilmari studied effects of speed, load and inlet pressure on ignition delay. His formula showed good agreement with the experimental results. On average the formula was 6.15% in error for normal engine operation, and 22.1% with a throttled intake.

6.4 IGNITION DELAY MEASUREMENT

One aim of the work was to measure the ignition delay period in a swirl prechamber diesel engine with high compression ratio, under different operating conditions. The ignition delay periods were expected to be very small, due to high compression temperature and pressure, and high speed operation of the engine. Extreme accuracy was needed to measure the ignition delay period satisfactorily, and to be able to detect its variation with engine running conditions. A very fast and reliable data logging system was used to achieve the required measurement accuracy. Details of the test apparatus and data logging technique are given below.

6.4.1 Test Installation

Fig. (6.1) is a schematic diagram of the test installation used for ignition delay measurements. The details of the tape recorder data logging system and sampling technique have been presented in Chapter 2.

Three transducers were used, two pressure transducers and an injector needle position transducer, the details of which also appear in Chapter 2. The two pressure transducers were used, one fitted in the cylinder and the other in the prechamber, to obtain the pressure difference between the two combustion chambers of the instrumented cylinder (NO.5). The transducers were calibrated statically and then dynamically by mounting them in the single chamber of a high compression DI engine. Under motoring conditions it was possible to achieve an accuracy of adjustment, for the two transducer-amplifier systems, corresponding to ±0.068 Bars.

The shaft encoder provided a train of pulses of $\frac{1}{4}^{o}$CA resolution. The (DLCU) (section 2.52) was then used to produce five additional "ghost" pulses

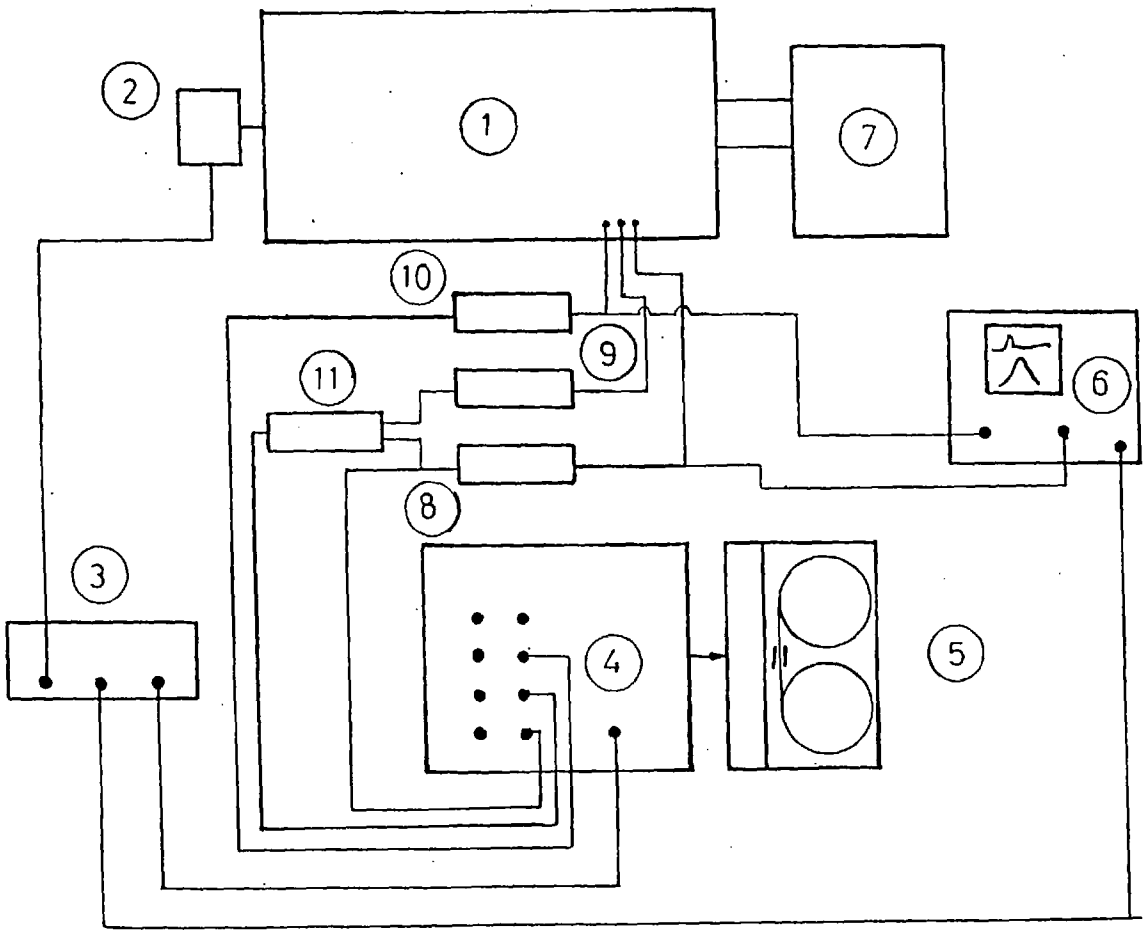

1. Engine
2. Shaft Encoder
3. Data Logging Control Unit
4. Signal Processing Box
5. Tape Recorder
6. Oscilloscope
7. Hydraulic Brake
8. Main Chamber Transucer Amplifier
9. Swirl Chamber Transducer Amplifier
10. Needle Lift Transducer Tuner and Amplifier
11. Pressure Difference Amplifier

Fig. (6.1) Data Sampling System

for every digitiser pulse. This allowed the data to be sampled at the very fast resolution of 1/24th ^{o}CA. This was the highest sampling rate possible, dictated by the maximum continuous sampling rate of the tape recorder system. Although the sampling resolution was fixed in ^{o}CA, it varied in the time domain from 5.26 to 3.156 μs at 1320 and 2200 rpm respectively.

Cylinder pressure, needle lift and pressure difference signals were recorded. Fifty engine cycles were sampled for every running condition. For every engine cycle approximately 117 ^{o}CA around TDC position were recorded.

6.4.2 Injection and Ignition Moments

For each engine running condition, the recorded data was analysed on a CDC computer, and average and standard deviation values at every sampled point within the cycle were calculated. This provided an average representative engine cycle at every running condition. This average cycle was further analysed to obtain injection and ignition moments.

The injection moment was obtained by considering the injector needle lift diagram. The intersection of the tangent to the rising part of the diagram with the zero lift line identified the injection moment. The moment of ignition was identified as the moment at which a deviation occurred from the motoring trend in the pressure difference signal. Pressure difference between the two chambers is particularly small near TDC and any sudden change due to ignition is easily detected.

To study the effect of changing the dynamic injection timing on ignition delay, the fuel pump position was altered at every engine speed to obtain the required injection advance at full load. The fuel pump position was not changed at other loads. An oscilloscope was used to display both the needle lift and the cylinder pressure diagrams. The injection advance was thus set to the required value visually, using the time scale of the oscilloscope. Naturally, the accuracy of this method is not good, but it was adequate to obtain a "Nominal" value of the dynamic timing, which is an approximation

of the injection moment.

6.4.3 Test Results and Discussion

The effect of engine speed, load and injection timing on the ignition delay period was studied. Data was recorded at three engine speeds (1320, 1680, 2200 RPM), three loads (full load, 70% and 40%) and three dynamic injection timings (2^{o}, 7^{o}, 12^{o} BTDC). Table (6.1) summarises the test results and ignition delay values obtained.

The different ignition delay values are plotted in Figs.(6.2,3,4) to show the effects of speed, load and injection timing. The ignition delay periods measured were very small (less than 0,7 ms) as expected in a swirl prechambered, high-compression engine. The high swirling motion in the pre-chamber ensures very good mixing and rapid evaporation and formation of combustible mixtures with the result of a shorter physical delay. The walls of the swirl chamber are generally very hot, inducing higher compression temperatures. High compression ratio means high compression temperature and pressure, both reducing the chemical part of the delay period.

Although the accuracy of the measured delay period in terms of crank angle is fixed at $\frac{1}{8}$th of a degree, the equivalent time interval changes with engine speed. It varies from 15.78 to 9.47 μs at 1320 and 2200 rpm respectively.

Although some scatter is evident in the experimental results, they showed a reasonable trend of variation with the major engine variables. As expected, the delay period decreased, in ms, with increasing both engine speed and load and with retarding fuel injection. Higher engine speed results in higher air swirl velocities, and hence faster mixing of air and fuel i.e. shorter physical delay period. For a fixed load, higher speeds also result in a higher charge compression temperature at injection point. Similar effects result with increase of engine load due to increased wall temperatures at high load, which increases charge compression temperature.

Table 6.1

Measured Ignition Delay Values

Run No.	Speed (rpm)	Nominal Dynamic Timing	Load %	Injection Point $^{o}_{CA}$	Ignition Point $^{o}_{CA}$	Ignition Delay	
						$^{o}_{CA}$	ms
1	1320	2	100	- 4.292	- 0.958	3.334	0.421
2			70	- 4.042	- 0.333	3.609	0.456
3			40	- 3.992	+ 0.292	4.284	0.540
4		7	100	- 9.792	- 5.958	3.834	0.484
5			70	- 8.917	- 5.083	3.834	0.484
6			40	- 9.292	- 5.083	4.209	0.5315
7		12	100	-14.167	- 9.083	5.084	0.6419
8			70	-13.292	- 8.333	4.959	0.626
9			40	-13.661	- 8.333	5.334	0.6735
10	1680	2	100	- 4.292	- 0.333	3.959	0.3935
11			70	- 4.167	+ 0.167	4.334	0.430
12			40	- 3.792	+ 1.042	4.834	0.479
13		7	100	- 9.292	- 4.583	4.709	0.4665
14			70	- 9.042	- 4.083	4.959	0.4915
15			40	- 8.542	- 3.473	5.069	0.5025
16		12	100	-13.667	- 7.958	5.709	0.566
17			70	-13.167	- 7.458	5.709	0.566
18			40	-12.292	- 6.708	5.584	0.554
19	2200	2	100	- 5.042	- 0.083	4.960	0.376
20			70	- 5.542	+ 0.042	5.584	0.423
21			40	- 4.042	+ 1.677	5.719	0.433
22		7	100	- 8.792	- 3.458	5.334	0.404
23			70	- 8.417	- 3.083	5.334	0.404
24			40	- 7.542	- 1.958	5.584	0.423
25		12	100	-12.542	- 6.458	5.834	0.442
26			70	-12.417	- 6.708	5.709	0.4325
27			40	-11.042	- 5.458	5.584	0.423

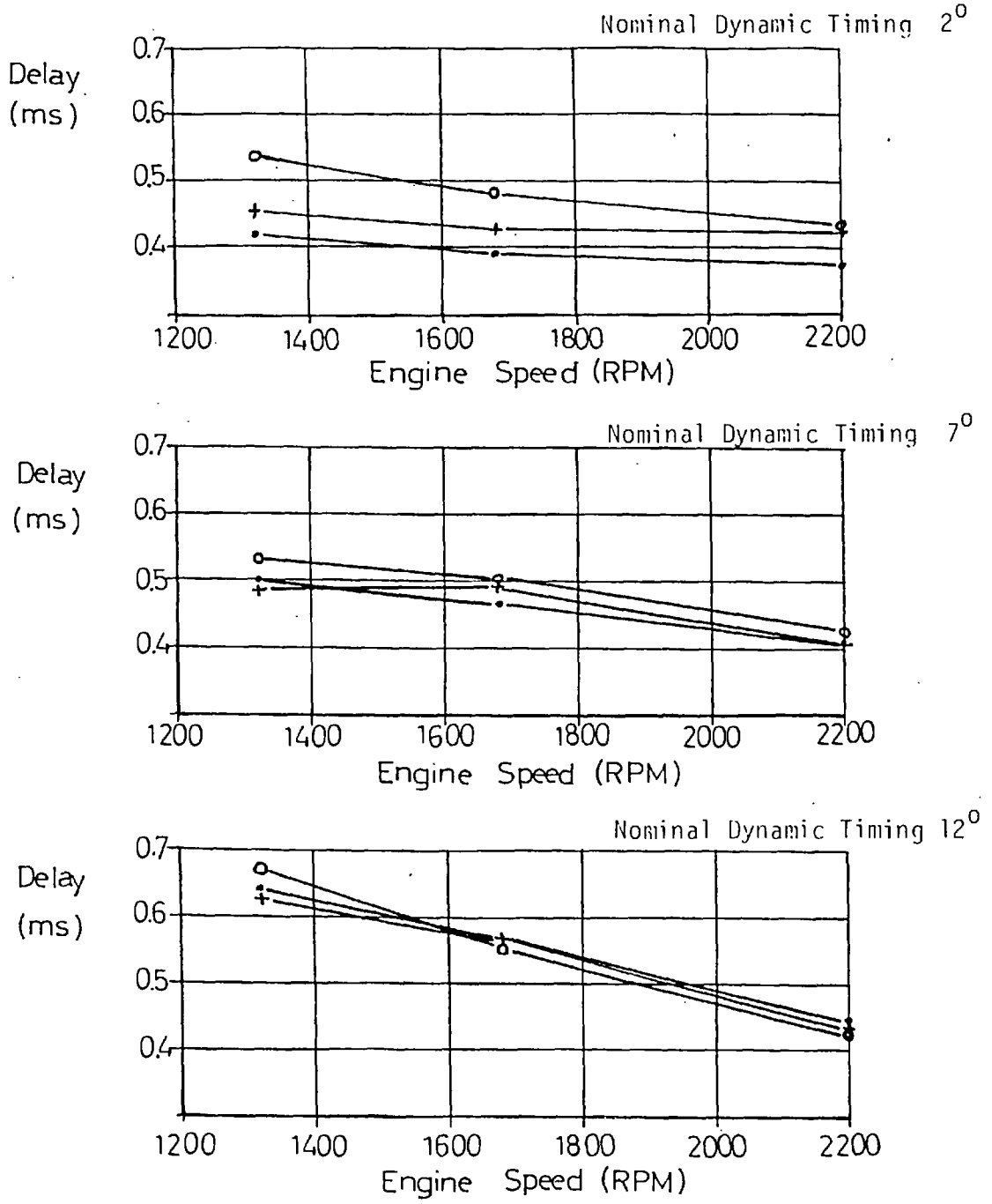

Fig. (6.2) Effect of Engine Speed on Ignition Delay Period

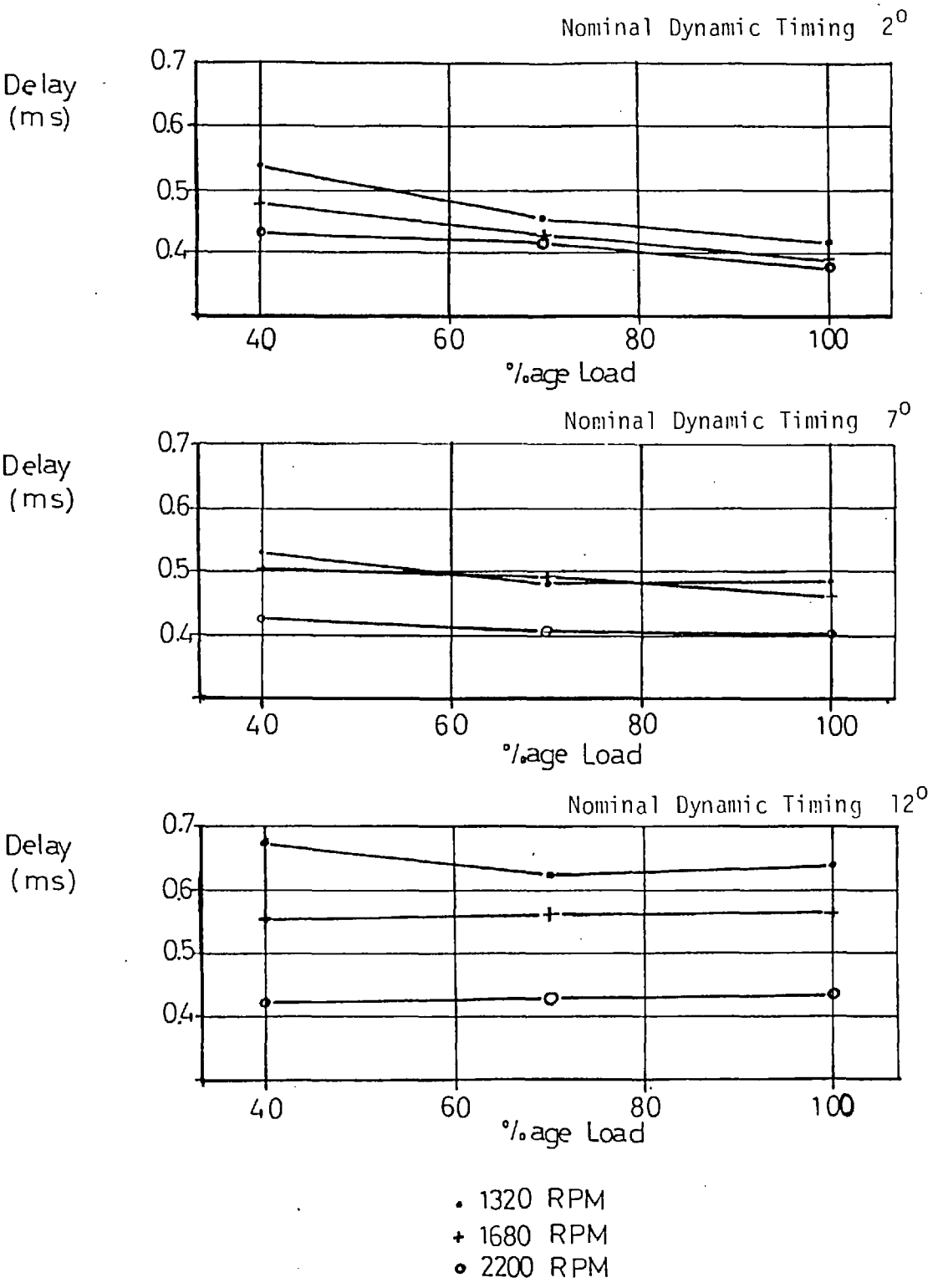

Fig. (6.3) Effect of Engine Load on Ignition Delay Period

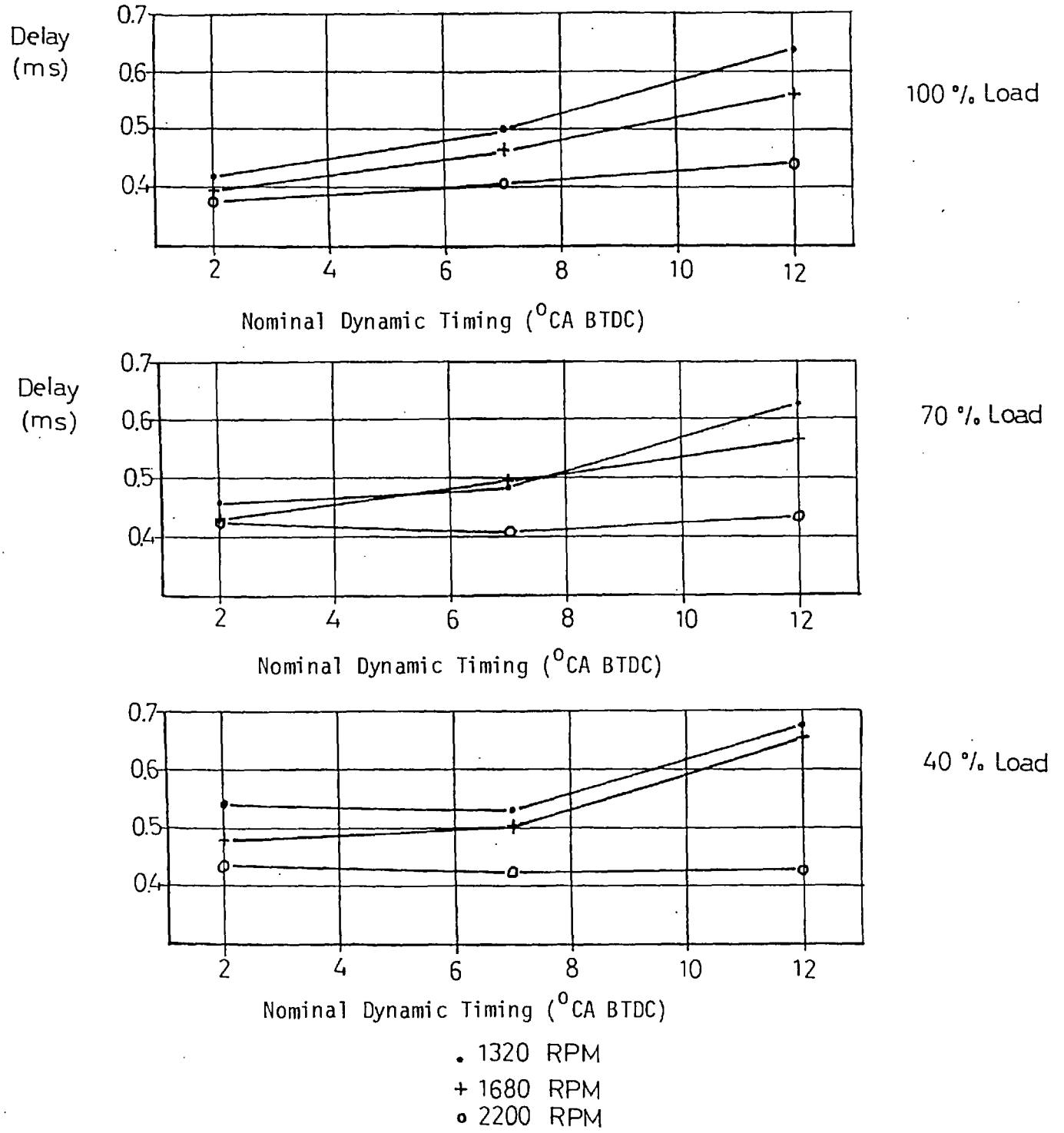

Fig. (6.4) Effect of Dynamic Injection Timing on Ignition Delay Period

Injection retard allows the fuel jet to develop at higher temperature and pressure with the resulting reduction in the ignition delay period.

The measured behaviour of the delay period reflects all the above phenomena, and was thus considered satisfactory. Detected discrepancies in some of the results is considered to be a probable result of inaccuracies in the identification of the injection point.

6.5 IGNITION DELAY CORRELATION

After studying the effects of varying engine operating condition on the ignition delay period, an attempt was made to express ignition delay periods mathematically. Mathematical expressions for delay have become more important with the growing use of mathematical simulations of engine cycles, combustion models and heat release correlations.

The idea of correlating experimental data directly with the major engine variables (speed, load and timing) was excluded. Such a correlation would have no direct theoretical support and would not relate ignition behaviour to its basic controlling parameters. A more basic approach was required; e.g. to correlate the ignition delay to the chamber pressure and temperature. First, currently available correlations were studied.

Tsao's formula (107) was used to calculate delay periods under different running conditions, for the engine under investigation in present work. The values obtained were found to differ by a large order of magnitude compared to the measured, and were negative in some cases. Since the shape of the formula had no physical support, no attempt was made to readjust the seven constants involved. The formula was finally discarded as being unsuitable for the present engine.

The concept of the physical and chemical parts of the delay period was acknowledged in the present investigation. This necessitates calculating the physical delay period. Recently, Pedersen (86) published a formula expressing the physical delay as a function of air temperature and pressure,

fuel temperature, droplet mean diameter and jet velocity relative to air, as follows:

$$t_{ph} = 0.00642 \cdot \exp\left[\frac{3.53.\ T_{A_{ref}}}{T_A}\right] \cdot \left[0.22\ \frac{P_A}{P_{A_{ref.}}} + 0.78\right] \cdot \left[\frac{d}{d_{ref}}\right]^{1.77} \left[1.74 - 0.74\ \frac{T_F}{T_{F_{ref}}}\right] \left[\frac{W}{W_{ref}}\right]^{-0.17}$$

where

t_{ph} = Physical Delay (ms)

T_A = Air Temperature (K)

$T_{A_{ref}}$ = Reference Air Temperature (823 K)

P_A = Air Pressure (Bar)

$P_{A_{ref}}$ = Reference Air Pressure (34.47 Bar)

d = Droplet Mean Diameter (μm)

d_{ref} = Reference Droplet Mean Diameter (25 μm)

W = Relative Droplet Velocity (m/s)

W_{ref} = Reference Velocity (200 m/s)

T_F = Fuel Temperature (K)

$T_{F_{ref}}$ = Reference Fuel Temperature (293K)

However, the range of total delay periods studied was 1 to 3 ms, exceeding the 0.5 ms range in the present work, hence Pedersen's correlation could not be used.

Due to the similarity between the geometry of the swirl combustion chambeer of the tested engine, and that used by Ilmari (55), the spray impingement theory for ignition proposed by him was therefore considered.

As explained in section (6.36) the theory implies the termination of

the physical delay once the fuel jet hits the wall. The time interval between injection and impingement is calculated using an average jet velocity (v_{J_m})

$$v_{J_m} = 0.9\ v_{J_o}$$

where

v_{J_o} = Initial jet velocity

$= C_{d_{inj}} \sqrt{2g\ P/\rho_f}$

and

ΔP = Initial Pressure Difference between the Injection Pressure and Chamber Pressure

$= P_{inj} - P$

g = Gravitational Acceleration

ρ_f = 835 Kg/m^3 and P_{inj} = 150 Bars

The range of values of discharge coefficient $C_{d_{inj}}$ is reported by Gellales (44) to lie between 0.6 and 0.7, for the injector type used. The physical delay is hence given by;

$$t_{ph} = S_J/v_{m_j}$$

where S_J is the distance from the injector nozzle to the impingement point (30mm in the tested engine).

From the above relations, physical delay periods were calculated at all engine running conditions, using measured values of chamber pressure at injection. Small variations existed between them, and the average physical delay for all conditions was 0.338 ms, compared to the 0.4 ms value obtained by Ilmari. The difference was considered to be due to different values of P_{inj}, P, ρ_f and S_J in Ilmari's investigation.

No apparent trend was detected for the variation of calculated physical delay periods with any of the engine parameters, e.g. speed, load and injection timing. This was considered to be a disadvantage of the calculation method,

as physical delay period was expected to decrease with the increase of engine speed due to better mixing. The factor (0.9) used in the v_{J_m} relation is also considered large. The need for a better method of calculation for the physical part of the delay period is apparent. A simplified method was developed for this purpose and is explained in the following section.

The suitability of the available correlations by Sitkei (96), Wolfer (116) and Ilmari (55) concerning the chemical delay period were considered. Regarding the present work, Sitkei's formula could not be applied since it requires distinctive identification of the two stages of the chemical delay periods, and such data was not available for the present work. The difference between Wolfer's and Ilmari's correlations is in the extra temperature term $(\frac{RT}{E_a})^{\bar{m}}$ in the latter (equation 6.10). As explained in section (6.3.5), this temperature term is a disadvantage of the correlation, thus Ilmari's correlation form was also excluded. The Wolfer type correlation was therefore considered to be the most suitable and was used to correlate the measured ignition delay behaviour.

6.5.1 The Physical Delay

In the previous section an average value of 0.338 was determined for the physical delay using Ilmari's method (55) and the disadvantages of the calculation method were explained. Physical delay has been considered to be a constant by Ilmari (55) and Sitkei (96); and they quoted values of 0.45 and 0.5 ms respectively. This supported the order of magnitude (0.338 ms) obtained for the present engine.

The physical delay was examined furthermore by considering the following form of the total delay formula;

$$t_d = \frac{a}{pb}\, e^{\frac{C}{T}} + d \qquad (6.13)$$

where

a, b, c and d are constant

In the above relation, measured values of chamber pressure were used,

while charge temperatures were obtained using the cycle analysis computer program, explained in Chapter 3. Pressure and temperature values substituted in the equation are average for corresponding values during the delay period. Non-linear curve fitting of the experimental delay values, results in the best fit constants being as follows:

$$\begin{aligned} a &= 0.5876 \times 10^{-4} \\ b &= 1.04 \\ c &= 10277.0 \\ d &= 0.3522 \end{aligned} \qquad \text{(a)}$$

Equation (6.13) rendered an estimate for the physical delay (0.3522 ms) which is higher than calculated using Ilmari's method. Although this might suggest that Ilmari's method underestimates the physical delay, further considerations are needed before a decision is made. The percentage errors of the correlated values with respect to the experimental, at every test, are shown in Table (6.2), and are plotted in Fig. (6.5). The average error for all tests is ±5.297%. Fig. (6.5) shows that the percentage error, at every engine speed and injection timing, changes from positive to negative with reduction of engine load. This was expected to be due to the effect of engine load on the cylinder wall temperatures. Since no account was made for the change of wall temperature with engine load, in obtaining the average temperature of the chamber charge in equation (6.13a), errors arise with load variation.

Effect of engine load on the chamber wall temperature has been found to be considerable (Fig. (4.47)). This effect was therefore considered in predicting the average charge temperature for different engine loads, by changing the wall temperature accordingly. Using these new temperatures, alternative values for constants a, b, c and d were obtained

$$\begin{aligned} a &= 0.91507 \times 10^{-7} \\ b &= 0.14207 \\ c &= 14008.0 \\ d &= 0.3202 \end{aligned} \qquad \text{(b)}$$

Table 6.2

Errors in Using Correlations 13a, 13b and 19

Run No.	Measured Delay (ms)	Percentage Error from Correlation		
		Equn. 13.a	Equn. 13.b	Equn. 19
1	0.421	10.6829	4.9841	11.0518
2	0.456	2.2807	1.3961	4.5189
3	0.540	-13.5549	-10.0506	-9.8512
4	0.4841	9.3545	3.7376	6.8551
5	0.4841	6.8582	6.5042	7.2357
6	0.5315	-2.2526	2.4587	0.7947
7	0.6419	4.3734	-2.8893	0.3094
8	0.6261	-0.8194	0.5092	1.0421
9	0.6735	-4.9767	1.1637	-0.5231
10	0.3935	10.4608	5.4205	9.2809
11	0.430	1.0627	-0.3123	1.4058
12	0.479	-8.9957	-6.9773	-7.2573
13	0.4665	0.7935	-4.4575	-1.9969
14	0.4915	-5.390	-6.811	-5.9165
15	0.5025	-6.7544	-5.1153	-6.3035
16	0.5664	1.0389	-6.2874	-3.9484
17	0.5664	-4.1378	-1.8263	-1.9285
18	0.554	-5.4898	0.5687	-1.6159
19	0.376	7.0073	2.5204	3.4025
20	0.423	-4.489	-5.0726	-6.3739
21	0.4332	-7.1813	-3.347	-7.193
22	0.404	3.9342	0.2159	-0.2646
23	0.404	3.4846	3.3541	1.2477
24	0.423	-2.5026	2.1372	2.2177
25	0.442	4.2536	0.8558	-0.4313
26	0.4325	6.7296	10.0356	6.1446
27	0.423	4.201	14.8544	8.1808

(for identification of Run No. see Table 6.1)

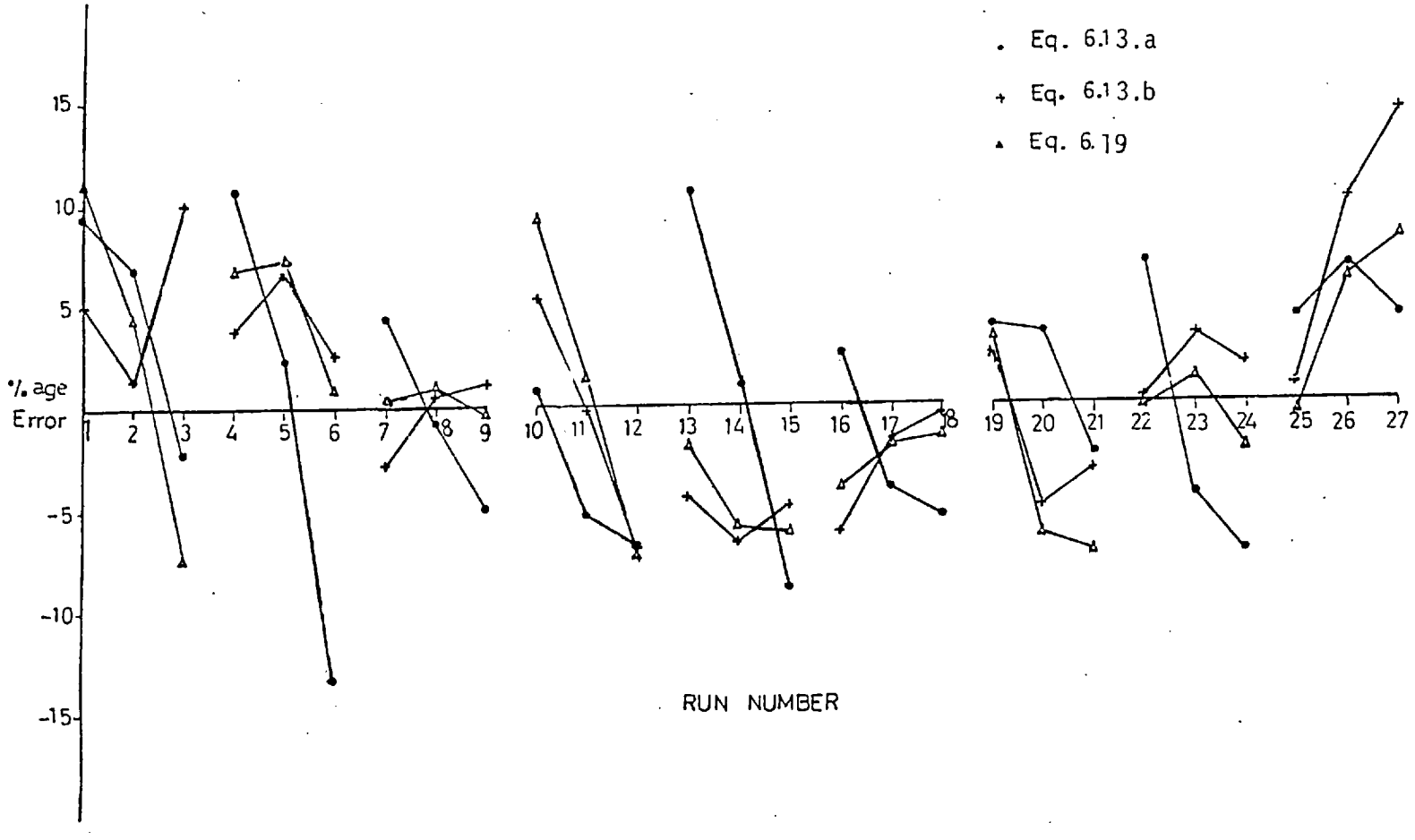

Fig. (6.5) Percentage Error Between Calculated and Measured Delay Periods

The percentage errors from this new correlation (6.13b) are shown in Table (6.2) and Fig. (6.5). The average error has now reduced to ±4.217% and the dependence of percentage error values on engine load is not apparent. Although these reflect how close the correlation is to the experimental values, the value of constant (a) is very small which is a result of the pressure term index (b) being small. A small value of (b) implies that pressure has a small effect on the chemical delay, which is questionable. The physical delay period is, according to equation (6.13b), 0.3202 ms, which is even smaller than the value obtained using Ilmari's (55) method. This signifies that physical delay has terminated before impingement on the wall. A further look at the physical part of the ignition delay was essential to conclude the investigation.

The physical delay period was defined as the time lapse from the moment of injection till the moment when a combustible mixture is formed. This time was calculated using a simplified approach of a jet in a cross wind. The results of Patrick (84), (85) were used for the determination of the jet centreline position, concentration and velocity at any time after injection, for every running condition. (Patrick's relationships are also published in Ref. (12))

$$\frac{y_J}{d_J} = \lambda_J^{-0.85} \left(\frac{x_J}{d_J}\right)^{0.34} \tag{6.14}$$

where

$$\lambda_J^2 = \frac{\rho_a}{\rho_f} \left(\frac{v_a}{v_{J_o}}\right)^2 \tag{6.15}$$

v_{J_o} = Initial fuel velocity in a direction perpendicular to air stream

The ratio (λ^2) of spray and air momentum was reported to be satisfactory when used by Morris (75) for simulating fuel-air mixing in engines. In the present investigation only the component of the fuel jet perpendicular

to the swirling air stream in the prechamber was considered, for simplicity.

The centreline concentration at any moment after injection, according to Patrick (84) is expressed by;

$$\frac{C_o}{C_m} = \frac{S_a}{d_J} \left(\exp\left(7.8\,\lambda_J - 1.85\right)\right)^{1.18} \tag{6.16}$$

A free jet concentration distribution was assumed across the jet cross-section. Although real profiles differ in a spray deflected by lateral flow, this assumption has been shown by Adler (3) to be acceptable. The concentration of any radius within the jet cross section is thus obtained from;

$$\frac{C_r}{C_m} = 1 - \left(\frac{r_J}{R_J}\right)^{1.5}$$

A combustible mixture is assumed to be formed when the half radius concentration equals the stoichiometric value. This would ensure the presence, within the jet, of a range of concentrations varying from very rich at the centreline, to very lean near the outer radius. If this occurred before the fuel jet hits the wall, physical delay is terminated.

$$C_{r)_{\frac{1}{2}}} = C_m \left(1 - \left(\tfrac{1}{2}\right)^{1.5}\right) \tag{6.17}$$

$$= 0.647\ C_m$$

The velocity of the jet centreline was given by Patrick (85) as having the form

$$\frac{v_{J_o}}{v_c} = 0.75\ \frac{C_o}{C_m} - 0.15 \tag{6.18}$$

In the above equation, air velocities were obtained from the cycle simulation program discussed in Chapter 3. The velocity values were those obtained using the method explained in Chapter 4. Velocities were estimated from computer results of motored runs for each engine speed. Table (6.3) shows the physical delay values obtained by solving equations (6.14) to (6.18)

Table 6.3

Calculated and Correlated Physical Delay Periods
(for identification of Run No. see Table 6.1)

Run No.	Calculated Physical Delay (ms)	Average (ms)	Value from Equn.(6.19) (ms)
1	0.41025	0.4003	0.4097
2	0.3829		
3	0.4234		
4	0.41305		
5	0.3947		
6	0.3827		
7	0.4402		
8	0.3789		
9	0.3768		
10	0.3264	0.37417	0.3857
11	0.3448		
12	0.3449		
13	0.37955		
14	0.3331		
15	0.4065		
16	0.42565		
17	0.427		
18	0.3796		
19	0.2935	0.3115	0.3606
20	0.2798		
21	0.2826		
22	0.3016		
23	0.3163		
24	0.2776		
25	0.3557		
26	0.3535		
27	0.3426		

using a step-wise technique, while Fig. (6.6) shows the jet centreline at full load and three engine speeds; the final downstream point denotes the end of physical delay. Examining Table (6.3) there is no apparent trend of physical delay variation with either engine load or injection timing. There is, however, an obvious decrease of the physical delay with engine speed, and for this reason all values at each engine speed were averaged to render a representative value of the physical delay at that speed. This is a necessary approximation in view of the absence of any alternative representative value. The decrease of physical delay with engine speed is expected to be a result of better and faster mixing of fuel and air due to higher air velocities.

At the same engine speed, the absence of any apparent trend of physical delay with engine load or injection timing, could be interpreted as being a result of the simplifying assumption made in the calculations. It is believed, however, that mixture formation could be a stronger function of engine speed rather than engine load or injection timing, in the range investigated. In the absence of reliable data concerning physical delay behaviour with respect to engine running conditions, the results obtained were considered to be approximately indicative of the behaviour encountered in the tested engine.

The range of the physical delay (0.4-0.31 ms) is in good agreement with the findings of other researchers (55,96) considering the high compression ratio engine used in the present work.

6.5.2 Final Correlation

Physical delay period calculations indicated a dependence on engine speed. It was, therefore, concluded that the parameter (d) in equation (6.13b) must be a function of engine speed, and was included accordingly in the final correlation as,

$$t_d = t_{ch} + t_{ph}$$

$$= \frac{a}{pb}\, e^{c/T} + \frac{d}{(N/1000)^e} \qquad (6.19)$$

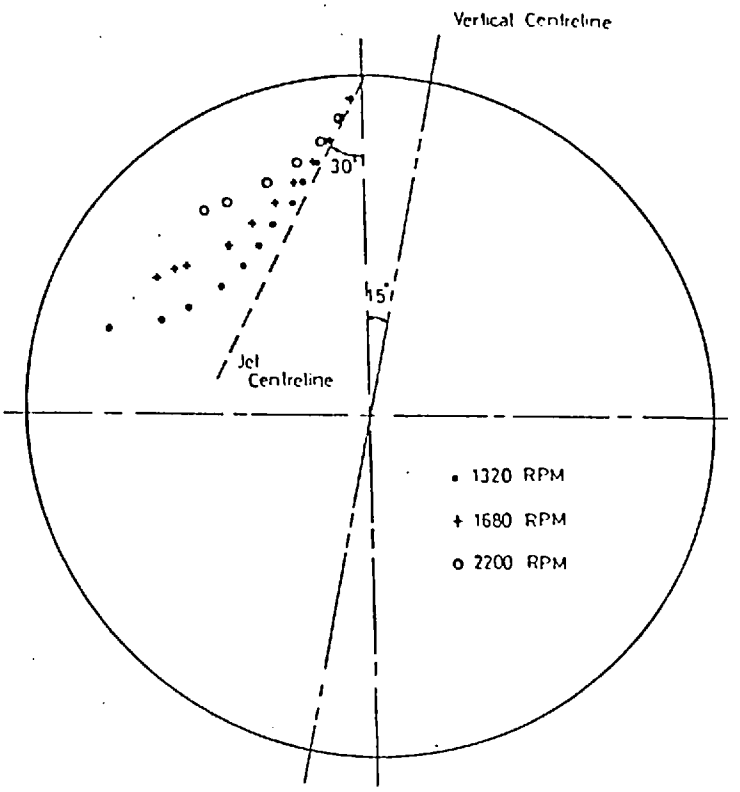

Fig. (6.6) Fuel Jet Centreline Trajectories

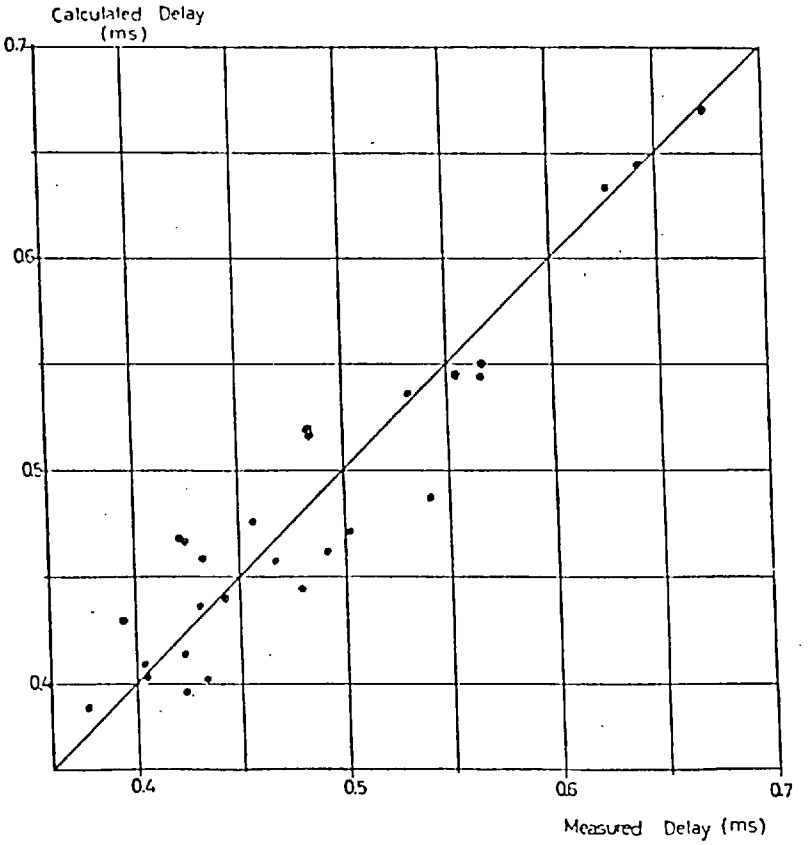

Fig. (6.7) Measured and Calculated Delay Periods

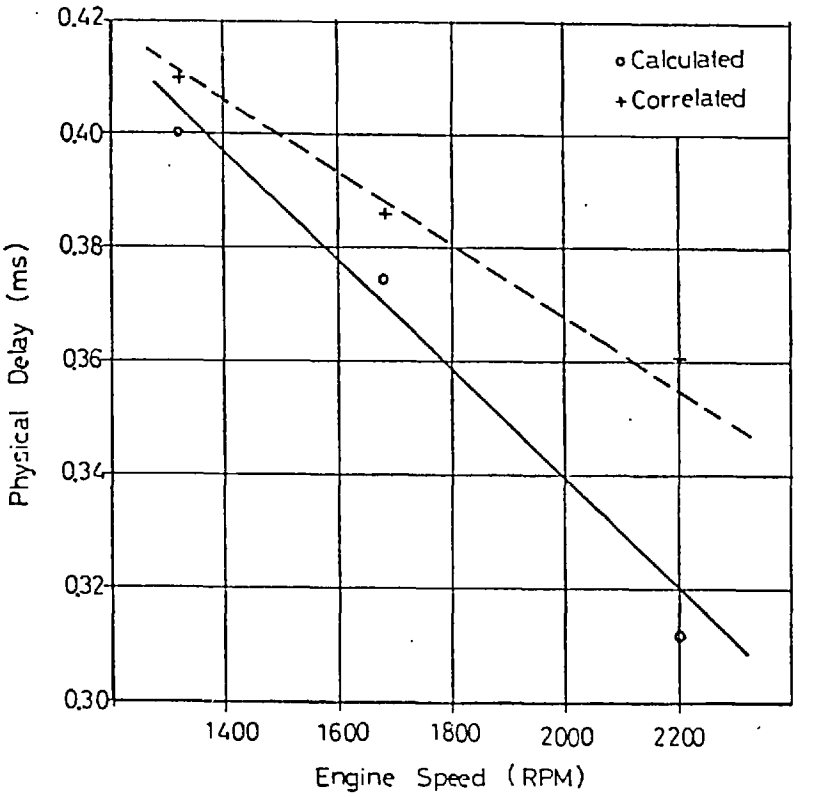

Fig. (6.8) Calculated and Correlated Physical Delay Periods

The constants were determined by non-linear curve fitting:

$$a = 0.34882 \times 10^{-4}$$

$$b = 1.6162$$

$$c = 13262.0$$

$$d = 0.43913$$

$$e = 0.25$$

Percentage errors between measured and correlated delay values, using equation (6.19), are shown in Table (6.3) and Fig. (6.8). The average error for all the test runs is ±4.35%. Good agreement is apparent as measured delay periods are plotted against correlated values, as shown in Fig. (6.7).

The calculated and correlated physical delay periods are shown in Fig. (6.8). They both have the same decreasing trend with engine speed. The differences between calculated and correlated values increase with engine speed. Although better correlated values can probably be obtained by changing the form of the physical delay term in equation (6.19), this could be considered misleading. The calculated physical delay periods are not claimed to ne exact, but only an indication of the expected trend of the behaviour with engine speed. Therefore, comparison with them and the consequent conclusions have to be considered with this in mind. In view of the absence of reliable information regarding physical delay behaviour, the correlated physical delay periods are considered to be indicative of the expected behaviour.

The order of magnitudes of constants a, b and c in equation (6.19) is acceptable, showing a realistic dependence of the chemical delay on charge pressure and temperature.

6.5.3 Conclusions

The ignition delay period of a high compression prechamber diesel engine has been measured with an accuracy of $\pm\frac{1}{8}$th of a degree crank angle. Investigations were made regarding calculating and correlating both the physical and the chemical parts of the delay period. The following conclusions were

arrived at:

1. The test arrangement and methods of detecting injection and ignition moments proved entirely satisfactory and consistent.

2. Although the range of delay periods measured was very small (<0.7 ms), the very high sampling rate used permitted accurate detection of the ignition delay behaviour of the engine under study.

3. The expected trends of delay period variation with speed, load and dynamic timing were observed. Small deviations were noticed at high engine speeds. This was probably due to the shorter delay periods - timewise - at this high speed.

4. Investigation of the available correlations for the delay period lead to the conclusion that an Arrhenius type relationship would express the chemical part of ignition delay satisfactorily.

5. In the particular engine used in the present work, the physical part of ignition delay was found to form a considerable part of the total delay.

6. The effect of engine speed on the charge velocity at injection, and hence on the physical delay period, was detected. This effect was taken into consideration in the final correlation.

7. Equation (6.19) was the final correlation arrived at, having considered both the chemical and the physical parts of the delay.

CHAPTER 7

EVALUATION OF SIMULATION TECHNIQUE

7.1 INTRODUCTION

A successful mathematical simulation of any actual system must be representative of all the major processes involved, and its evaluation should be based on the accuracy with which it reproduces the behaviour of the system, over a wide operational range. In this chapter, the validity of the simulation program is examined through comparisons between predicted and measured engine performance. Additionally the rate of heat release calculations are evaluated, and predicted conditions in both combustion chambers of the cylinders are presented and discussed.

7.2 EXPERIMENTAL RESULTS

The experimental facilities and data acquisition system were described in Chapter 2. A selection of the results obtained are now presented. Figs. (7.1-7.6) show the measured main chamber pressure, pressure difference between chambers, fuel line pressure and needle lift against crank angle position, for several running conditions. The figures show variations with engine speed, load and dynamic injection timing. Injector needle lift diagrams are shown as a percentage of the maximum lift at full load for each particular engine speed and dynamic timing.

The effect of thermal shock on pressure transducers was studied separately (see Appendix A), and the problem was overcome by using thermal shielded transducers. No significant thermal shock effect is detectable at the running conditions indicated. The oscillations noticed in the pressure difference diagrams are thought to be the result of pressure waves propagating through the combustion chambers. These disappear quickly as the smoother diffusion burning prevails.

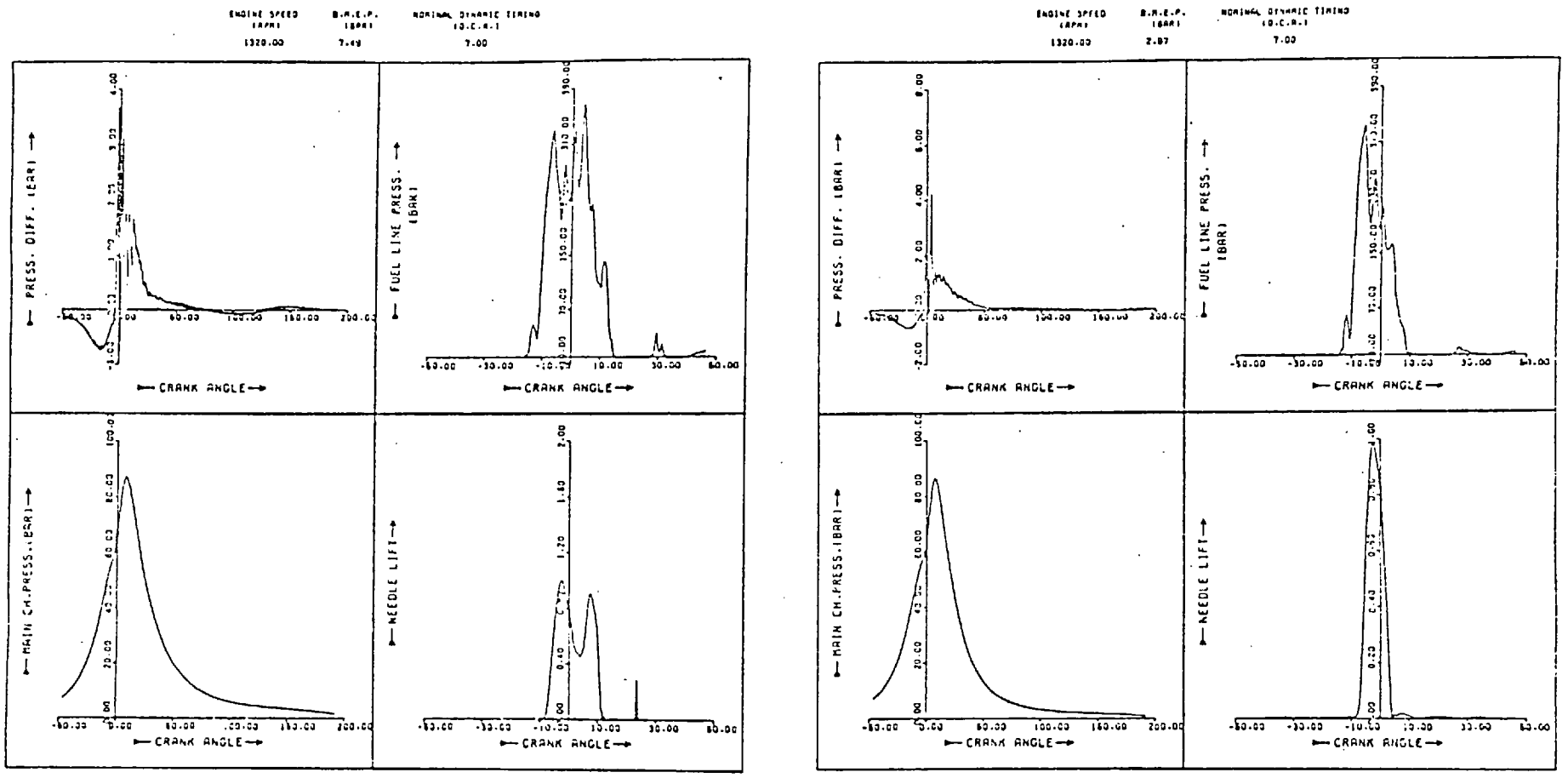

Fig. (7.1) Experimental Results at 1320 rpm

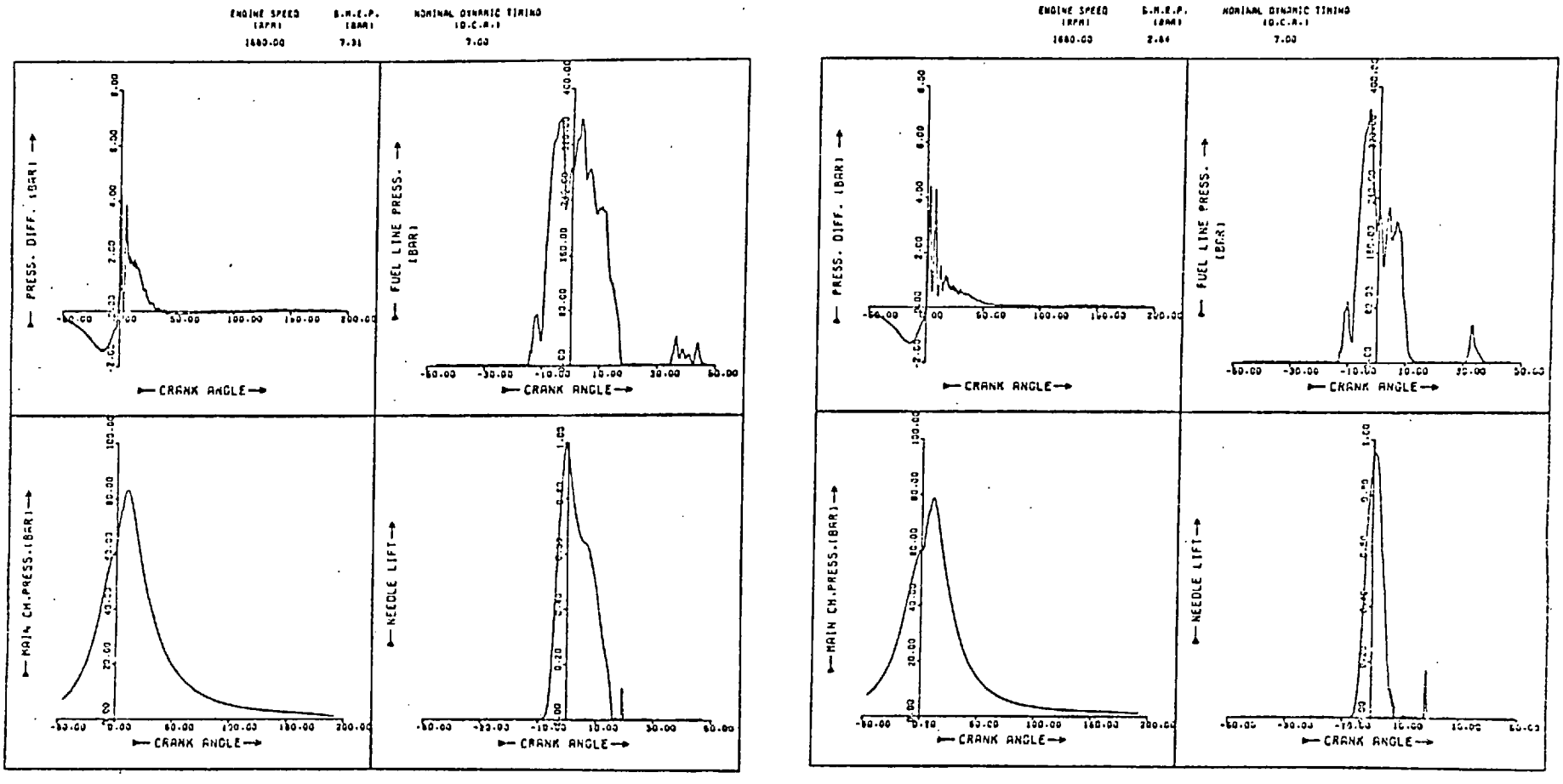

Fig. (7.2) Experimental Results at 1680 rpm

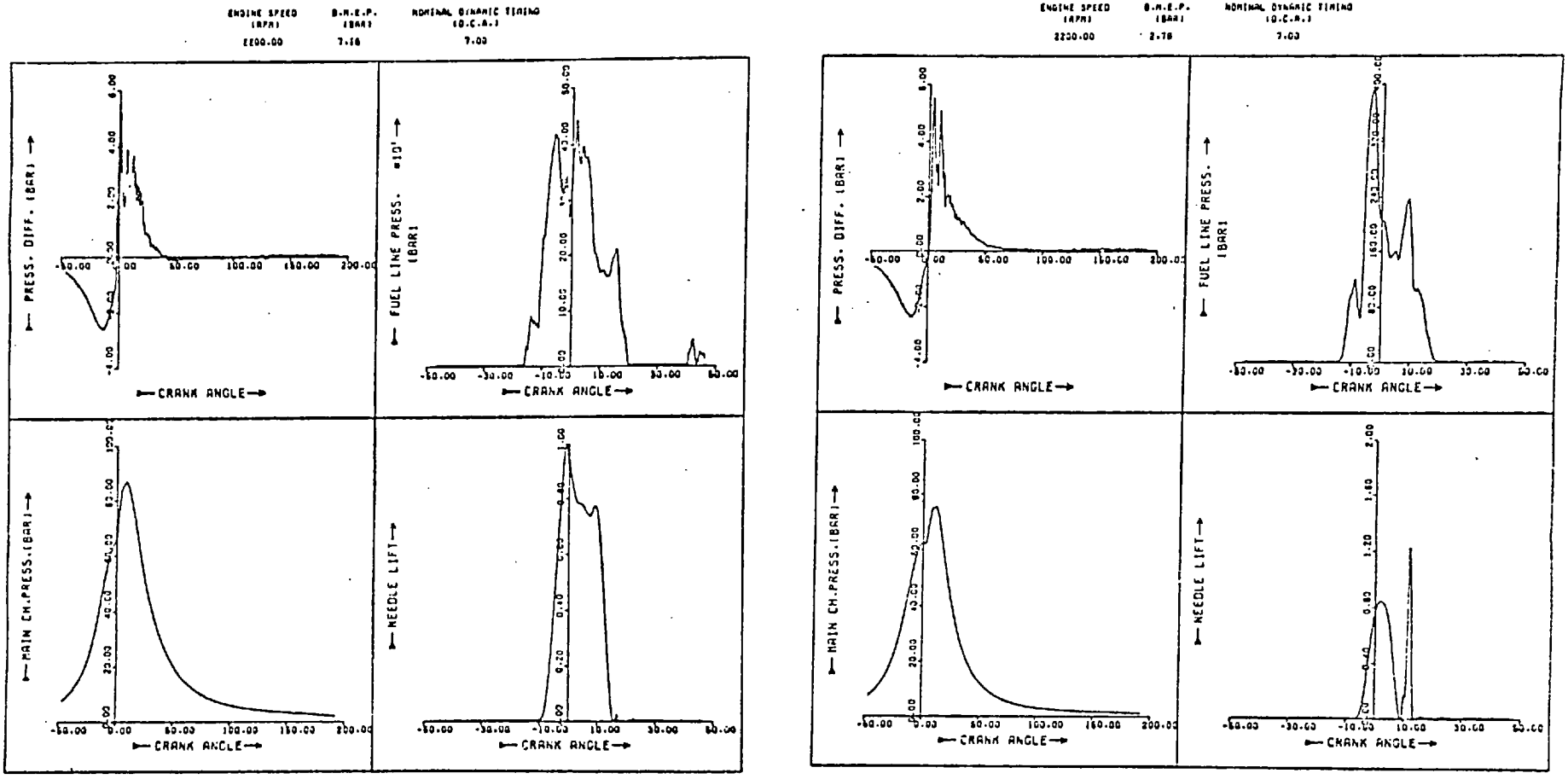

Fig. (7.3) Experimental Results at 2200 rpm

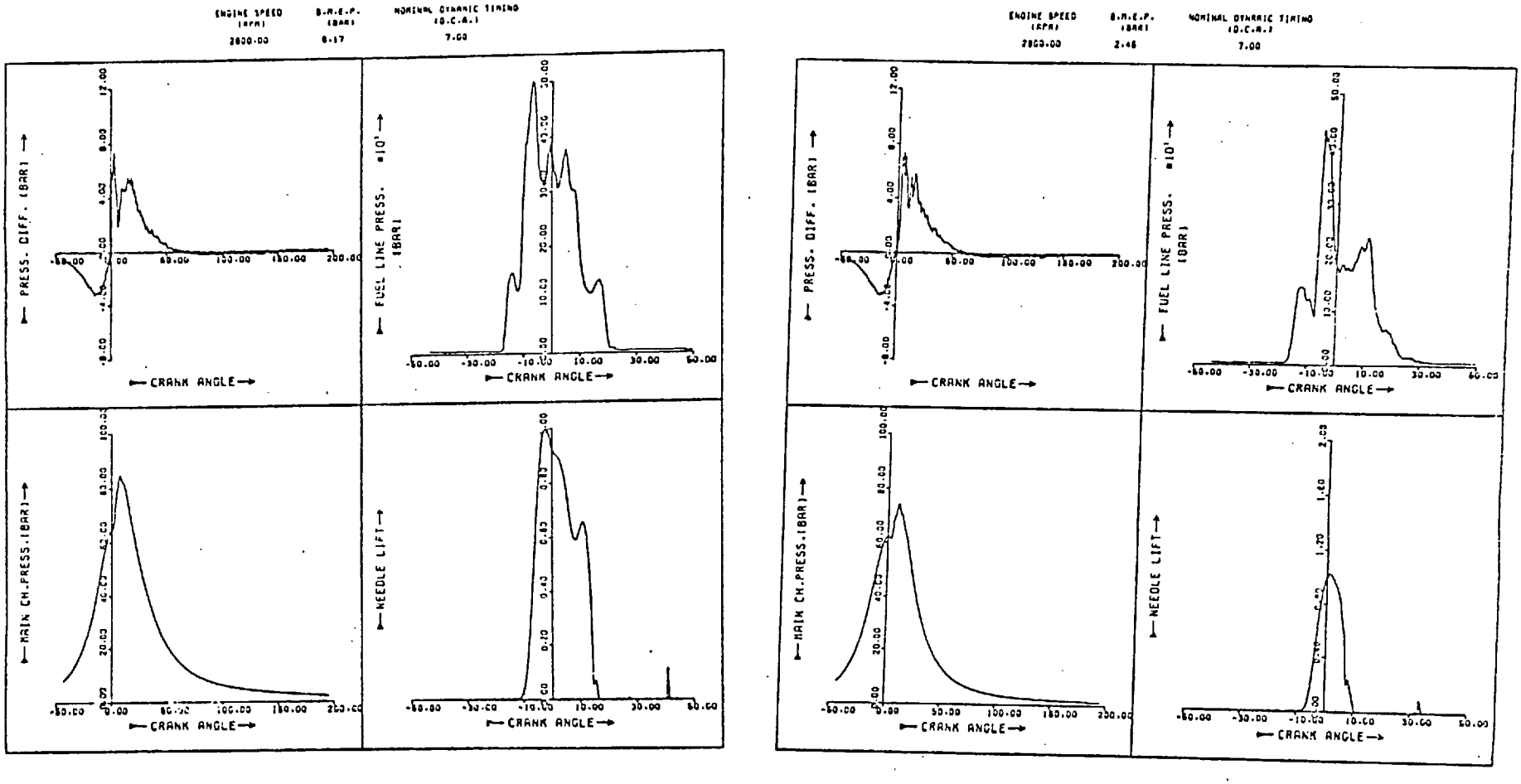

Fig. (7.4) Experimental Results at 2800 rpm

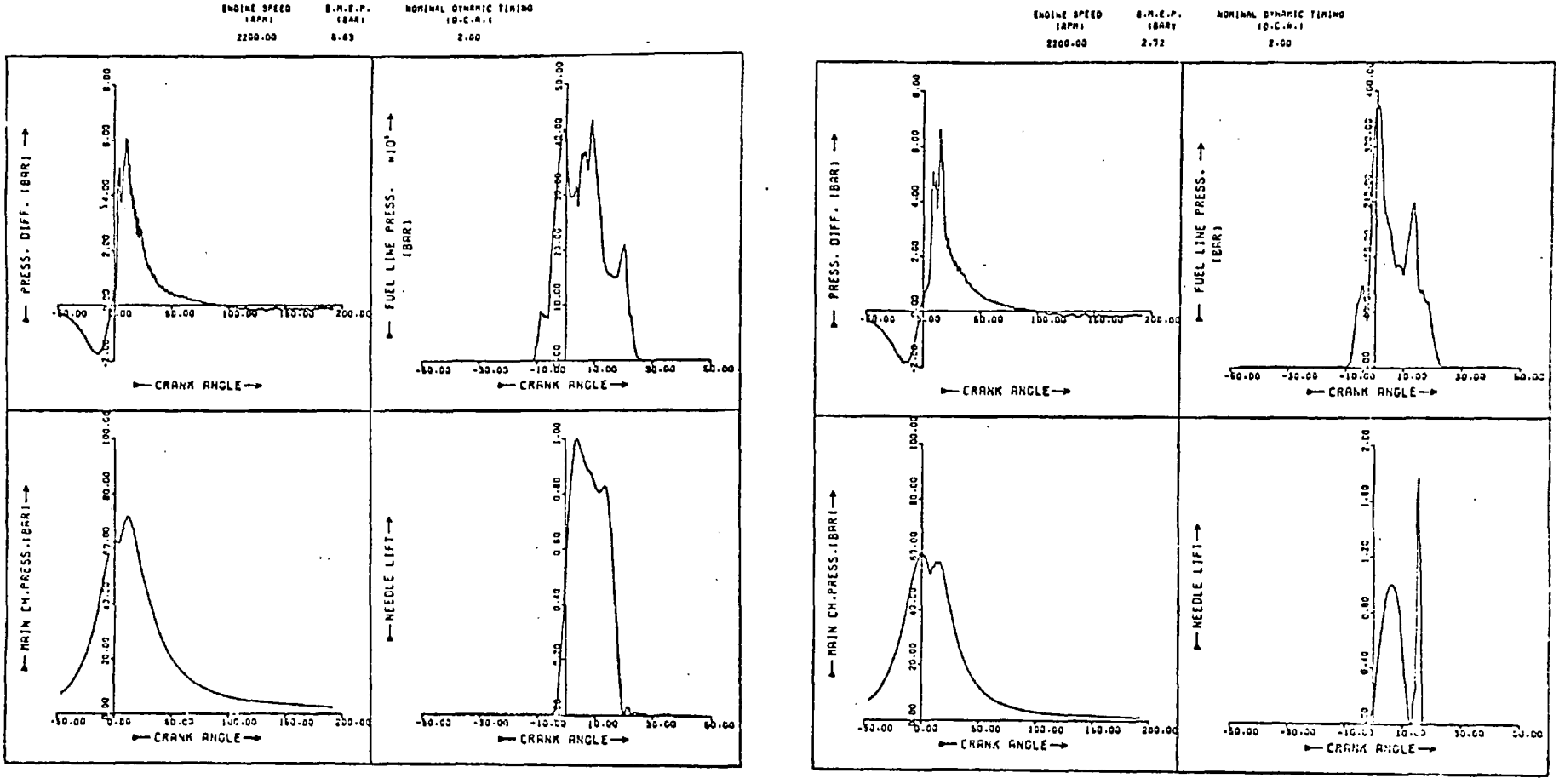

Fig. (7.5) Experimental Results at 2200 rpm 2^{o} BTDC Timing

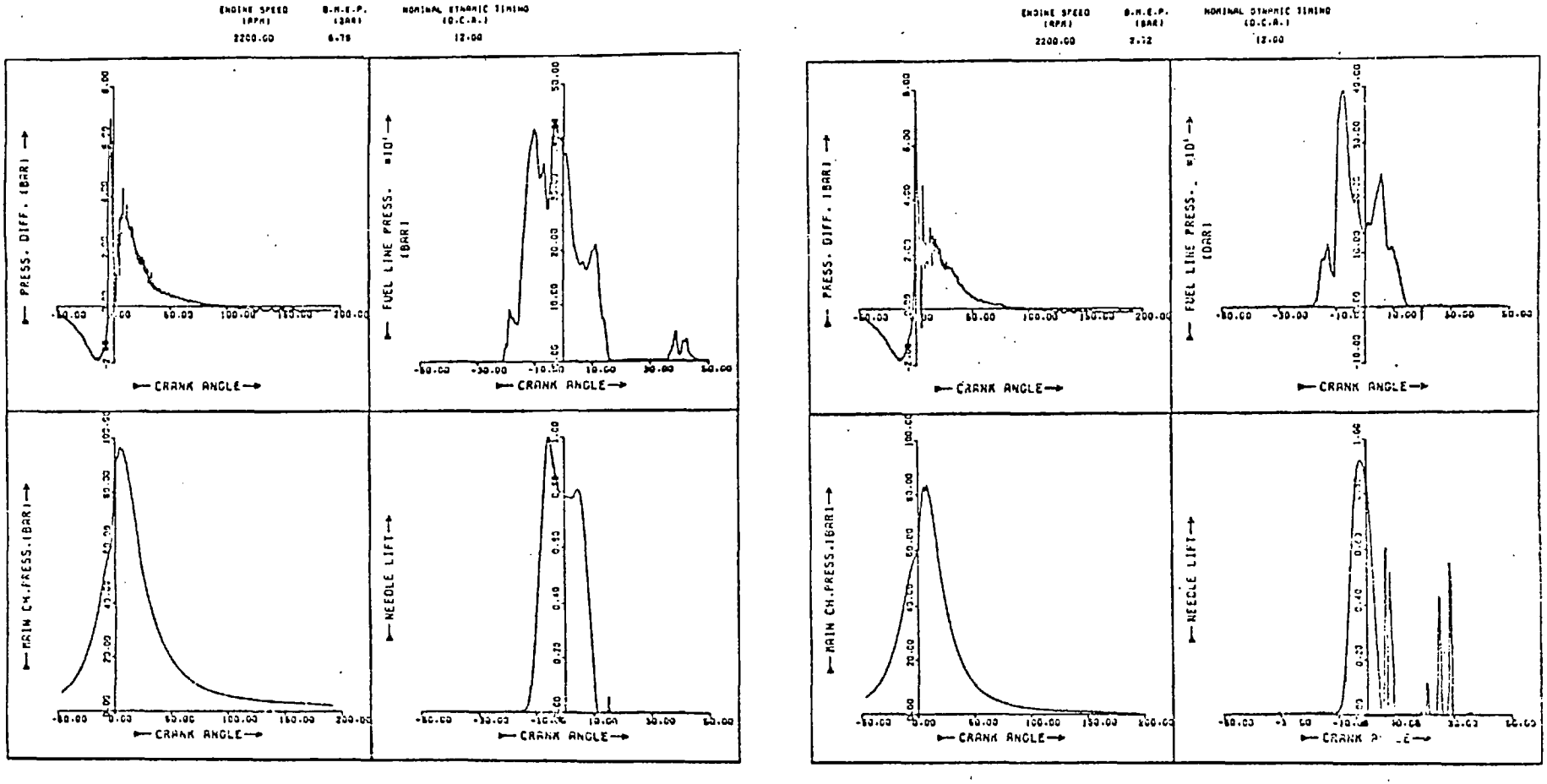

Fig. (7.6) Experimental Results at 2200 rpm , 12^{0} BTDC Timing

The needle lift signal was very small and required amplification before being sampled. The signal was subject to noise, creating the unrealistic pulses shown in some of the needle lift diagrams after the needle has closed, or when there is insignificant fuel line pressure.

The increase of the fuel line pressure with engine speed is an expected trend. Some similarity is recognisable, between the full load and part load runs at different speeds or dynamic timings. The same similarity is also detectable in the needle lift signal, where a tendency for a second peak is apparent in all full load runs.

Motoring cylinder pressure and chamber pressure difference diagrams at four engine speeds are shown in Figs.(7.22 and 7.23). A small increase in the cylinder peak pressure is evident at high engine speed. This is expected to be a result of the reduction, at high speed, of heat loss to the cylinder walls, due to less time for heat transfer being available.

The pressure difference signal is of special importance, as it monitors the interaction between the main and prechambers. A negative pressure difference signifies pressure in the main chamber being higher than that in the prechamber, while a positive value signifies the reverse. Higher values of pressure difference are experienced with engine speed increase, as a result of faster piston displacement. Asymmetrical pressure difference signal around TDC is a result of the different discharge coefficient values encountered for flow in either directions.

TDC position was defined statically, and then checked dynamically. The dynamic TDC was defined as the position which corresponds to the peak cylinder pressure, and this was found to be consistent with the static value, for engine speeds up to 2200 rpm, within $\pm 0.5^{o}$CA. At 2800 rpm, however, the position of the cylinder peak pressure was seen to be displaced so that it occurred about 2^{o} CA earlier. This is expected to be a result of the delayed effect of flow inertia through the connecting passage, which becomes apparent at high engine speeds.

For the present investigation, only the main chamber and pressure difference signals were studied. They were used to obtain heat release curves and to compare the actual engine performance with that predicted. These processes are described in the following sections.

7.3 CALCULATED HEAT RELEASE DIAGRAMS

In Chapter 3 the computer program developed for heat release calculation was described. The program was used to estimate instantaneous ROHR for both the main and prechambers. For every engine running condition, a representative engine cycle was analysed, which was the average of 50 cycles sampled. For ROHR calculation, instantaneous values of pressure and rate of change of pressure for each chamber were required. Smoothing of the pressure diagrams was necessary to remove the waviness of the pressure values at low pressures due to quantisation, and to damp the pressure oscillations encountered during the early mode of combustion. The smoothing procedure uses values of standard deviations at all test points to slightly change their values and hence obtain a smooth diagram, with the overall deviation between actual and smoothed diagram not exceeding a specified limit. A spline function routine was used for this purpose, and also to calculate rate of change of pressure. Smoothing of pressure diagrams for ROHR calculations is a common and useful procedure, but care should be taken such that the process does not introduce distortion in the diagram. This is particularly significant for an IDI engine as demonstrated in Fig. (7.7). The standard deviations obtained by averaging 50 engine cycles were used in Fig. (7.7) causing a distortion in the pressure difference diagram as shown. Due to the interaction between the two combustion chambers, a sudden drop of the ROHR in the prechamber occurred, and consequently a sharp rise in the ROHR in the main chamber resulted. After about 15^{o} ATDC, the distortion in the pressure difference diagram is rectified, and the ROHR values in both chambers show reasonable behaviour; decay in the prechamber and

Fig. (7.7) Heat Release Calculations Results

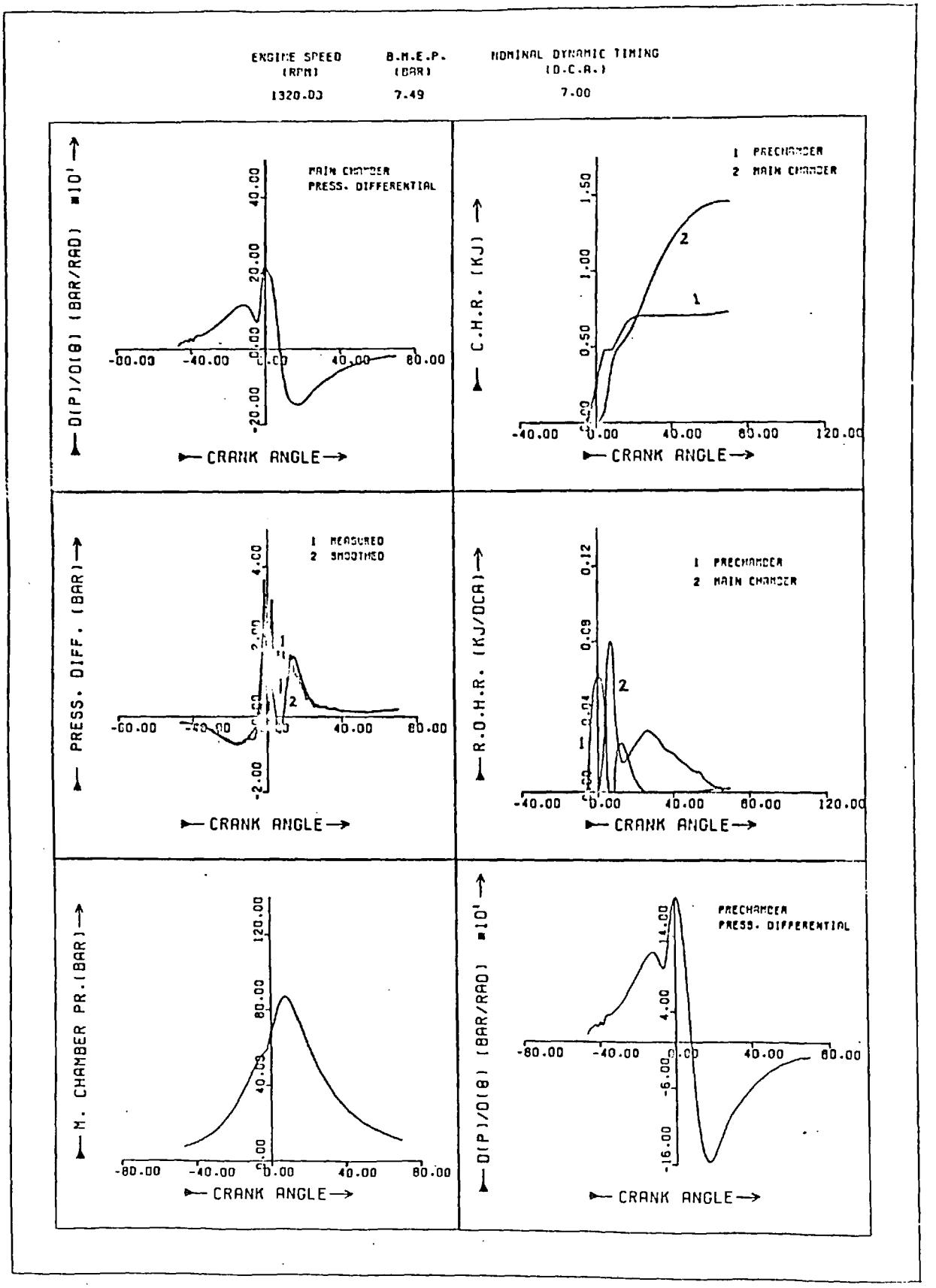

Fig. (7.8) Heat Release Calculations Results

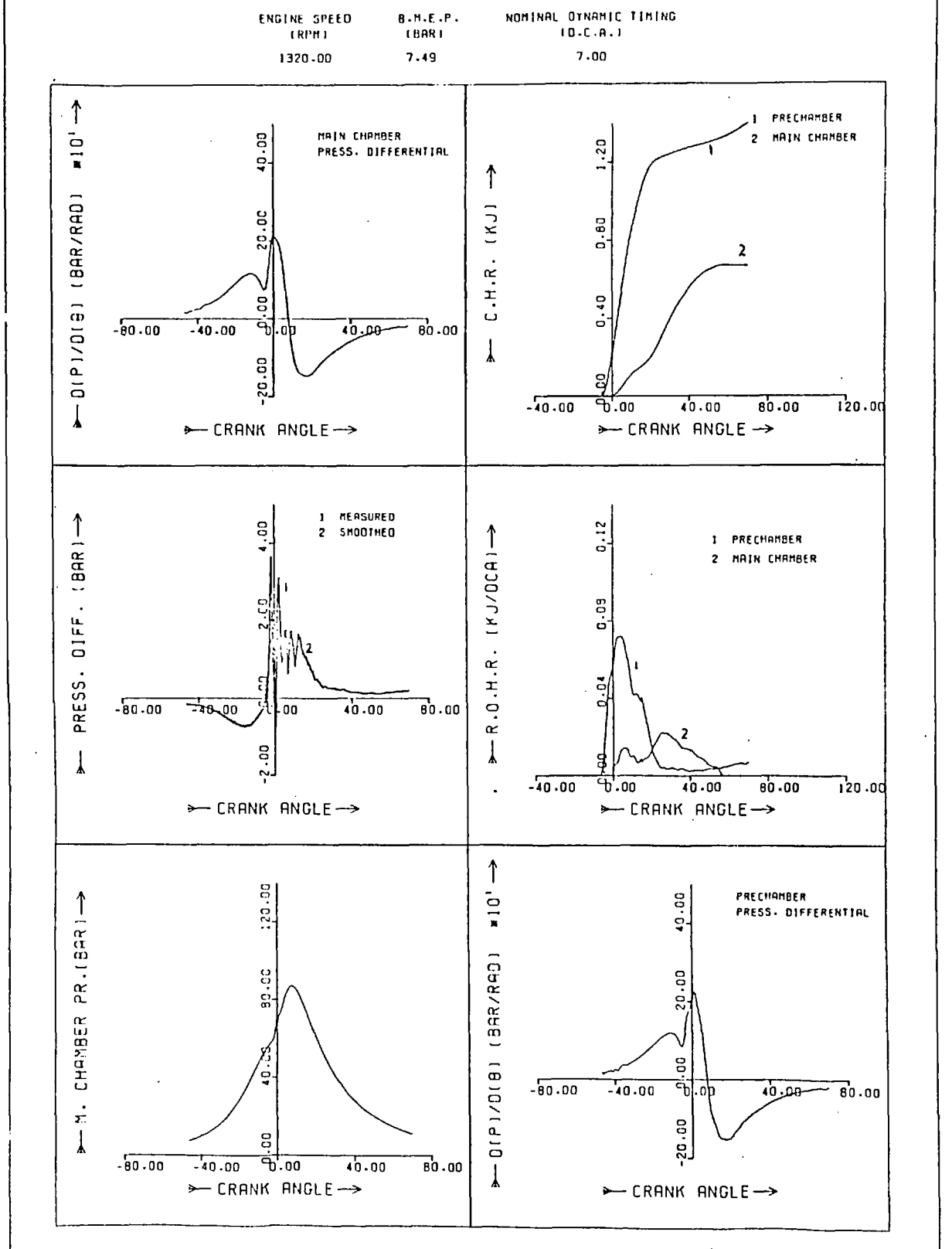

a higher apparent rate in the main chamber. Some constraints were imposed on the smoothing technique, mainly on the instantaneous standard deviation values used, to ensure non-distorted pressure diagrams and non-oscillatory pressure derivatives, and hence smooth ROHR diagrams.

Fig. (7.8) shows results obtained with reasonable smoothing of the pressure diagrams for engine conditions shown in Fig. (7.7). The pressure difference diagram shows no distortion, while the oscillations have been damped. The resulting ROHR diagrams exhibit reasonable trends, with the initial peak of the ROHR in the main chamber having disappeared. The effect of smoothing on the pressure derivatives in both chambers is now apparent by comparing Figs. (7.7, 7.8).

The importance of the pressure difference diagram, as a direct method for detecting distortion of pressure diagrams in both chambers due to smoothing, is obvious.

Another observation on the ROHR in the prechamber in Fig. (7.8), is the positive value beyond 40^{o} ATDC. The same effect is shown in Fig. (7.9) which is a part load condition at the same engine speed. This is unrealistic and was brought about in the calculations due to extrapolation of the combustion products equations beyond their range. Over-rich mixtures were predicted, by the ROHR calculation routine, to prevail in the prechamber down the expansion stroke at both the full and part bad running conditions. This also resulted in predicting excessively high gas temperatures as will be shown later (Fig. (7.31)). Detailed investigation of the over-rich mixture properties expressions was outside the scope of the present investigation. Fortunately, over-rich mixtures only occurred on rare occasions, and then only in the prechamber after most of the heat had been released, therefore not affecting the results significantly.

Over-rich mixtures were found to prevail for low engine speed conditions, Figs. (7.8, 7.9), and advanced fuel injection cases, Fig. (7.16), at 2200 rpm.

Fig. (7.9) Heat Release Calculations Results

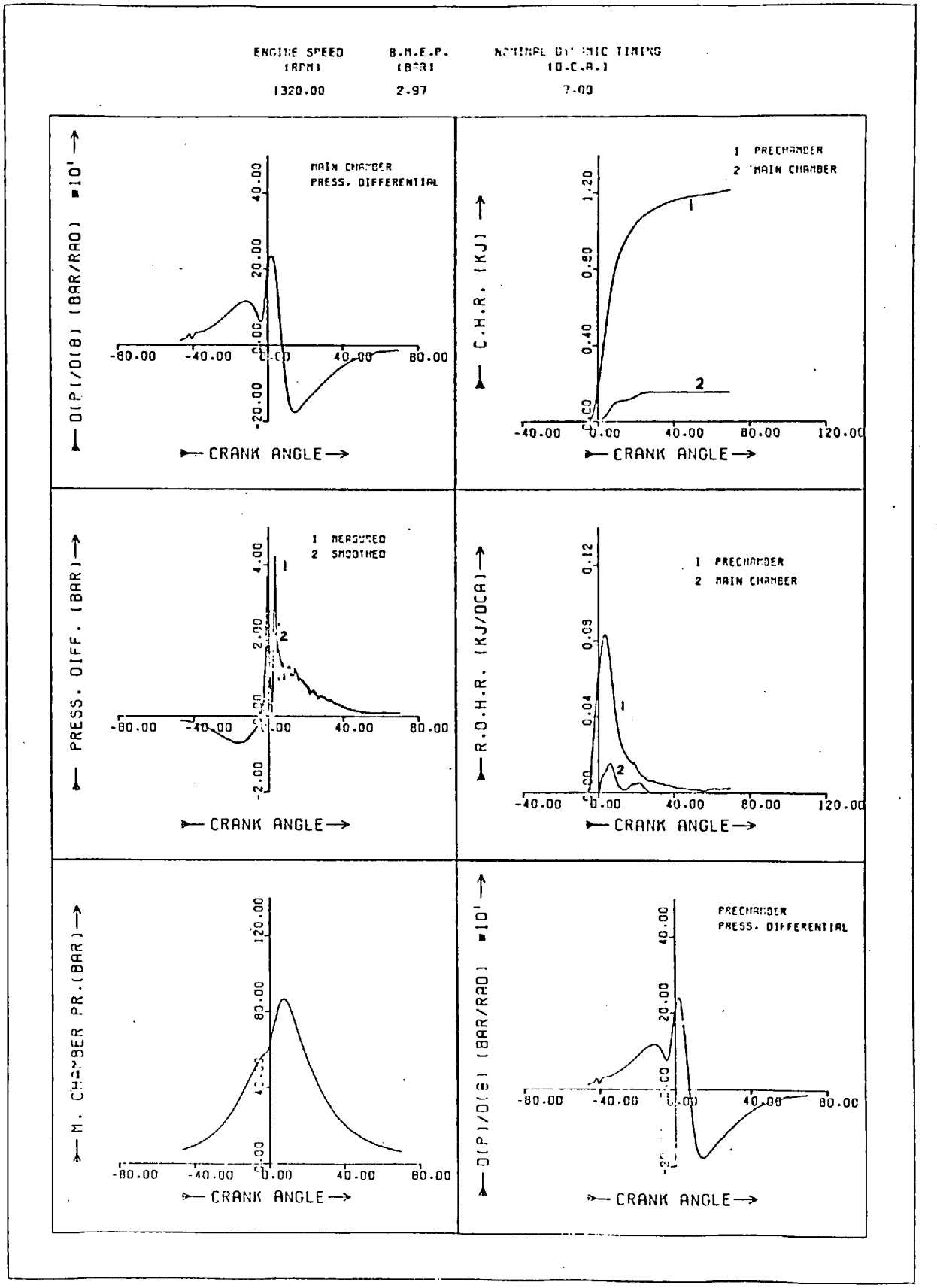

Fig. (7.10) Heat Release Calculations Results

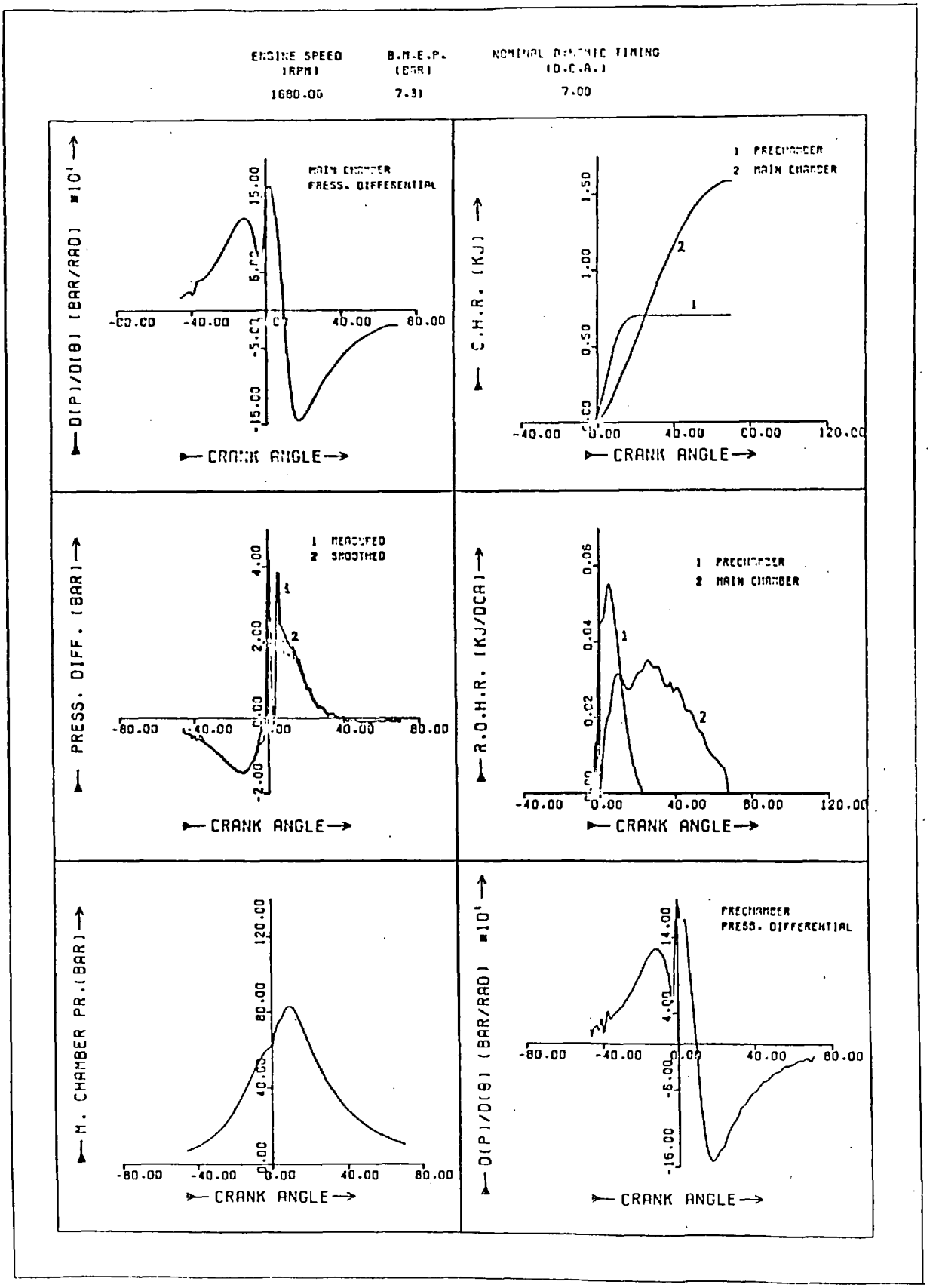

Fig. (7.11) Heat Release Calculations Results

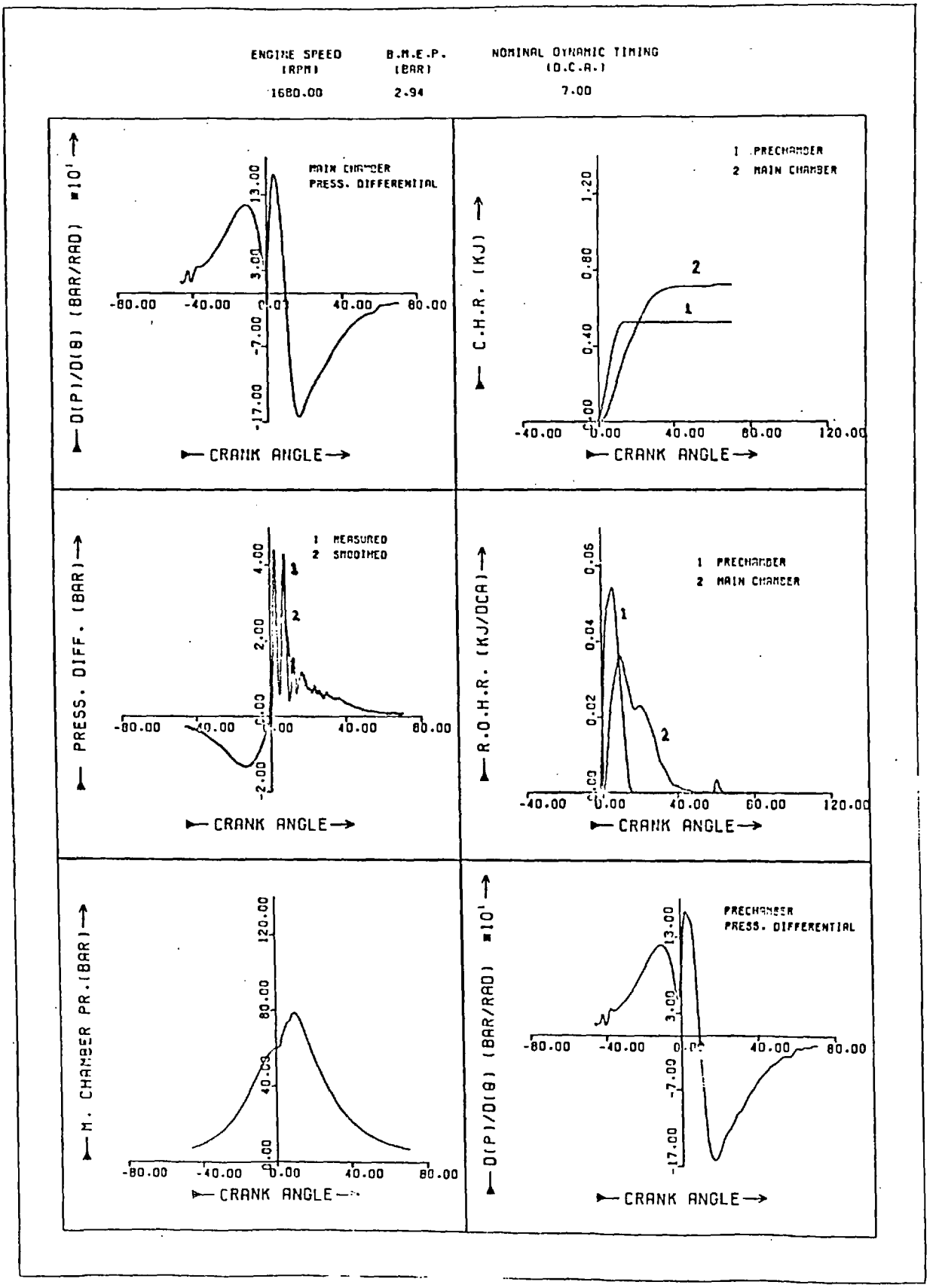

Fig. (7.12) Heat Release Calculations Results

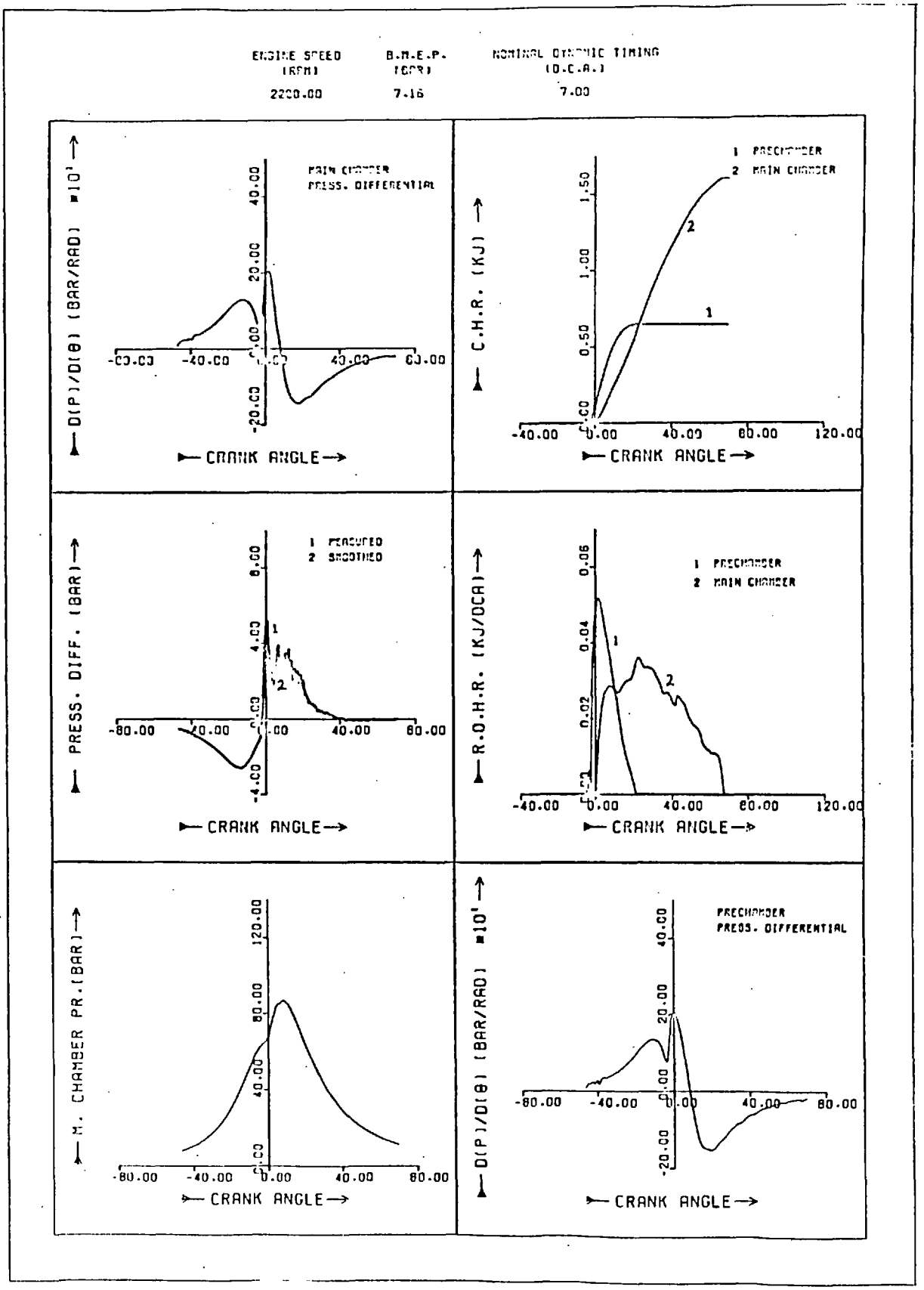

Fig. (7.13) Heat Release Calculations Results

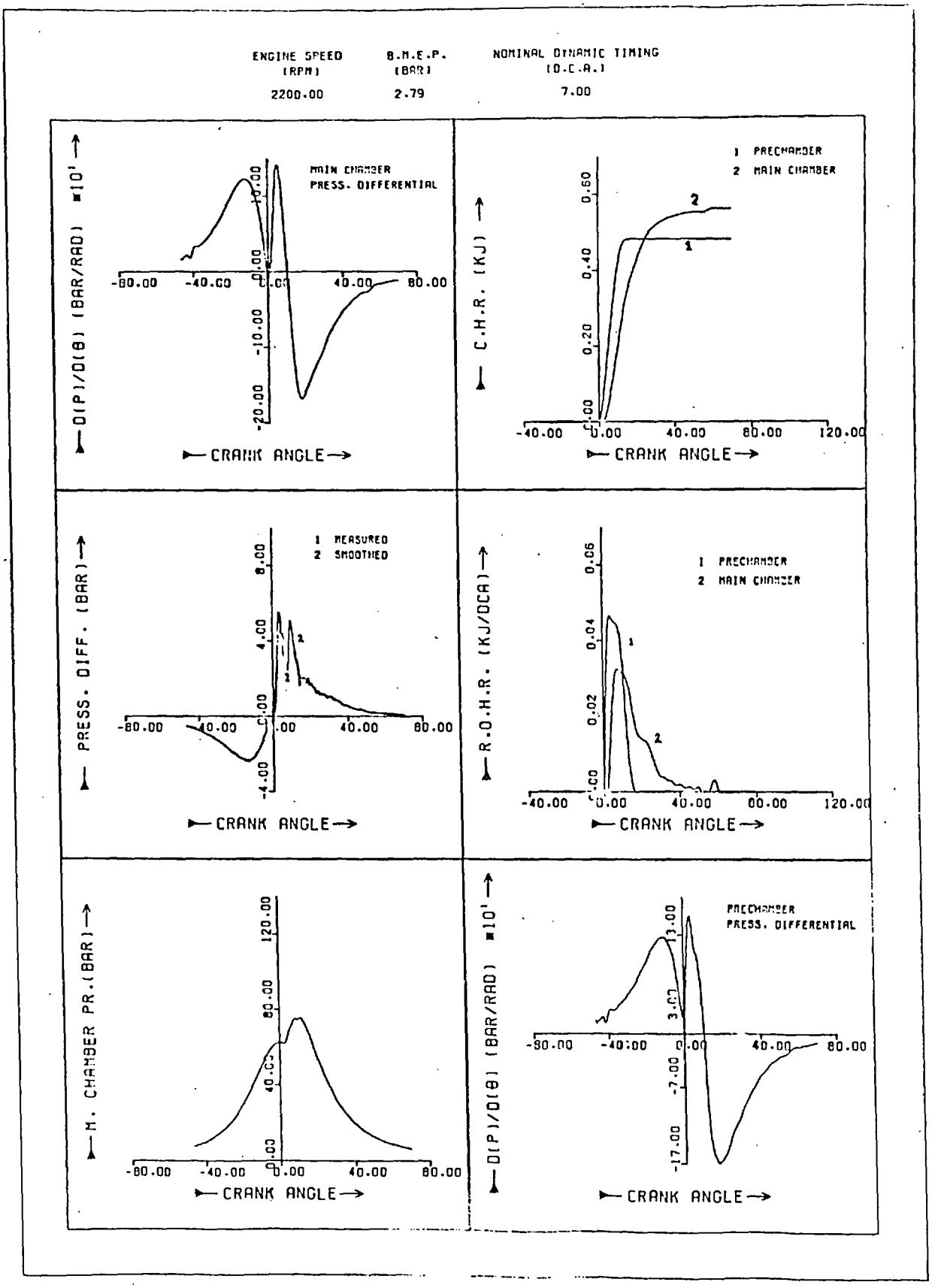

Fig. (7.14) Heat Release Calculations Results

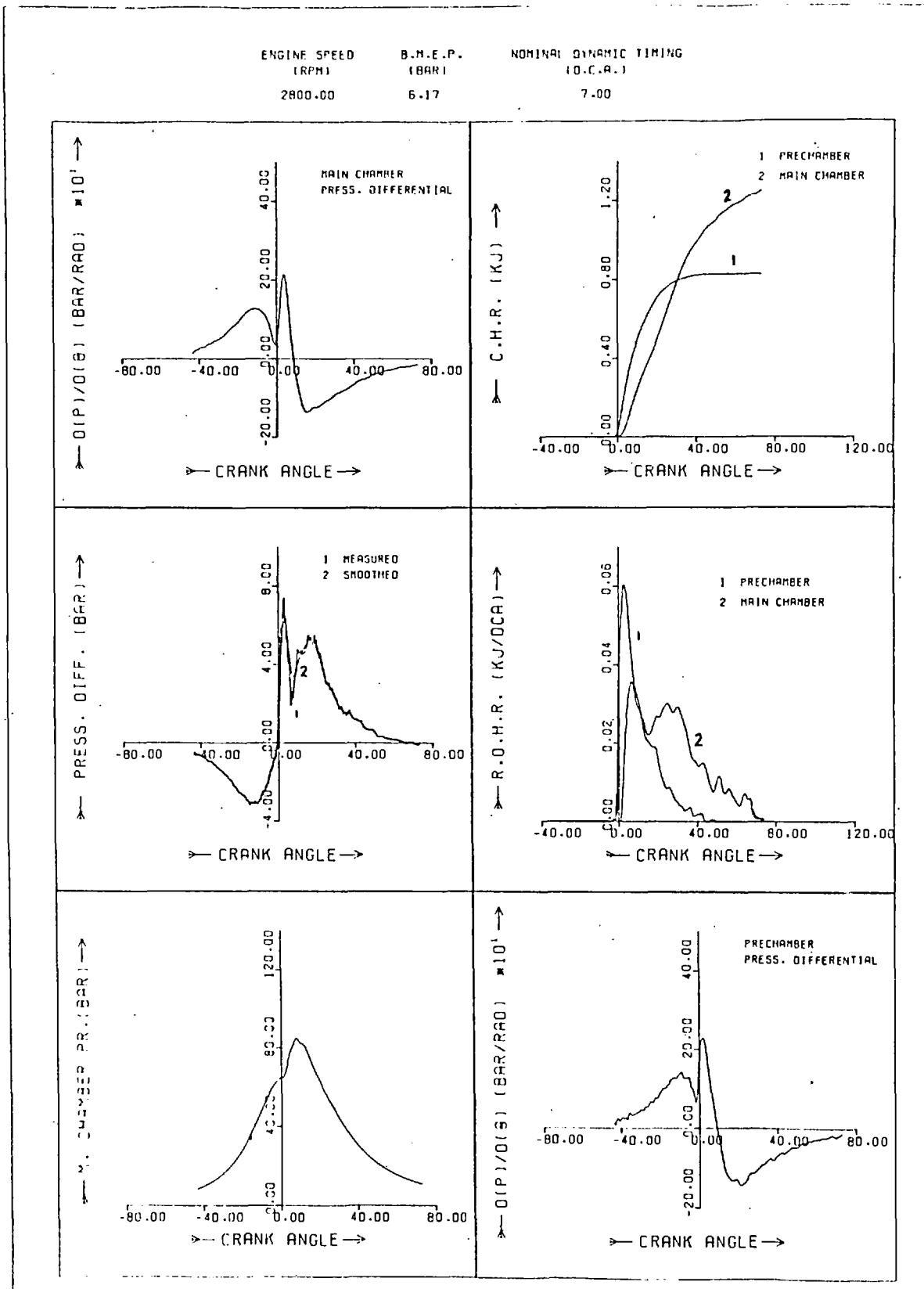

Fig. (7.15) Heat Release Calculations Results

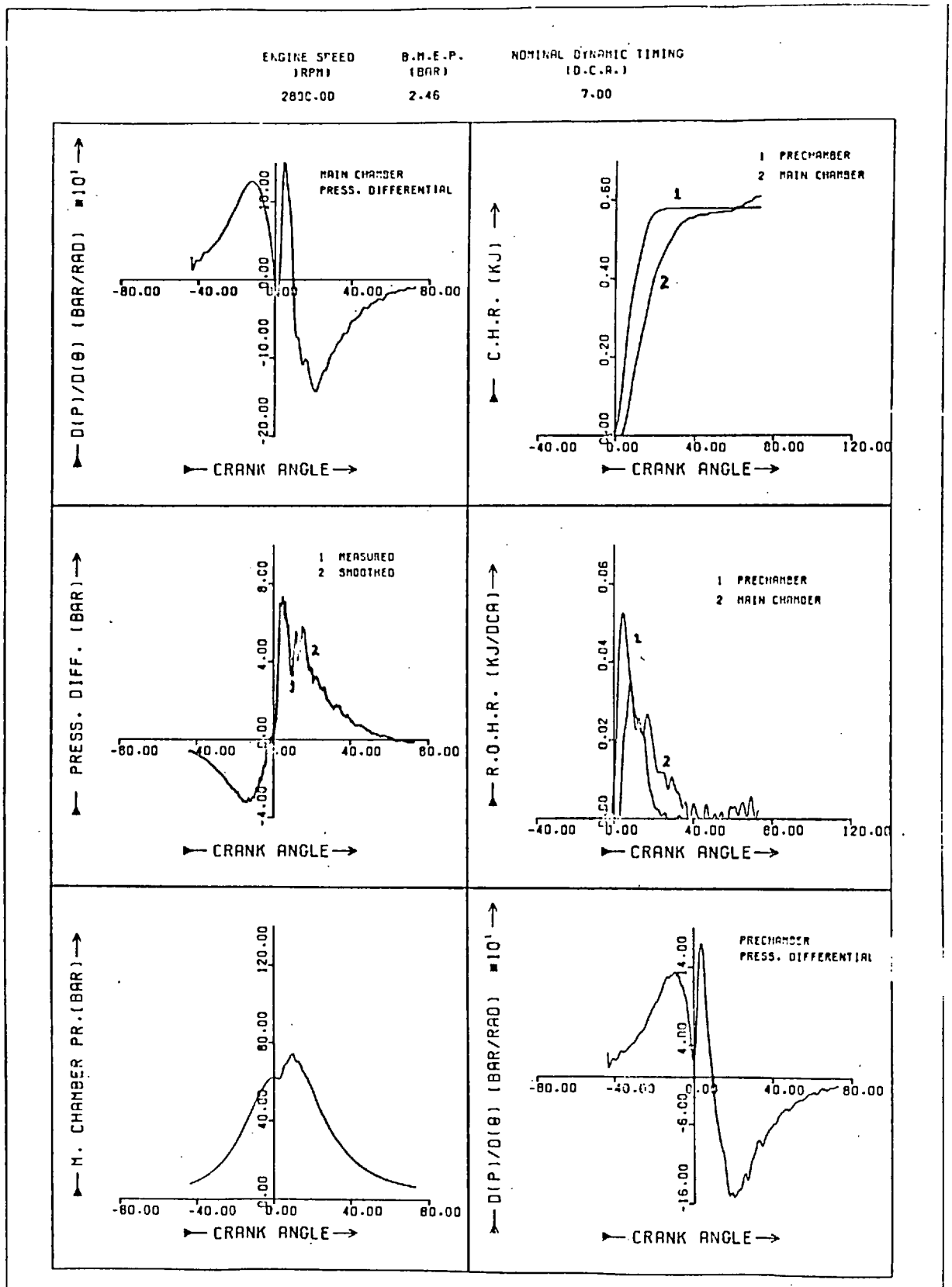

Fig. (7.16) Heat Release Calculations Results

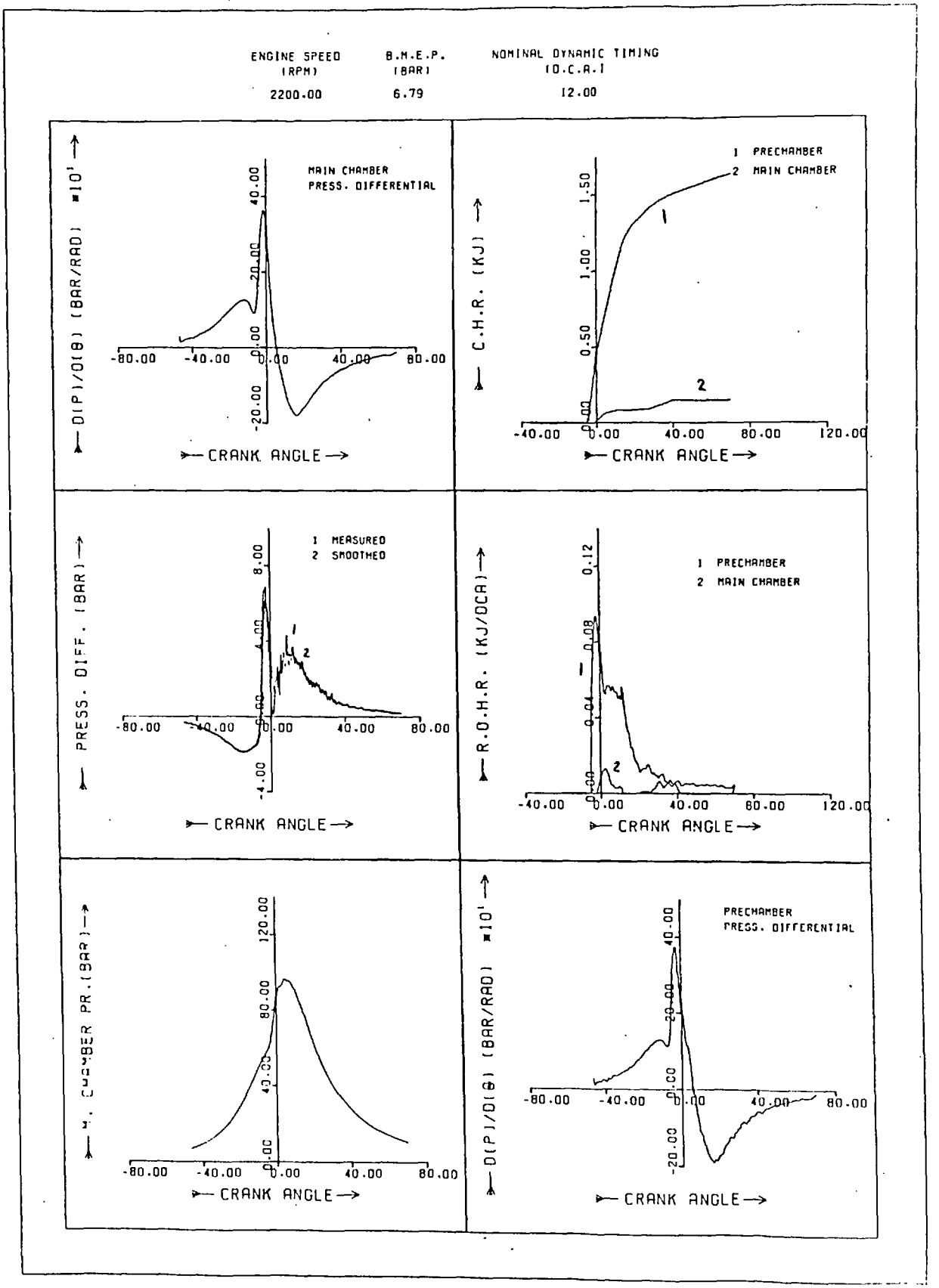

Fig. (7.17) Heat Release Calculations Results

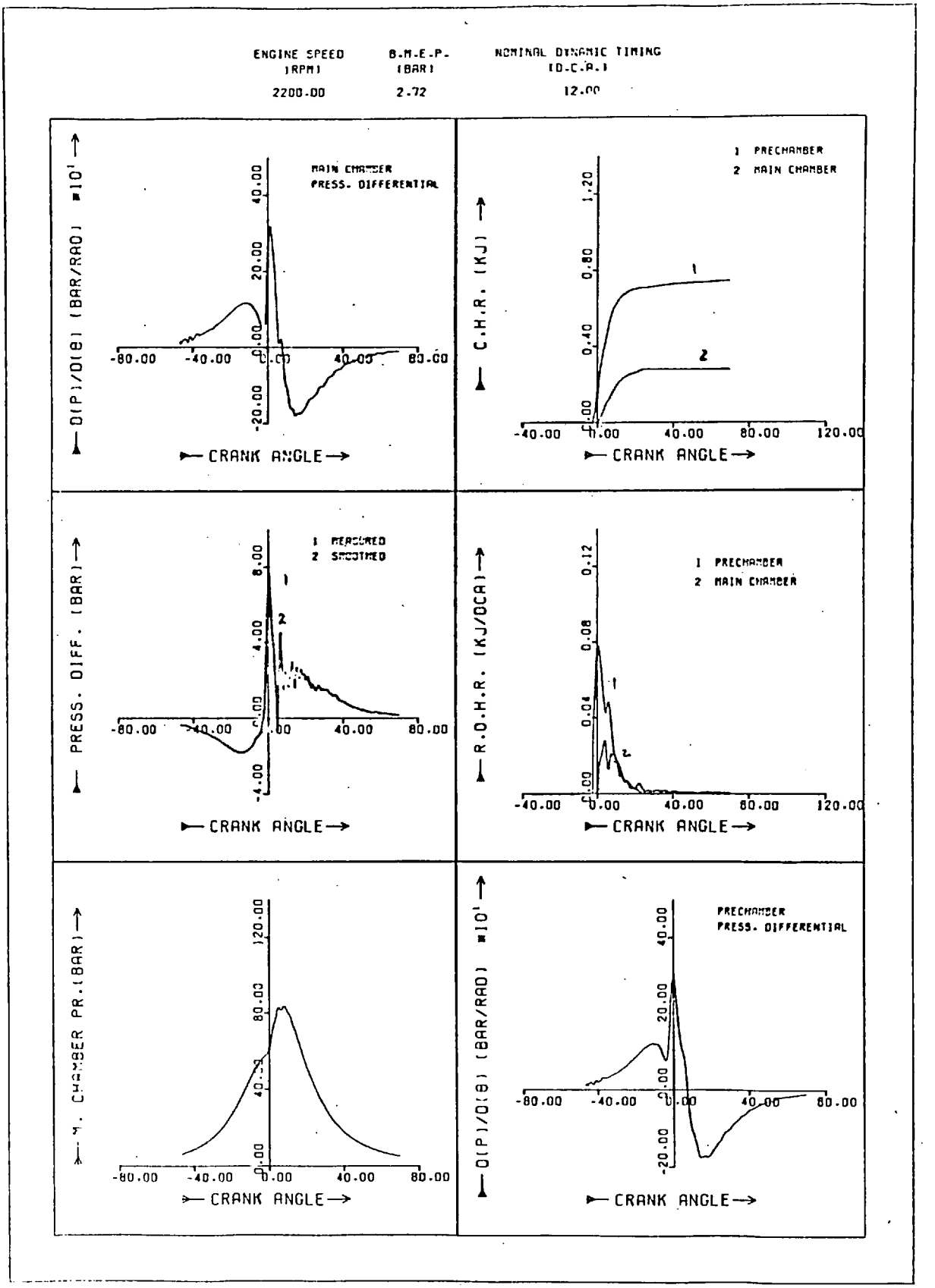

Fig. (7.18) Heat Release Calculations Results

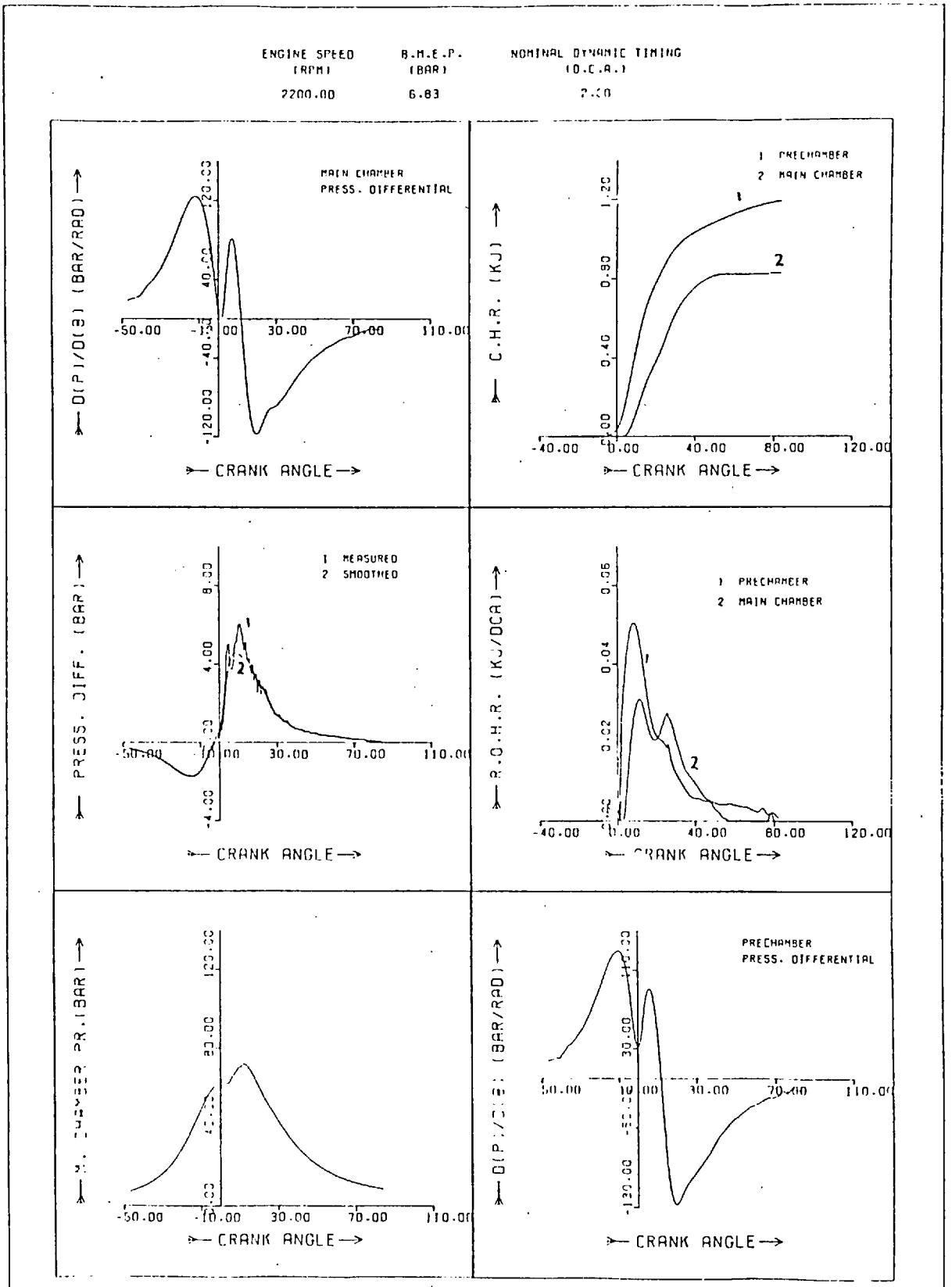

Fig. (7.19) Heat Release Calculations Results

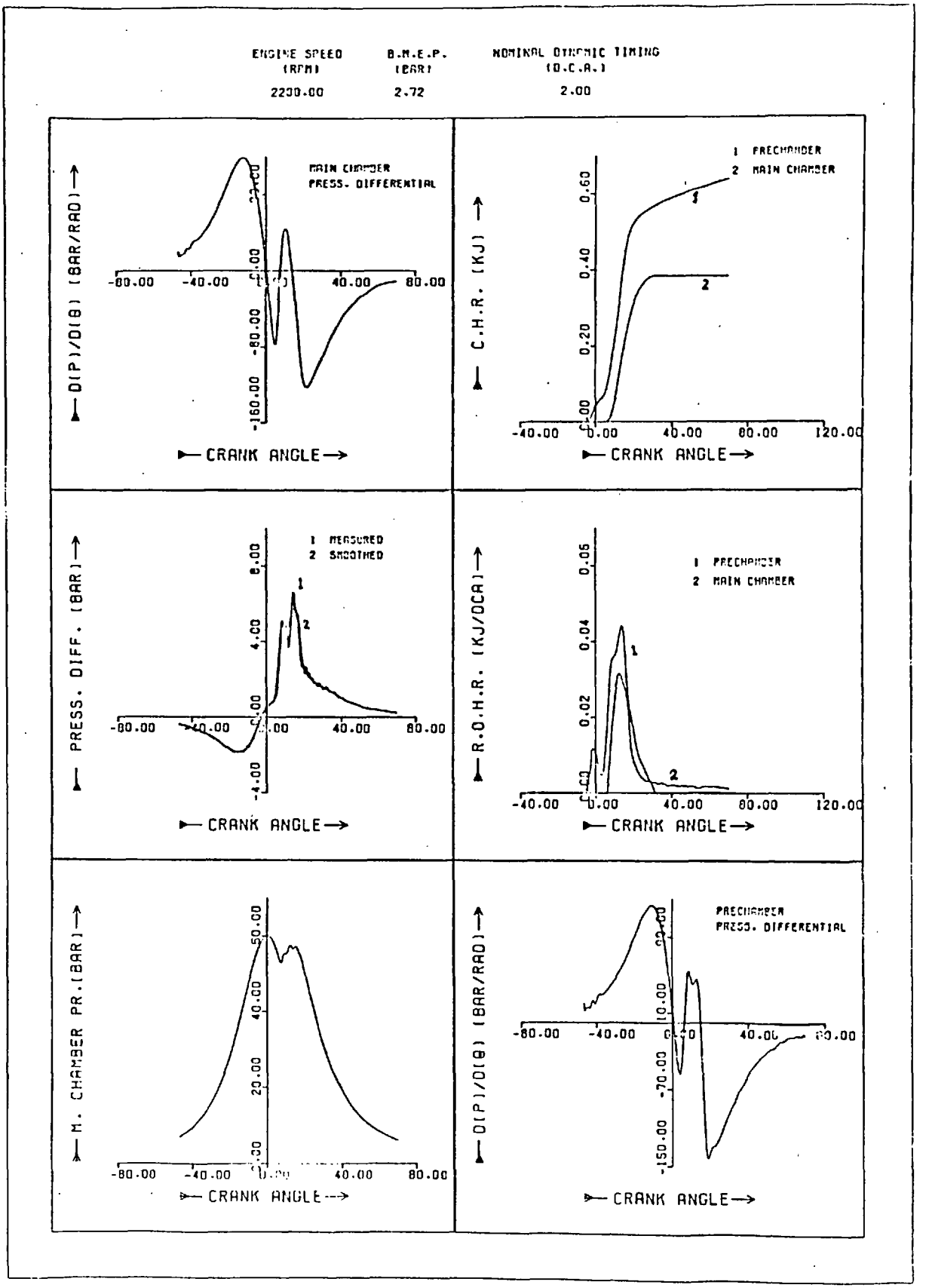

Fig. (7.20) Heat Release Calculations Results

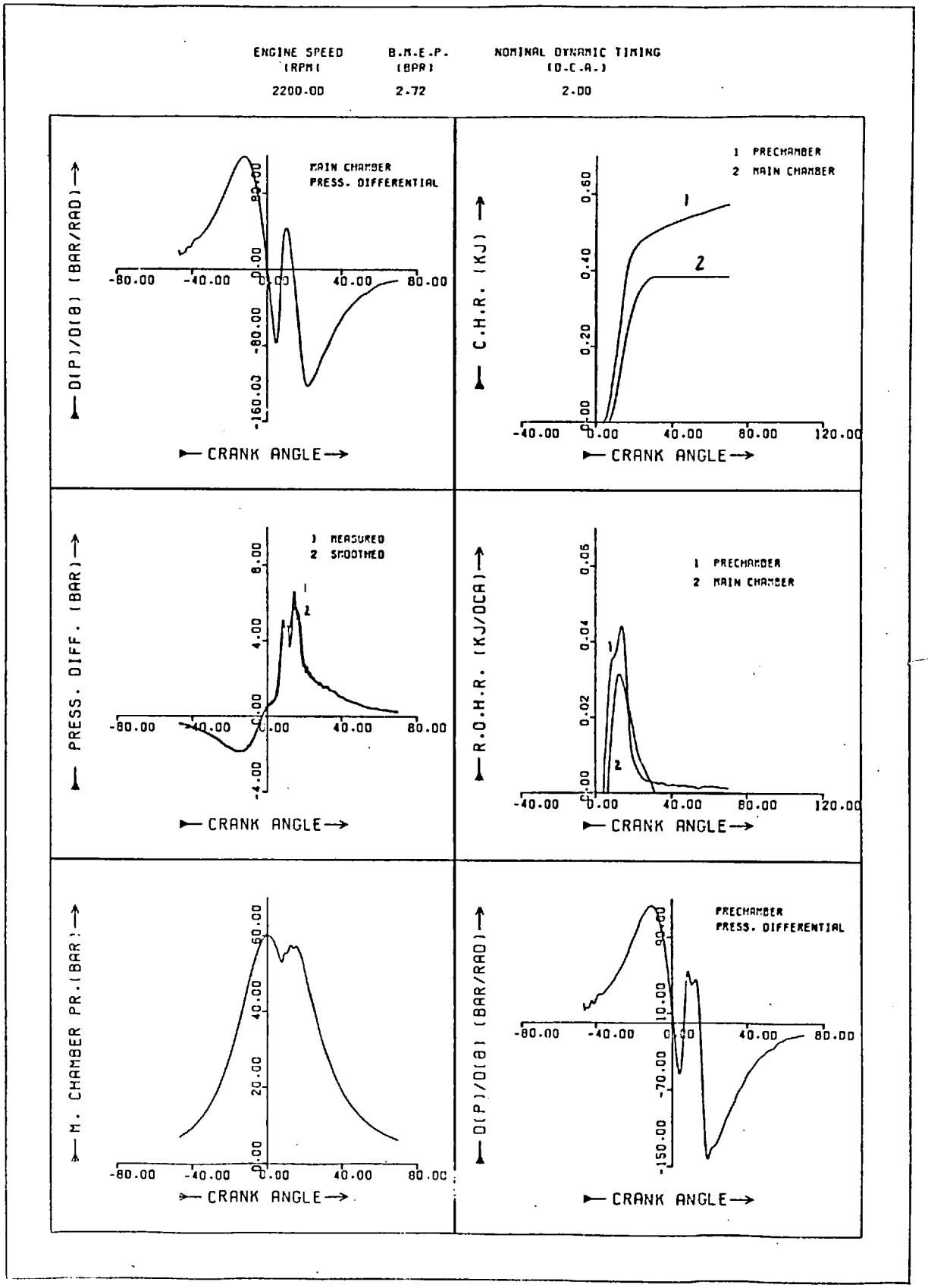

This suggests that a link exists between over-rich mixture formation, and residence time of burning charge in the prechamber. More time is available at both low engine speed and early injection conditions.

Figs. (7.8 to 7.20) show calculated ROHR diagrams for different running conditions covering the entire engine operating range. Effects of speed, load and injection timing were investigated. At all speeds and timings, the effect of reducing engine load is more apparent on the ROHR diagram for the main chamber rather than the prechamber. This is in good agreement with the reasoning that combustion, at particular engine speed and injection timing, proceeds in the prechamber in a specific manner almost irrespective of the amount of fuel injected, i.e. engine load. This is assuming the amount of fuel is sufficient for the full ROHR diagram in the prechamber to be concluded. The effect of load reduction would thus show directly as a reduction of the heat released in the main chamber. Small variations in the shape of the ROHR diagram in the prechamber, under different load conditions, are thought to be due to changes in injection point, ignition delay period and wall and charge temperatures.

Similarity is apparent in ROHR diagrams obtained for full load conditions at 1680 and 2200 rpm (Figs. 7.10 and 7.12), and also between the part load results Figs. (7.11 and 7.13) at the two speeds. Although this could not be explained conclusively as it involves detailed combustion study, similarities are expected in the ROHR diagrams, particularly for the prechamber, since the dynamic injection timing was fixed and variation in ignition delay behaviour (Chapter 6) were found to be small.

Figs. (7.14 and 7.15) demonstrate the high degree of dependence of ROHR calculation on the rate of pressure rise. Oscillations in the rate of pressure rise are directly linked to oscillations in the ROHR curve. This also outlines the importance of pressure diagram smoothing, in order to obtain smooth ROHR diagrams.

In Fig. (7.16), over-rich mixture in the prechamber was experienced. Similarity exists between Fig. (7.16) and (7.8) where over-rich mixtures were also present. In both conditions, ignition occurred considerably earlier than TDC position. This is also indicated in Fig. (7.9) but to a lesser extent. This supports the previously mentioned argument regarding early ignition and over-rich mixture formation in the prechamber.

Another important phenomena in ROHR calculations was experienced for retarded timing conditions. In Figs. (7.18 and 7.19) a positive pressure difference is shown to exist at TDC. This is probably due to the fuel injected leading to increased prechamber pressure. Although this did not affect the calculations for the full load condition (Fig. (7.18)) since ignition occurred very near TDC, the part load condition in Fig. (7.19), shows a demonstrably erroneous heat release in the prechamber before TDC. Delayed ignition is apparent from the pressure difference diagram in the figure, and when heat release calculations were numerically controlled not to commence before TDC, in this particular condition, a more realistic ROHR diagram was obtained as shown in Figs. (7.18 and 7.20).

Satisfactory results were obtained from the ROHR calculation technique developed in the present work over a wide range of engine operation. This gave confidence in the technique, and the thermodynamic and mathematical aspects involved.

7.4 COMPARISONS OF PREDICTED AND MEASURED PERFORMANCE

7.4.1 Fuel Consumption

One of the final results of the heat release calculation was a deduced value of the total fuel burnt in every chamber, and hence the total fuel consumption. To examine the accuracy of the calculation technique, this data was compared with measured fuel consumption. The results are shown in Fig. (7.21). Good overall agreement is indicated. This gave confidence in the validity of the calculation technique in producing realistic ROHR and cumu-

Fig. (7.21) Measured and Calculated Fuel Flows

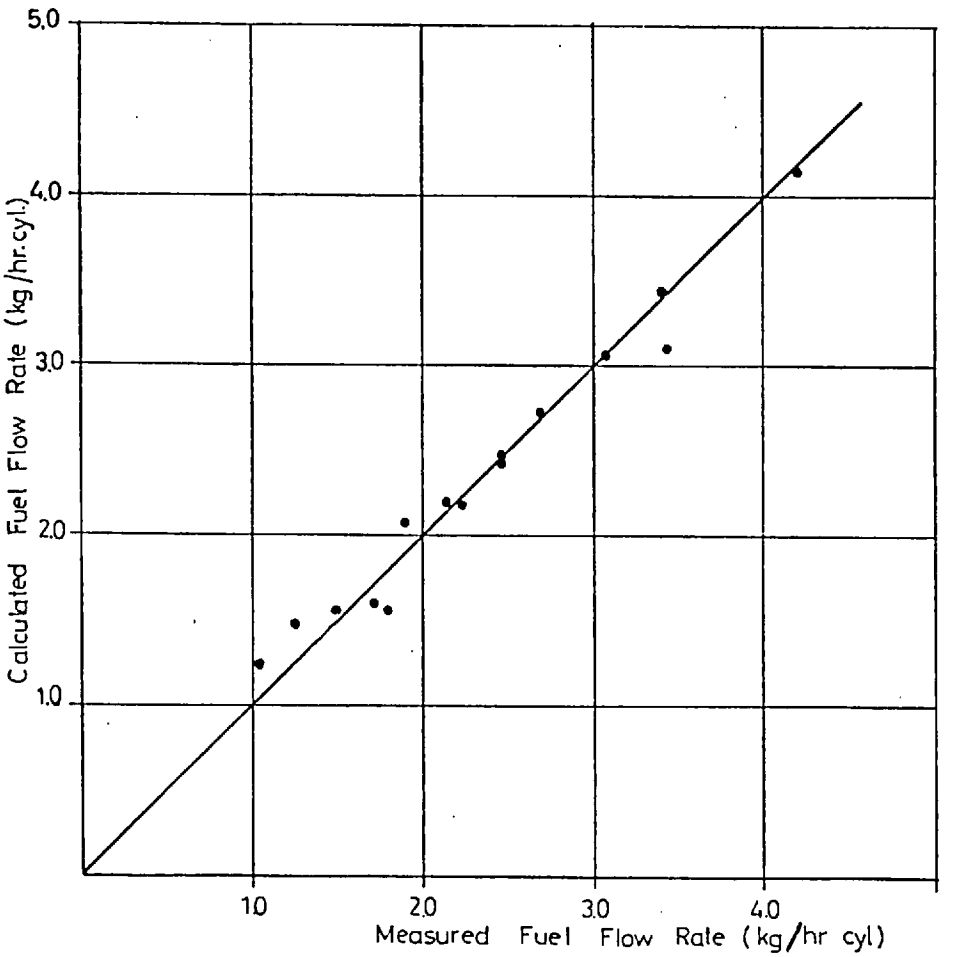

lative heat released and hence total fuel burnt.

7.4.2 Pressure and Pressure Difference Diagrams

Firstly, motored pressures and pressure differences were compared for the measured and predicted values. In the absence of combustion, better judgement of the simulation program could be made. Four monitoring speeds were considered and the comparisons are shown in Figs. (7.22 and 7.23). Favourable agreement is shown between the predicted and measured values. The behaviour of the pressure difference signal is predicted closely for the full speed range. The maximum pressure difference increases with engine speed increase. This is due to increase in pressure ratios across the passage, as a result of faster piston displacement at high speed, and leads to a drop in the passage discharge coefficient (see Chapter 5). Increased peak pressures at high engine speeds are expected to result from a reduction of heat loss to the walls.

For passage flow to the prechamber, the maximum pressure difference is shown to be lower than that in the reverse direction. The predicted behaviour shows the same trend. This supports the assumptions concerning the effect of the proximity of the piston on the passage discharge coefficient (section 5.4). Although the forward flow direction had essentially a lower C_d value than the reverse direction, as the piston approaches TDC, the value of C_d increases readily due to the approach velocity effects upstream of the passage.

At 2800 rpm, differences are shown to exist, in both the cylinder pressure and pressure difference diagrams, between measured and predicted value. It was shown in section (7.2) that, shifting of the peak cylinder pressure occurred at this speed. Since passage flow inertia was not included in the calculations, a shifting of the pressure diagram seems to exist between measured and predicted behaviour.

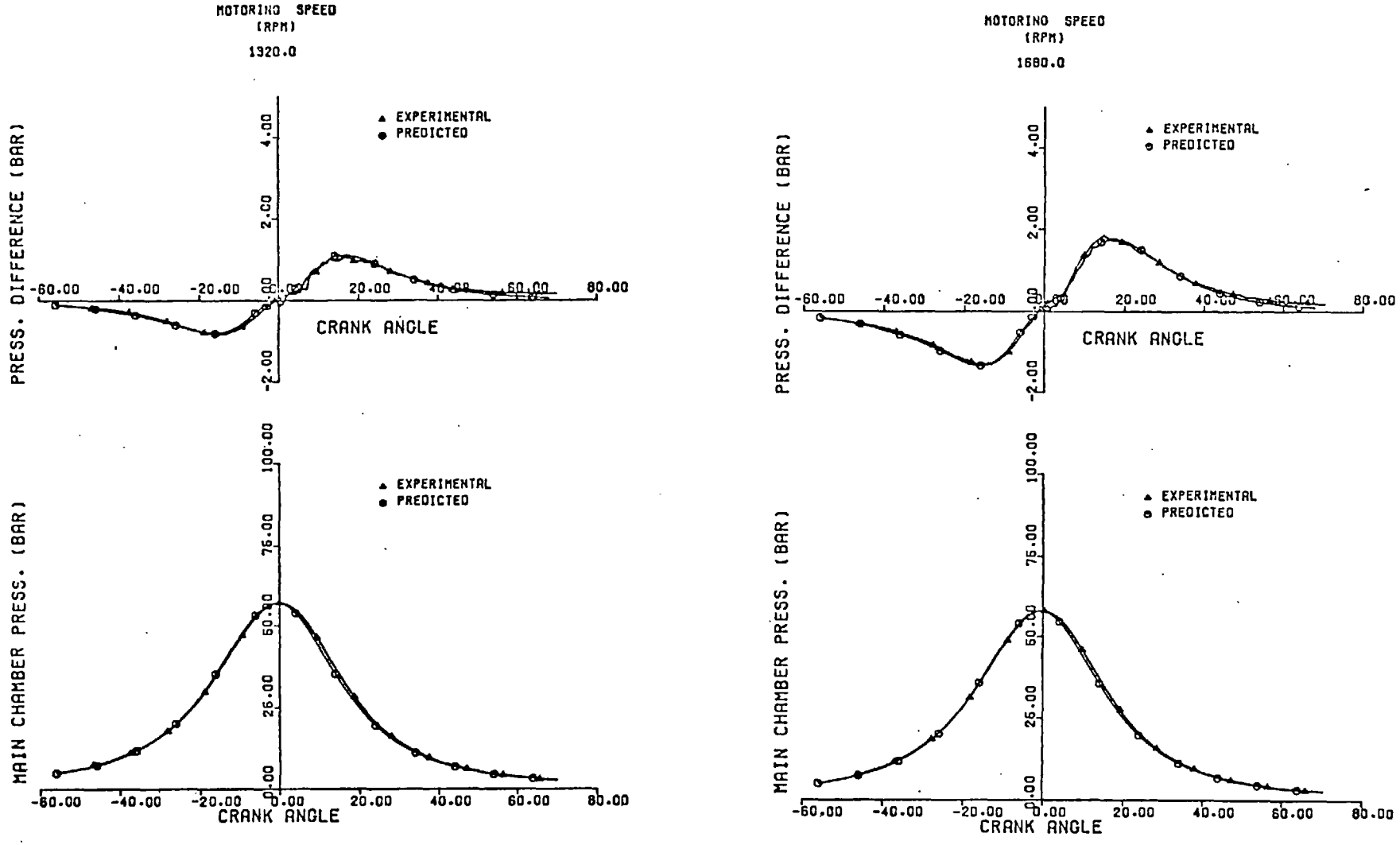

Fig. (7.22) Predicted and Experimental Pressures and Pressure Differences under Motoring Conditions

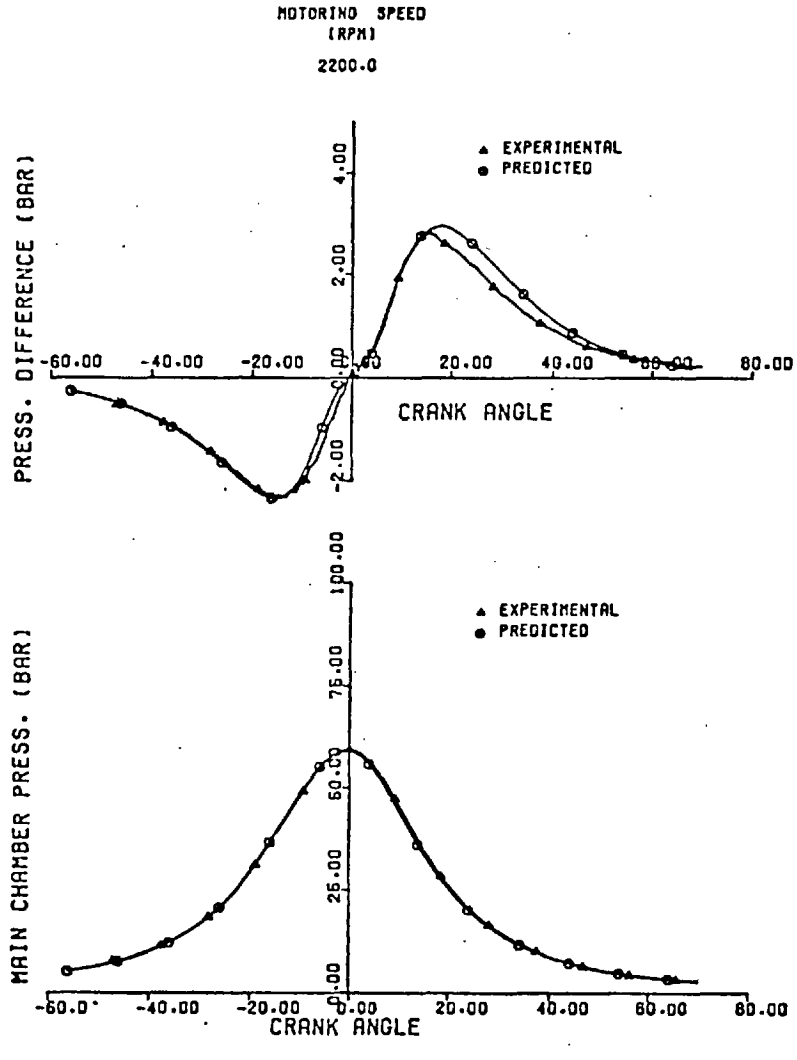

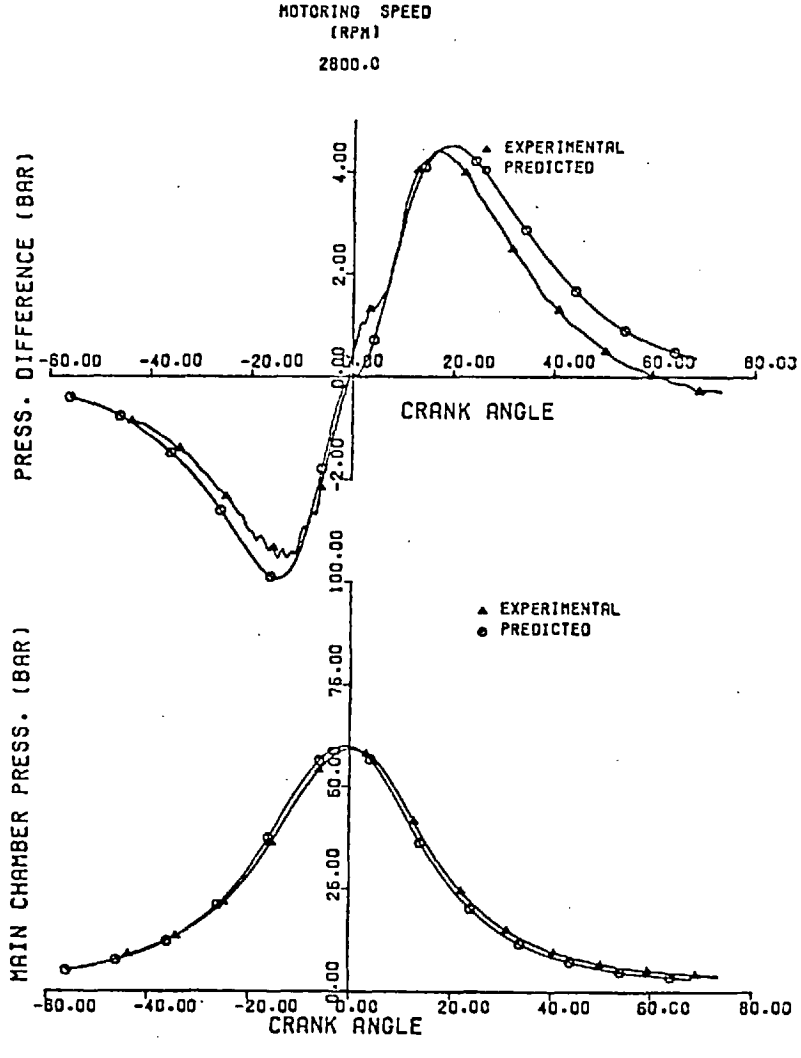

Fig. (7.23) Predicted and Experimental Pressures and Pressure Differences under Motoring Conditions

For fired operation, the ROHR diagrams obtained (see section 7.3) were used as input data for the cycle analysis program. The predicted and measured cylinder pressure and pressure difference diagrams are compared in Figs. (7.24) to (7.28). The figures show different engine running conditions covering the full range of operation i.e. engine speed, load and injection timing. Figs. (7.24) and (7.25) show full load runs at four engine speeds. Figs. (7.26) and (7.27) are for 40% load runs at four engine speeds. All the above mentioned runs are for a standard 7^{o} CA dynamic injection timing BTDC. Fig. (7.28) shows two part load runs at 2200 rpm engine speed, and dynamic injection timings of 2^{o} and 12^{o} BTDC. In all the figures it is clear that the oscillations in the pressure difference curves are not present. This is mainly due to the fact that the ROHR values were obtained from smoothed experimental pressure diagrams. Differences between predicted and measured pressure and pressure difference diagrams shown in Figs. (7.24) to (7.28) are generally small.

Differences are shown to be more pronounced near the peak pressure part of the cycle. This is expected to be mainly due to the damping effect on the initial rates of pressure rise due to smoothing. The figures provide support for this argument as the differences are shown to increase when the initial pressure difference peak is very much reduced in the prediction, Fig. (7.24 and 7.25) (1680 rpm) and Fig. (7.27) (2200 rpm). Examining Figs. (7.10, 7.11 and 7.13) show that the smoothed pressure difference diagrams show the same trend. The remarks made concerning the 2800 rpm results still apply.

For the ROHR calculations only the closed part of the engine cycle was considered. The simulation program, on the other hand, dealt with the full cycle, which entitled the inclusion of valve flows. Valve flow areas were approximated as shown in Chapter 3, with the resulting approximation of trapped conditions. This is believed to be a source of error in predicted pressures and pressure differences. Assumptions made concerning heat flux

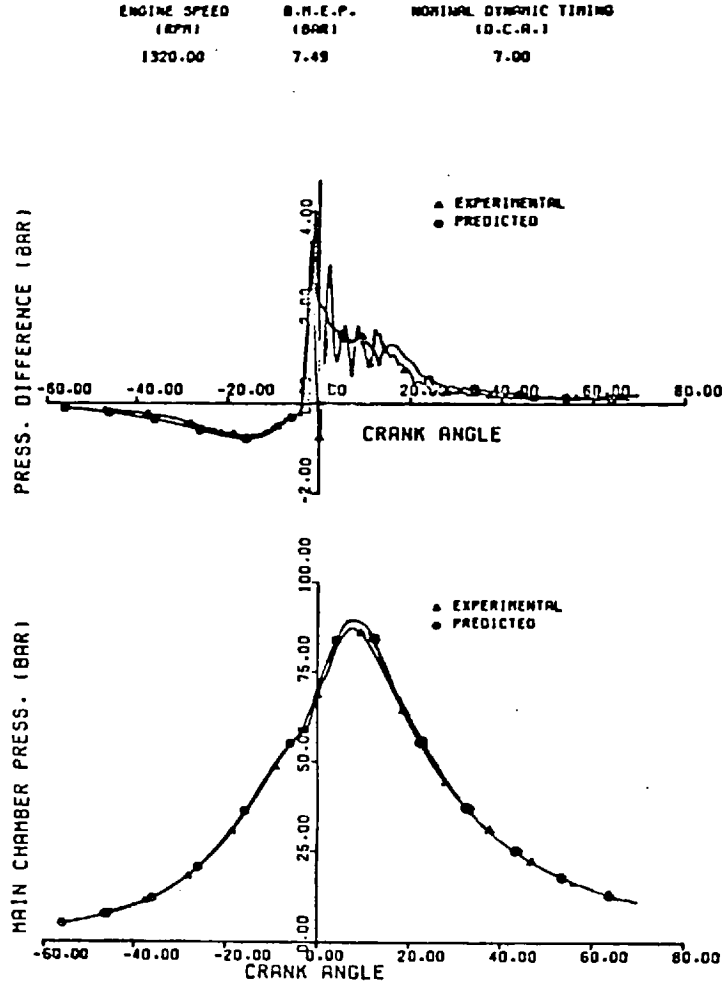

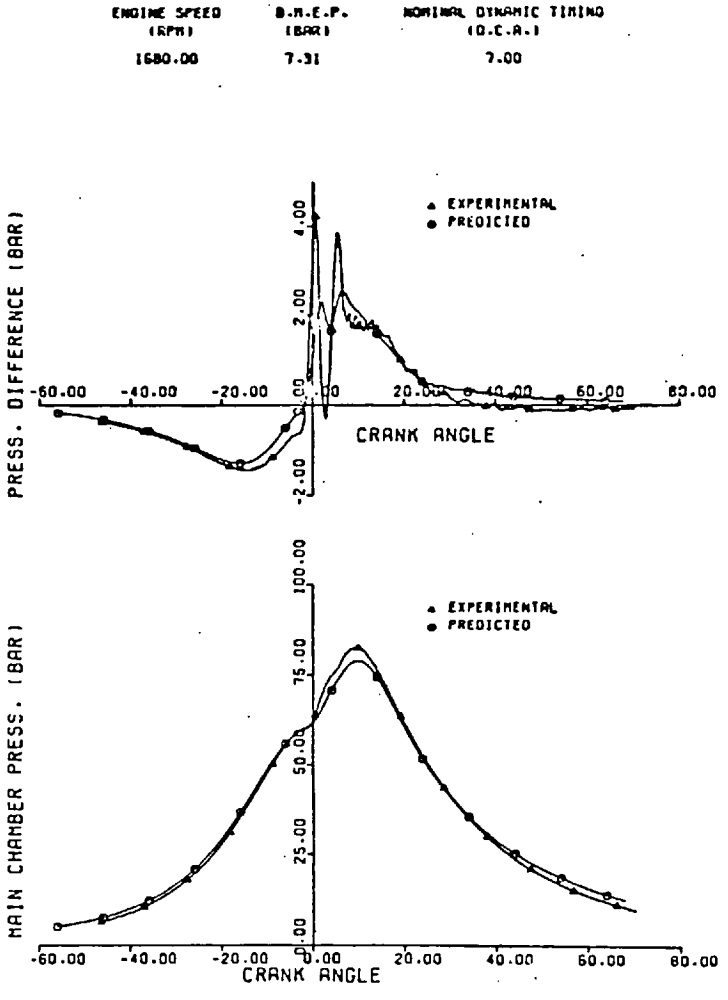

Fig. (7.24) Predicted and Experimental Pressures and Pressure Differences for Full Load Conditions

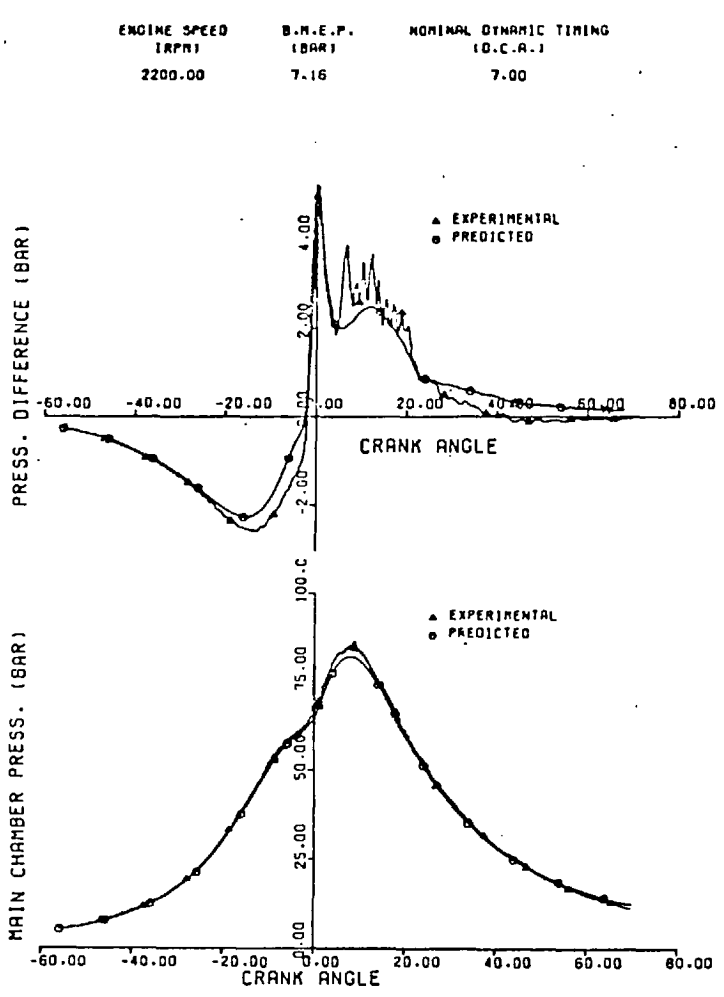

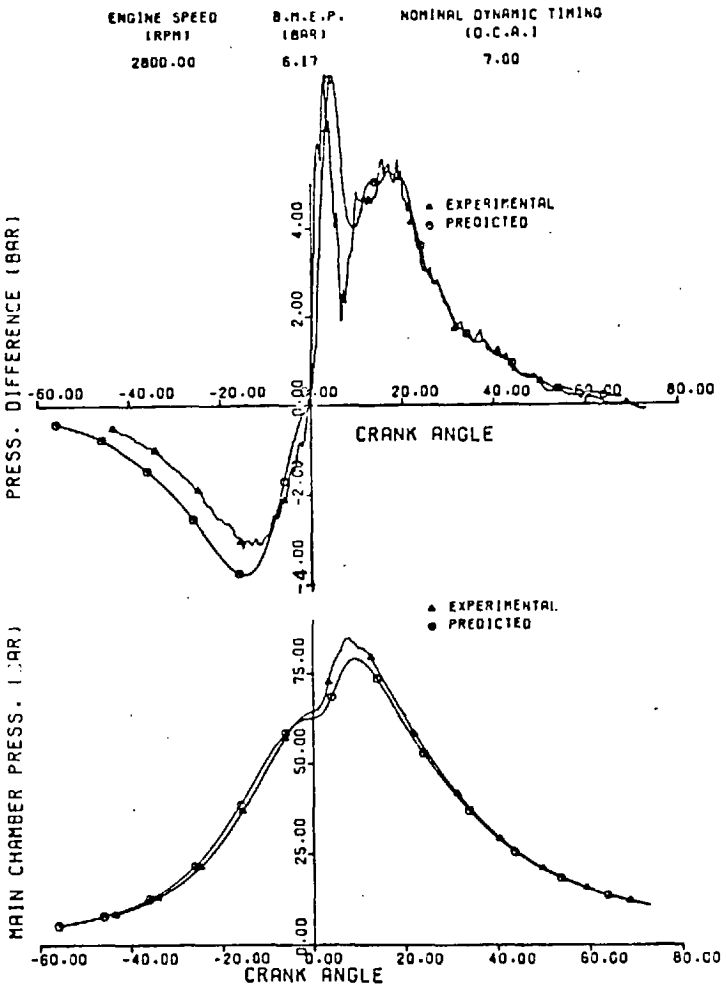

Fig. (7.25) Predicted and Experimental Pressures and Pressure Differences for Full Load Conditions

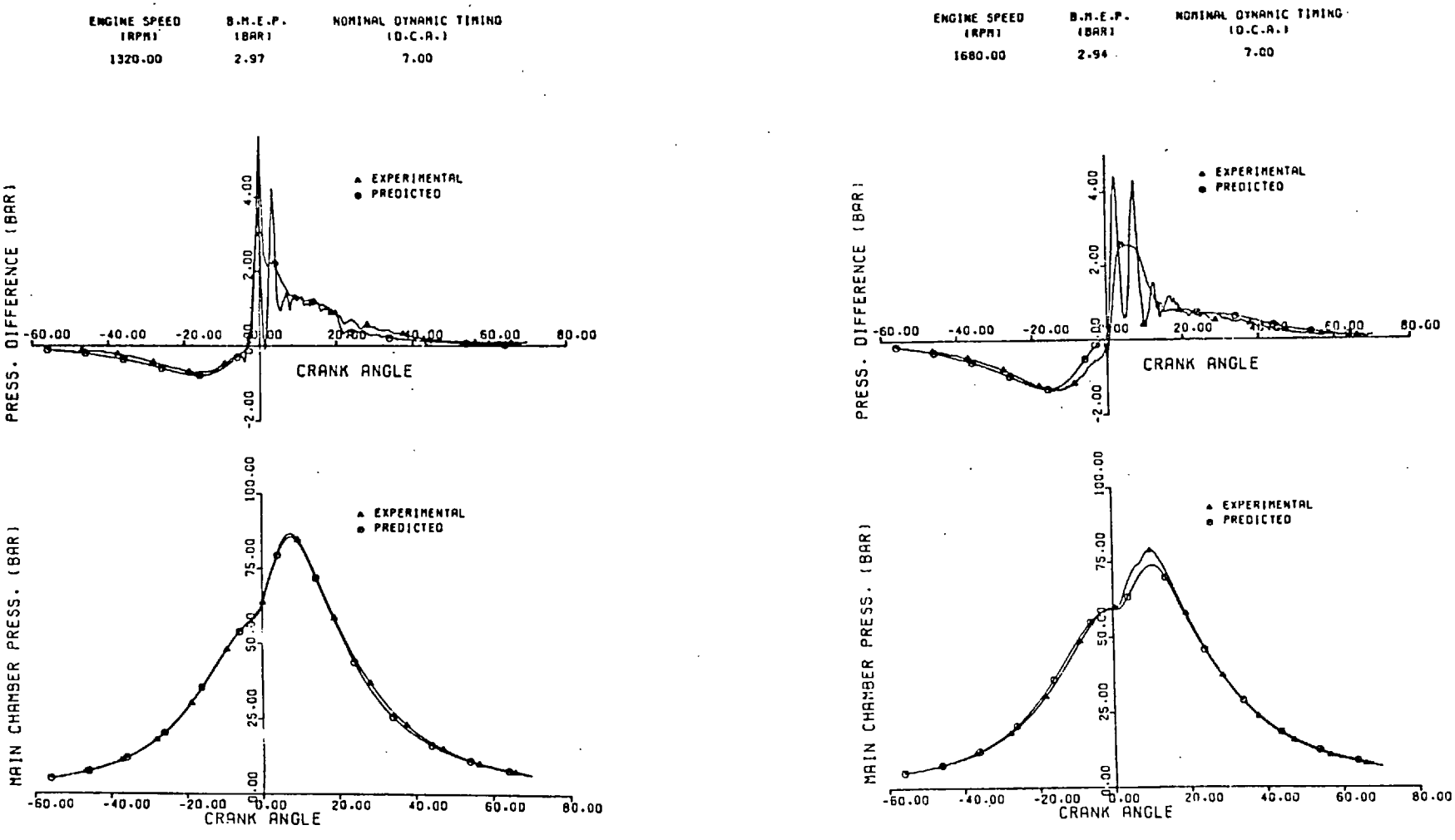

Fig. (7.26) Predicted and Experimental Pressures and Pressure Differences for 40% Load Conditions

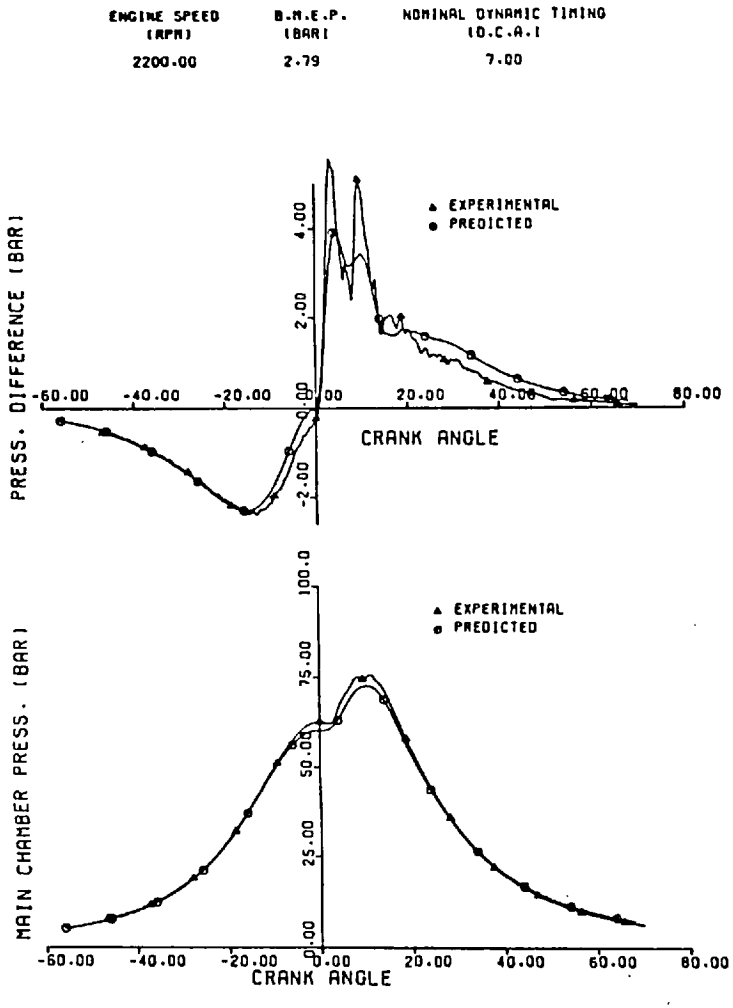

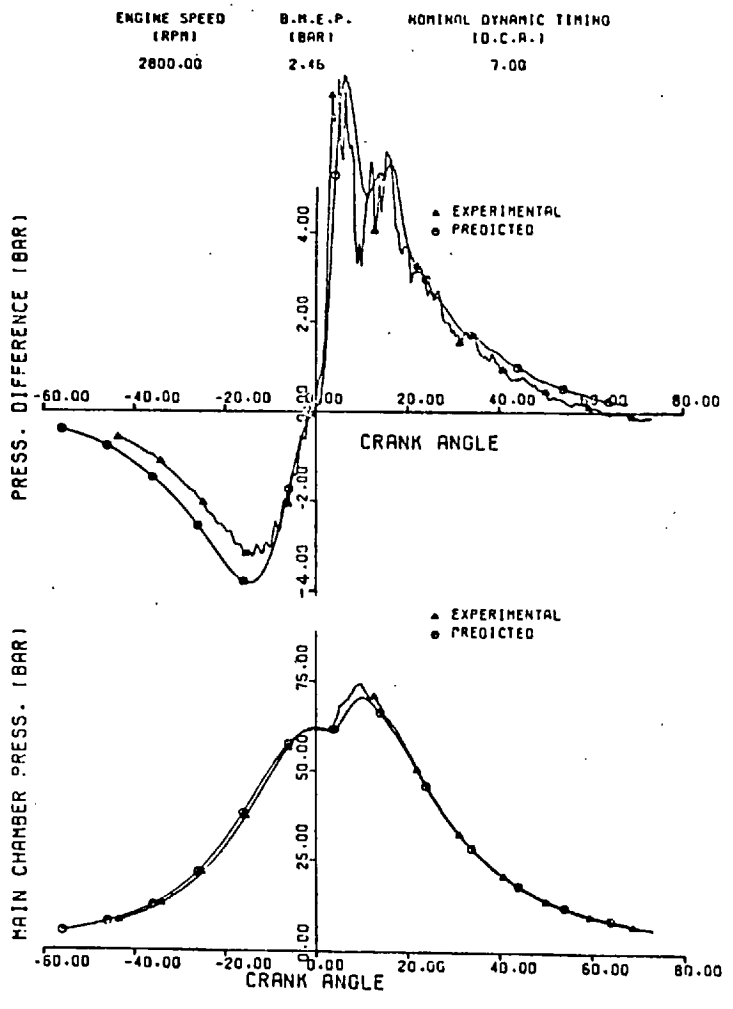

Fig. (7.27) Predicted and Experimental Pressures and Pressure Differences for 40% Load Conditions

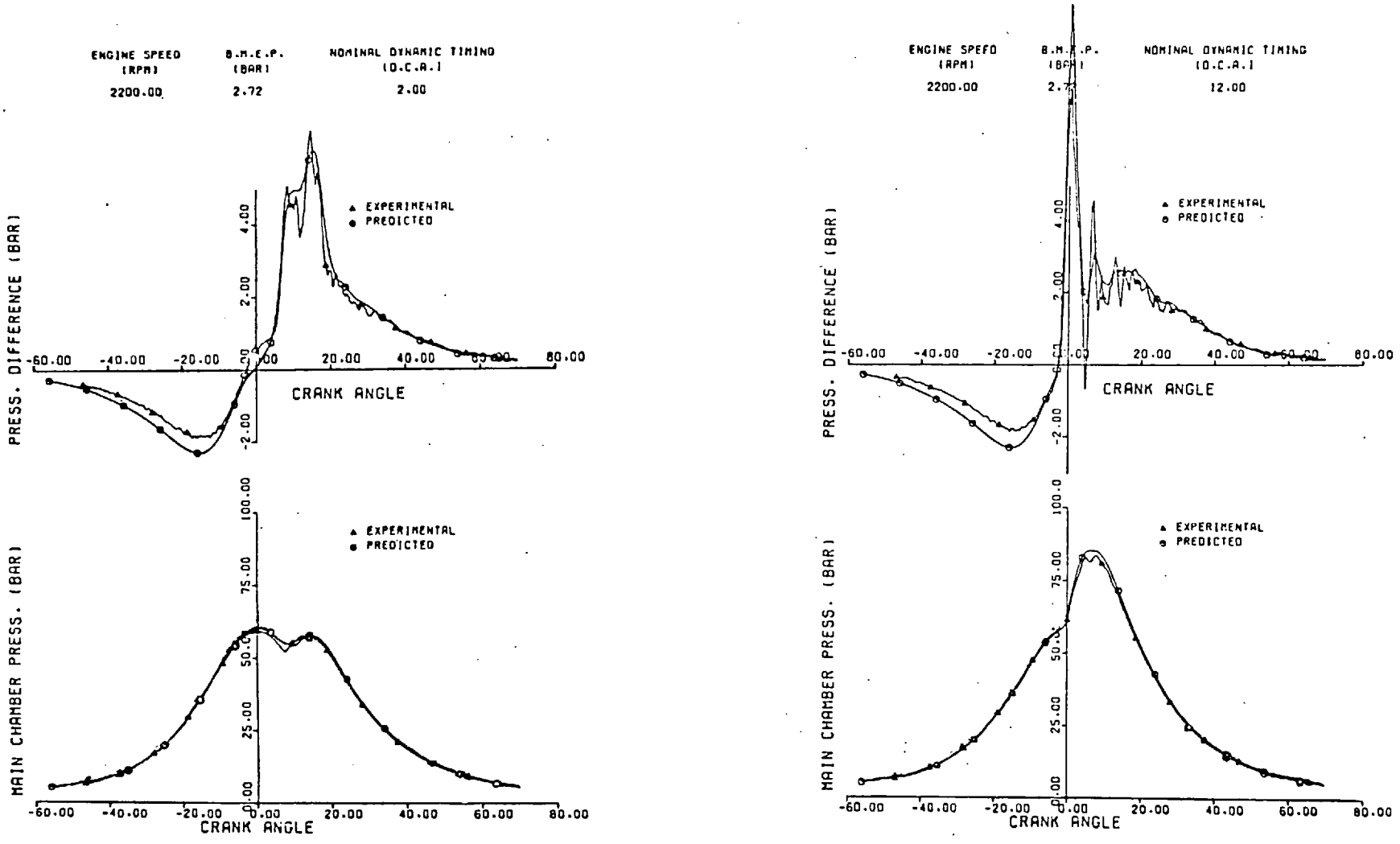

Fig. (7.28) Predicted and Experimental Results for Different Dynamic Injection Timings

distribution in the main chamber also could result in small errors in predicted main chamber pressure, which can also introduce errors in the pressure difference between the two chambers.

The predicted pressures and pressure differences, however, show an overall good agreement with the measured behaviour. Conditions covering a wide range of engine operation were covered and satisfactory results obtained.

7.4.3 Motoring and Friction Mean Effective Pressures

An attempt has been made to measure indicated mean effective pressures (IMEP) for the engine tested during motored and fired operation, by integrating measured instantaneous (P.dV) values over the full engine cycle. As exaplined by Brown (25) and Alyea (5), (IMEP) measurements require extreme accuracy in measuring instantaneous values of cylinder pressure and volume. Brown also outlined that the low pressure part of the cycle contributes even more to the total IMEP then the high pressure part. In contrast to Brown's work, in the present investigation the high pressure part of the cycle was the most important part, for the heat release calculations. Also the accuracy of the pressure measurements was dictated by the peak pressure expected and the Analogue-to-Digital conversion accuracy. This resulted in a pressure measurement accuracy of within ±0.138 Bar. In the low pressure part of the cycle, e.g. during the gas exchange part, this amounts to more than ±10% error in measured pressure.

Regarding instantaneous cylinder volume measurement, the digitizer provided a train of pulses defining the instantaneous crank positions which was used to define piston position, and thus the volume. The accuracy of position identification was $\pm 0.35^{o}$ CA. According to Brown (25) this would result in a phase-shift error in the measured IMEP of ±3.5%. Lancaster et al (64) also reported the need to average 300 cycles for a ±3% accuracy of measured IMEP.

From the above discussion, it is clear that the accuracy of IMEP measurement in this work is poor. However, IMEP measurement was outside the scope

Table 7.1

Measured Motoring M E P (BAR)

Speed (rpm)	Total	Closed Cycle
1320	0.91288	0.7805
1680	1.01264	0.72748
2200	1.1655	0.61616
2800	1.4376	0.6105

Closed cycle values define values obtained for the part of the engine cycle when all valves are closed.

Fig. (7.29) Motoring MEP Variation with Engine Speed

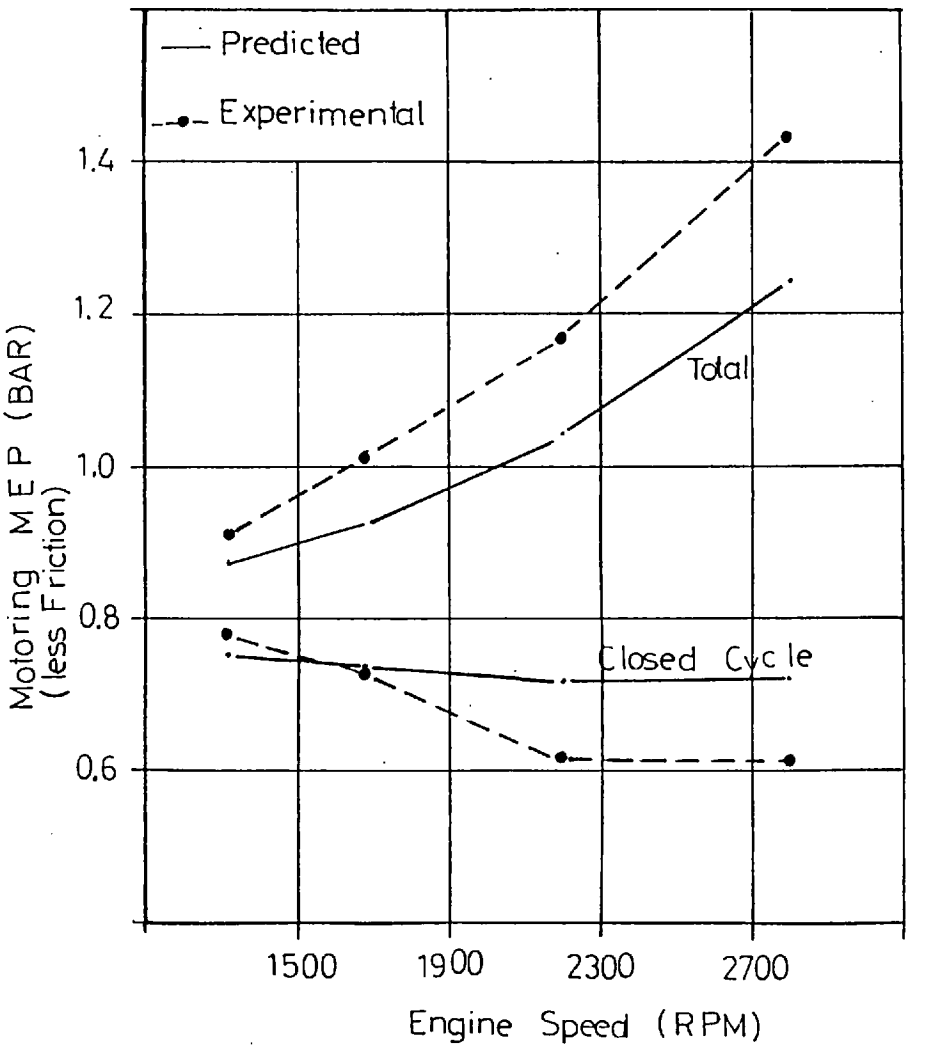

of this work and was only attempted in order to test the predicted behaviour against the trend of the measured IMEP. The friction mean effective pressures were calculated from the measured indicated and break mean effective pressures for the fired runs. Although they showed the expected trend with engine speed, they were too low to be considered as realistic (compared to expected values e.g. Ref. (112)), and are not shown.

The motoring mean effective pressure were also measured using the same technique. In the simulation program, the instantaneous piston work was integrated to obtain a predicted value for the motoring MEP, at the corresponding motoring speed. The measured and predicted values of the motoring MEP are shown in Table (8.1) and Fig. (7.29). It is clear from Fig. (7.29) that the motoring MEP values predicted by the simulation program follow the measured trend of variation with engine speed. The difference between the measured and predicted values shows an average error of 11% which is within the range of experimental error mentioned. Better measurement accuracy is required to arrive at firm conclusions.

7.5 COMBUSTION CHAMBER INTERACTION

The full cycle analysis program was used to predict instantaneous conditions inside the cylinder and the prechamber of the engine cylinder. Different running conditions were predicted for fired engine operation using the calculated heat release curves. The results of these predictions are shown in Figs. (7.30) to (7.38). The figures show, main chamber pressures, pressure differences between the main chamber and the prechamber, the instantaneous temperature and equivalence ratio in each chamber and the velocity estimates and charge mass in each chamber. Fig. (7.31) is of particular interest as it shows a running condition for which the prediction fails due to inadequate charge property relations. The prechamber temperature shows a rising trend near 200^{o} ATDC. This is unrealistic, as there should be no heat release

Fig. (7.30) Full Cycle Predictions Showing Combustion Chamber Interaction

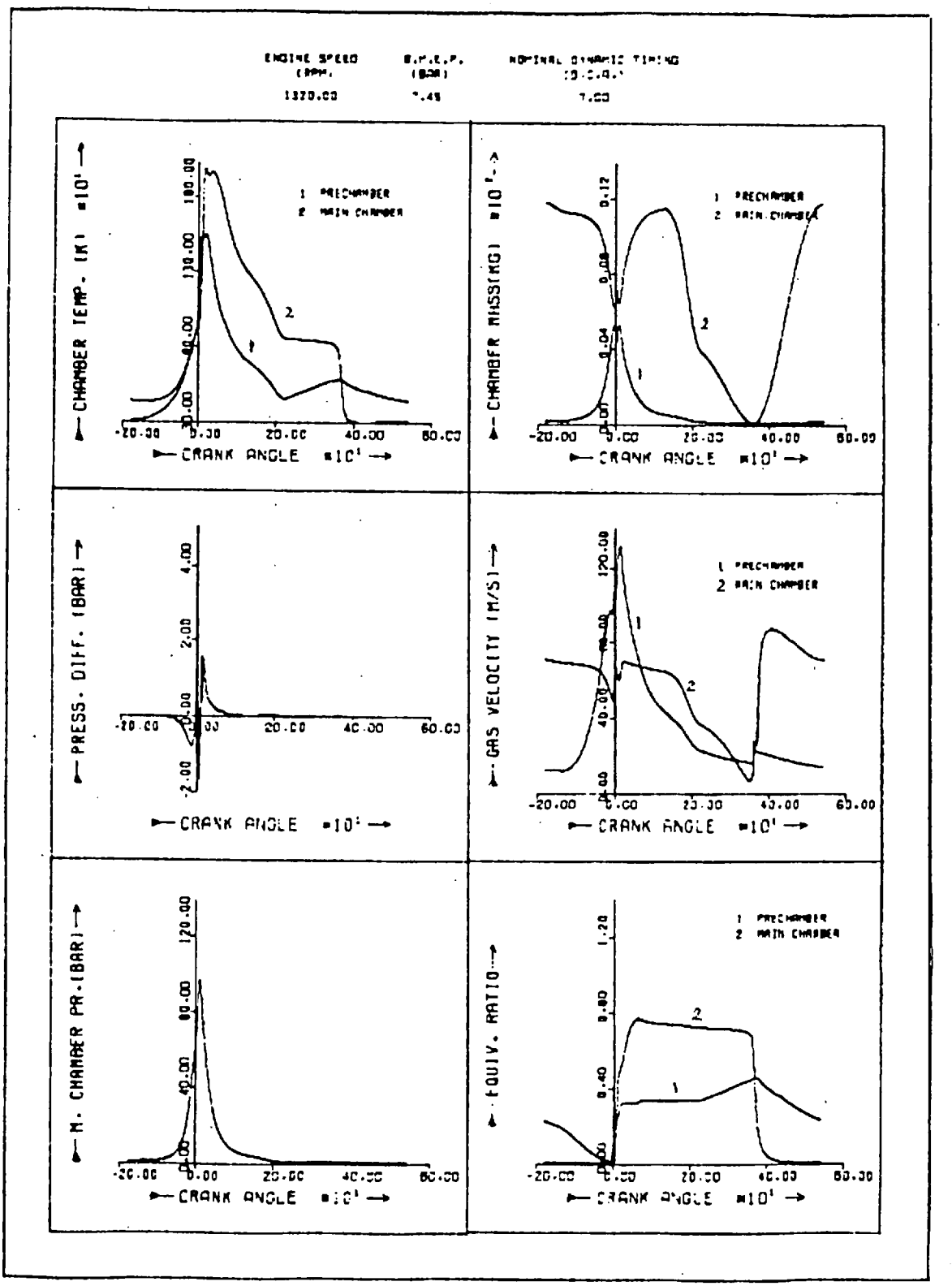

Fig. (7.31) Full Cycle Predictions Showing Combustion Chamber Interaction

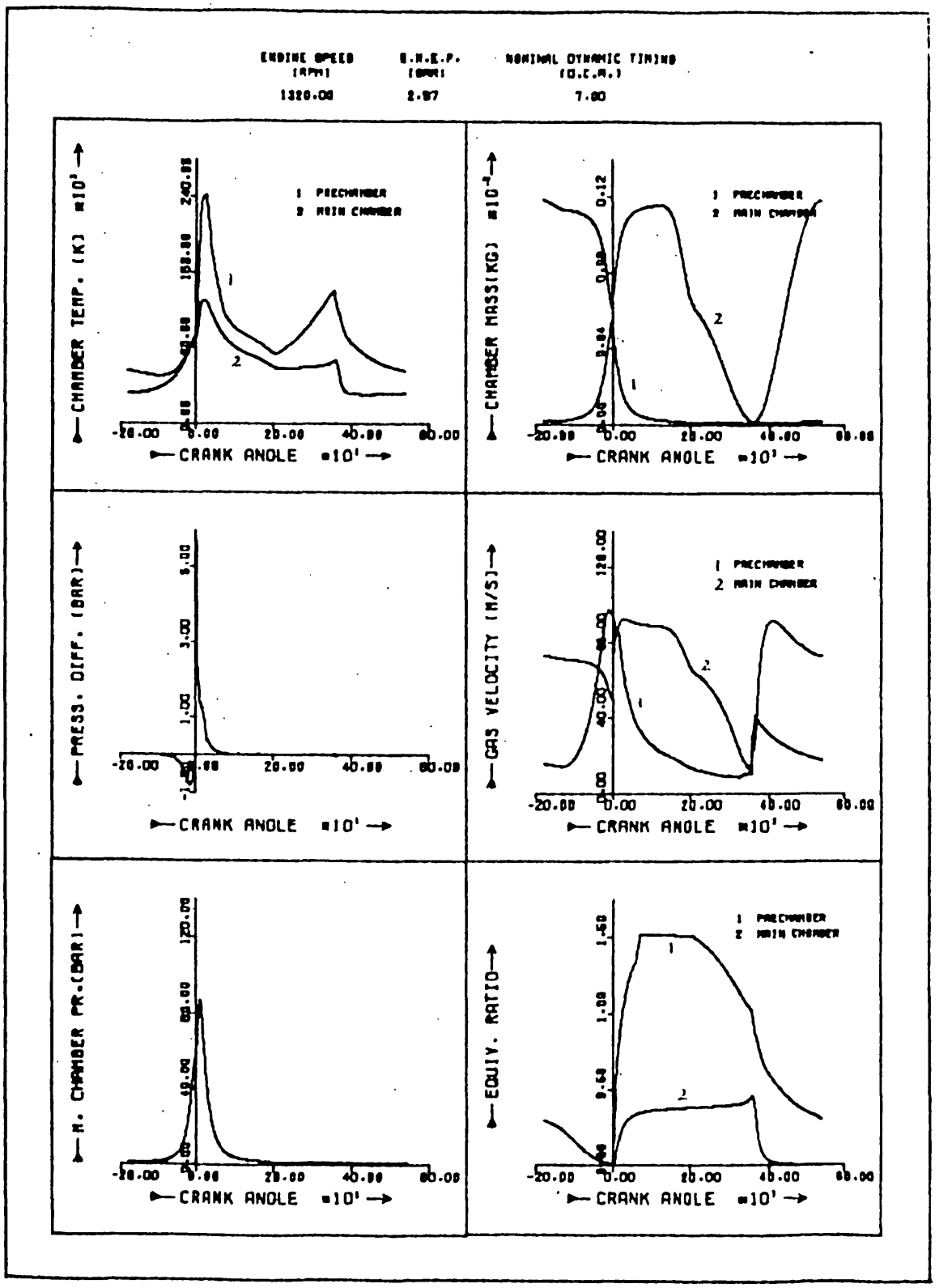

Fig. (7.32) Full Cycle Predictions Showing Combustion Chamber Interaction

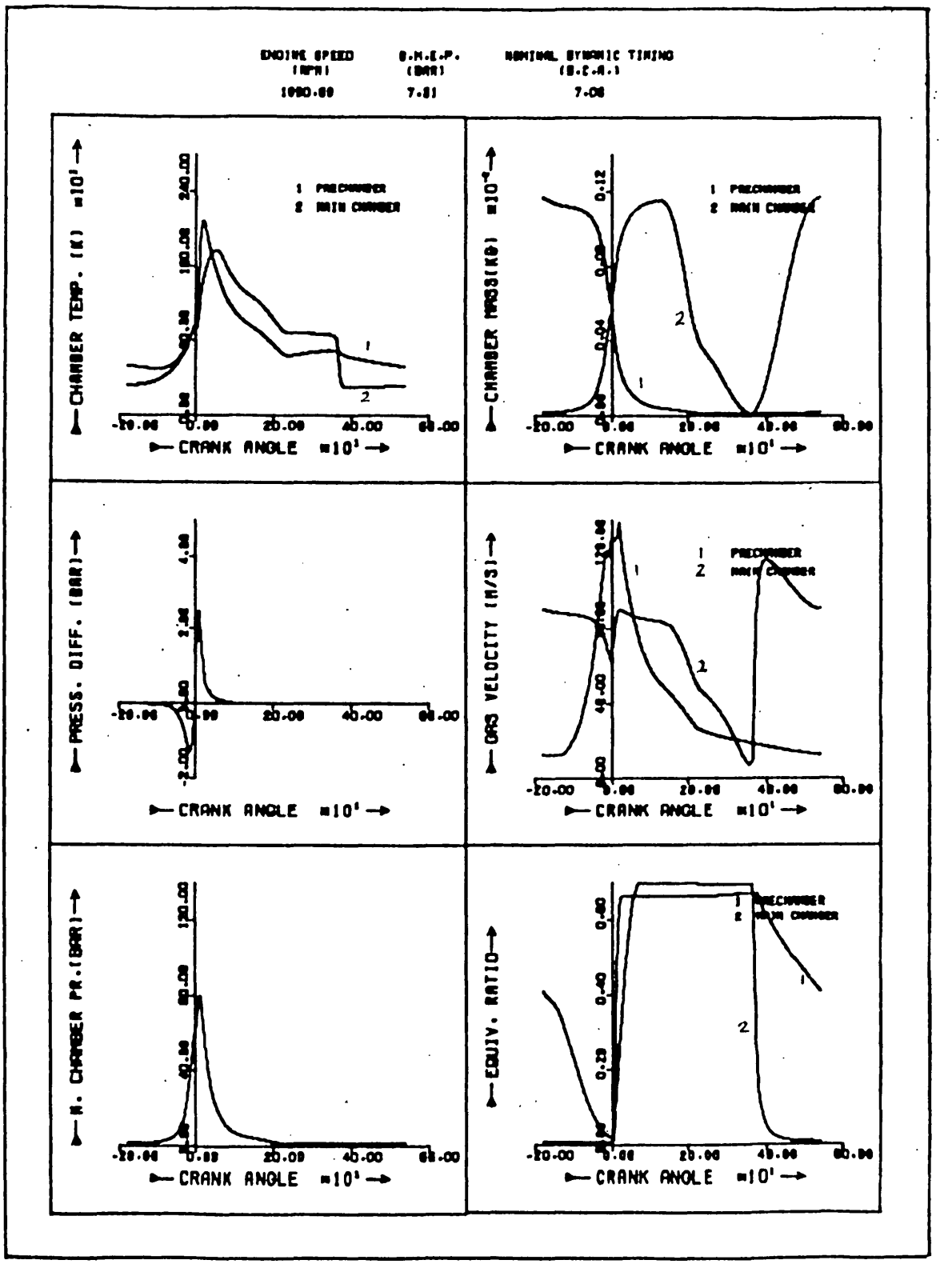

Fig. (7.33) Full Cycle Predictions Showing Combustion Chamber Interaction

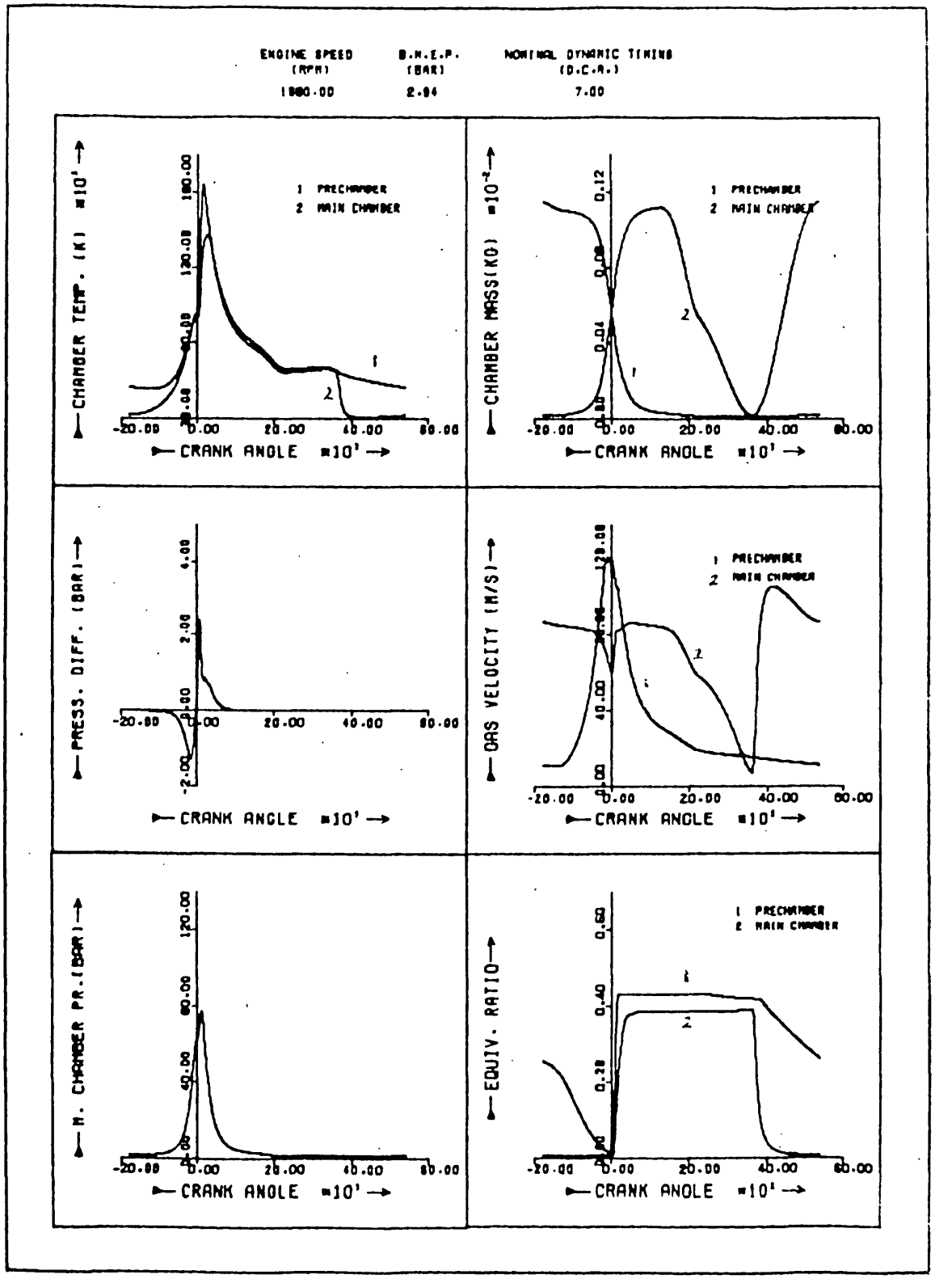

Fig. (7.34) Full Cycle Predictions Showing Combustion Chamber Interaction

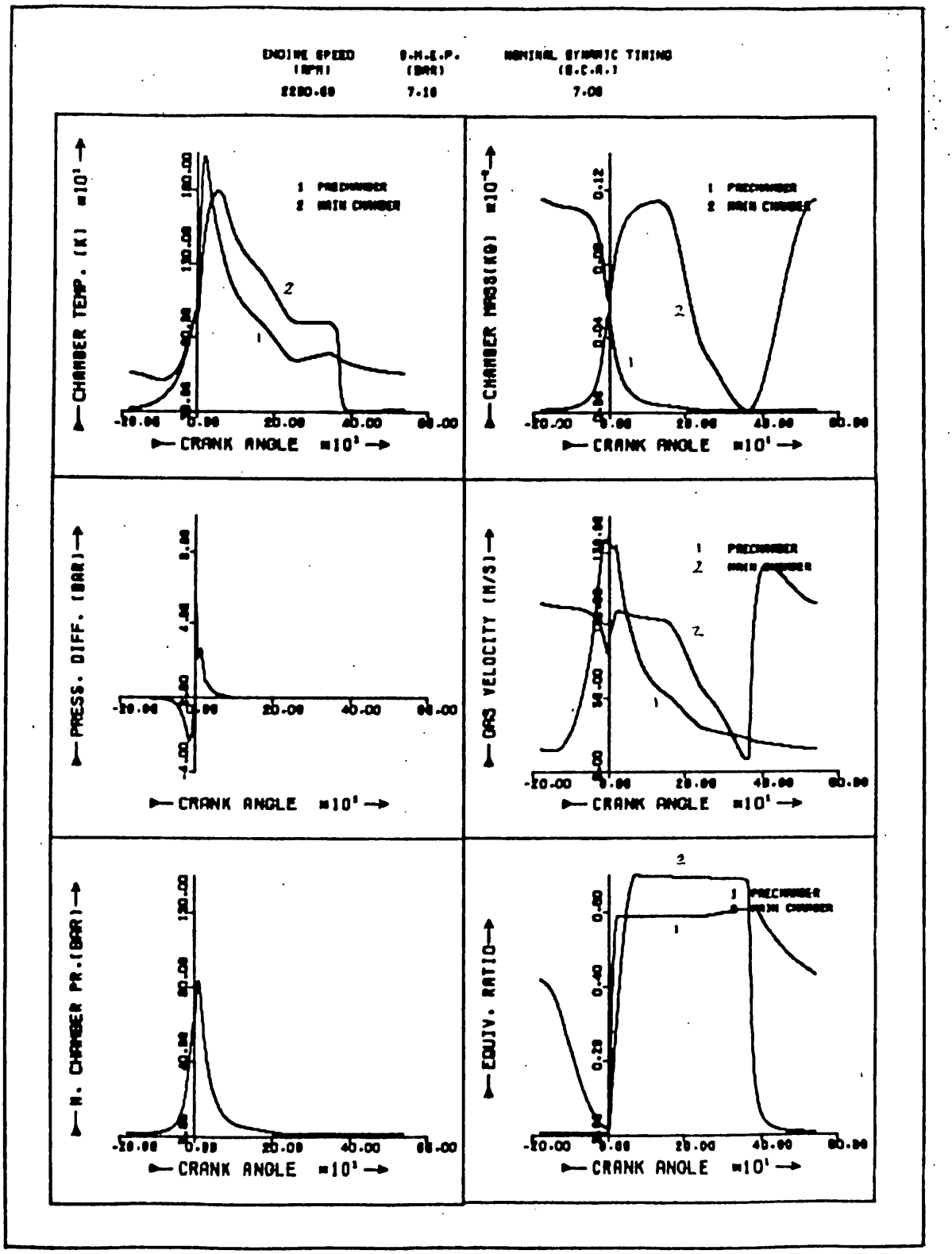

Fig. (7.35) Full Cycle Predictions Showing Combustion Chamber Interaction

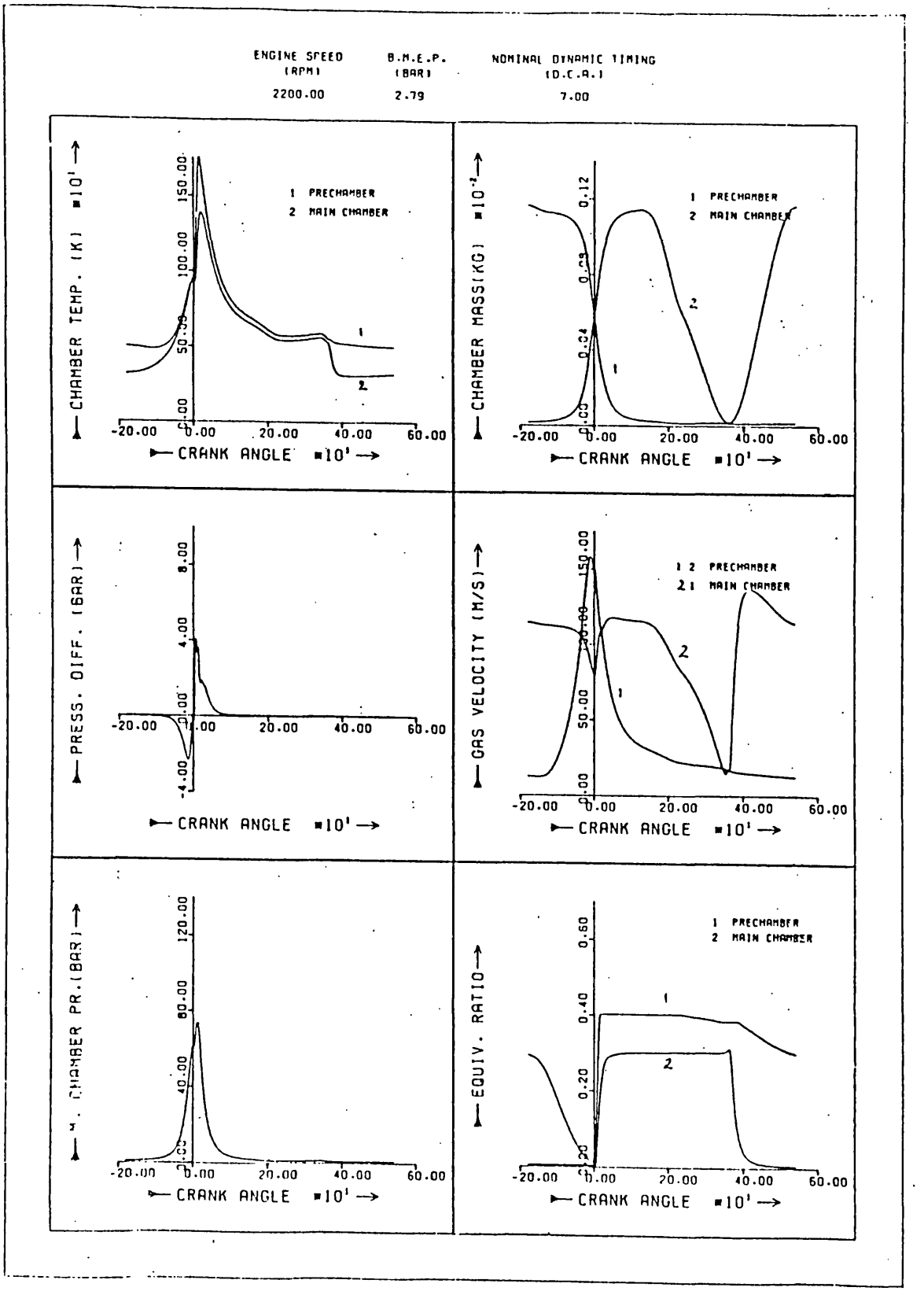

Fig. (7.36) Full Cycle Predictions Showing Combustion Chamber Interaction

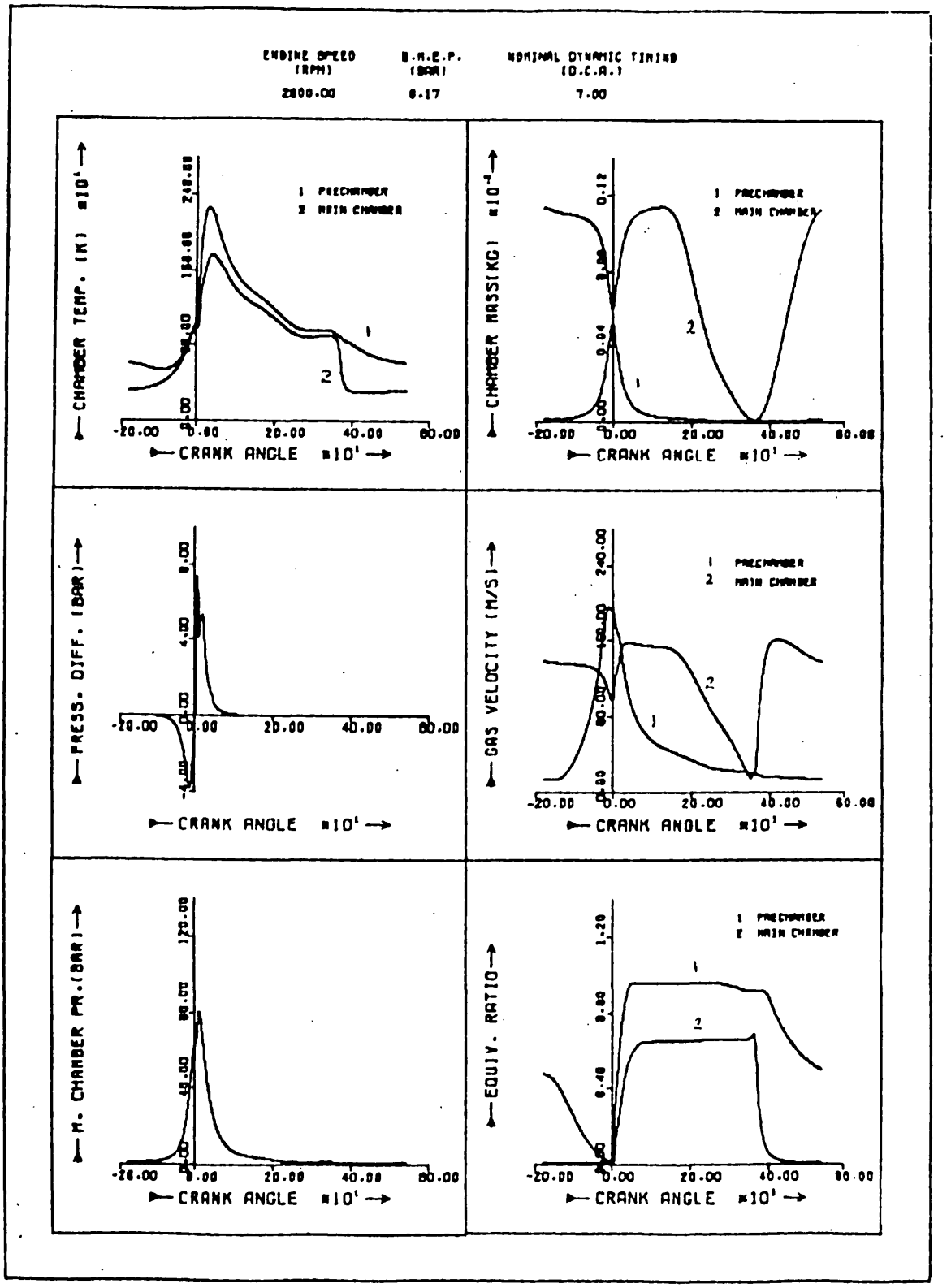

Fig. (7.37) Full Cycle Predictions Showing Combustion Chamber Interaction

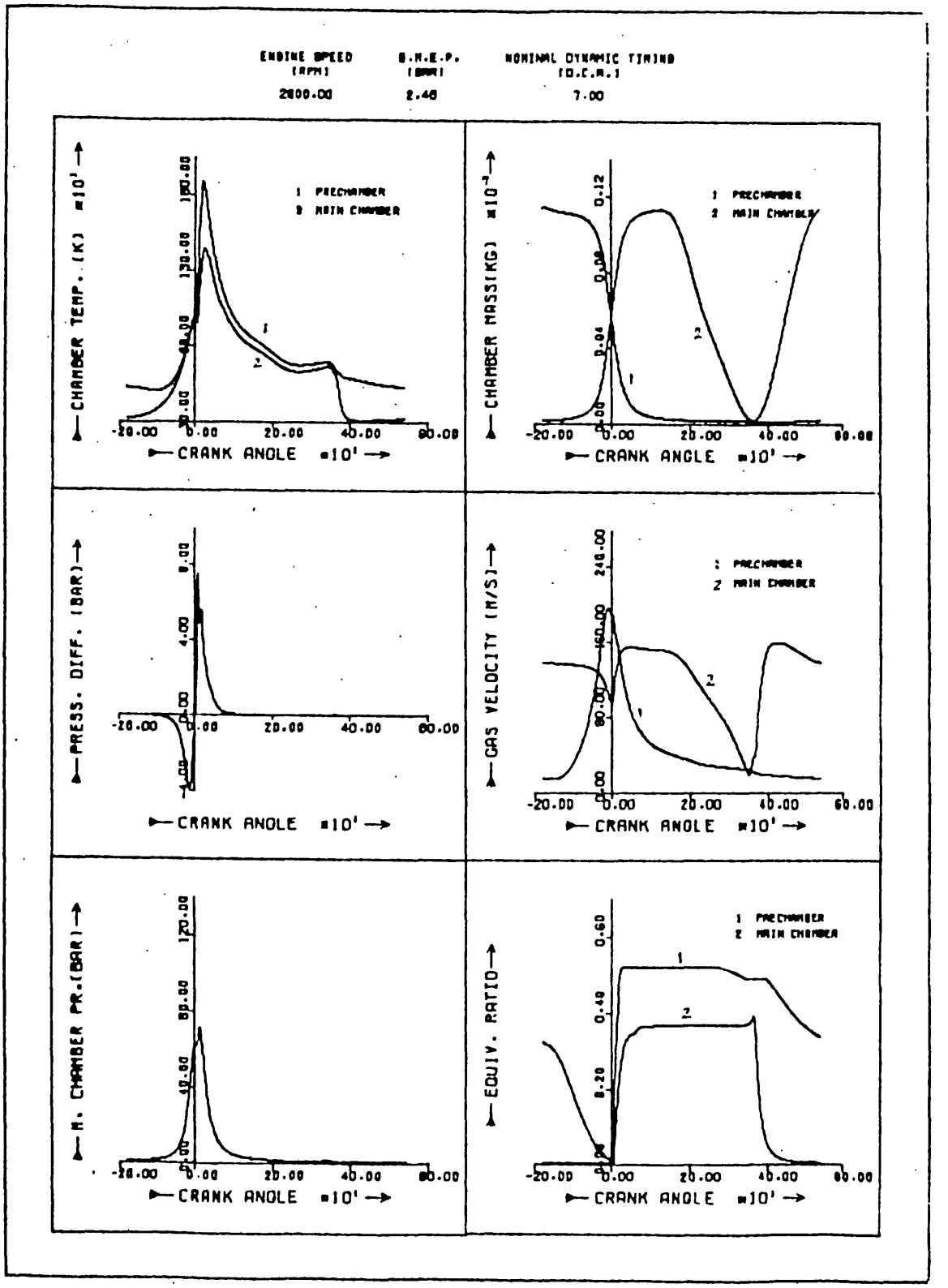

Fig. (7.38) Full Cycle Predictions Showing Combustion Chamber Interaction

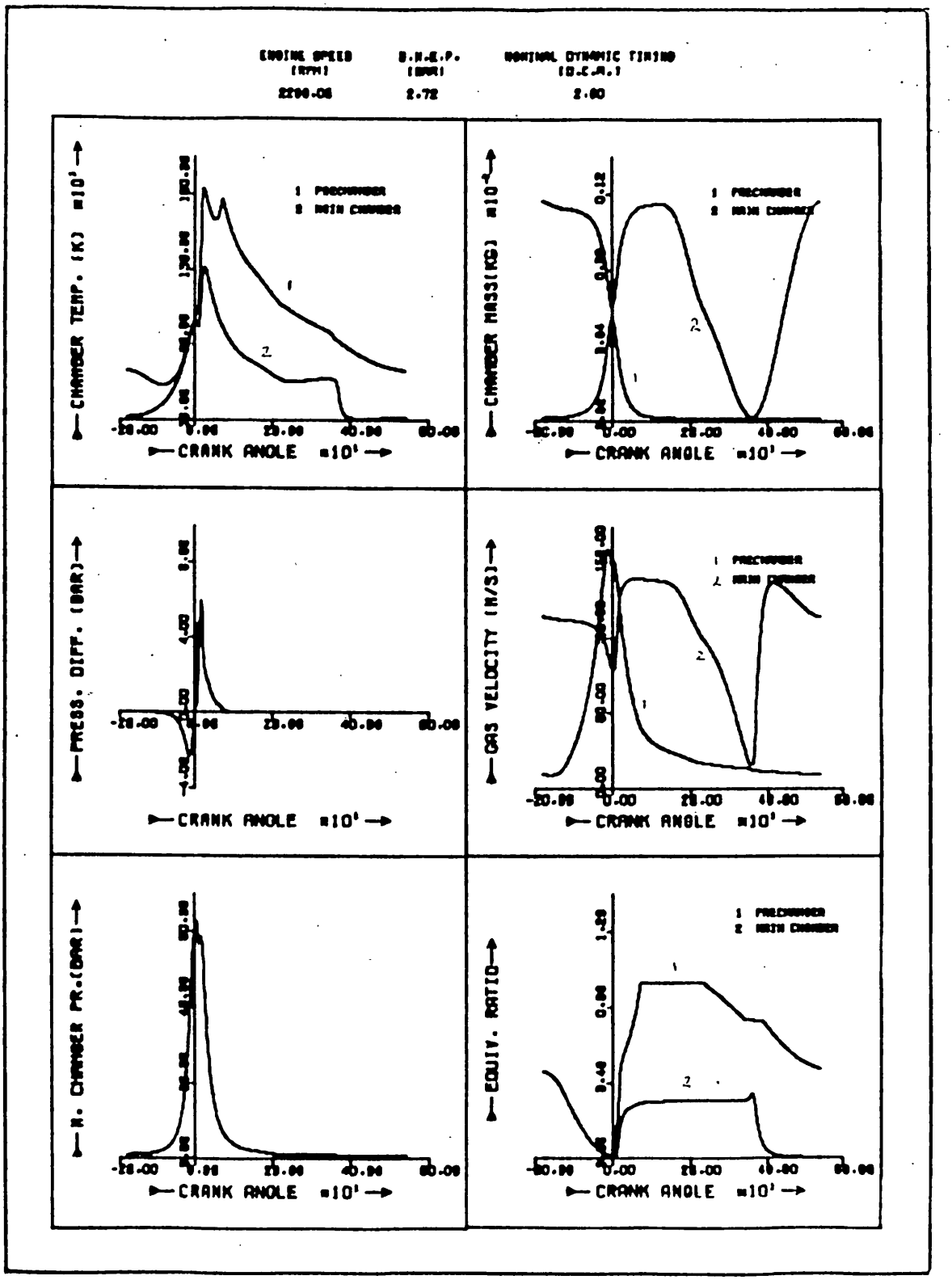

or mixing with hotter charge giving rise to such a temperature increase. The main reason for the discrepancy is the inadequacy in the charge properties expression for such high equivalence ratios (~1.5). The same argument can be applied to explain the excessive temperature of the prechamber charge for the same running condition, near TDC.

During the exhaust stroke, charge flows from the main to the prechamber. Mixing results in a drop of the prechamber equivalence ratio (F) as shown in Fig. (7.31). This results in a large reduction of the gas constant (R) obtained from the rich mixture property expression. Since the charge temperature is obtained by applying the equation of state,

$$PV = m R T$$

this would result in an apparent increase of temperature T, since V is constant and changes in P and m are small. More work is needed on property correlations for over-rich mixtures, but was outside the scope of the present investigation.

The results obtained demonstrate the continuous interaction between the two combustion chambers. Fig. (7.30) show the corresponding results of conditions for which ROHR values were obtained in Fig. (7.7). It serves as a good example of chamber interaction, and some of the observations on it apply for the other conditions in Figs. (7.32) to (7.38). Reverse flow, i.e. flow from main chamber to prechamber, exists after TDC and is indicated in both the pressure difference and chamber mass diagrams. The same effect is also apparent on chamber charge temperature and velocity.

Beyond $\approx 200^{o}$ ATDC, i.e. during the exhaust stroke, small levels of mass transfer from the main chamber to the prechamber occur. This results in the indicated increase in prechamber charge equivalence ratio and temperature, provided the corresponding values for the main chamber are higher (Figs. (7.30, 7.32, 7.34)), or a decrease in both if main chamber values are lower (Figs. (7.31, 7.33, 7.35-7.38)).

When the prechamber equivalence ratio is higher than that for the main

chamber, a sharp rise in the main chamber value occurs near 360° ATDC; Figs. (7.31, 7.35-7.39). This again is due to mixing of charge from the prechamber with that in the main chamber, but the effect is augmented by the fact that chamber charges are already very small near TDC position.

A very rapid drop in the main chamber equivalence ratio occurs near 400° ATDC, as the induction air mixes with the residual charge. Changes in the prechamber value are slower, and rapid drop only occurs during the compression stroke as a result of mixing with the charge coming from the main chamber.

In all the figures, calculated values of instantaneous swirl velocities are shown for both chambers, and reflect a reasonable behaviour. Most of the main chamber charge motion is induction generated, except some generated near TDC due to interaction with the prechamber. Prechamber charge motion, however, is mainly the result of flow through the connecting passage, to or from the prechamber. Viscous friction always acts on the charge to decelerate motion. In the case of the prechamber kinetic energy is added to the charge due to the fuel jet energy.

Figs. (7.30-7.38) and the above discussion provide a description of the interaction between the two combustion chambers of the IDI engine investigated.

7.6 CONCLUSIONS

The technique adopted for calculating instantaneous ROHR values in both combustion chambers has been shown to give reasonable results. IMEP measurements require great accuracy particularly at low cylinder pressures. The validity of the cycle simulation program was tested under motored and fired conditions and satisfactory results were obtained. The interaction, throughout the engine cycle, between the two combustion chambers has also been demonstrated.

CHAPTER 8

INDIRECT INJECTION DIESEL ENGINE PERFORMANCE IN RELATION TO THE DIRECT INJECTION DIESEL

8.1 INTRODUCTION

In the previous chapters different aspects of indirect injection diesel engine performance testing and mathematical simulation have been discussed. It was concluded in Chapter 7 that a successful cycle analysis simulation program had been developed. This program predicts engine performance, and instantaneous cylinder conditions, throughout the engine cycle, for motored conditions, and for fired operation using ROHR data. The cycle analysis program was particularly developed to study another major feature of indirect injection diesel engine operation, namely high specific fuel consumption. The reasons for high specific fuel consumption were expected to be

1. Execessive heat loss due to high swirl velocities and surface area.
2. Loss due to gas pumping to and from the prechamber.
3. Combustion mode loss, due to the different pattern of combustion compared with the direct injection engine.

An isolation technique was developed to study the different sources of these losses separately. In this chapter the isolation technique is explained, together with the method of quantifying of different losses involved under motoring and fired conditions. Special consideration of the combustion mode effect for both IDI and DI engine is also discussed.

8.2 LOSS ISOLATION TECHNIQUE

The technique for isolating losses is based mainly on the use of the cycle simulation computer program, in its different modes of operation. The principle was to study the effect of one loss source at a time. The three

sources were summarized as

1. The passage.
2. Instantaneous heat fluxes and heat transfer areas.
3. The rate of heat release curve, for fired operation.

The comparison between the IDI and DI engines was made, keeping all other engine variables and engine geometry exactly the same, apart from changing heat transfer areas.

For motored engine operation, passage and heat flux losses were considered. Results for different engine motoring speeds were analysed. To quantify the motoring gas pumping and heat flux losses, the following program running conditions were considered

1. IDI engine operation.
2. Equivalent DI engine operation with instantaneous heat flux values of the IDI engine.
3. DI engine with its own heat flux calculations.

These computer simulation runs provided data for comparing IDI engine operation with the DI engine under motored conditions. Differences between runs 1 and 2 isolate the effect of the passage. The differences between runs 2 and 3 are entirely due to variations between instantaneous heat flux rates. Comparing runs 3 and 1 reflects the total difference.

For fired operation, for each engine running condition of speed, load and injection timing, the corresponding ROHR diagram was obtained in the manner described in Chapters 3 and 7. The following cases were considered,

A) IDI engine operation.

B) DI engine with instantaneous heat flux and ROHR values from the IDI engine.

C) DI engine, with ROHR values, but its own heat flux rate.

Comparing cases A and B, the differences would be the effect of gas pumping under fired operation. Differences between cases C and B would illustrate the effect of heat flux rates on the engine performance. The

final result of comparison of cases A, B and C, would be effects of heat losses and gas pumping losses on the overall performance of IDI engine in relation to the equivalent DI engine.

To decide on the combustion mode effect on the performance of the IDI engine, a typical DI engine heat release diagram was needed. For this the correlation obtained by Marzouk (73) was used. The correlation expresses the rate of heat release curve of the DI diesel engine as the sum of two functions, one for premixed combustion and the other for diffusion combustion of the total fuel.

$$FBR(\tau) = \beta\ FBR_p(\tau) + (1 - \beta)\ FBR_d(\tau)$$

where

$FBR(\tau)$ = Non dimensional burning rate distribution

$FBR_p(\tau)$ = Premixed burning distribution

$FBR_d(\tau)$ = Diffusion burning distribution

τ = Normalized crank position

$$= \frac{\theta - \theta_i}{\theta_e - \theta_i}$$

θ = Current crank position

θ_i, θ_e = Crank angle at ignition and end of burning

$= 125^o$ CA.

$$FBR(\tau) = \frac{dmb}{d\theta}(\tau) \cdot \frac{(\theta_e - \theta_i)}{M_{f_t}}$$

$$\beta = M_{f_p} / M_{f_t}$$

where

M_{f_t} = Total fuel burnt

M_{f_p} = Premixed fuel burnt

The premixed and diffusion burning rates are expressed as a function of

the ignition delay period (ms), the engine speed (N,rpm) and the total equivalence ratio (F).

$$FBR_p(\tau) = c_{p1} \cdot c_{p2} \; \tau^{(c_{p1}-1)} \; (1 - \tau^{c_{p1}})^{c_{p2}-1}$$

$$FBR_d(\tau) = c_{d1} \cdot c_{d2} \cdot \tau^{(c_{d2}-1)} \; \exp(-c_{d-} \cdot \tau^{c_{d2}})$$

where $c_{p2} = 5000.0$

$$c_{d2} = 0.791 \; (c_{d1})^{0.2477}$$

$$\beta = 1.0 - 0.9259 \; \frac{F^{0.3708}}{(t_d)^{0.2613}}$$

$$c_{p1} = 2.0 + 1.25 \times 10^{-8} \; (t_d \cdot N)^{2.4}$$

$$c_{d1} = 14.2/(F^{0.644})$$

$$t_d = 3.52 \; \frac{e^{2100.8/T}}{p^{1.0218}}$$

The above relations were used to calculate instantaneous ROHR values for a DI engine which had the same basic design and compression ratio as the IDI engine. This was used in the following program mode of operation:

D) DI engine proper, with its own ROHR values and instantaneous heat flux.

Case D, when compared with case A, would give the difference in performance between the IDI engine and a DI engine of the same basic design under fired operation. The differences include gas pumping, heat flux and combustion mode effects. As both gas pumping and heat flux loss effects are already quantified from cases B and C the combustion mode effect could then be deduced.

The above technique was used to study engine losses under several conditions of different engine speeds, loads and injection timings. The results obtained are discussed in the following sections.

8.3 MOTORED ENGINE OPERATION

The procedure of isolating losses was applied at four engine speeds covering its operating range under motored conditions. The three cases considered were

A) IDI engine.

B) $DI)_{eq}$ engine.

C) DI engine.

Cases A, B and C above correspond to the similar cases explained in the previous section, but without heat release. The results obtained are summarized in Tables (8.1), (8.2), (8.3), (8.4), (8.5) and (8.6) and are plotted in Fig. (8.1) and Fig. (8.2). Table (8.1) and Fig. (8.1) show the predicted motoring indicated mean effective pressures (IMEP) for the different cases of engines considered. Both full and closed cycle values are shown. The full cycle IMEP increases with the engine speed, as expected. For the closed cycle, however, the IMEP value drops with increasing engine speed. This is thought to be due to the decrease in the heat flux values at higher engine speeds. However, this increases again at 2800 rpm, due to increased passage gas pumping with engine speed.

The (IMEP) values for the $DI)_{eq}$ engine are lower than those for the IDI engine. The difference is due to the gas pumping through the passage. A greater reduction in the motoring (IMEP) was obtained for the DI engine, which is due to lower heat losses to the cylinder walls. When the heat transfer area of the clearance volume was reduced, to become more appropriate to that of a normal DI engine, lower (IMEP) values were obtained (Fig. (8.1)). Judging from Fig. (8.1) the excessive heat flux rates of IDI engines contribute far more to its higher (IMEP) motoring values, than the passage gas pumping.

The contribution of passage gas pumping and heat loss to the total increased (IMEP) of the IDI engine is better demonstrated in Tables (8.2), (8.3) and (8.4) and Fig. (8.2, I, II and III). Fig. (8.2,II)shows that the IDI engine

Table 8.1

Predicted Motoring I M E P (BAR)

Speed (rpm)	I D I		D I eq.		D I	
	Total Pumping	Closed Cycle Loss	Total Pumping	Closed Cycle Loss	Total Pumping	Closed Cycle Loss
1320	0.868	0.752	0.849	0.731	0.690	0.578
1680	0.922	0.737	0.888	0.700	0.732	0.550
2200	1.0370	0.717	0.979	0.652	0.828	0.509
2800	1.240	0.720	1.151	0.612	0.993	0.467

Table 8.2

Motored Closed Cycle (IMEP) As a Ratio of D I Engine

Engine Type / Engine Speed (rpm)	D I	D $I_{eq.}$	I D I
1320	1.0	1.265	1.300
1680	1.0	1.272	1.340
2200	1.0	1.279	1.408
2800	1.0	1.310	1.541

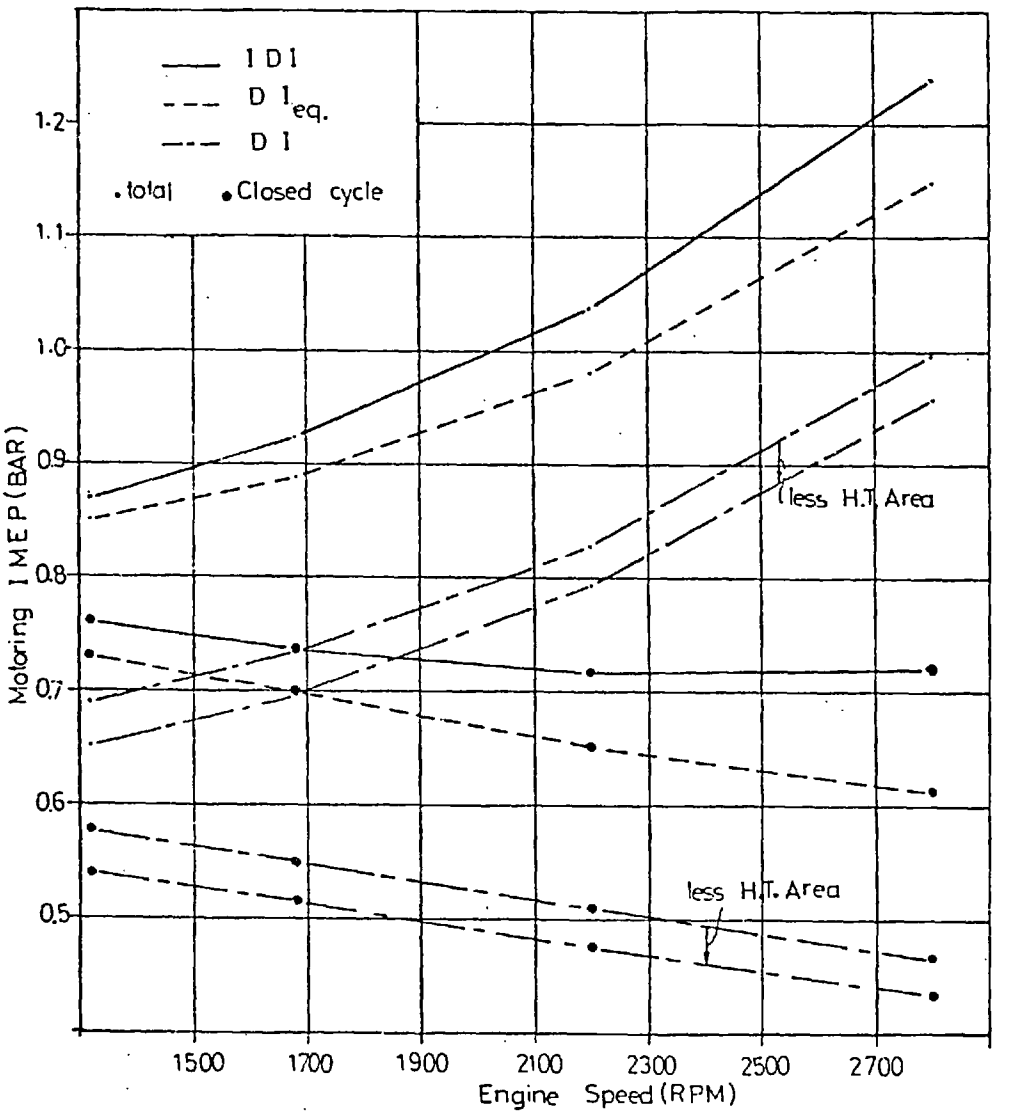

Fig. (8.1) Motoring IMEP for Different Engine Geometry

Table 8.3

Total Motored (IMEP) As a Ratio of D I Engine

Engine Type / Engine Speed (rpm)	D I	D I_{eq}	I D I
1320	1.0	1.229	1.257
1680	1.0	1.213	1.260
2200	1.0	1.182	1.252
2800	1.0	1.158	1.248

Table 8.4

Motored (IMEP) of I D I Engine As A Ratio of Equivalent D I

Engine Speed (rpm)	Closed Cycle		Total	
	D $I_{eq.}$	I D I	D $I_{eq.}$	I D I
1320	1.0	1.027	1.0	1.022
1680	1.0	1.053	1.0	1.038
2200	1.0	1.100	1.0	1.058
2800	1.0	1.176	1.0	1.077

Table 8.5

Total Motored Heat Loss To The Walls (kJ/Cyl.)

Engine Type / Engine Speed (rpm)	I D I		$DI_{eq.}$	DI	$\frac{DI_{eq.}}{DI}$
	Main Chamber	Prechamber			
1320	0.0390	0.0405	0.0796	0.0671	1.184
1680	0.0366	0.0386	0.0753	0.0624	1.205
2200	0.0335	0.0351	0.0686	0.0558	1.229
2800	0.0319	0.0332	0.0651	0.0508	1.281

Table 8.6

Cylinder Peak Pressure For Different Motored Engine Types (BAR)

Engine Speed (rpm) \ Engine Type	I D I	$DI_{eq.}$	DI
1320	58.05	57.66	58.93
1680	58.90	58.47	59.68
2200	59.93	59.40	60.49
2800	60.89	60.01	61.04

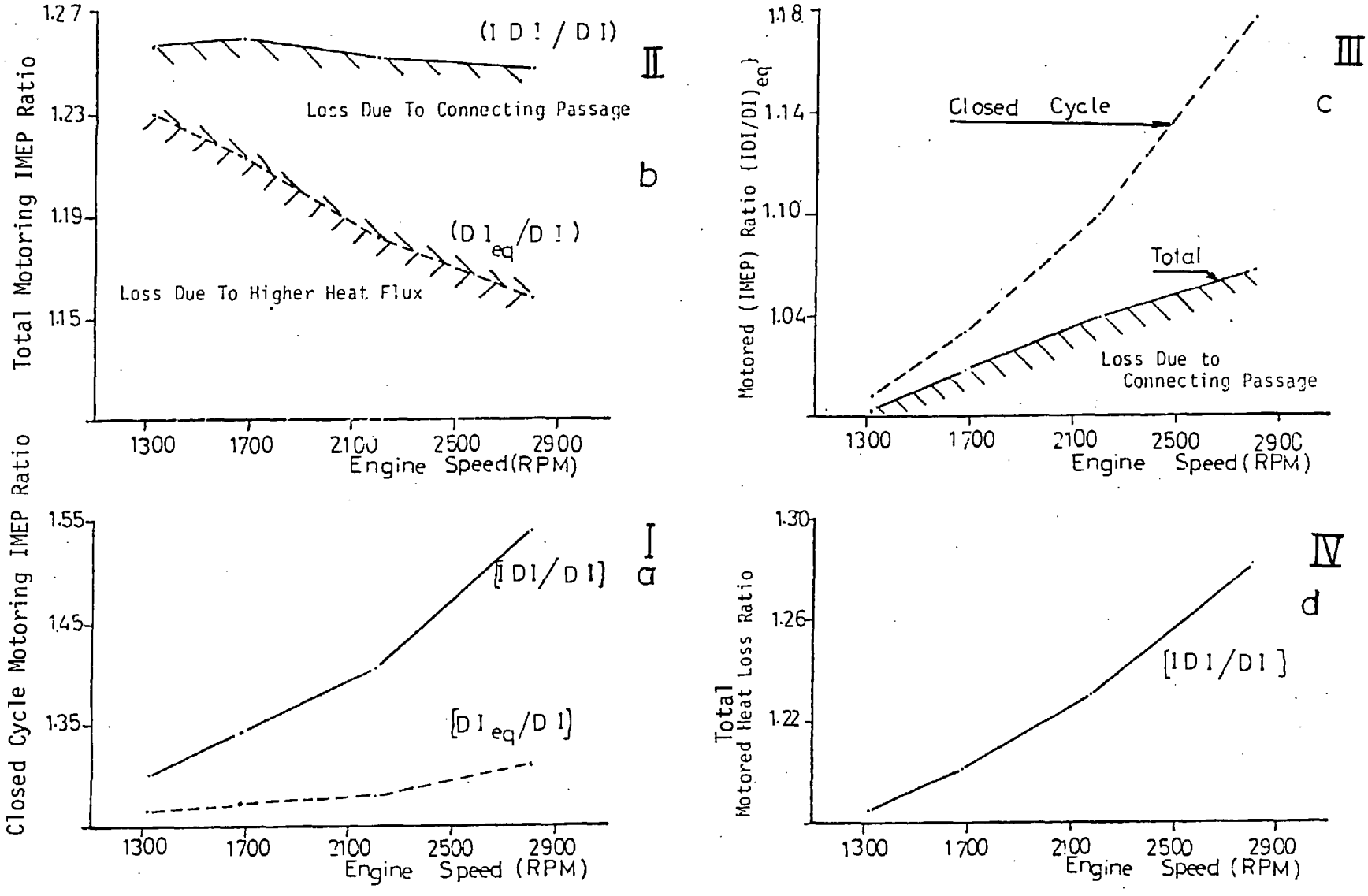

Fig. (8.2) Motored Engine Comparisons

requires, for the full range of speeds, about 25% more torque to motor it compared to the DI engine. Consulting Figs. (8.2.II) and (8.2.III), this difference is mainly due to the excess heat flux rates. While the excess heat fluxes were responsible for about 20% increase in the total (IMEP), the effect of the passage was only approximately 5%. Fig. (8.2.IV) shows the ratio of the total heat loss of the IDI engine compared to the DI engine. This increases with engine speed the maximum extra heat loss is about 28%.

Table (8.6) lists the predicted values of peak cylinder pressures. The differences between values for IDI engine and DI engine are small, with DI values always higher. This is also mainly due to less heat loss to the walls in the case of the DI engine.

8.4 FIRED ENGINE OPERATION

It was concluded from the motored engine IDI-DI comparisons in the previous section that excess heat fluxes contributed more than passage gas pumping work to the total reduced efficiency of the IDI relative to the DI engine. This conclusion may not necessarily be valid under fired operation. Both heat flux and passage flow are then entirely different. The loss isolation technique for the fired engine is more complicated than that for motored operation due to the presence of a new variable; the combustion mode. For fired engine operation the technique explained in section 8.2 was used.

Case D was considered to give an indication of typical DI engine operation. This simulates a hypothetical engine which has the same basic design as the corresponding IDI engine (but less heat transfer surface area), the same compression ratio, instantaneous valve areas etc. Such an engine would have some distinctive features that are different from the equivalent IDI engine. These are, different flow field inside the engine (which leads to different heat transfer coefficients at the walls), less heat transfer area, different injection characteristics and the absence of the passage

(i.e. a single combustion chamber). These differences were taken into consideration when simulating such engines. Figs. (8.3,4) show two examples of predicted combustion chamber conditions at two engine speeds. In the figures, the pressure difference diagram is meaningless and was brought about by using the general plotting routine for the DI case. Fuel jet kinetic energy was included in calculating the average charge velocity. It is clear from the figures that fuel jet effect is more significant at the low engine speed, since the average charge velocities are considerably low compared to those at the high engine speed conditions.

Comparisons between IDI and DI engines were made at one injection timing for each engine. The effect of injection timing was then studied separately for both engine types, to study the sensitivity of comparisons to changes in timing. The values of dynamic injection timings considered were chosen to be representative of typical IDI and DI engines. These were 7^{0} BTDC and 14^{0} BTDC respectively. The same total quantity of fuel was assumed to burn and release heat in both engines.

The comparisons were made at several engine speeds, at full and 40% load conditions. The predicted performance for all different cases, A to D, was expressed as indicated thermal efficiency (η_i) and percentage heat loss ($H_L\%$) of the total heat input (fuel burnt x calorific value). These are tabulated in Tables (8.7, 8.8). Table (8.9) shows the peak cylinder pressures obtained at each condition. All the results are shown in graphical form in Figs. (8.5, 8.6). Quantifying the different losses due to, the passage, excess heat flux and combustion mode is demonstrated better in Tables (8.10, 8.11) and Figs. (8.7, 8.8). The IDI engine (case A) was considered to be the DATUM and the performance of the other engine types (cases B, C and D) were calculated relative to it.

Fig. (8.5) exhibits a consistant improvement of performance, indicated by η_i increasing from case A to D at all speeds.

Fig. (8.3) Full Cycle Predictions for DI engine at 1680 rpm - Full Load

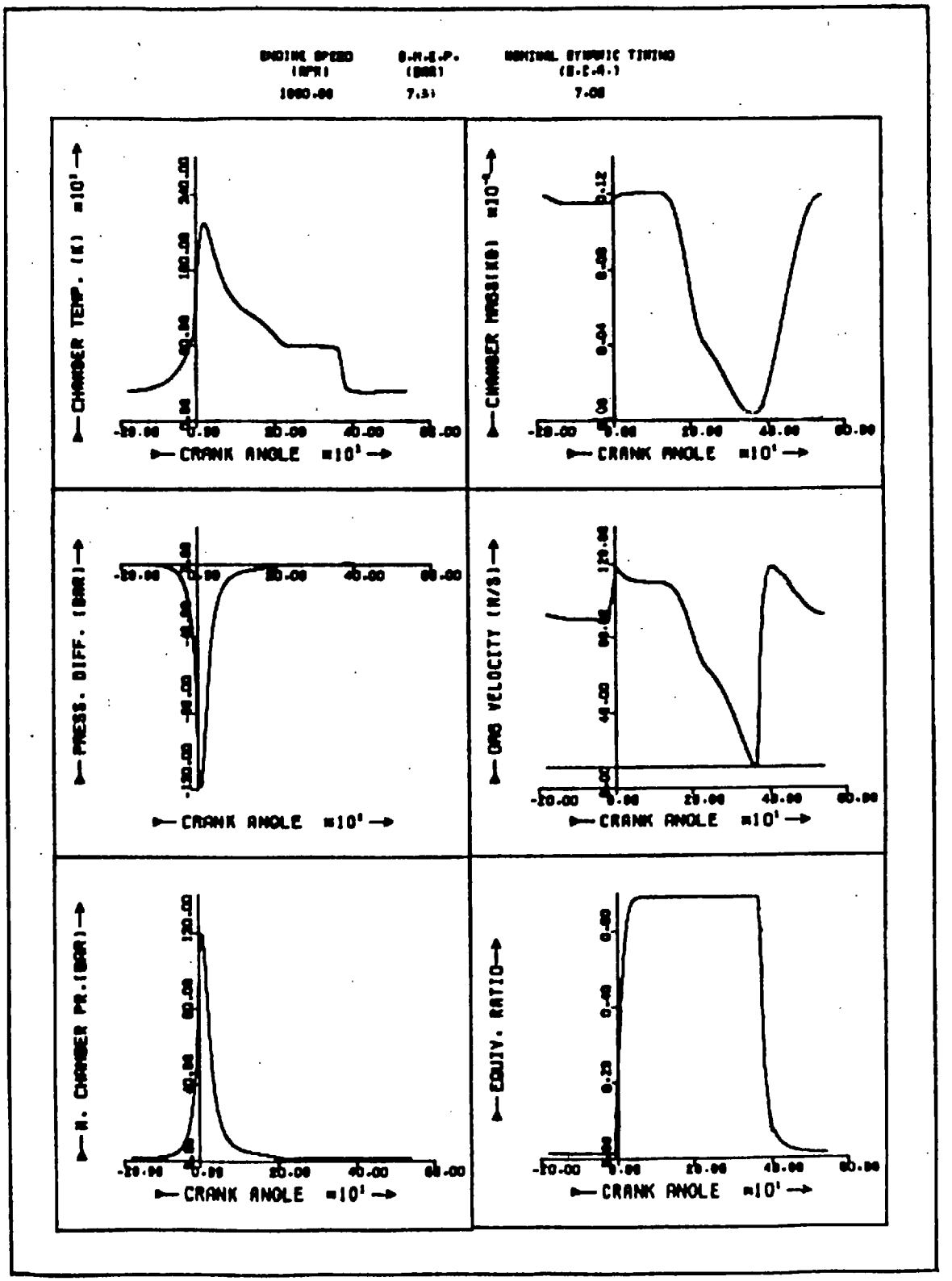

Fig. (8.4) Full Cycle Predictions for DI engine at 2800 rpm - Full Load

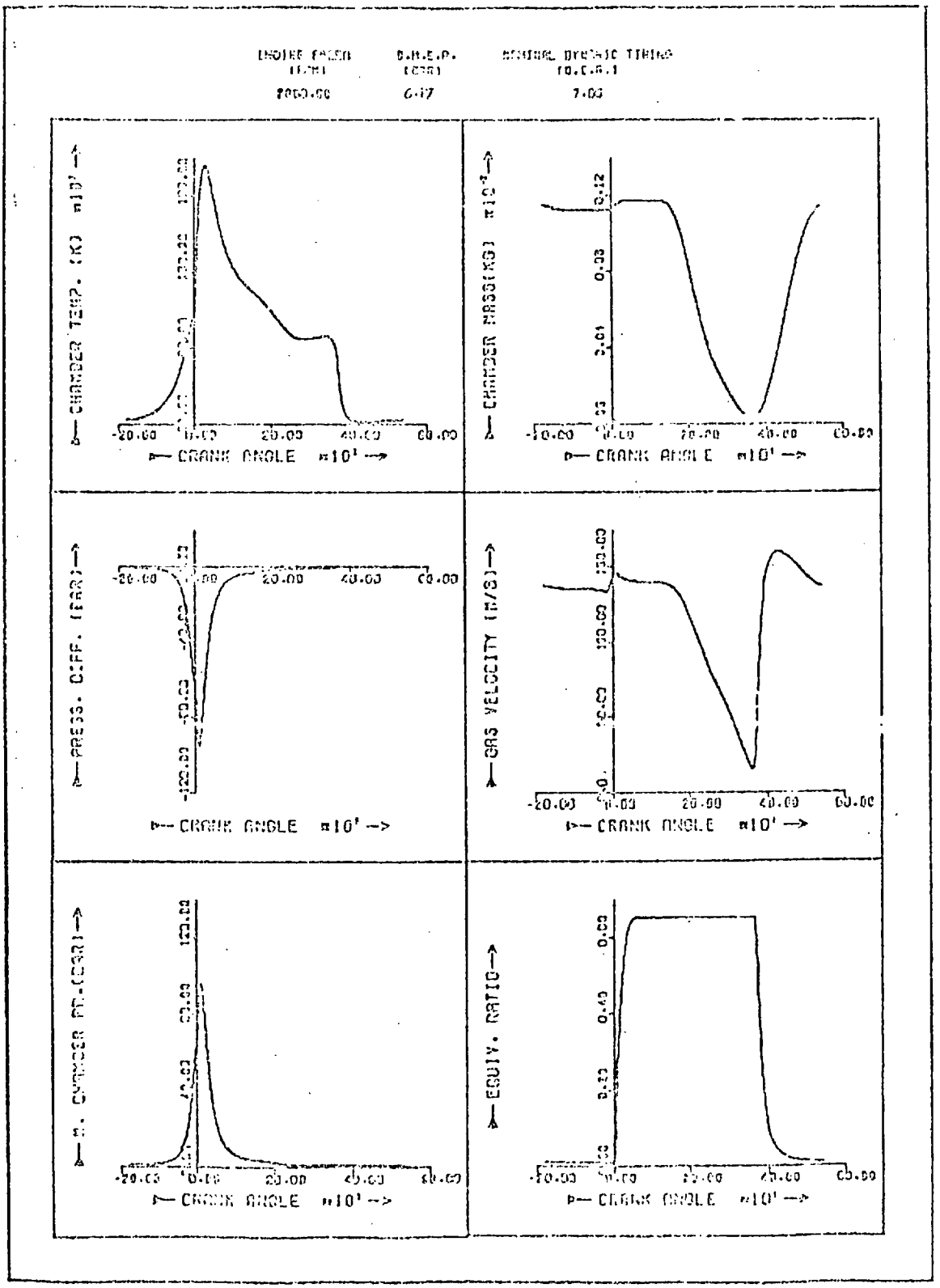

Table 8.7

Indicated Thermal Efficiency
(n_i)

Test Conditions			case A	case B	case C	case D
Speed	Load %	Timimg				
1320	100	7	54.18	55.23	56.23	59.98
1680	100	7	52.44	52.77	53.88	59.94
2200	100	7	52.59	52.96	54.07	60.23
2800	100	7	52.56	53.37	54.66	59.12
1320	40	7	52.84	56.86	60.54	59.91
1680	40	7	57.44	57.96	60.23	61.58
2200	40	7	56.52	57.41	59.91	61.03
2800	40	7	54.27	55.59	57.86	59.95
2200	40	2	53.47	55.04	58.10	
	40	12	56.26	57.44	60.79	

Table 8.8

Heat Loss as a Percentage of Total Heat Input
(H_L%)

Test Conditions			case A		case B	case C	case D
Speed	Load %	Timing	Cylin.	Pre.			
1320	100	7	10.66	4.91	15.57	15.18	15.30
1680	100	7	9.91	4.60	14.51	13.56	14.43
2200	100	7	8.81	3.91	12.72	11.53	12.05
2800	100	7	8.96	3.72	12.68	10.38	11.44
1320	40	7	15.17	7.45	22.62	16.99	18.44
1680	40	7	13.80	6.69	20.49	17.05	16.42
2200	40	7	11.82	6.07	17.89	14.39	14.12
2800	40	7	10.75	4.97	15.72	12.06	12.07
2200	40	2	12.45	6.63	19.08	14.06	
	40	12	13.46	7.13	20.59	15.61	

Table 8.9

Peak Cylinder Pressure
(BAR)

Test Conditions			case A	case B	case C	case D
Speed	Load %	Timing				
1320	100	7	96.66	97.57	98.81	120.77
1680	100	7	79.81	81.58	82.54	110.38
2200	100	7	83.53	85.01	85.99	106.84
2800	100	7	80.22	82.17	82.83	95.93
1320	40	7	86.95	90.16	91.57	94.66
1680	40	7	74.98	76.36	77.43	95.12
2200	40	7	73.55	75.21	76.18	85.90
2800	40	7	71.26	73.28	74.07	80.98
2200	40	2	62.83	62.85	63.84	
	40	12	86.47	88.95	89.99	

Table 8.10

(η_{ir})

Indicated Thermal Efficiencies Relative to The I D I Engine
(%age)

Running Conditions			case A	case B	case C	case D
Speed	Load %	Timing				
1320	100	7	100	101.94	103.77	110.70
1680	100	7	100	100.63	102.75	114.29
2200	100	7	100	100.70	102.81	114.53
2800	100	7	100	101.54	104.00	112.48
1320	40	7	100	107.61	114.56	113.38
1680	40	7	100	100.90	104.85	107.70
2200	40	7	100	101.57	105.99	108.52
2800	40	7	100	102.43	106.62	110.46
2200	40	2	100	102.94	108.66	
	40	12	100	102.10	108.05	

Table 8.11

Heat Loss Relative to the I D I Engine
(Hr%)

Running Conditions			case A	case B	case C	case D
Speed	Load %	Timing				
1320	100	7	100	100	97.50	98.28
1680	100	7	100	100	93.45	99.46
2200	100	7	100	100	90.64	95.05
2800	100	7	100	100	81.86	90.20
1320	40	7	100	100	75.11	81.51
1680	40	7	100	100	83.21	80.15
2200	40	7	100	100	80.44	78.93
2800	40	7	100	100	76.72	76.79
2200	40	2	100	100	73.65	
	40	12	100	100	75.81	

Table 8.12

Effect of Dynamic Timing
(2200 rpm. Full Load)
(DI Engine)

Dynamic Timing (^{o}CA)	η_i %	Peak Pr. (BAR)	Heat loss (KJ)	HL %	η_{ir} %	Hr %
-18	59.20	120.56	0.269	10.88	112.57	85.53
-14	60.23	112.90	0.279	11.27	119.53	88.60
-10	59.19	106.94	0.270	10.91	113.80	85.77

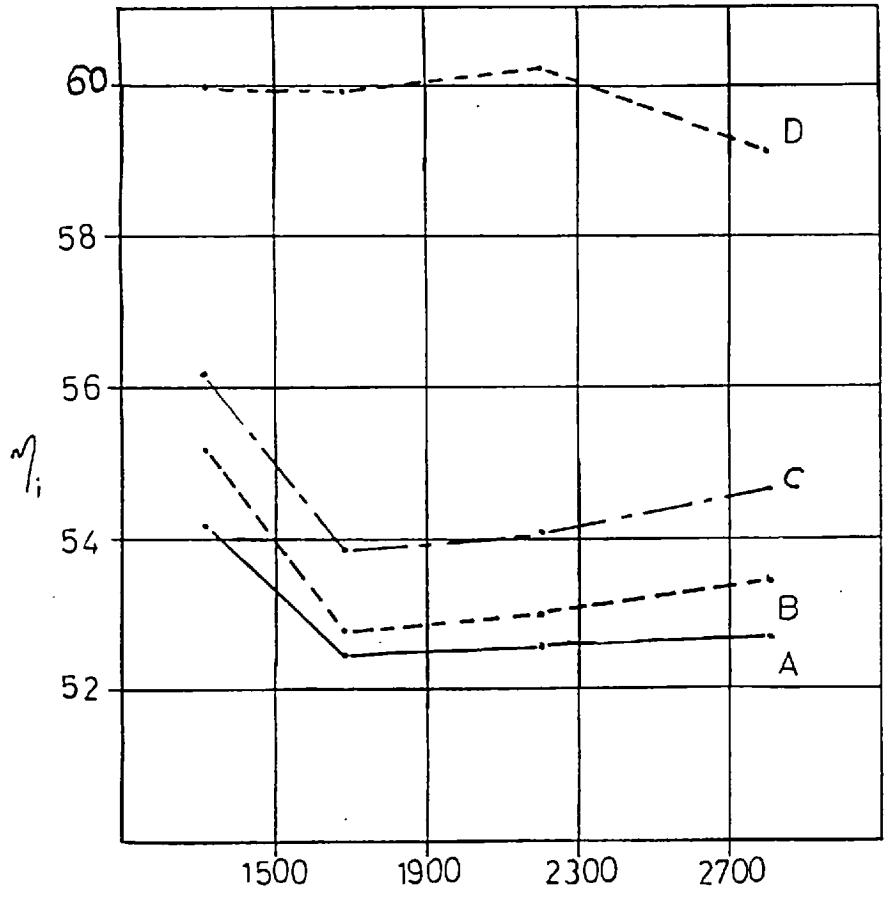

Fig. (8.5) Effect of Engine Speed on Thermal Efficiency for Different Engine Cases.

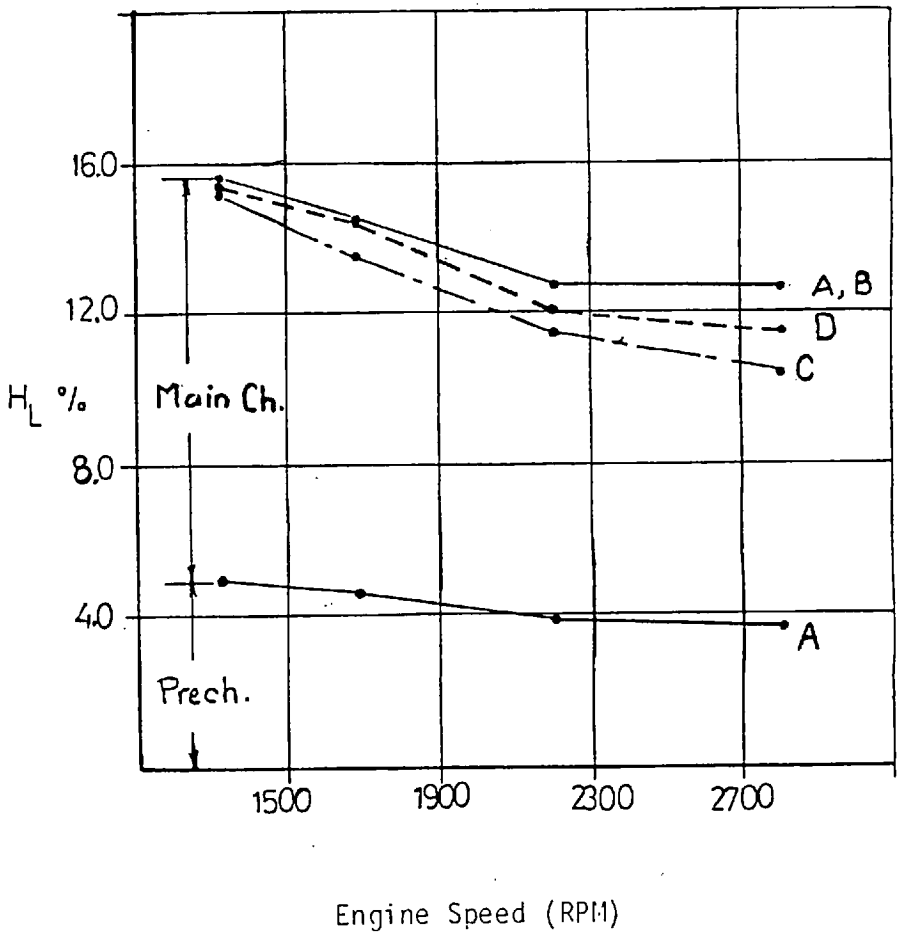

Fig. (8.6) Effect of Engine Speed on Heat Loss for Different Engine Cases.

Examining Fig. (8.5), which compares cases A and B, it is concluded that the passage is responsible for about -0.5% loss in the overall η_i. Examining Table (8.9) and Fig. (8.9), an increase of peak cylinder pressure of about 1.5 (bar) is detected between cases A and B. This infers that the effect of the passage on the IDI engine performance is a loss of -0.5% in the indicated thermal efficiency of the engine and a reduction of 1.6 Bar in peak cylinder pressure. The passage is also responsible for the high swirl velocities in the prechamber, leading to higher heat flux rates. These effects will be considered separately.

The effect of heat loss on the overall performance of the IDI engine is obtained by comparing cases B and C. In the absence of the passage and using the same ROHR diagram as for the IDI engine, the difference is due solely to changes in heat transfer to the walls. This is demonstrated in Fig. (8.5) and (8.6). An overall gain in η_i of about +1.0% was obtained when heat transfer rates to the walls used were corresponding to a DI engine. Fig. (8.6) shows that the improvement of total heat loss ratio H_L for case C over case B is small and, on average, amounts to only $\approx$-1.5% of the total heat loss for case B. It also shows that the prechamber heat loss is only $\approx$30% of the total heat loss. This is particularly important in judging the heat transfer loss in the IDI engine. It proves that despite very high heat flux rates in the prechamber in the neighbourhood of the TDC position, during compression and expansion, most of the heat is lost through the walls of the main cylinder. This is essentially due to larger heat transfer areas and lower wall temperatures. As a result, the effect of the high heat flux rates in the prechamber of an IDI engine on its η_i is small. Heat transfer , as shown in Fig. (8.9), has a very small effect on the peak cylinder pressure.

The effect of the different combustion mode between the IDI and DI engine is investigated by comparing cases C and D. In case C, the ROHR diagram of an IDI was used, while in case D that of the equivalent DI was

used. The differences between C and D are due to combustion effects. The difference due to heat flux rates was expected to be small, and to be mainly due to combustion effects on cylinder charge properties. This is shown in Fig. (8.5) and (8.6). An interesting result is that, although case D showed higher heat loss than case C, η_i was also higher. This proves that the gain in η_i is only due to the difference in the ROHR curve shape (i.e. the difference in combustion mode between the IDI and the DI engines). The combustion mode effect contributes to about a +5 % increase in η_i. The peak cylinder pressure, however, increased by about 22.5 (bar) on average, as shown in Fig. (8.9).

Considering the IDI engine (case A) as the datum, it is apparent from Fig. (8.7) that the corresponding DI engine would be, on average, +13% more efficient. The improvement is, +1.0% due to the absence of the passage pumping losses, +2.0% resulting from lower heat flux losses to the cylinder walls and +10% due to the difference in combustion mode. A drawback of this improvement is the increase of peak cylinder pressure by an average of 22.5 bar. This would lead to higher bearing loads, and hence increased friction loss. However, in practice the compression ratio of the DI engine is lower, reducing peak pressure significantly and efficiency slightly.

As shown in Fig. (8.8), with the heat loss ratio of case A as a datum, case C/A exhibits a -10% change in the total heat loss due to the absence of the prechamber. Case D/A however exhibits only -5% change in the total heat loss. Both cases C/A and D/A are for a DI engine, the difference is only due to different ROHR diagrams. This again outlines the importance of the combustion mode effect on the heat flux rates and thermal efficiency.

The effect of injection timing on the performance of the engine types investigated has been examined. The dynamic injection timing for the IDI engine has been changed and one value of timing considered on either side of

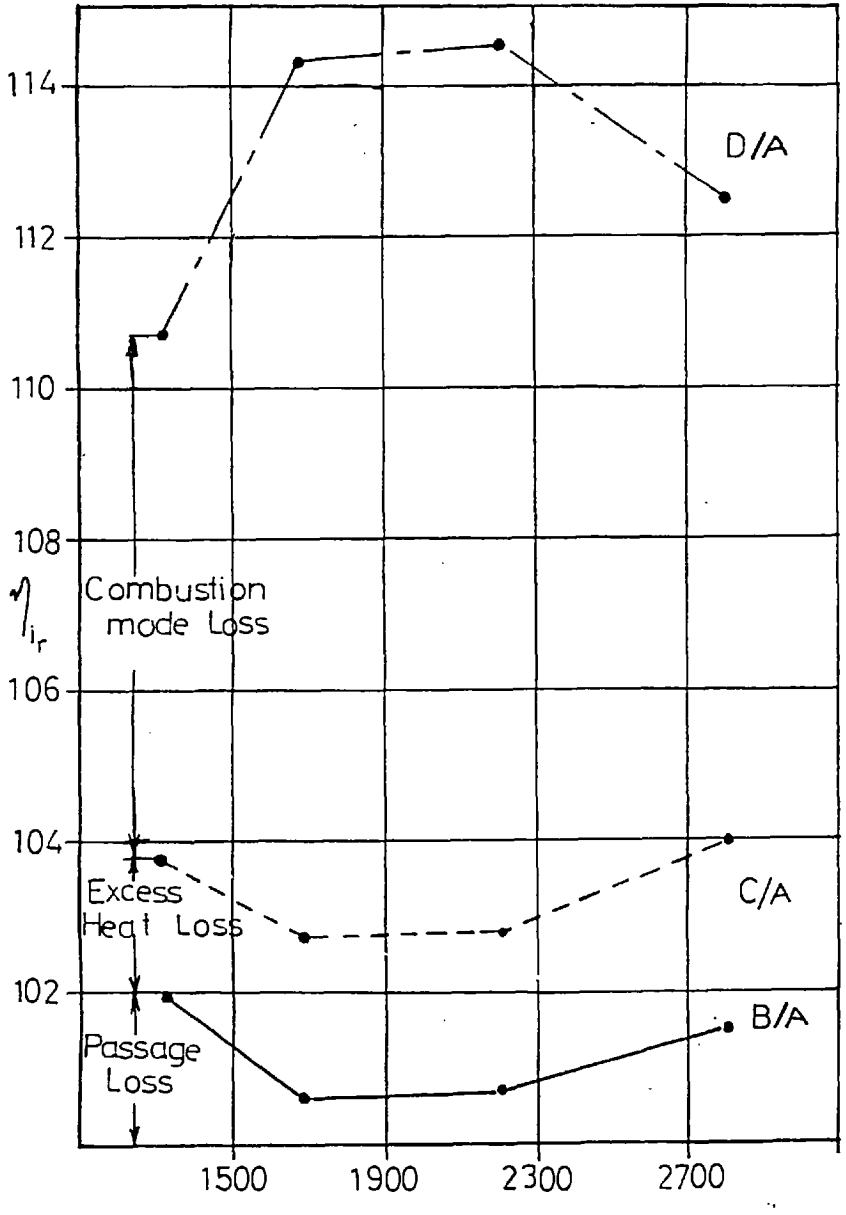

Fig. (8.7) Effect of Speed on Relative Thermal Efficiency for Different Engine Cases.

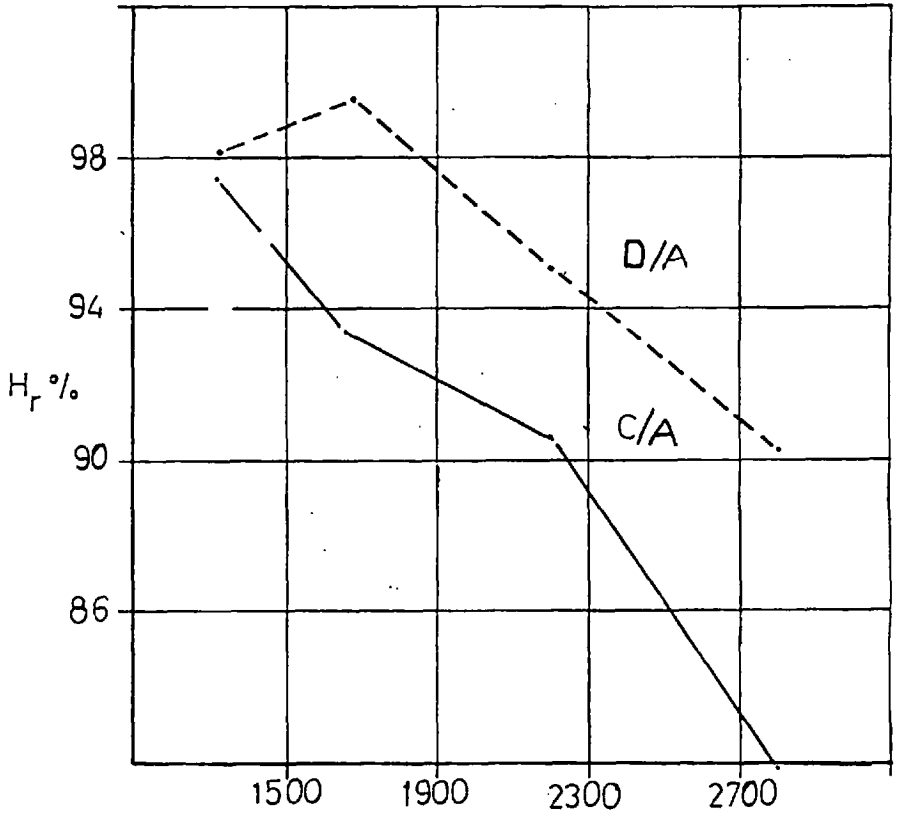

Fig. (8.8) Effect of Engine Speed on Heat Loss Ratio for Different Engine Cases.

Fig. (8.9) Effect of Engine Speed on Peak Cylinder Pressure for Different Engine Cases

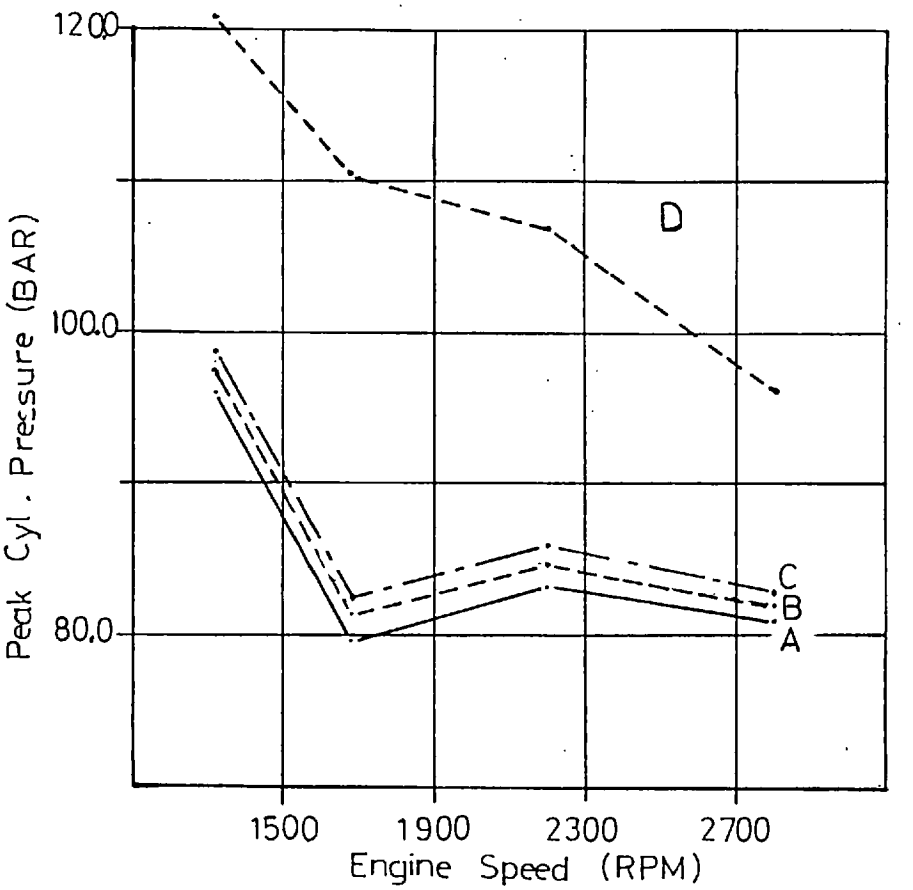

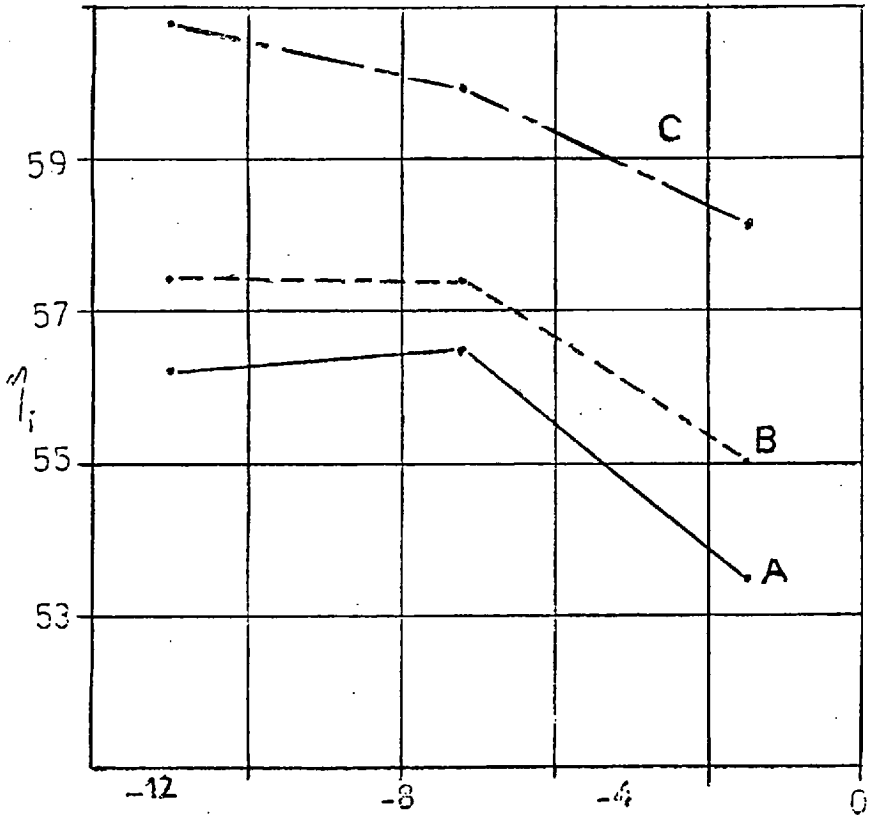

Fig. (8.10) Effect of Injection Timing on Thermal Efficiency for Different Engine Cases

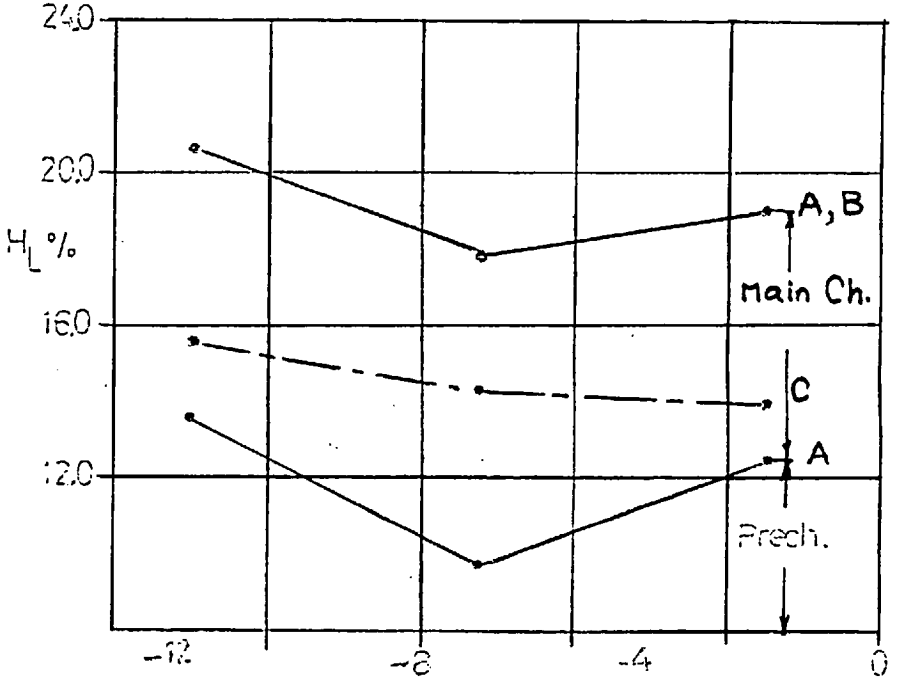

Fig. (8.11) Effect of Injection Timing on Heat Loss for Different Engine Cases.

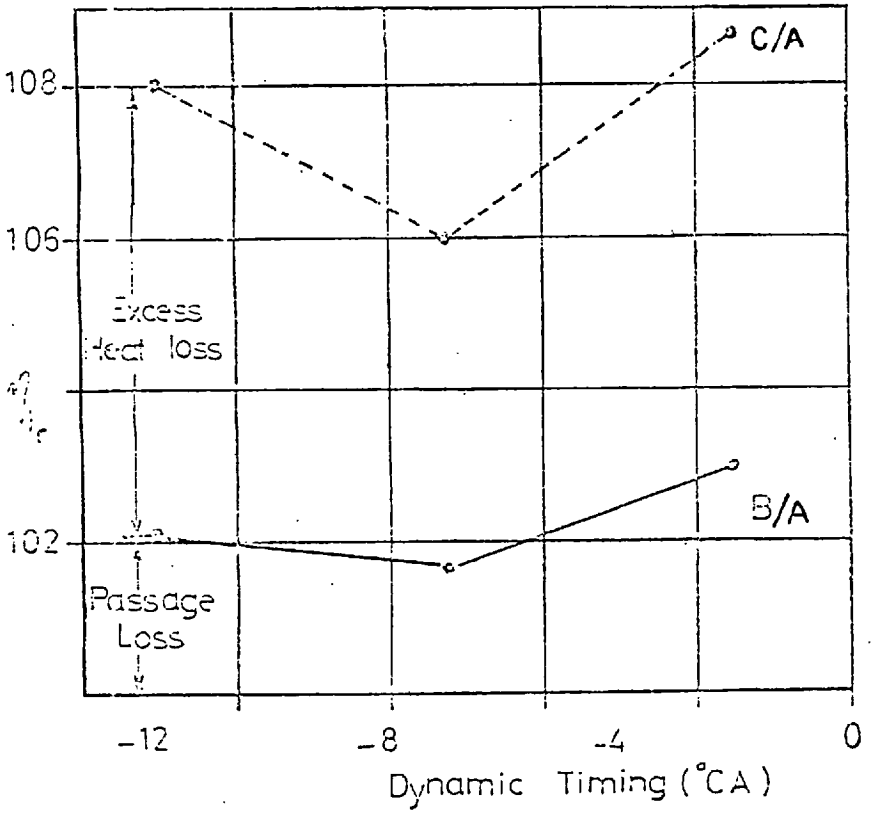

Fig. (8.12) Effect of Injection Timing on Relative Thermal Efficiency for Different Engine Cases.

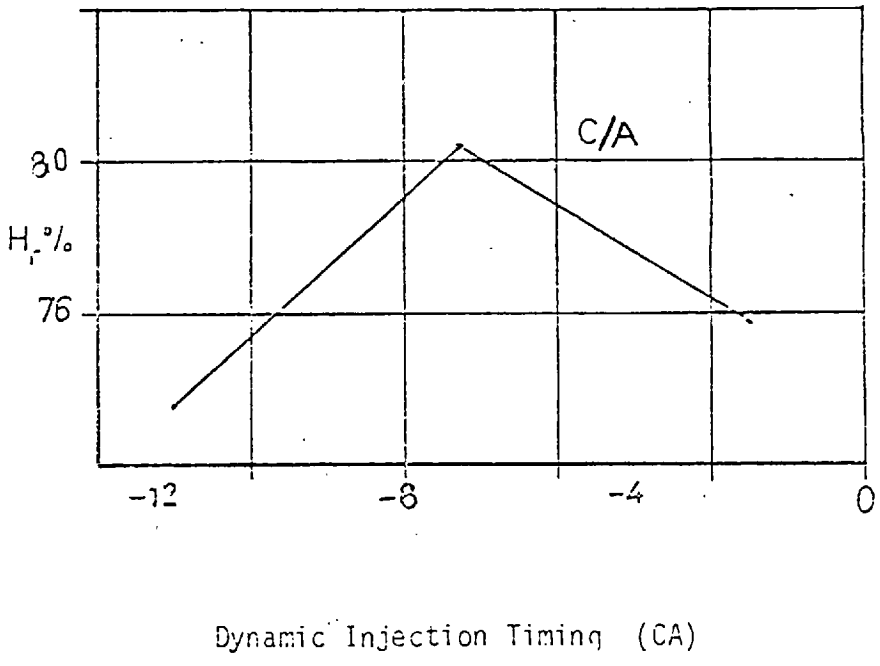

Fig. (8.13) Effect of Injection Timing on Heat Loss Ratio

Fig. (8.14) Peak Cylinder Pressure for Different Engine Cases and Different Injection Timing

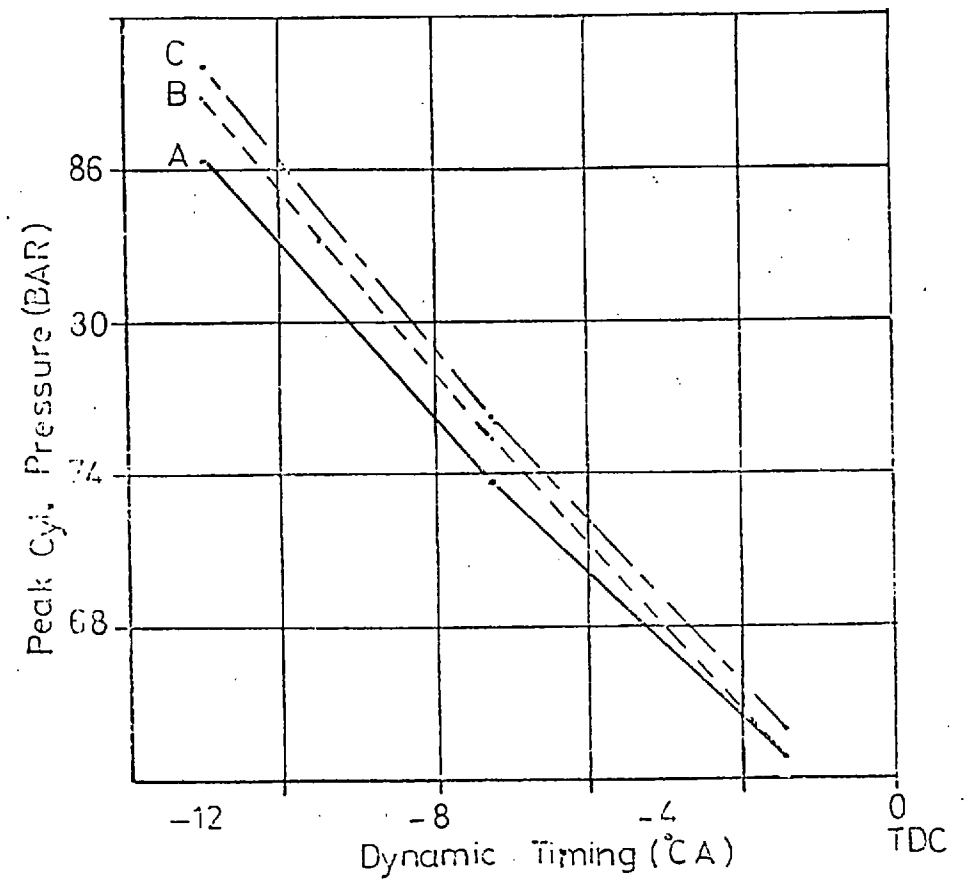

the datum. Part load conditions were considered to avoid errors introduced due to over-rich mixture formation in the prechamber at full load and early injection. The resulting effects have been considered for cases, A, B and C and are shown in Tables (8.7 to 8.11), and Figs. (8.10 to 8.14). The figures show that the conclusions arrived at for the optimum injection timing still apply for other timings; an improvement of +1.0% in η_i due to the passage and +3.0% due to heat loss effect. The improvements in Fig. (8.12) reveal the same trend as before but of larger magnitude. Examining Tables (8.7 to 8.11) it is apparent that at part load the improvement between cases A to D decreases. The η_i for case A at 1320 rpm part load, is believed to be an underestimation of the true value. For this condition, over-rich mixtures were encountered in the prechamber, resulting in underestimation of the overall IMEP. The reason for the large improvement in performance at part load is combustion related, and is explained in the following section.

In Fig. (8.10) delayed injection (from the datum) resulted in a drop in η_i for cases A, B and C. Delayed injection also resulted in higher heat loss in the prechamber. Early injection has a similar effect on the prechamber heat loss, and the total heat loss. The contribution of the prechamber to the total heat loss increased when the injection timing was advanced relative to the datum condition.

Changes in η_i and H_L with changing injection timing are thought to be combustion related. These changes are explained by considering the corresponding ROHR and cumulative heat release diagrams obtained for every case. These are shown in Fig. (8.15). Early injection leads to longer delay periods and hence higher initial ROHR due to more fuel being prepared during the delay period. This results in most of the heat being released in the prechamber, and hence more heat loss there (Fig. (8.11)). This also results in high peak cylinder pressure as shown in Fig. (8.14). The improvement of η_i is very small. In case A, η_i drops at the early injection conditions which

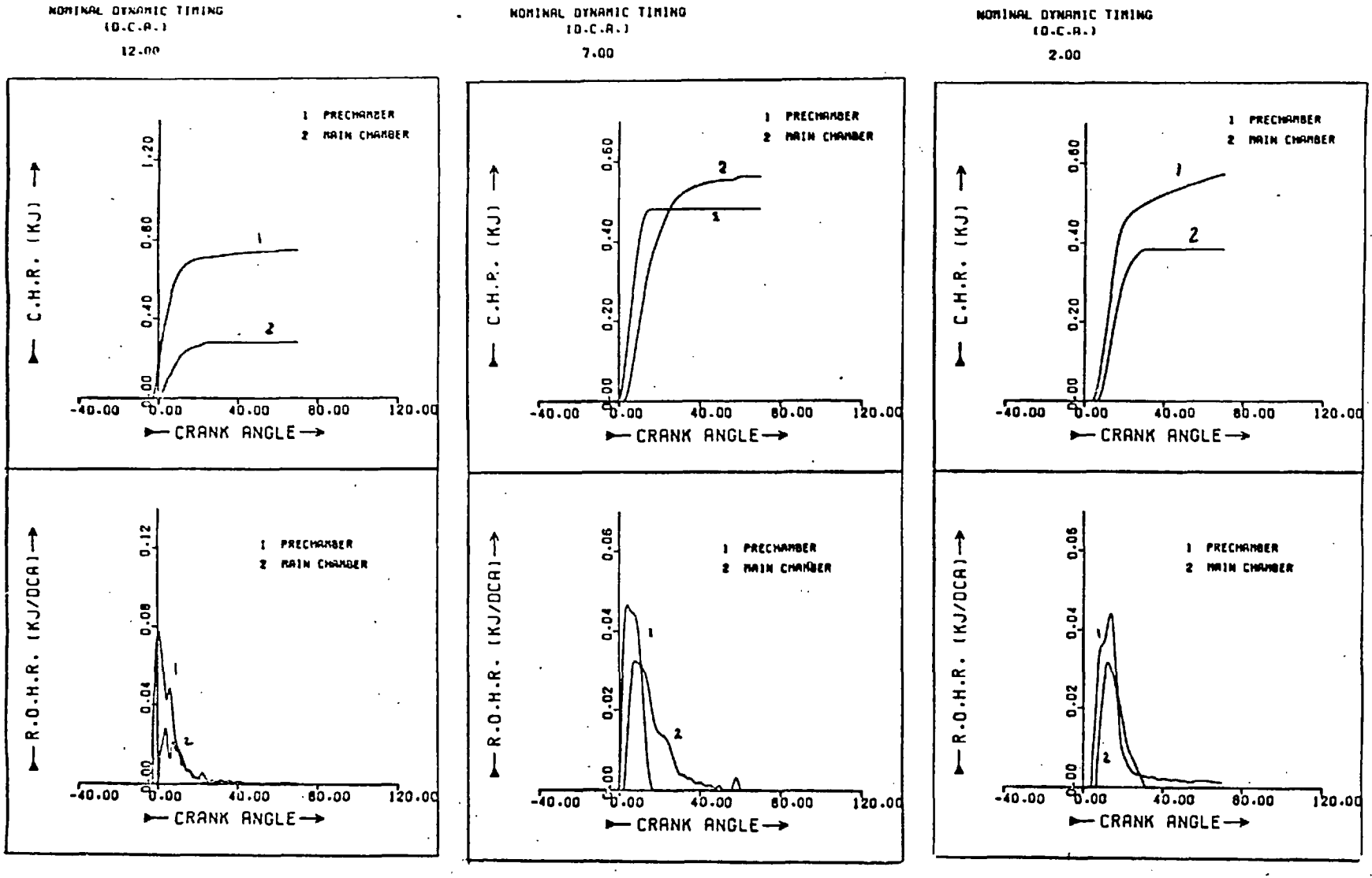

Fig. (8.15) ROHR and Cumulative Heat Release for IDI Engine for Different Injection Timing

is thought to be due to increased heat loss and a longer delay period, which counteracts the improvement due to early injection. As shown in Figs. (8.12 and 8.13) the effect of excess heat flux at the early injection is large.

For delayed injection, η_i drops sharply, while there is a small increase in H_L, compared to the datum timing conditions. Consulting Figs. (8.15) and (8.11) the increased heat loss occurs mainly in the prechamber due to more heat being released in the prechamber. The deterioration of η_i is a result of delayed combustion and heat release as shown in Fig. (8.15). Delayed injection also results in the drop in peak cylinder pressure indicated in Fig. (8.14). The change of η_i with timing does not explain the low η_i of IDI engines.

As shown in Fig. (8.11) the increase of H_L by injection advance for case C/A is small. This explains the behaviour seen in Fig. (8.13), since for the different C/A cases considered, both C and A values are at the same injection timing. The same comments apply for Fig. (8.12).

8.5 COMBUSTION MODE CONSIDERATIONS

In the previous section the importance of the combustion mode as a major parameter in the performance of the IDI engine relative to a DI version was emphasised. This is examined in greater detail herein.

Fig. (8.16) shows the fuel burning rate diagrams for the IDI and DI engines at the same speed and load. Several observations can be made on the apparent difference in shape between the two diagrams. Combustion starts earlier in the DI engine with a very high initial rate, due to early injection. The initial rate in the IDI case is considerably smaller, due to shorter delay, and therefore less fuel being prepared before ignition. Another important observation is the considerable amount of heat released in the IDI engine, late in the expansion stroke, relative to the DI version.

Firstly, the effect of injection timing of the DI engine was investigated. One injection timing was considered on either side of the datum value used. The results obtained are shown in Table (8.12). The values of η_i and H_L for

Fig. (8.16) Fuel burning Rate Curves For IDI and DI Engines
(2200 rpm. Full Load)

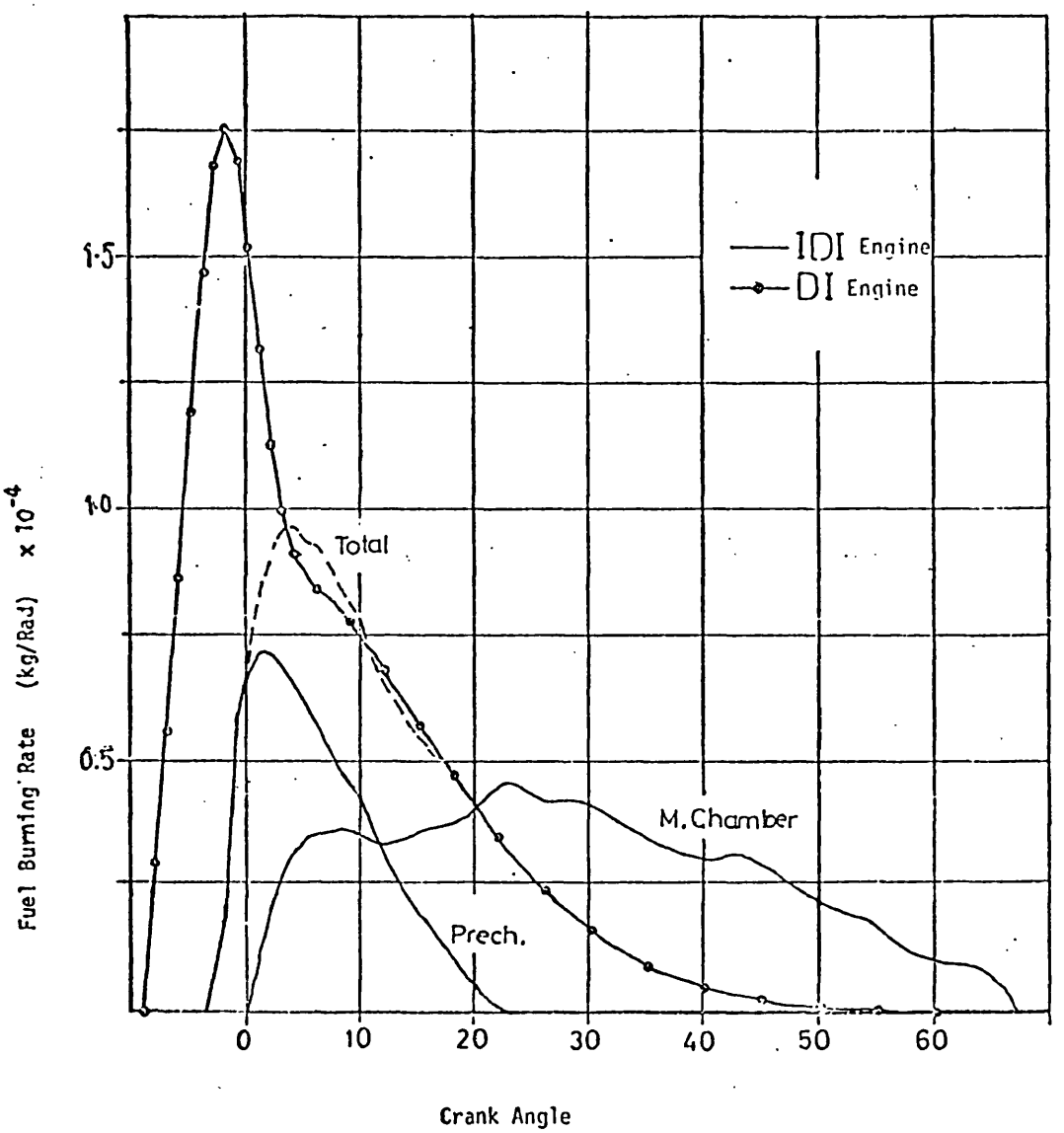

Table 8.13

DI Engine
Effect of Shifting R O H R Curve
(2200 rpm. Full Load)

Starting Point ^{o}CA	η_i %	Peak Pr. (BAR)	Heat Loss (KJ)	HL %	η_{i_r} %	H_r %
-12	60.82	135.70	0.312	12.59	115.65	98.98
-10	60.93	129.27	0.302	12.20	115.86	95.91
- 8	60.87	122.72	0.293	11.86	115.74	93.24
- 6	60.64	112.90	0.286	11.55	115.31	90.8
- 4*	60.23	109.54	0.279	11.27	114.53	88.60
- 2	59.67	102.73	0.273	11.04	113.46	86.79
0	58.96	95.84	0.268	10.84	112.11	85.22

* Original case

Table 8.14

IDI Engine

Effect of Shifting R O H R Curve
(1680 rpm. 40% Load)

Starting Point ^{o}CA	η_i %	Peak Pressure (BAR)	Heat Loss (KJ)	H_L %	η_{i_r} %	H_r %
-15	57.31	113.87	0.299	24.41	99.77	119.1
-10	58.94	103.81	0.275	22.45	102.61	109.6
- 5	58.89	91.00	0.257	20.98	102.52	102.4
0*	57.44	74.98	0.251	20.49	100.0	100.0
+ 5	54.32	59.84	0.264	21.55	94.57	105.2
+10	50.81	59.79	0.276	22.53	88.46	119.1

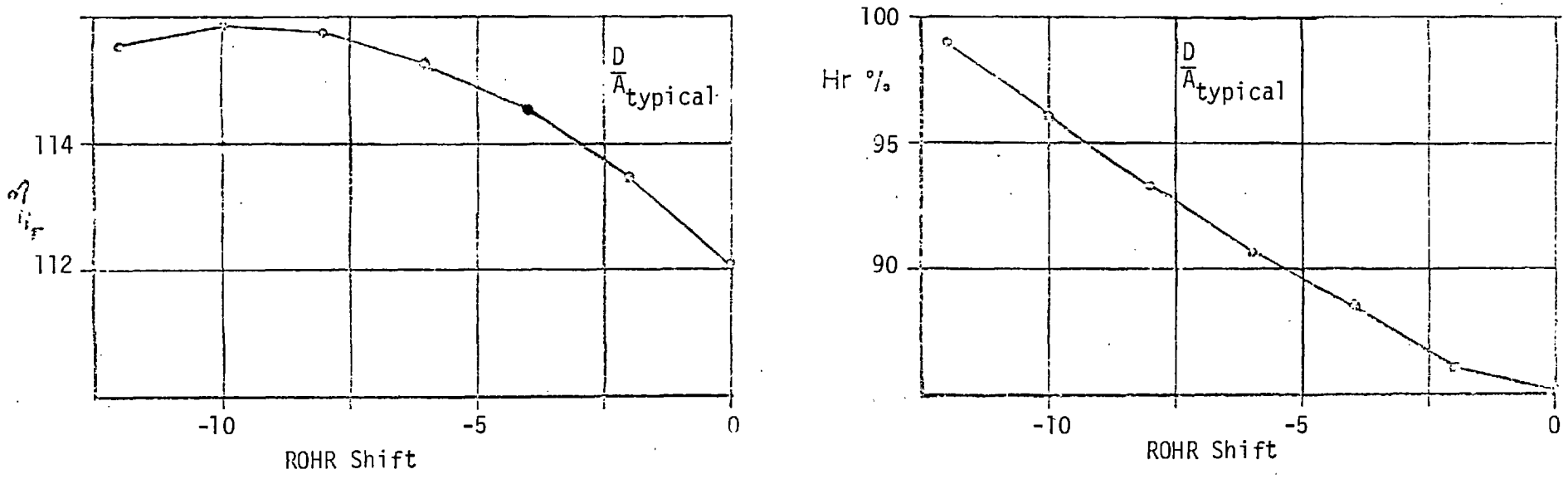

Fig. (8.18) Effect of Shifting R O H R Shifting on Relative Thermal Efficiency and Heat Loss Ratio for DI engine

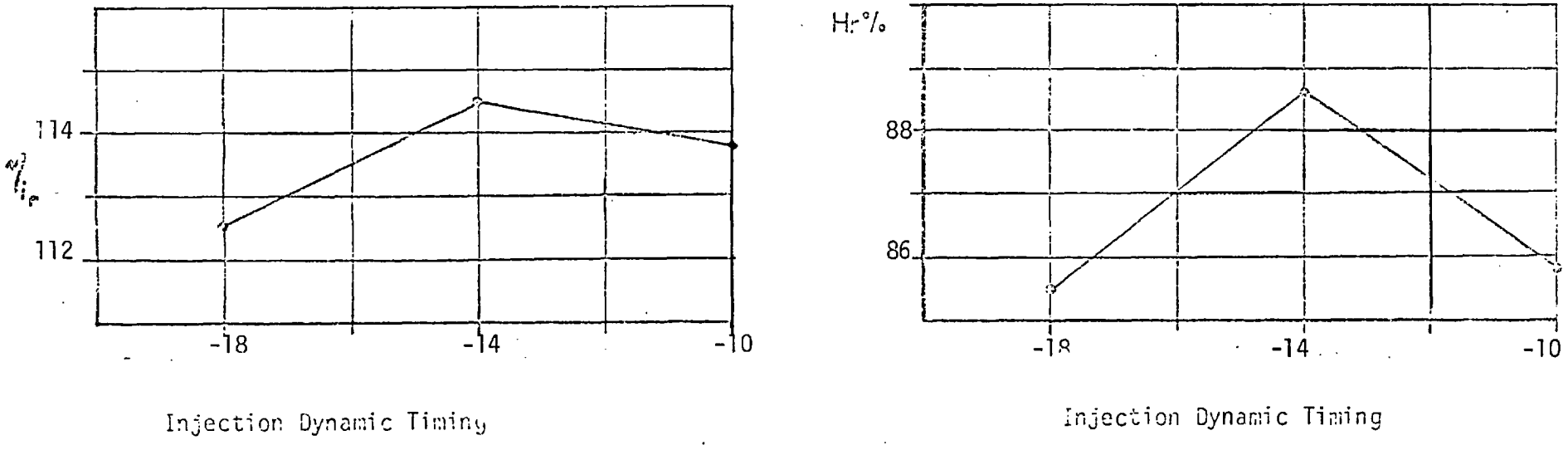

Fig. (8.17) Effect of Dynamic Injection Timing on Relative Efficiency and Heat Loss Ratio for DI engine

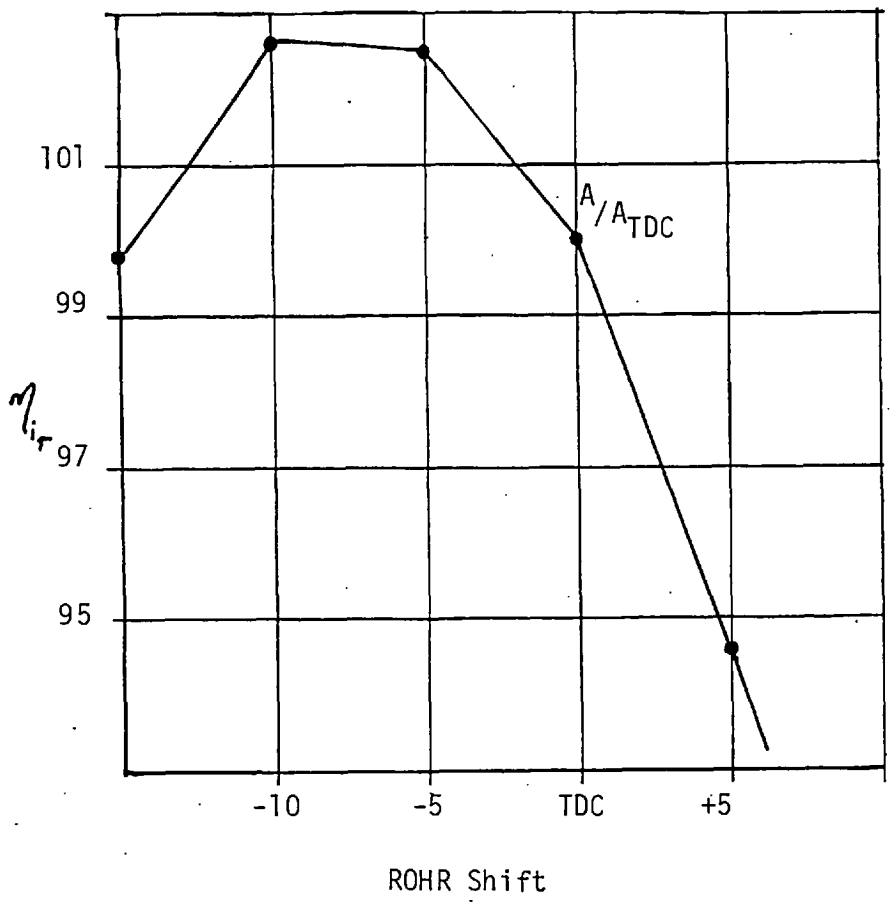

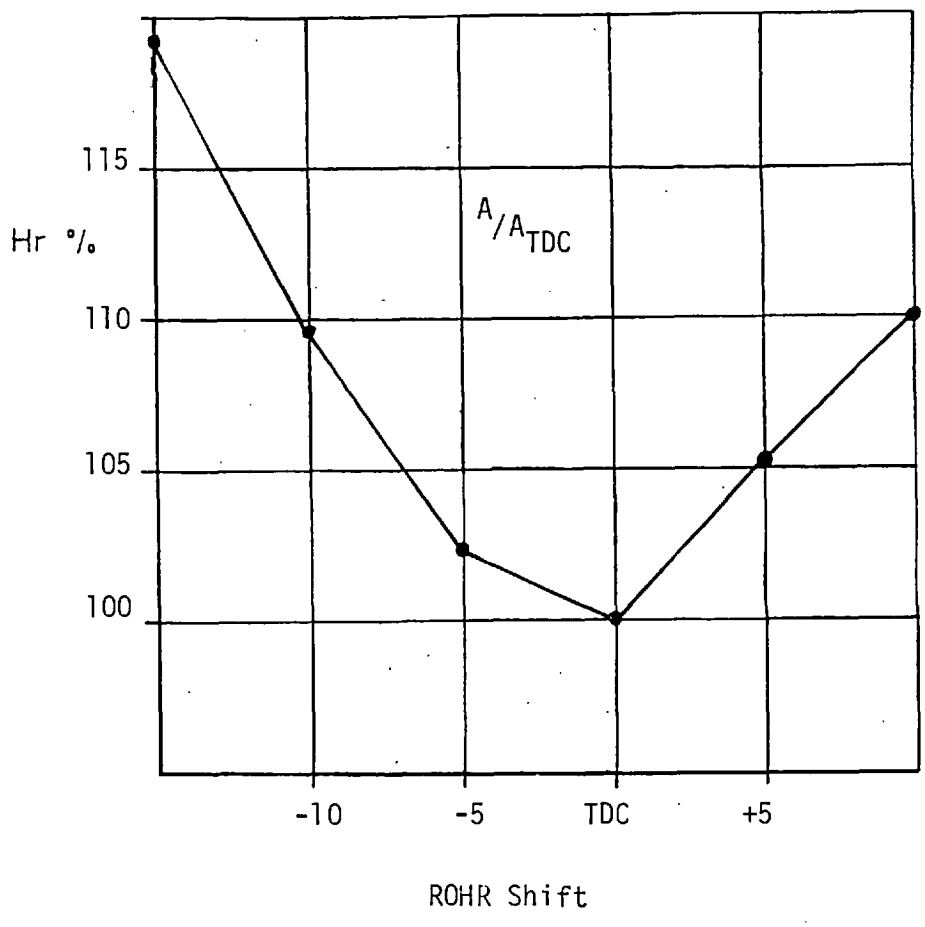

Fig. (8.19) Effect of Shifting ROHR Curve on Relative Efficiency and Heat Loss Ratio for IDI engine

the IDI engine at its typical timing were considered as the datum for the DI cases. Fig. (8.17) shows the values of η_{ir} and H_r obtained when altering the injection timing. The change of η_{ir} with injection timing is small, particularly when injection is retarded. This shows that injection timing (within the typical range studied for the DI engine), is not a major source of the large η_i differences between DI and IDI engines. Indeed, injection timing affects the delay period and hence the shape of the ROHR diagram and the ignition moment. This is studied separately.

The timing of ignition in the DI engine was studied by shifting in Table (8.13) and Fig. (8.18). The IDI engine case was chosen to be the datum for the η_{ir} and H_r values. The figure shows that, although the total heat loss falls as the starting point is retarded towards TDC, η_{ir} also reduces. The figure also shows that combustion timing is optimum at 10^0 BTDC. The value of η_{ir}, when ignition occurs at TDC, is large, showing that the effect of ROHR starting point cannot account for the large differences in η_i between DI and IDI engine. The figure also shows a consistant fall in H_r as the starting point approaches TDC, which is as to be expected.

Table (8.14) and Fig. (8.19) show results obtained from an investigation of the effect of shifting the ROHR on the overall performance of the IDI engine, case A. The same ROHR diagram was used for all cases changing only its starting point. Fig. (8.18) shows an increase of η_{ir} as the starting point was advanced. A maximum improvement of about 2.5% was reached at 10^0 BTDC beyond which η_{ir} dropped. The improvement in η_{ir} was obtained while heat loss (H_r) increased, supporting the previous arguments concerning the relative importance of combustion and heat transfer. Heat release starting after TDC has an adverse effect on both η_{ir} and H_r.

From the above considerations of the combustion mode in both the IDI and the DI engines, certain conclusions can be drawn. The shape of the rate of heat release diagram is of great importance to the behaviour of both engines.

Although delayed injection in the IDI engine case has a bad effect on its efficiency, due to delayed combustion, the major source of reduced efficiency of performance of the IDI engine in relation to the DI engine, is the large heat release down the expansion stroke.

Investigating Table (8.10) and Fig. (8.7), more evidence can be drawn to support the above conclusion. It is apparent that the improvement in DI efficiency, as measured by the increase in η_{ir}, is greater at medium engine speeds; 1680 and 2200 rpm. It was found, in Chapter 7, that for these two speeds a large part of the heat was released in the main chamber very late in the expansion stroke (see Fig. (7.10) and (7.12)). This would result in low η_i values for the IDI engine at these speeds. Another example from Fig. (8.7) is that η_{ir} is lowest at 1320 rpm. Consulting Fig. (7.8), a very small percentage of the heat is released late during expansion for this particular running condition, resulting in high η_i.

For part load conditions, it is shown in Table (8.10) that η_{ir} (i.e. case D/A) is less than the corresponding values at the full load conditions. This is except for the 1320 rpm case, which was discussed previously. At part load, less fuel is burnt than the full load case, which results in less heat being released late in the expansion stroke, as indeed was found in Chapter 7. This leads to some improvement in η_i values for the IDI engine at part load.

8.6 CONCLUSIONS

The sources of high specific fuel consumption, and hence low thermal efficiency, of the IDI engine have been examined. Passage gas pumping, excess heat loss to the walls and the influence of the combustion mode were considered to be the main parameters affecting IDI engine performance, relative to an equivalent DI version. Each parameter was successfully isolated and studied, for the IDI engine case. A hypothetical DI engine of same basic design and compression ratio as the IDI engine, was also considered.

It was concluded that the most important parameter is the combustion mode effect. This was responsible, at full load conditions, for the DI engine being an average of +5% greater in efficiency than the IDI engine. Excess heat loss contributed +1.0% and the passage loss +0.5%, on average.

It was also found that the performance of the IDI engine (relative to the DI engine) improved slightly at part load conditions. The reasons are mainly due to combustion effects.

For the DI engine, fuel is injected earlier than the IDI engine, leading to longer ignition delay, and hence more rapid initial ROHR as a result of more fuel being prepared before ignition. In the IDI engine, delay periods are very short due to late injection, high swirl and high compression ratio, which results in considerably lower initial ROHR values. Hence more fuel is burnt during the initial premixed phase of burning in the DI engine than the IDI case. As a result, the IDI engine experiences more diffusion burning than the equivalant DI. This results in a longer combustion period in the IDI engine. The resulting late heat release during the expansion stroke is not favourable and leads to a large loss in thermal efficiency.

CHAPTER 9

CONCLUSIONS AND RECOMMENDATIONS FOR FUTURE WORK

A detailed study of IDI engine operation, which includes isolating and investigating the different sources of losses in such engines was aimed at. For such an investigation, a reliable cycle analysis program is essential. This program would be required to reproduce IDI engine performance in accurate detail. It would then replace the actual engine, when conducting the loss isolation analysis.

Detailed information regarding IDI engine operation was needed to evaluate this cycle analysis program. Such data is not available at present and there is also lack of knowledge in IDI engine research concerning heat flux to the walls of each of the combustion chambers, instantaneous heat release rates in both chambers, behaviour of the connecting passage and ignition delay period. A sophisticated experimental arrangement was developed to test a swirl chamber type IDI engine, to furnish such information. A reliable and very rapid data acquisition system was used to record the experimental data required. Great accuracy was achieved in the different measurements involved.

To calculate instantaneous ROHR values in both combustion chambers of the engine tested, accurate pressure histories are required. This was achieved with special considerations for the pressure difference between the two chambers. The pressure difference monitors the continuous interaction between the two chambers. The main chamber pressure, and the pressure difference between the two chambers, were recorded for the closed part of the engine cycle. Averaging over 50 engine cycles and statistical considerations of the data obtained were completed. Conditions covering the entire operating range of

the engine were analysed. Injector needle lift diagrams and fuel line pressures were also measured simultaneously at each running condition.

Thermal shock effects were found to be more significant on the pressure transducer fitted in the prechamber, than that for the main chamber, due to the higher temperatures encountered therein. Thermal shock effects on pressure transducers were investigated and it was concluded that they could be reduced by recessing the pressure transducers. Heat shielded transducers also gave good behaviour against thermal shock effects. These were used to obtain the required main chamber pressure and pressure difference diagram.

Analysis of the pressure diagrams obtained to calculate ROHR in both chambers requires information about instantaneous heat transfer to the walls. A surface thermocouple having a very fast response, was used to measure instantaneous wall temperatures for both the prechamber and the cylinder head. Using Fourier Analysis, the corresponding instantaneous heat fluxes were determined. Heat flux rates were found to be higher for the prechamber than the main chamber, but the prechamber contribution to the total heat loss was only about 30%.

For an IDI engine, the connecting passage is the link between the two combustion chambers, and therefore affects their interaction. A theoretical investigation was conducted which provided an understanding of the flow through sharp and thick orifices. This also furnished an explanation for differences in published discharge coefficient values used by various researchers. The passage for the engine tested was found to be of the sharp orifice group. Discharge coefficients for this passage were determined experimentally under steady flow conditions. They were found to be dependnet on flow direction and pressure ratio. Piston proximity was also found to be important in determining the discharge coefficient. It was not possible however to theoretically model the effect of the angle of inclination of the passage, which is a recommended area for further work. It was found that

unsteady flow and pressure wave effects on the passage were negligible for the low pressure ratios involved. However, the effect of inertia of the gas flowing through the passage is expected to become significant at high engine speeds. In the present work evidence for this was only found at the high speed end. Charge inertia effect is a research area where future work is recommended.

Complete thermodynamic simulation of an IDI engine was then conducted, taking into consideration all thermodynamic operations involved. This was then formulated mathematically in order to calculate instantaneous ROHR values in both combustion chambers simultaneously, by analysing experimentally obtained pressure diagrams. For this a model was needed for the calculations of heat transfer.

The concept of kinetic energy conservation was used to obtain average characteristic velocity estimates in the main and prechambers. Energy dissipation by viscous friction from rotating disc data, was adopted. Satisfactory values of Re were obtained and compared with values measured by Hassan. The convective heat transfer was found to be reasonably represented by a (Nu-Re) relationship for turbulent convection. For fired operation, radiative heat flux calculations were included together with an allowance for the kinetic energy induced from the fuel jet. Comparison between measured and calculated heat fluxes showed good agreement.

ROHR diagrams were obtained for a wide range of engine operating conditions. The importance of the pressure difference signal in monitoring distortion of pressure diagrams due to smoothing, has been outlined. The rate of pressure rise was found to be the most dominant factor in the calculations. Reasonable ROHR diagrams were obtained for both combustion chambers. It was found that over-rich mixtures of fuel and air prevailed in the prechamber down the expansion stroke in specific conditions, namely low engine speeds and early injection. This is thought to be due to a longer residence time for fuel burning in the prechamber under these conditions.

Mathematically expressing the properties of over-rich mixtures of fuel and air combustion products, is another area where future work will be useful.

The results obtained from the ROHR calculations identified a low initial ROHR, which reflects the short ignition delay periods. A test arrangement was developed to facilitate very accurate measurement of the delay period. The delay periods of the engine tested were measured for different conditions of speed, load and injection timing. Ignition delay periods were found to be less than 0.7 ms, decreasing with engine speed and load and with injection retard. The measured behaviour was correlated taking account of both the physical and chemical delay periods. The physical delay was found to form a considerable part of the total delay period, and to decrease with engine speed.

Correlating ignition delay periods and ROHR curves would provide very useful analytical expressions for fuel burning in the IDI engine. This is an important recommended extension to the present work.

The thermpdynamic and mathematical simulation used for ROHR calculation was also extended for a full cycle analysis program. This program was checked against the measured performance of the engine to ensure that it reproduced engine behaviour closely under motored and fired conditions. Once this was achieved the subsequent step of loss isolation commenced.

Passage pumping, excess heat flux and combustion mode effects on IDI engine operation were successfully isolated and quantified. A hypothetical DI engine, which had the same basic design and compression ratio, as the IDI engine, was also considered. Comparisons between the predicted IDI and DI engine performance permitted the following conclusions to be drawn, regarding the low thermal efficiency of the IDI engine, and hence high specific fuel consumption in relation to the equivalent DI engine. The passage pumping contributes only 0.5 to 1.0 of the total 7.0 percentage efficiency points difference between IDI and DI engine. Extra heat fluxes contribute 1.0 to 2.0

percentage points of the total, while the combustion mode effect is responsible for about 5.0 percentage points. The reduced efficiency at full load was found to be greater than that at part load. The main reason for this was found to be due to combustion mode, i.e. variation of the shape of the ROHR curve with load. It was also concluded that the shape of the ROHR diagram and particularly heat release late in the expansion stroke in the IDI engine, was the predominant factor resulting in low thermal efficiency compared to the DI engine.

A possible extension to the present work could be an analysis of the turbocharged IDI engine. This could be included in the cycle analysis program developed in the present study with minor modifications.

APPENDIX A

EFFECT OF THERMAL SHOCK ON CYLINDER PRESSURE TRANSDUCERS

In a piezo-electric pressure transducer, an electrical charge is produced by exerting a force on a quartz crystal, the electrical charge being a function of the force. Due to different thermal expansion coefficients and different thicknesses of the elements comprising the pressure transducer, thermal shock effects are important. A rapid application of heat produces uneven expansion of the diagraphm of the transducer, resulting in a force exerted on the quartz crystal. This produces an electric charge which could be wrongly interpreted as being a pressure signal. Although some pressure transducers have temperature compensation, which would tend to bring the signal back to zero after an application of a thermal shock (after a short time), it seems doubtful that it could be effective at the high frequencies involved in engine research applications (Brown, (25)).

The thermal shock distortion of pressure signals can be seen in Fig. (A.1, a and b). The figures show a pressure difference signal, between main and prechamber, under the same engine running conditions. In Fig. (A.1.a) the pressure transducer is suffering from a thermal shock effect which is indicated as a positive pressure difference throughout the expansion stroke, at the end of which it should fall to approximately zero. Fig. (A.1.b) shows a signal obtained when using thermal shielded transducers which, as indicated, do not suffer from the thermal shock effect.

A test apparatus was arranged to measure and study the thermal shock effect on piezo-electric pressure transducers and investigate the effects of coating the transducer face. Fig. (A.2) indicates the test arrangement. A D.C. motor was mounted vertically with its shaft coupled to another shaft carrying a

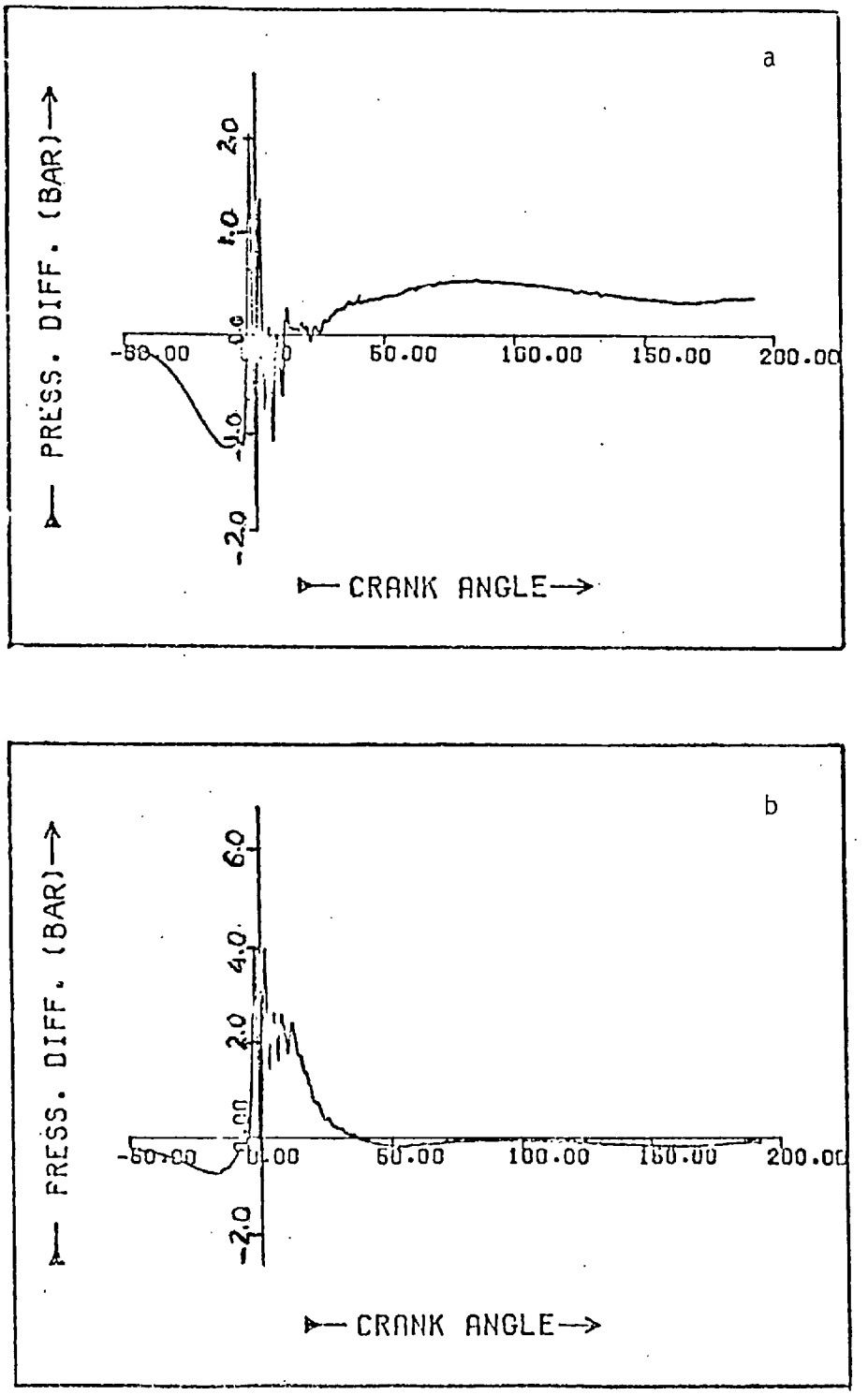

Fig. (A.1) Thermal Shock Effect on Pressure Difference between combustion chambers

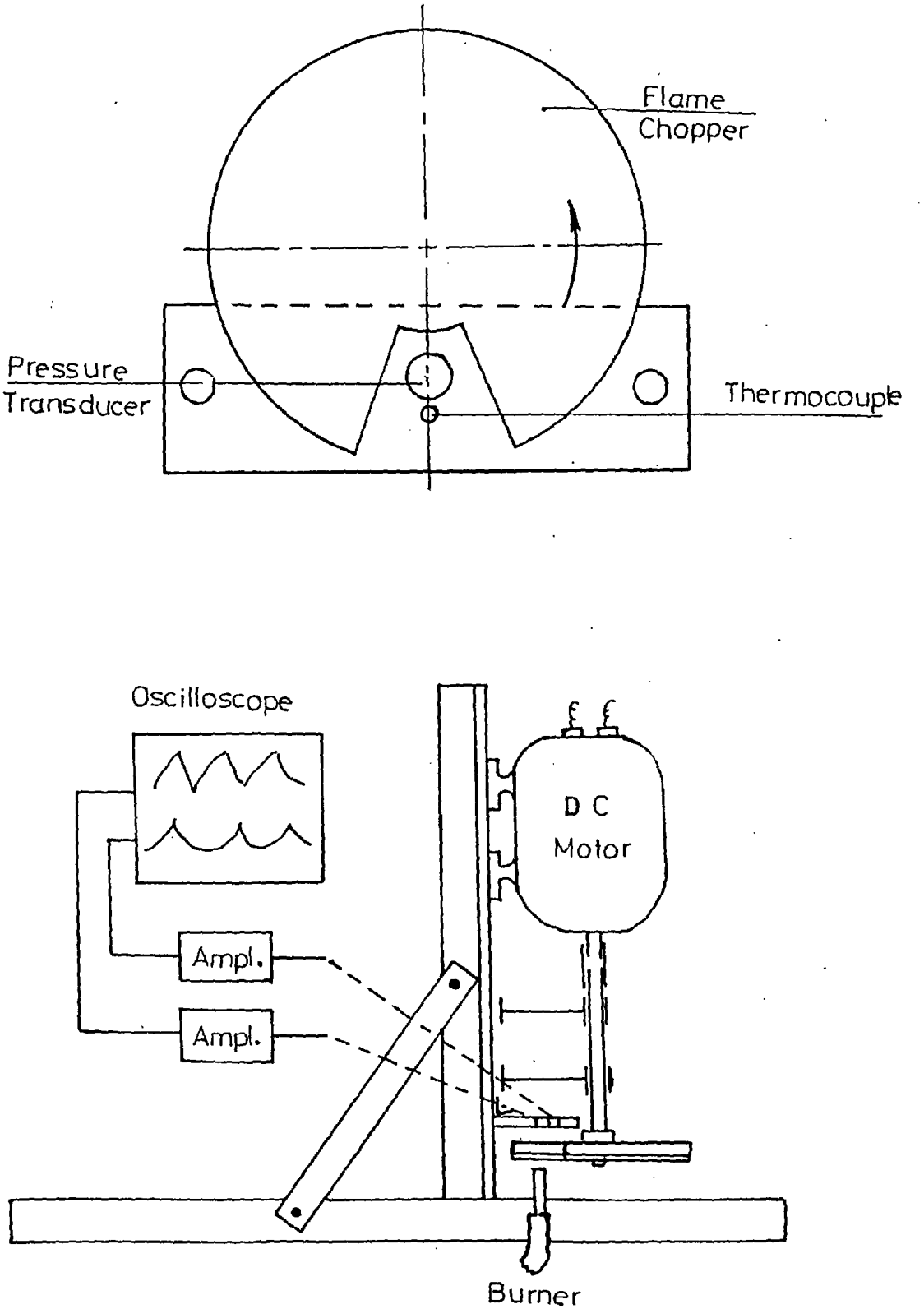

Fig. (A.2) Thermal Shock Test Arrangement

sector wheel. A flame was applied below the wheel using a propane burner. The flame chopper (sector wheel) was made of aluminium, with a thermal guard of asbestos. Behind the wheel the transducer under test and a thermocouple were mounted, the amplified output from both being displayed in a storage oscilloscope. A polaroid camera was used to take photographs of the traces. Using this arrangement it was possible to study thermal shock effect under single shot, alternate and cyclic mode conditions. Examples of the results of each mode of testing are shown in Fig. (A.3).

To study the effects of transducer face coating on its thermal shock behaviour, the thermal shock input had to be kept constant for the comparative tests. This was ensured by using high response thermocouple wires spot welded with a very small bead. The thermocouple used was made from nickel chromium-constantan, with wires of 200 micron diameter. The propane flame was adjusted in each case to give a fixed temperature rise and rate of temperature rise, for similar test conditions.

Fig. (A.4) shows the final results of the investigation. Two different coatings were tried, RTV silicone rubber and ceramic fibre of different thickness. A thermal shielded (AVL 12QP 505CLK) transducer was also tested. The results show a noticeable improvement of the thermal shock behaviour of the transducer (AVL 12QP 500C)when the ceramic fibre coating was used. Although the improvement in behaviour when using the RTV rubber coating was smaller than that with ceramic fibres, it enabled the relative importance of specific areas on the transducer face to be examined. From the figure it is apparent that the middle zone (A) and the diaphragm (B) are more important than zone (C).

As both RTV rubber and ceramic fibre coating were not expected to last long in a fired engine, an alternative was examined to dampen the effect of thermal shock. It was found (see Fig. (A.4)) that recessing of the pressure transducer reduced its thermal shock sensitivity by a large margin. Examining Fig. (A.4) it is clear that a recessed transducer has a behaviour which is

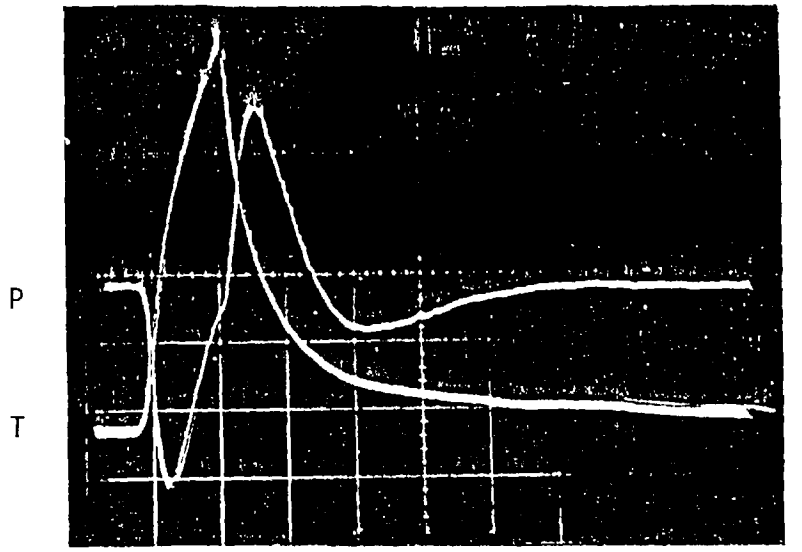

1.0 S/cm

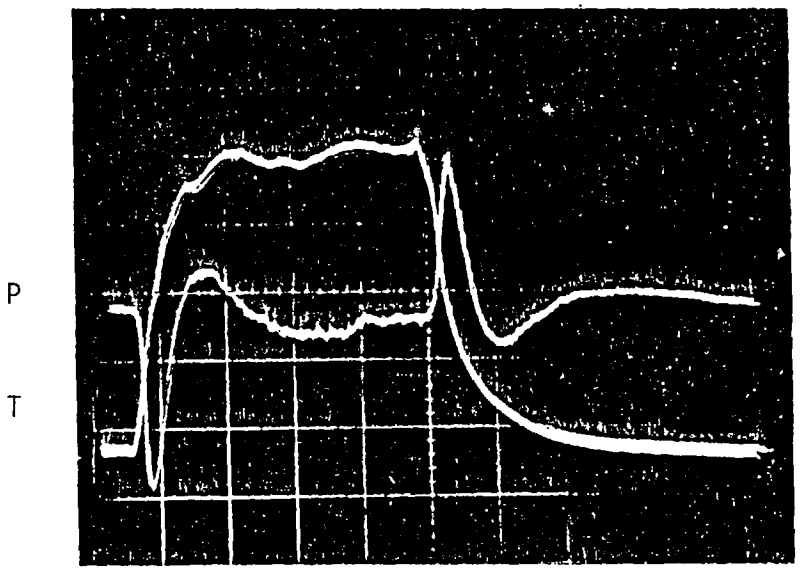

2.0 S/cm

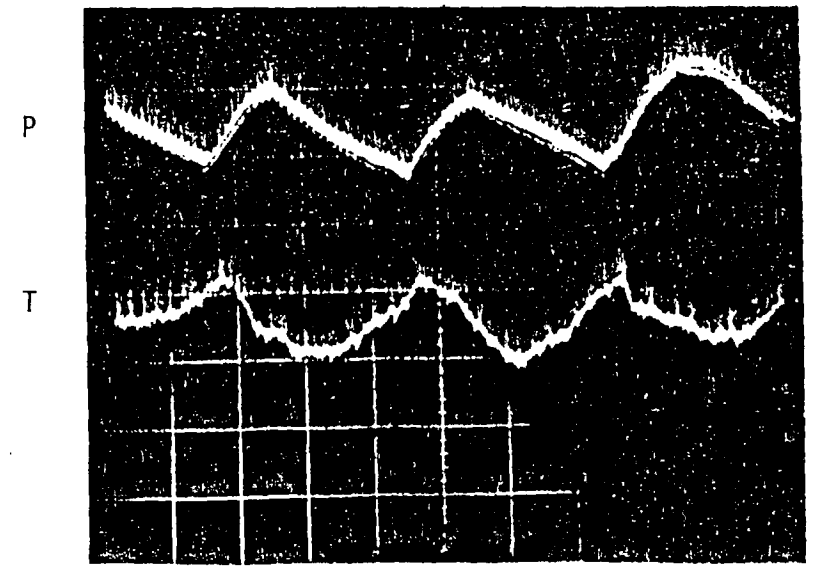

0.1 S/cm

Fig. (A.3) Thermocouple and Pressure Transducer Traces
(46.3 ^{o}C/Cm and 0.21 Bar/Cm)

Criteria of Application of Thermal Shock \ Coating Conditions at Transducer Face				No Coating (Flush)	No Coating Back Mounted	RTV Rubber at (A),	RTV Rubber at (A),(C)	RTV Rubber at (A),(B)	RTV Rubber at (B)	RTV Rub. at (B) Ceramic 1m/2m at (A)	Ceramic F.(2mm) at (A), (B),(C)	Ceramic F.(1.0 mm) at (A), (B),(C)	Thermal Shielded Trans-ducer
				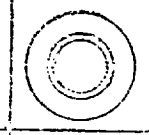	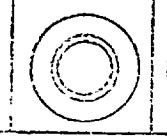	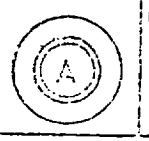	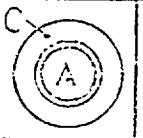	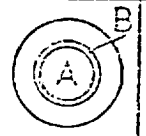	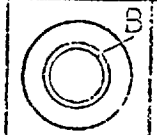	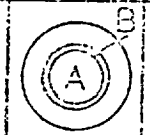	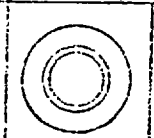	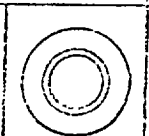	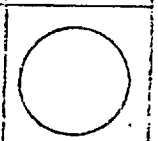
Single Shot	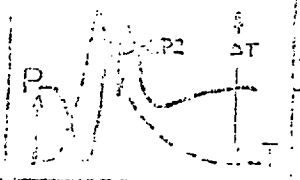	$\frac{\Delta P_1}{\Delta T}$	$10^2 \times \frac{BAR}{^oC}$	0.235	0.141	0.080	0.172	0.164	0.201	0.279	0.080	0.149	0.185
		$\frac{\Delta P_2}{\Delta T}$		0.235	0.141	0.068	0.068	0.103	0.201	0.100	0.072	0.058	0.273
Alter-nate		$\frac{\Delta P_1}{\Delta T}$		0.086	0.032	0.044	0.053	0.032	0.032	0.027	0.037	0.053	0.092
		$\frac{\Delta P_2}{\Delta T}$		0.258	0.108	0.258	0.222	0.146	0.162	0.139	0.094	0.089	0.185
Cyclic	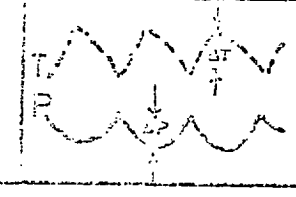	$\frac{\Delta P}{\Delta T} \times 10^5$	$\frac{BAR}{^oC}$	0.542	0.102	0.474	0.407	0.163	0.313	0.214	0.163	0.058	0.345

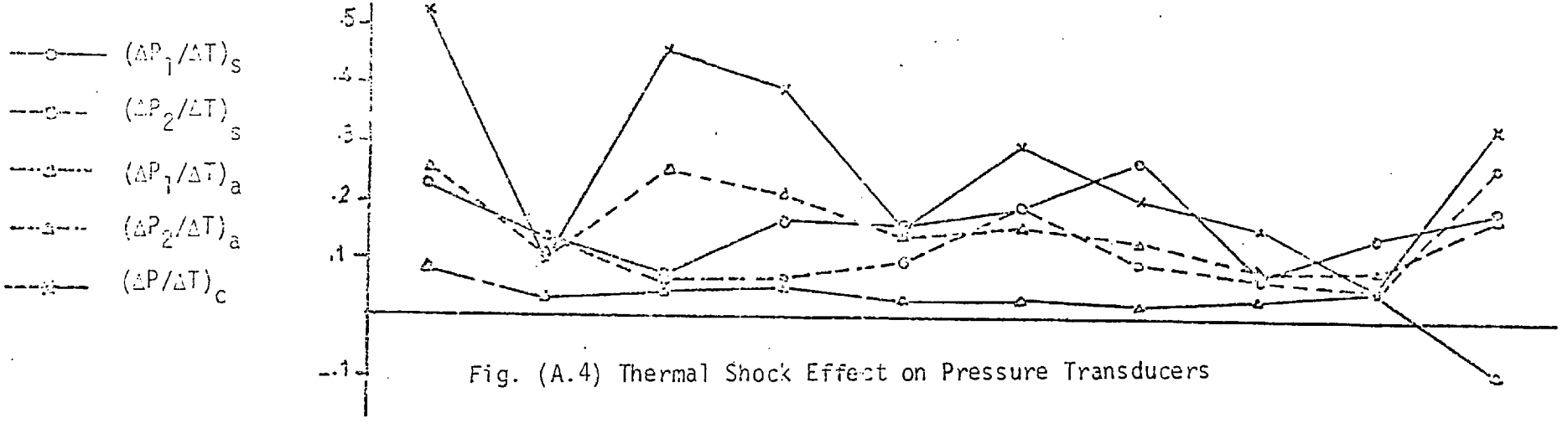

Fig. (A.4) Thermal Shock Effect on Pressure Transducers

even better than the thermal shielded transducer when flush mounted.

In conclusion, when mounting a pressure transducer in an engine, it was found that recessing it would overcome some of the thermal shock effects. Alternatively, a thermal shielded transducer can be used, flush mounted, and still render good overall behaviour.

APPENDIX B

EXHAUST EMISSIONS MEASUREMENTS

An analysis of the emissions contents of the exhaust gases was performed, the measured species being smoke, carbon monoxide, nitrogen oxides and hydrocarbons.

A sample of the exhaust gases was continuously connected to a conventional optical smoke meter. The smoke content, in Hartridge units, was measured at all running conditions. The results are shown in Table (2.1). The variation of smoke with engine speed, load and timing is shown in Fig. (B.1). The results show a decreasing trend of smoke with increasing engine speed except at 12^{o} BTDC dyanmic timing. The smoke concentration also shows a decreasing trend as the dynamic injection point approaches TDC.

As combustion takes place, simultaneously, in two chambers, the phenomena of smoke formation is complex. Part of the smoke formed during diffusion burning in the prechamber could burn, later, in the main chamber. The increase of smoke content of the exhaust gases, with increase of engine load, could be explained as being a result of more fuel burnt through diffusion burning. A full combustion model is required to investigate, and relate, the effect of engine speed and dynamic injection timing on smoke, and other exhaust emissions, formation. This was outside the scope of the present work.

A special sampling probe, with radial sampling holes, was inserted along the exhaust pipe axis. This provided a representative sample of the exhaust gas for analysis. This sample was divided into two parts. One part was passed through an electrically heated line to a Flame Ionization Detector (FID) (IPM German make-model RS5) where the hydrocarbons concentration was

Table B.1

Measured Exhaust Emissions

Load %	Speed		1320			1680			2200			2800		
	D.Timing		2°	7°	12°	2°	7°	12°	2°	7°	12°	2°	7°	12°
100	CO	ppm	105	215	750	112	197	367	65	28	35.0	330	450	200
	HC*	ppm	9.5	11.5	25.0	10.0	13.0	20.5	6.8	7.9	5.2	2.6	11.0	10.5
	NO	ppm	345	435	390	330	310	445	395	440	515	430	485	470
	Smoke*		16.5	48.0	72.5	18.0	38.0	71.0	17.5	37.0	50.0	10.0	27.0	71.0
87.5	CO	ppm	85	120	155	77	80	125	80	25.0	25.0	300	320	75
	HC	ppm	12.0	11.0	23.0	9.5	9.5	13.0	5.7	7.3	5.4	4.5	6.2	11.5
	NO	ppm	365	405	370	365	425	450	400	375	505	450	455	475
	Smoke		13.5	32.0	35.0	12.5	23.0	37.0	7.5	11.5	24.0	7.0	15.0	28.0
75	CO	ppm	85	120	155	77	80	125	60	25.0	25.0	160	250	50.0
	HC	ppm	11.5	15.0	24.0	12.0	23.0	26.0	9.0	6.9	5.5	9.8	11.5	13.9
	NO	ppm	342	425	455	330	410	470	385	345	520	420	470	465
	Smoke		10.5	21.0	26.0	8.5	11.0	12.0	2.5	6.0	12.0	4.0	8.0	12.0
50	CO	ppm	85	67	135	88.0	70.0	90.0	52.0	18.0	20.0	-	-	0.0
	HC	ppm	19.0	18.5	34.5	14.5	26.5	27.0	10.0	12.5	5.7	8.5	8.5	11.0
	NO	ppm	310	400	490	315	360	500	335	350	540	350	445	460
	Smoke		3.0	4.0	4.5	7.5	7.0	4.0	1.0	2.0	2.5	1.0	2.0	3.5
25	CO	ppm	175	95.0	97.0	118	97.0	63.0	75.0	20.0	20.0	-	-	0.0
	HC	ppm	21.0	31.0	45.0	20.5	22.0	30.0	12.0	10.0	8.4	7.8	7.4	11.0
	NO	ppm	295	280	435	230	280	350	300	315	450	290	360	485
	Smoke		2.5	3.5	2.5	6.5	5.5	1.5	1.0	1.0	1.5	0.0	1.0	2.5
2	CO	ppm	450	230	150	440	225	125	230	28.0	28.0	-	-	0.0
	HC	ppm	17.0	22.0	39.0	26.5	28.0	16.5	27.0	19.5	7.5	17.0	7.8	11.0
	NO	ppm	12.0	210	355	220	245	235	195	250	405	200	260	435
	Smoke		3.0	2.0	1.0	6.0	4.0	2.0	3.5	2.5	1.0	0.0	0.0	2.0

* Smoke - in Hartridge units
* Hydrocarbons - expressed as propane

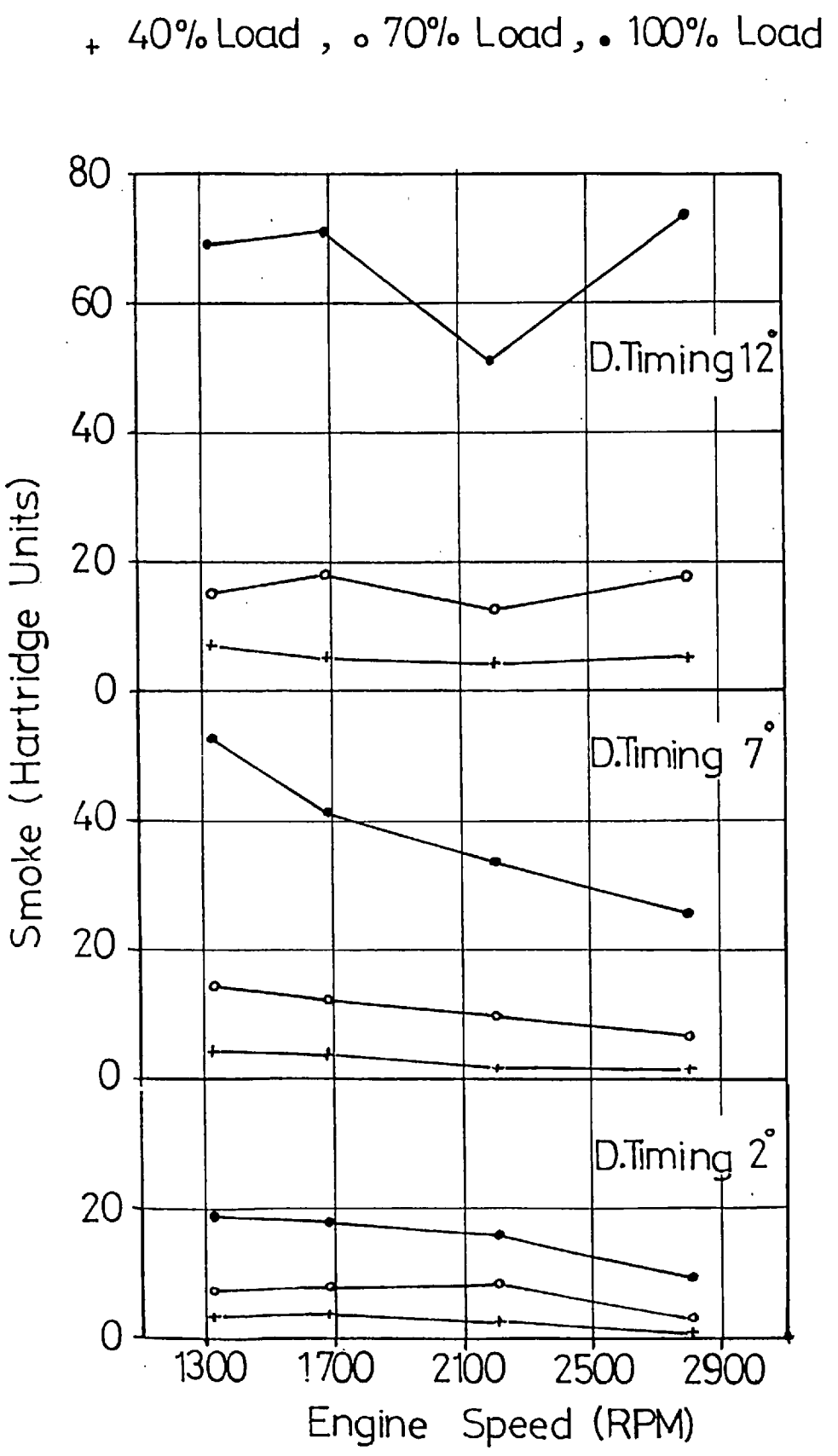

Fig. (B.1) Results of Smoke Measurements

determined. The other part of the exhaust sample was filtered and refrigerated through a special unit before further analysis took place. The CO concentration was determined using an Infra red gas analyzer (model UNOR 6). The nitrogen oxides concentration was measured using a Luminox Analyzer.

The results of the emissions measurements under different engine speeds, loads and dynamic injection timings are shown in Table (B.1).

REFERENCES

1. Abbott, D.E. and Kline, S.J. "Experimental Investigation of Subsonic Turbulent Flow over Single and Double Backward Facing Steps". ASME Transactions, J. of Basic Engineering, September, 1962.
2. Abu-Romia, M.M. "Appropriate Mean Absorption Coefficients for Infrared Radiation of Gases". ASME Transaction, November, 1967.
3. Adler, D. and Lyn, W.T. "The Evaporation and Mixing of a Liquid Fuel Spray in a Diesel Air Swirl". Instn. Mech.Engrs 1969-70. Vol 184, pt. 3J.
4. Alcock, J.F. "Some more light on Diesel Combustion". Proc. Instn mech. Engrs, Auto. Div., 1962-63, No. 5, p. 179-191.
5. Alyea, J.W., Uyehara, O.A. and Myers, P.S. "The Development and Evaluation of an Electronic Indicated Horsepower Meter". SAE Paper 690181, Vol. 78, 1969.
6. Anisitis, F. "Experimentelle Bestimmung und analytische Fassung der Brennverlaufe fur Vorkammer-Dieselmotoren als Randbedingung fur die Prozebberechnung". Ph.D. Thesis, 1973, Der Technischen Universitat Carolo-Wilhelmina zu Braunschweig.
7. Anisitis, F. "Pressure Development Evaluation Methods and Electronic Calculation of the Combustion Process in Diesel Engines with Divided Combustion Chambers". M.T.Z., Number 12 - December, 1971.
8. Annand, W.J. "Heat Transfer in the Cylinders of Reciprocating Internal Combustion Engines". Proc. Instn. Mech. Engrs., 1963, Vol. 177, No. 36.
9. Annand, W.J. "Choice of a Computing Procedure for Digital Synthesis of Reciprocating Engine Cycles". J. of Mech. Eng. Sci., 10, (3), 1968.
10. Annand, W.J. "Instantaneous Heat Transfer Rates to the Cylinder Head Surface of a Small Compression-Ignition Engine". Proc. Instn Mech. Engrs 1970-1971. Vol. 185 72/71.
11. Annand, W.J. "Heat Transfer from Flames in Internal Combustion Engines". "Heat Transfer in Flames". Edited by N.H. Afgan and J.M. Beer, 1974.

12. Beer, J.N. and Chigier, N.A. "Combustion Aerodynamics". Applied Science Publishers Ltd., 1972, London.

13. Begg, R.D. "Method of Force Defect Coefficients applied to Asymmetric Two-Dimensional Orifice". ASME Trans.,Journal of Mech. Eng. Science, Vol. g, No. 4, 1967.

14. Belinski, L.M. "Thermal radiation in the Combustion Chamber of a high-speed Compression Ignition Engine". Trudi N.I.L.D. No. 1, Moscow, 1955.

15. Benedict, R.P. "Some Comparisons between Compressible and Incompressible Treatments of Compressible Fluids". Journal of Basic Eng., Trans. ASME, Series D, Vol. 86, No. 3, 1964, p. 527.

16. Benedict, R.P., Carlucci, N.A. and Swetz, S.D. "Flow Losses in Abrupt Enlargements or Contractions". ASME Trans., Journal of Engineering for Power, Jan. 1966.

17. Benedict, R.P. "Generalized Contraction Coefficient of an Orifice for Subsonic and Supercritical Flow" ASME Trans., Journal of Basic Engineering, June, 1971.

18. Benson, R.S. and Pool, D.E. "The Compressible Flow Discharge Coefficients for a Two-Dimensional Slit". Int. F. Mech. Sci., 7 (No. 5), p. 337.

19. Benson, R.S. and Pool, D.E. "Compressible Flow through a Two-Dimensional Slit", Int. F. Mech. Sci., 7 (No. 5) p. 315.

20. Benson, R.S. "Discussion on paper number 7". Proc. Instn mech. Engrs, Vol. 180 pt 3F, 1965-66.

21. Benson, R.S. "A comprehensive Computer Program to simulate a Compression Ignition Engine Including Intake and Exhaust Systems". Paper 71073 presented at SAE Automotive Engineering Congress, Detroit, January 1971.

22. Bloxham, R.D. "Computer Control for I.C. Engines' Development". CME, 19, (9), October, 1972.

23. Borman, S.L. "Mathematical Simulation of Internal Combustion Engine Processes and Performance including Comparisons with Experiment". Ph.D. Thesis, University of Wisconsin, 1964.

24. Bragg, S.L. "Effect of Compressibility on the Discharge Coefficient of Orifices and Convergent Nozzles". Trans. of ASME, Journal of Mech. Eng. Science, Vol. 2, No. 1, 1960.

25. Brown, W.L. "Methods for Evaluating Requirements and Errors in Cylinder Pressure Measurement". SAE Paper No. 670008, 1967.

26. B.S. 1042, British Standard on "Flow Measurements", 1943.

27. Conte, S.D. "Elementary Numerical Analysis". McGraw-Hill Book Co., New York, U.S.A.

28. Daily, J. "Chamber Dimension Effects on Induced Flow and Frictional Resistance of Enclosed Rotating Discs". Trans. ASME, Vol. 82, Series D, March 1960, p. 217.

29. Deckker, B.L. and Chang, Y.F. "An Investigation of Steady Compressible Flow through Thick Orifices". Proc. Instn Mech. Engrs , Vol. 180, Pt 3F, 1965-66.

30. Dent, J.C. and Derham, J.A. "Air Motion in a Four-Stroke Direct Ignition Diesel Engine". Proc. Instn Mech. Engrs , 1974, Vol. 188, 21/74.

31. Dent, J.C. and Suliaman, S.J. "Convective and Radiative Heat Transfer in a High Swirl Direct Ignition Diesel Engine". SAE Paper No. 770407, 1977.

32. Dicksee, C.B. "The High Speed Compression Ignition Engine". Blackie and Son, London, 1940.

33. Ebersole, G.D., Myers, P.S. and Uyehara, O.A. "The Radiant and Convective Components of Diesel Engine Heat Transfer". SAE Paper 701C, June 1963.

34. Edwards, D.K., Glassen, L.K. and Tuchsher, J.S. "Radiation Heat Transfer in Non Isothermal Non Grey Gases". ASME Transaction. August 1967.

35. Eichelberg, G. "Some New Investigations on Old Combustion-Engine Problems". Engineering, London 1939, 148, 463 and 547.

36. Elliott, M.A. "Combustion of Diesel Fuel Oils". Trans. ASME, 1948, New York, p. 57-125.

37. Elser, K. "Der Instantionaire Warmeubergang in Diesel motoren". Mitt. Inst. Thermodyn, No. 15 Zurich, 1954.

38. El-Wakil, M., Mayers, P.S. "Fuel Vaporisation and Ignition Lag in Diesel Combustion". SAE Trans. Vol. 64, 1956, p. 712-726.

39. Fitzgeorge, D. and Allison, J.L. "Air Swirl in a Road-Vehicle Engine". Proc Instn Mech. Engrs , Aut. Div., 1962-63, 25.

40. Fluid Meters, Their Theory and Application, Report of ASME Research Committee on Fluid Meters, 5th Ed, 1959.

41. Flynn, P., Mizusawa, M., Uyehara, O.A. and Myers, P.S. "An Experimental Determination of the Instantaneous Potential Radiant Heat Transfer within an Operating Diesel Engine". SAE Trans. Vol. 1, 1972, Paper 720022.

42. Frank, W.L. and Hardenberg, H.O. "Noise, Emissions and Performance of the Diesel Engine - A Comparison between DI and IDI Combustion Systems". SAE paper 750796, Vol. 84, 1975.

43. French, C.C. and Hartles, E.R. "Engine Temperatures and Heat Flows under High Load Conditions". Proc. Instn Mech. Engrs 1964, Vol. 179, Pt. 3C. paper 8.

44. Gellales, A.G. "Coefficient of Discharge of Fuel Injection Nozzles for Compression Ignition Engines". NACA Report 373, 1931.

45. General Electric Company, "Properties of Combustion Gases /System: $C_n H_{2n}$-Air." Vol. 1 and 2 G.E.C. Aircraft Gas Turbine Development Department, Cincinnati, Ohio, U.S.A., 1955.

46. Giffen, E. "The Atomisation of Liquid Fuels". Chapman and Hall, London, 1953, p. 246.

47. Gray, P. and Harper, M.J. "Thermal Explosions part I. Induction Period and Temperature Changes before Spontaneous Ignition". Trans. Far. Soc., Vol. 55, pt. 4, 1959, p. 581-590.

48. Hassan, H. "Unsteady Heat Transfer in a Motored Internal Combustion Engine". 1968. Loughborough Univ. of Tech., Ph.D. Thesis.

49. Hassan, H. "Unsteady Heat Transfer in a Motorec I.C. Engine Cylinder". Proc. Instn Mech. Engrs , 1970-71, Vol. 185.

50. Henein, N. "Instantaneous Heat Transfer Rates and Coefficients between the Gas and Combustion Chamber of a Diesel Engine". SAE Paper No. 969B, 1965.

51. Henein, N.A. "Analysis of Pollutant Formation and Control and Fuel Economy in Diesel Engines". Prog. Energy Combust. Sci., Vol. 1, pp. 165-207, 1976.

52. Hinhselwood, C. "Kinetics of Chemical Change". Oxford, London, 1949.

53. Hottel, H.C. "Radiant Heat Transmission". Chapter III in 'Heat Transmission' by McAdams, McGraw-Hill Book Co., 1954.

54. Hussmann, A. "Measurement of Air Movements in Internal Combustion Engine Cylinders". DISA Information, No. 8, July 1969.

55. Ilmari, E.J. "The Spray Impingement Theory of Ignition Delay in Small Swirl Chamber Diesel Engine". Ph.D. Thesis, Institute of Technology, Helsinki, 1965.

56. Jankov, R. "Flow Phenomena and Mixture Formation in Swirl Chamber Diesel Engines". Translated from German text on behalf of Perkins Engines Company, Peterborough, England, November, 1972.

57. Jobson, D.A. "On the Flow of a Compressible Fluid through Orifices". Proc. Instn Mech. Engrs , Vol. 169, No. 37, 1955.

58. Kamel, M. "A Study of Diesel Engine Simulation and Performance Prediction". M.Sc. Thesis, Imperial College, 1973.

59. Kamimoto, T., Matsouka, S., Matsui, Y. and Aoyagi, Y. "The Measurement of Flame Temperature and the Thermodynamic Analysis of the Combustion Process in a Direct Injection Diesel Engine". Paper C96/75, Proc. Instn mech. Engrs, 1975.

60. Knight, B. "The Problem of Predicting Heat Transfer in Diesel Engines". Proc. Instn Mech. Engrs , 1964-65, Vol. 179, pt. 3G.

61. Krieger, R.B. and Borman, G.L. "The Computation of Apparent Heat Release for Internal Combustion Engines". ASME paper No. 66-WA/DGP-4, 1966.

62. Kunitomo, T. "Mean Emissivity of a Luminous Flame". Heat Transfer-Japanese Research, Vol. I, No. 2, 1972, pp. 57-64.

63. Kunitomo, T. and Kodama, K. "Radiation from Luminous Flame at High Pressures". Bulletin of the JSME, Vol. 17, No. 113, 1974, pp. 1486-1493.

64. Lancaster, D., Krieger, R. and Lienesch, J. "Measurement and Analysis of Engine Pressure Data". SAE paper 750026, Vol. 84, 1975.

65. Landen, E.W. "Combustion Studies of the Diesel Engine". SAE Journal, Vol. 54, 1946, p. 270.

66. Lefeuvre, T., Myers, P. and Uyehara, O. "Experimental Instantaneous Heat

54. Fluxes in a Diesel Engine and their Correlation". SAE No. 690464, 1969.

67. Lewis, G.D. Thirteenth Symposium on Combustion, pp. 625-629. The Combustion Institute, 1971.

68. Lightarowicz, A., Duggins, R.K. and Markland, E. "Discharge Coefficients for Incompressible Non-Cavitating Flow through long Orifices". J. Mech. Engng Sci., 1965, no. 7, p. 210 , ASME Trans.

69. Lyn, W.T. "Diesel Combustion Study by Infra Red Emission Spectroscopy". J. Inst. Pet. Vol. 43, 1957.

70. Lyn, W.Y. and Valdmanis, E. "The Effects of Physical Factors on Ignition Delay". Proc. Instn of Mech. Engrs, Vol. 181, Pt2A, no. 1, 1966-67.

71. Lyn, W.T. and Valdmanis, E. "The Application of High Speed Schlieren Photography to Diesel Combustion Research". J. Photo. Science, 1962, 10.

72. Lyn, W.T., Samaga, B.S. and Bowden, C.M. "Rate of Heat Release in High Speed Indirect Injection Diesel Engines". Proc. Instn Mech. Engrs , 1969-70, Vol. 184, Pt. 3J-paper 12.

73. Marzouk, M. "Transient Response of Turbocharged Diesel Engines". Ph.D. Thesis, Imperial College, ,1976.

74. Moon, L.F. and Rudinger, G. "Velocity Distribution in an Abruptly Expanding Circular Duct". Transaction of the ASME, Journal of Fluids Engineering, March 1977.

75. Morris, C.J. and Dent, J.C. "The Simulation of Air Fuel Mixing in High Swirl Open Chamber Diesel Engines". Proc. Instn Mech. Engrs,. 1976, Vol. 190, 47/76.

76. Nagao, F. and Jakimoto, H. "The Combustion Process in Swirl Chamber Type Diesel Engines". Memoirs of the Faculty of Engineering, Kyoto University, Vol. 22, 1960, p. 176.

77. Nagao, F., Ikegami, M. and Miyashita, N. "The Relationship between Rate of Pressure Rise and Connecting Passage Area in a Swirl Chamber Type Diesel Engine". Bulletin of JSME, Vol. 7, No. 27, 1976.

78. Nagao, F., Ikegami, M. and Banbaj, T. "Air Motion and Combustion in Swirl Chamber Type Diesel Engine". Bulletin of JSME, Vol. 10, No. 41, 1967.

79. Nagao, F. and Kakimoto, H. "Swirl and Combustion in Divided Combustion Chamber Type Diesel Engines". SAE Trans. 70, 680-699, 1962.

80. Nakajima, K. "An Experimental Research on the Air Swirl Motion and Combustion in the Swirl Chamber of Diesel Engines". XII FISITA Congress, Barcelona, 1968.

81. Oguri, T. and Inabo, S. "Radiant Heat Transfer in Diesel Engines". SAE Trans. Vol. 81, 1972, paper 720023.

82. Oguri, T. and Kunitomo, T. "Prediction of Radiative Heat Flux in a Diesel Engine". SAE paper no. 750786, 1975.

83. Okaya, T. "On the Friction to the Disc Rotating in a Cylinder". Jap. J. of Physics, Vol. XIII, No. 1, 1939.

84. Patrick, M.A. "Experimental Investigation of Mixing and Flow in a Round, Turbulent Jet injected perpendicularly into a Main Stream". Sheffield Univ. Fuel Society Bulletin, 1965.

85. Patrick, M.A. "Experimental Investigation of Mixing and Flow in a Round, Turbulent Jet injected perpendicularly into a Main Stream". Ph.D. Thesis, Sheffield Univ., 1965.

86. Pedersen, P.S. and Quale, B. "A Model for the Physical Part of the Ignition Delay in a Diesel Engine". SAE Paper No. 740716, 1974.

87. Perez, J.M. and Landen, E.W. "Exhaust Emission Characteristics of Precombustion Chamber Engine". SAE Paper 680421, 1968.

88. Powell, H.N. "Application of an Enthalpy-Fuel/Air Ratio Diagram to 'First Law' Combustion Problems". ASME, Gas Turbine Power and Machine Design Divisions, Semi-Annual Meeting, Cleveland, Ohio, 17-21 June, 1956.

89. Ricardo, H.R. "The High Speed Internal Combustion Engine". 1953, Blackie, London.

90. Schmidt, F.A.F. "Theoretische Untersuchungen und Versuche uber Zundverzug und Klopfvorgang" VDI-Forschungsheft 392, 1938.

91. Scott, N.M. "Noise of small Indirect Injection Diesel Engines". SAE Internation Automotive Engineering Congress, Detroit, Michigan, paper 730242, January 1973.

92. Semenov, E. "Studies of Turbulent Gas Flow in Piston Engines" "Combustion in Turbulent Flow". Translated from Russian.

93. Shimamoto, Y. "A Study of Squish in Open Combustion Chamber of a Diesel Engine". Bulletin. JSME, 1970, 13, 1096-1103.

94. Shroff, H.D. "The Simulation and Optimisation of the Thermodynamic Processes of a Diesel Engine". Ph.D. Thesis, 1971, Cranfield Inst. of Techn.

95. Shroff, H.D. and Hodgetts, D. "Simulation and Optimisation of Thermo-Dynamic Processes of Diesel Engine". SAE Paper 740194, Vol. 83, 1974.

96. Sitkei, G. "Uber den Dieselmotorischen Zundverzug" MTZ, 24 Ig, Heft 6, Juni 1963, p. 190-194.

97. Sitkei, G. "A Rational Approach for Calculation of Heat Transfer in Diesel Engines". SAE Paper 720027, 1972.

98. Sitkei, G. "Heat Transfer and Thermal Loading in Internal Combustion Engines". Budapest, 1974.

99. Stanton, T.E. "The Flow of Gases at High Speeds". Proc. Roy. Soc. A., Vol. 111, p. 306, 1926.

100. Statement by Daimler-Benz before the Subcommittee on Air and Water Pollution, Committee on Public Works, United States Senate, Ninety-Third Congress, First Session, May 14, 17, 18 and 21, 1973, Serial No. 93-H9, U.S. Government Printing Office, Washington, D.C., 1973.

101. Stock, D. "Untersuchungen Der Gemischbildings, Zund und Verbrennungs-vorgange eines Directeinspritzenden Diesel Motors". Dr. Ing. Dissertation, T.U. Berlin, July 1970.

102. Streit, E.E. and Borman, G.L. "Mathematical Simulation of a Large Turbocharged Two-Stroke Diesel Engine". Trans. SAE paper 71076, 1971.

103. Tanaka, S., Seki, S. and Nakamura, H. "An Example of Development in Automotive Small High Speed Diesel Engine". SAE Paper No. 978C, Int. Auto. Engng Congress, Detroit, 1965.

104. Taylor, C.F. and Taylor, E.S. "Ignition of Fuels by rapid Compression". SAE Trans. Vol. 4, 1950, p. 232-274.

105. Torpey, P.M., Whitehead, M.J. and Wright, M. "Experiments in the Control of Diesel Emissions". Paper C 124/7, presented at Conference on Air Pollution in Transport Engines, Institute of Mechanical Engineers, Solihull, England, Nov. 9-11, 1971.

106. Trengrouse, G.H., Inrie, B.W. and Male, D.H. "Comparison of Unsteady Flow Discharge Coefficients for Sharp-Edged Orifices with Steady Flow Values". ASME Trans., J. of Mechanical Engineering Science, Vol. 8, No. 3, 1966.

107. Tsao, K.C., Myers, P.S. and Uyehara, O.A. "Gas Temperatures during Compression in Motored and Fired Diesel Engines". SAE Trans. 1962, 70, 136.

108. Ubbelohde, A.R. "Survey of Collision Processes in the Combustion of Hydro-Carbons". Fifth Int. Symp. on Combustion, Reinhold, New York, 1955, p. 74-79.

109 Uyehara, O.A., Myers, P.S., Watson, K.M. and Wilson, L.A. "Diesel Combustion Temperatures - The Influence of Operating Variables". ASME Trans. Vol. 69, 1947.

110 Wakuri, K. "Studies on the Penetration of Fuel Spray in a Diesel Engine". Bull. JSME., 1969, Vol. 3, No. 9.

111 Walder, C.J. "Reduction of Emissions from Diesel Engines". SAE International Automotive Engineering Congress, Detroit, Michigan, paper 730213, 1973.

112 Walder, C.J. "Some Problems Ecountered in the Design and Development of High Speed Diesel Engines". SAE Paper 978A, 1965.

113 Whitehouse, N.D. "Heat Transfer in a Quiscent Chamber Diesel Engine". Proc Instn Mech. Engrs , Vol. 185, 1971-72, pp. 963-975.

114 Williams, T.J., Tindal, M.J. and El Khafagi, A.H. "Gas Flow Measurements in Engines Cylinders". SAE Paper No. 740719, 1974.

115 Witze, P.O. "Measurements of the Spatial Distribution and Engine Speed Dependence of Turbulent Air Motion in an I.C. Engine". SAE Paper No. 770220, International Automotive Engineering Congress and Exposition, Cobo Hall, Detroit, February 28th-March 4th, 1977.

116 Wolfer, H.H. "Der Zundverzug im Diesel-motor". VDI Forschungsheft, 392, 1938, p. 15-24.

117 Woschni, G. "A Universally Applicable Equation for the Instantaneous Heat Transfer Coefficient in the Internal Combustion Engine". Paper 670931 presented at SAE Combined National Meetings, Pittsburgh, Oct. 1967.

118 Zimmermann, K.D. "Uber den Zundverzug bei der Diesel Motorischen Verbrennung". Diss. Karlsruhe, 1962, p. 138.

Errata

After binding this thesis, a mistake was discovered in the numbering of pages; page 87 should precede page 113. The reader should take this into consideration.

Page	Line	Error	Correction
31	26	Frouds	Froude
43	9	case	care
43	14, 27	DLCB	DLCU
51	3	mas	mass
55	10	$(\gamma-1)$	$2(\gamma-1)$
63	3rd Box	enery	energy
67	26	for	from
80	3	at	of
84	10-21	Re	Re_d
90	1	29	2g
113	12, 14, 16	x_w	x
114	20	analysus	analysis
145	13, 15	F	F_d
148	11	β	β_b
154	1	$p_w - p_o$	p_w/p_o
155	8	ratios	ratio
158	28	18	68
181	23	t	t_d
182	6	$(\frac{\bar{n}}{2} - 1)$	$(\frac{\bar{n}}{2} - 1)$!
182	19	t	t_d
193	22	chambeer	chamber
205	17	ne	be
234	5	monitoring	motoring
237	20	25	26
243	14	then	than
246	11	(8.1)	(7.1)
257	2	39	38
257	12	neat	near
261	4	$- C_d -$	$- C_{d2}$
285	12	C/A	(C)
288	Fig. (8.18)	ROHR Shifting	ROHR Curve
290	9	in	ROHR,
290	21	8.18	8.19
309	25	W.J.	W.J.,Ma,T.H.
312	22	246	146